THE UNIVERSITY *of* EDINBURGH

THE UNIVERSITY
of EDINBURGH

Assessing the potential for Compressed Air Energy Storage using the offshore UK saline aquifer resource

Julien Mouli-Castillo

Thesis submitted in fulfilment of
the requirements for the degree of
Doctor of Philosophy
to the
University of Edinburgh
March 2018

Abstract

In the context of the development of renewable energy sources in the U.K., and of the increase in anthropogenic atmospheric CO_2, it is important to develop alternative ways of providing energy to the community. The shift to renewable sources of electricity comes to a cost: variable generation. At present, an important part of the renewable electricity capacity is being curtailed during low demand periods. One way to ensure that electricity supply matches demand is to store excess energy when it is available and deliver it when demand cannot be met by primary generation alone. Compressed Air Energy Storage (CAES) allows this storage. The aim of this project is to build upon existing knowledge on CAES using porous rocks (PM-CAES) to assess the technical feasibility for this storage technology to be developed offshore of the UK. The focus is on inter-seasonal storage. This assessment is undertaken by developing geological and power plant models to calculate the storage potential of offshore UK formations. Modelling of a conceptual aquifer air store enables approximations of the subsurface pressure response to CAES operations. These pressure changes are coupled with surface facilities models to provide estimates of both load/generation capacity and roundtrip efficiencies. Algebraic predictive models can be developed from the results of a sensitivity analysis of the store and plant idealised models. Screening of the CO_2 Stored database, containing data on geological formations offshore of the UK (initially developed for CO_2 storage), was then performed to estimate PM-CAES potential using the predictive models. The results suggest that there is substantial PM-CAES potential in the UK. Results indicate an energy storage potential in the range of 77-96 TWh, which can be released over 60 days. A geographic information system (GIS) study was then performed to identify the portion of the identified storage potential colocated with offshore windfarm. 19 TWh of the storage potential identified is colocated with windfarm and would be achievable at an average levelised cost of electricity of 0.70 £/kWh.

Lay Summary

In the context of the development of electricity generation from renewable energy sources in the U.K., and of the rise in man-made carbon greenhouse gases emissions, including carbon dioxide, it is important to develop alternative ways of providing energy to society. The shift to renewable sources of electricity comes at a cost: variable generation. At present, an important part of the renewable electricity capacity is not being generated when the need for electricity is low, for example in the height of summer or at night time. Indeed, it is a common occurrence that windfarms are prevented from generating electricity. However, this has to be done because electricity has to be consumed or transported as soon as it is generated. A deficit or an excess can result in a failure of the entire UK electrical grid. A few methods exist to prevent these failures from happening, all of which aim at balancing out the demand and supply of electricity. One of those methods is to store excess electricity when it is available and deliver it when demand cannot be met by installed power plants or renewables alone. Compressed Air Energy Storage (CAES) allows this storage. This technology consist in using excess electricity when the society does not need it to compress air underground. The pressurised air remains stored for a duration of hours to months. When electricity demand is high and, for example, wind is not blowing, then the stored air can be released through a turbine capable of generating electricity. The aim of this project is to build upon existing knowledge on CAES using porous rocks (PM-CAES) to assess the technical feasibility for this storage technology to be developed offshore of the UK. The idea, is to store the air within the mm-scale gaps within rocks, such as sandstone. Offshore UK vast amounts of these porous rocks can be found, most of which are soaked in very saline water unusable for drinking, and are called saline aquifers. These rocks represent millions of meters cubed of storage volumes. The focus is to study inter-seasonal storage between summer and winter. This assessment is undertaken by developing computer models of the porous rock store and the surface plant containing the compressor and turbine, in order to calculate the storage potential of offshore UK porous rocks. Mathematical predictive models can be developed from the results of the store and plant computer models, these have the advantage that they are simpler to use than computer models. Screening of the CO_2 Stored database, containing data on saline aquifers offshore of the UK (initially developed for CO_2 storage), was then performed to estimate PM-CAES storage potential using the predictive models. The results suggest that there is substantial PM-CAES potential in the UK. Results indicate an energy storage potential in the range of 77-96 TWh, which can be released over 60 days. This storage is equivalent to about 160% of the UK's electricity consumption for January and February of 2017. This study was

also able to identify areas offshore UK which contain 19 TWh of the storage potential and are located underground windfarms.

Declaration and attribution of work

I declare that this thesis has been composed solely by myself and that it has not been submitted, in whole or in part, in any previous application for a degree. Except where stated otherwise by reference or acknowledgment, the work presented is entirely my own.

Julien Mouli-Castillo

March 2018

Acknowledgements

I would like to thank my principal supervisor Dr. Mark Wilkinson from the University of Edinburgh, for always keeping a door open (literally) for my questions and doubts. He gave me the time, technical support and guidance I needed, first as a mentor and then as a colleague, without him the project would never have reached this stage. I would also like to thank my supervisor Dr. Chris McDermott from the University of Edinburgh, for taking the time to share with me his technical expertise and supporting me at times of doubt. He gave me a taste for modelling which shaped my research interests. A thank you is also in order for my supervisor Dr. Dimitri Mignard from the University of Edinburgh, whose help and passion was invaluable in getting some understanding of the field of mechanical engineering through a one-of-a-kind franco-english dialect. I would also like to thank my supervisor Prof. R. Stuart Haszeldine from the University of Edinburgh for sharing with me his valuable insight making sure this project kept a foot in reality. Last but not least, I would like to thank my supervisor Prof. Zoe Shipton from the University of Strathclyde, for offering me an opportunity outside of the University of Edinburgh, to share my research and thoughts, through demonstrating opportunities and research group meetings. Finally I would like to say that despite having had five supervisors, I was given the freedom I needed to be in control of the project and allowed to make mistakes as a growing researcher.

I would like to thank the funders of the project: EPSRC, ETP and Scottish Power without whom the project would not have been possible. I would like to thank all the members of the GeoEnergy research group for providing a space to discuss ideas and get feedback. In particular, to Dr. Andrew Fraser Harris from the University of Edinbrugh, for his friendly advice and help with OpenGeoSys. I am grateful to Dr. Mark Naylor from the University of Edinbrugh, for taking some time to meet when I needed it. I would like to thank Dr. Wenqing Wang of UFZ for answering any queries I had regarding OpenGeoSys.

Un grand Merci à tous mes amis ‘Les Joyeux Galériens’ et le ‘Chatals’ pour leur soutien, malgré la distance et les obligations de chacun. Vous m’avez tous bien aide à profiter de la vie en dehors du doctorat!

Merci également à toute ma famille pour leur incessant soutien dans toutes les épreuves que j’ai eu à traverser jusqu’à present. Maman, Papa, merci d’avoir toujours cru en moi quand je ne le pouvais pas moi- même.

Finally, I am deeply grateful to Emma for her constant support and understanding; for putting up with me when I was upset and sharing my joy when I was happy

Contents

List of Figures

List of Figures

List of Figures

List of Tables

List of Tables

List of Tables

List of Tables

List of Symbols

Symbol	Description	Units Used	SI Units	SI Base Units	Dimensions
$^{*}P_{wc}$	Well collapse pressure after store depletion	bar	Pa	$kg \cdot m^{-1} \cdot s^{-2}$	$ML^{-1}T^{-2}$
·	Denotes derivative over time				
A	Flow area	m^2	m^2	m^2	L^2
A	coefficient matrix	-	-	-	-
c_p	Constant pressure specific heat capacity	$J \cdot kg^{-1} \cdot K^{-1}$	$J \cdot kg^{-1} \cdot K^{-1}$	$m^2 \cdot K^{-1} \cdot s^{-2}$	$L^2T^{-2}\Theta^{-1}$
C_t	Compressor investment expenditure	US$ 2015			
c_v	Constant volume specific heat capacity		$J \cdot kg^{-1} \cdot K^{-1}$	$m^2 \cdot K^{-1} \cdot s^{-2}$	$L^2T^{-2}\Theta^{-1}$
d	Pore throat diameter	m	m	m	L
div	Divergence operator				
D_t	Decommissioning expenditure	US$ 2015			
e	Exponential notation				
E_{cv}	Total energy in control volume	Wh	J	$kg \cdot m^2 \cdot s^{-2}$	ML^2T^{-2}
E_f	Thermal energy resulting from fuel combustion	Wh	J	$kg \cdot m^2 \cdot s^{-2}$	ML^2T^{-2}
E_M	Electrical energy consumed by the compressor	Wh	J	$kg \cdot m^2 \cdot s^{-2}$	ML^2T^{-2}
E_{mass}	Energy associated with a mass (i.e. kinetic and potential energy)	Wh	J	$kg \cdot m^2 \cdot s^{-2}$	ML^2T^{-2}
E_T	Electrical energy produced by the turbine	Wh	J	$kg \cdot m^2 \cdot s^{-2}$	ML^2T^{-2}
E_t	Electrical energy produced	Wh	J	$kg \cdot m^2 \cdot s^{-2}$	ML^2T^{-2}
f_f	Fanning friction coefficient	dimensionless	dimensionless	dimensionless	dimensionless
f	Feed mass flow rate	$kg \cdot s^{-1}$	$kg \cdot s^{-1}$	$kg \cdot s^{-1}$	MT^{-1}
f_D	Darcy-Weisbach friction factor	dimensionless	dimensionless	dimensionless	dimensionless
F	flux	$kg \cdot m^{-2} \cdot s^{-1}$	$kg \cdot m^{-2} \cdot s^{-1}$	$kg \cdot m^{-2} \cdot s^{-1}$	$ML^{-2}T^{-1}$
F_i	Feed molar flow rate	mol/s	mol/s	mol/s	T-1
F_t	Fuel expenditure	US$ 2015			
g	Acceleration due to gravity	$m \cdot s^{-2}$	$m \cdot s^{-2}$	$m \cdot s^{-2}$	LT^{-2}
grad	Gradient operator				
h	Specific enthalpy	$J \cdot kg^{-1}$	$J \cdot kg^{-1}$	$m^2 \cdot s^{-2}$	L^2T^{-2}
h_a	Height of air layer inside the store	m	m	m	L

List of Symbols

h_F	Formation thickness	m	m	m	L
$H_{combustion}$	Heat produced by combustion of one mole of methane and air	$J \cdot mol^{-1}$	$J \cdot mol^{-1}$	$kg \cdot m^2 \cdot s^{-2} \cdot mol^{-1}$	
i	Hydraulic gradient	dimensionless	dimensionless	dimensionless	dimensionless
K	Hydraulic conductivity	$m \cdot s^{-1}$	$m \cdot s^{-1}$	$m \cdot s^{-1}$	LT^{-1}
k	Intrinsic permeability	mD	m^2	m^2	L^2
k_{eff}	Effective permeability	mD	m^2	m^2	L^2
$k_{rel,w}$	Water relative permeability	-	-	-	-
$k_{rel,\alpha}$	Relative permeability of phase alpha	-	-	-	-
k_α	Effective permeability of phase alpha	mD	m^2	m^2	L^2
L	Length	m	m	m	L
$\dot{m}$	Mass flow rate	$kg \cdot s^{-1}$	$kg \cdot s^{-1}$	$kg \cdot s^{-1}$	MT^{-1}
M	Mass matrix	-	-	-	-
M_t	Fixed operation and maintenance expenditure	US$ 2015			
m_{TGV}	Mass of total gas volume stored	kg	kg	kg	M
n	normal vector to boundary	-	-	-	-
n	Polytropic exponent	-	-	-	-
n	time index of solution	-	-	-	-
Nj	Shape function used to interpolate between two nodes	-	-	-	-
Ni	weighting function equal to shape function	-	-	-	-
n	Number of moles	mol	mol	mol	
n	Project lifetime	years	s	s	T
p	combustion product mass flow rate	$kg \cdot s^{-1}$	$kg \cdot s^{-1}$	$kg \cdot s^{-1}$	$M \cdot T^{-1}$
P	combustion product molar flow rate	$mol \cdot s^{-1}$	$mol \cdot s^{-1}$	$mol \cdot s^{-1}$	T-1
P_a	Air pressure	bar	Pa	$kg \cdot m^{-1} \cdot s^{-2}$	$ML^{-1}T^{-2}$
p_c	Capillary pressure	bar	Pa	$kg \cdot m^{-1} \cdot s^{-2}$	$ML^{-1}T^{-2}$
p_F	Pressure at the formation edge	bar	Pa	$kg \cdot m^{-1} \cdot s^{-2}$	$ML^{-1}T^{-2}$
P_{sc}	Pressure at standard conditions		Pa	$kg \cdot m^{-1} \cdot s^{-2}$	$ML^{-1}T^{-2}$
P_{wc}	Well collapse pressure before store depletion	bar	Pa	$kg \cdot m^{-1} \cdot s^{-2}$	$ML^{-1}T^{-2}$
P_x	Intermediate pressure between two compression or expansion stages	bar	Pa	$kg \cdot m^{-1} \cdot s^{-2}$	$ML^{-1}T^{-2}$

List of Symbols

P_α	Phase alpha pressure	bar	Pa	$kg \cdot m^{-1} \cdot s^{-2}$	$ML^{-1}T^{-2}$
Q	Volumetric flow rate	$m^3 \cdot s^{-1}$	$m^3 \cdot s^{-1}$	$m^3 \cdot s^{-1}$	L^3T^{-1}
q	mass flow rate	$kg \cdot s^{-1}$	$kg \cdot s^{-1}$	$kg \cdot s^{-1}$	MT^{-1}
$\dot{Q}_{cv}$	Heat transfer rate between control volume and surroundings	$J \cdot kg^{-1}$	$J \cdot kg^{-1}$	$m^2 \cdot s^{-2}$	L^2T^{-2}
R	specific molar gas constant	$J \cdot kg^{-1} \cdot K^{-1}$	$J \cdot kg^{-1} \cdot K^{-1}$	$m^2 \cdot s^{-2} \cdot K^{-1}$	$L^2T^{-2}\Theta^{-1}$
r	sources and sinks term	$m^3 \cdot s^{-1}$	$m^3 \cdot s^{-1}$	$m^3 \cdot s^{-1}$	L^3T^{-1}
r	Discount rate	-	-	-	-
Re	Reynold number	-	-	-	-
r_F	Formation radius	m	m	m	L
r_w	Well radius	m	m	m	L
S	Entropy	$J \cdot K^{-1}$	$J \cdot K^{-1}$	$kg \cdot m^2 \cdot s^{-2} \cdot K^{-1}$	$ML^2T^{-2}\Theta^{-1}$
s	Number of compression or expansion stages				
S_e	Effective water saturation of a porous medium	-	-	-	-
S_{gen}	Entropy generation	$J \cdot K^{-1}$	$J \cdot K^{-1}$	$kg \cdot m^2 \cdot s^{-2} \cdot K^{-1}$	$ML^2T^{-2}\Theta^{-1}$
S_i	First order sensitivity index	dimensionless	dimensionless	dimensionless	dimensionless
$S_{r\alpha}$	Residual saturation of phase alpha	-	-	-	-
S_t	Compressor electricity expenditure	US$ 2015			
S_{Ti}	Total order sensitivity index	dimensionless	dimensionless	dimensionless	dimensionless
S_w	Water saturation	-	-	-	-
t	time	s	s	s	T
T	Temperature	C or K	K	K	Θ
T_b	Thermodynamic temperature at the boundary of the system	K	K	K	Θ
T_{sc}	Temperature at standard conditions	C or K	K	K	Θ
T_t	Turbine investment expenditure	US$ 2015			
u	The solution to the multiphase flow problem				
$\tilde{u}$	the approximate solution				
$\hat{u}$	the discrete value of the solution				
$\bar{u}$	Specific internal energy	$J \cdot kg^{-1}$	$J \cdot kg^{-1}$	$m^2 \cdot s^{-2}$	L^2T^{-2}
v	Specific discharge, air velocity	$m \cdot s^{-1}$	$m \cdot s^{-1}$	$m \cdot s^{-1}$	LT^{-1}
V	Volume, control volume	m^3	m^3	m^3	L^3

List of Symbols

v	Velocity	$m \cdot s^{-1}$	$m \cdot s^{-1}$	$m \cdot s^{-1}$	LT^{-1}
$\bar{v}$	Specific volume	$m^3 \cdot kg^{-1}$	$m^3 \cdot kg^{-1}$	$m^3 \cdot kg^{-1}$	L^3M^{-1}
$\mathbf{v}_a$	Average fluid velocity	$m \cdot s^{-1}$	$m \cdot s^{-1}$	$m \cdot s^{-1}$	LT^{-1}
V_h	Pore volume filled with hydrocarbons contained within geological traps	m^3	m^3	m^3	L^3
V_{traps}	Pore volume contained within geological traps	m^3	m^3	m^3	L^3
V_{usable}	Pore volume which can be used to store air	m^3	m^3	m^3	L^3
$\mathbf{v}_\alpha$	Phase alpha velocity	$m \cdot s^{-1}$	$m \cdot s^{-1}$	$m \cdot s^{-1}$	LT^{-1}
W	weighting function used in Finite Element Method	-	-	-	-
W	work	Wh	J	$kg \cdot m^2 \cdot s^{-2}$	ML^2T^{-2}
$\dot{W}_{sys}$	Work flow rate outside control volume	$J \cdot kg^{-1}$	$J \cdot kg^{-1}$	$m^2 \cdot s^{-2}$	L^2T^{-2}
W_{is}	Work from an isentropic process	Wh	J	$kg \cdot m^2 \cdot s^{-2}$	ML^2T^{-2}
W_{real}	Work from a real process	Wh	J	$kg \cdot m^2 \cdot s^{-2}$	ML^2T^{-2}
W_{rev}	Work from a reversible process	Wh	J	$kg \cdot m^2 \cdot s^{-2}$	ML^2T^{-2}
W_t	Well investment expenditure	US$ 2015			
Z	Compressibility factor	dimensionless	dimensionless	dimensionless	dimensionless
α	Storage pressure parameter	-	-	-	-
ΔE_{sys}	Change in total energy of a system	Wh	J	$kg \cdot m^2 \cdot s^{-2}$	ML^2T^{-2}
ΔKE	Change in kinetic energy of a system	Wh	J	$kg \cdot m^2 \cdot s^{-2}$	ML^2T^{-2}
ΔPE	Change in potenital energy of a system	Wh	J	$kg \cdot m^2 \cdot s^{-2}$	ML^2T^{-2}
δQ	Differential heat transferred between a system and its surroundings	J	J	$kg \cdot m^2 \cdot s^{-2}$	ML^2T^{-2}
ΔT	Geothermal gradient	$°C \cdot km^{-1}$	$K \cdot m^{-1}$	$K \cdot m^{-1}$	$ΘL^{-1}$
ΔU	Change in internal energy of a system	Wh	J	$kg \cdot m^2 \cdot s^{-2}$	ML^2T^{-2}
ε	Well absolute roughness	m	m	m	L
η_c	Compressor efficiency	-	-	-	-
η_{ee}	Overall CAES system efficiency (Liu et al. 2014)	-	-	-	-
η_h	Ratio of V_h to V_{traps}	-	-	-	-
η_{is}	Isentropic efficiency	- or %	-	-	-
η_{NG}	Efficiency with which fuel energy is converted to electrical energy	- or %	-	-	-
η_{pol}	Polytropic efficiency	-	-	-	-

List of Symbols

η_{RT}	Roundtrip efficiency	- or %	-	-	-
$\eta_{storage}$	Fraction of total formation pore volume usable for air storage	-	-	-	-
η_{sys}	System efficiency	-	-	-	-
η_T	Turbine efficiency	- or %	-	-	-
θ	Contact angle	degrees or radians	rad	rad	rad
κ	Thermal conductivity of the rock surrounding the well	$W \cdot m^{-1} \cdot K^{-1}$	$W \cdot m^{-1} \cdot K^{-1}$	$kg^1 m^1 s^{-3} K^{-1}$	$M^1 L^1 T^{-3} \Theta^{-1}$
λ	Pore size distribution index	-	-	-	-
μ	Dynamic viscosity	Pa·s	Pa·s	$kg \cdot m^{-1} \cdot s^{-1}$	$ML^{-1}T^{-1}$
μ_a	Air dynamic viscosity	Pa·s	Pa·s	$kg \cdot m^{-1} \cdot s^{-1}$	$ML^{-1}T^{-1}$
μ_w	Water dynamic viscosity	Pa·s	Pa·s	$kg \cdot m^{-1} \cdot s^{-1}$	$ML^{-1}T^{-1}$
μ_α	Phase alpha dynamic viscosity	Pa·s	Pa·s	$kg \cdot m^{-1} \cdot s^{-1}$	$ML^{-1}T^{-1}$
ρ	Density	$kg \cdot m^{-3}$	$kg \cdot m^{-3}$	$kg \cdot m^{-3}$	ML^{-3}
ρ_W	Water density	$kg \cdot m^{-3}$	$kg \cdot m^{-3}$	$kg \cdot m^{-3}$	ML^{-3}
σ	Interfacial tension	$dyn \cdot cm^{-1}$	$N \cdot m^{-1}$	$kg \cdot s^{-2}$	MT^{-2}
σ_{max}	Maximum horizontal stress acting on the well	Pa or bar	Pa	$kg \cdot m^{-1} \cdot s^{-2}$	$ML^{-1}T^{-2}$
σ_{min}	Minimum horizontal stress acting on the well	Pa or bar	Pa	$kg \cdot m^{-1} \cdot s^{-2}$	$ML^{-1}T^{-2}$
τ_0	Cohesive rock strength	Pa or bar	Pa	$kg \cdot m^{-1} \cdot s^{-2}$	$ML^{-1}T^{-2}$
ϕ	Porosity	- or %	-	-	-
ϕ	Rock friction angle	degrees or radians	radians	radians	radians
ϕ_α	Volume fraction occupied by phase alpha	-	-	-	-
Γ	Domain boundary	-	-	-	-
Γ_D	Boundary on which Dirichlet boundary conditions apply	-	-	-	-
Γ_N	Boundary on which Neumann boundary conditions apply	-	-	-	-
w	Finite Difference parameter	-	-	-	-

List of Symbols

Chapter 1 Introduction

1.1 Background

"Electricity", a term first coined by William Gilbert in 1600, has been of great importance to mankind since the invention of the electrical telegraph in the 19th century (Gilbert, 1600; Meyer, 1971). Electricity is part of everyday life, essential to communication, lighting, heating and much more, hence, continuous electricity supply is essential to society. Electricity is characterized by the flow of negatively charged electrons through a conductive medium. It results from the rotation of an electromagnet inside coils of conductive materials. For example, in a power station, steam is produced using heat from either fossil fuel combustion, or nuclear fission. This steam is used to drive a turbine, causing the rotation of a shaft on which an electromagnet is attached. Many large coils are located around the electromagnet causing a large flow of electrons, i.e. electricity. Unfortunately, just as the flow of water in a stream cannot be stored, electricity in the form of a flow of electrons, cannot be stored either, and as a result, needs to be consumed as it is generated. Consequently, the conversion of electricity to another form of energy and the subsequent storage of that energy, is an important field of research on the world scene.

1.2 The Need for Electricity Storage

To tackle the issue of climate change, it is widely acknowledged that reducing greenhouse gas emissions, by shifting the energy sector towards renewable energy sources, is essential (UN, 2015). The shift to renewable energy sources, and the variability in 'primary' energy, such as wind, or solar radiation, puts the challenge of electrical energy storage in the forefront of modernisation.

Renewable electricity generation is increasing, yet, the actual amount of electricity generated from infrastructure capable of converting 'primary' energy into electricity is much less than would be achieved if primary energy was constantly available when needed, in order to match the electricity demand. This discrepancy is known as the capacity factor, which for wind turbines is around 30 to 40% (Cavallo, 1995). One way to increase the reliable generation capacity of existing renewable generation assets, and to mitigate against the natural variability in primary energy and fluctuations in electricity demand, is to convert and store excess electricity as another form of energy. Hereafter electricity conversion and storage will be simply referred to as "electricity storage". Adding the appropriate means of storing electricity is therefore essential for modern power systems to increase their reliance on variable renewable electricity generation.

Introduction

The need for electricity storage covers a wide range of energy capacities (i.e. amounts of energy), power capacities (i.e. rate at which energy can be stored and delivered), and time scales (i.e. duration of a storage cycle, from electricity conversion, to storage, and to redelivery). In power systems where over 80% of electricity generation is achieved using renewable energy sources, inter-seasonal storage of electricity is required to ensure electricity demand can be met throughout the year (Elliott, 2016). Such storage has to accommodate vast amounts of energy and offer a power output in the range of 100s of MW to GW. No technology capable of meeting this need is currently available (Blanco and Faaij, 2018). Yet, surprisingly little research has been done on inter-seasonal grid-connected electricity storage. This is why it will be the focus of this study.

First of all it is important to consider if commercially proven and widely used technologies could be used to address inter-seasonal storage. Currently 98% of the 165 GW of large scale electricity storage, connected to power grids around the world, is achieved using pumped hydroelectric storage (PHS) (USDOE, 2017). Such technology consists in using excess electricity to pump water in a storage reservoir located above the electricity generating turbines. When electricity is needed, the water in the reservoir is discharged downhill into electricity generating turbines. PHS is reliable but affected by shortages in water supply, geographical constraints, and social and environmental concerns (Rosenberg, Bodaly and Usher, 1995; Succar and Williams, 2008). Some research suggests that PHS would be altogether unsuitable for inter-seasonal storage, for the reasons stated above, and the low energy density of the technology (Blanco and Faaij, 2018). The other popular electricity storage technology group is batteries. Although diverse, they are generally ill suited for inter-seasonal grid-connected storage because they have high maintenance costs and offer limited power capacity on discharge (Chen *et al.*, 2009). The inability of widely used technologies, such as PHS and batteries, to perform inter-seasonal storage, highlights the need to diversify the portfolio of technologies which could be improved to meet the need for inter-seasonal electricity storage.

Three candidate technologies for inter-seasonal storage exist: Compressed Air Energy Storage in porous rocks (PM-CAES described in the next section), power to gas (which can be used to convert power to natural gas or hydrogen, aimed at being used in the current gas network), and finally underground hydrogen storage (usually considered independently from conventional Power to Gas as it is aimed to be used outside the existing gas network). Which of these technologies is the most suited for inter-seasonal electricity storage is uncertain, and in reality is likely to be a mix of all three of them. The cost benefits of one over the other are not evident.

Hydrogen and CAES have been compared with diverging conclusions (Schoenung and Hassenzahl, 2003; Steward *et al.*, 2009; Converse, 2012; Maton, Zhao and Brouwer, 2013). Out of those three technologies, CAES is a commercially mature technology, with over 40 years of operation. Although in its current state, the technology is unable to achieve inter-seasonal storage, using porous rock stores could solve this limitation. Even in its current state, CAES achieves as much grid-connected storage worldwide as all the grid connected battery arrays in the world (USDOE, 2017). Furthermore, air is safe to use, safe to store, and is free and readily available. In addition, limited research exists on this interesting alternative, compared to that available for hydrogen storage and power to gas. Therefore this research studies the potential for Compressed Air Energy Storage (CAES) to be used for inter-seasonal electricity storage.

1.3 Compressed Air Energy Storage

In its current state, CAES is a commercially proven and available technology, able to provide stored energy for a duration of days and at powers of 10s or 100s of MW. The two existing CAES plants, Huntorf in Germany and McIntosh in the USA, have power outputs of 321 and 110 MW, and storage capacities of 642 MWh and 2,860 MWh, respectively (Crotogino, Mohmeyer and Scharf, 2001; PowerSouth Energy Cooperative, 2014; Kaiser and Efzn, 2015). They operate by using excess electricity to compress air, up to around 70 bars, in caverns mined in salt, around 700 m below the ground (Crotogino, Mohmeyer and Scharf, 2001; PowerSouth Energy Cooperative, 2014). When electricity is needed, the compressed air is released to the surface, where it is heated by being burned with natural gas. The hot compressed air is then expanded through a turbine to generate electricity. This mode of compression and expansion operation is known as "conventional CAES". Conventional CAES produces around 228 gCO_2/kWh during generation, significantly less than the 388 gCO_2/kWh stated for combined cycle gas turbines used in gas power plants (Mason and Archer, 2012). Assuming the compression of air will be done using electricity generated by renewable sources it will not result in any CO_2 emissions, except those embedded in the life cycle of the coupled renewable-CAES system. CAES necessitates a smaller amount of land surface area per kWh of storage than PHS, as underground stores are used (Succar and Williams, 2008).

For CAES to be used for the purpose of inter-seasonal storage, capable of meeting fluctuations in electricity demand at the grid-scale, stores able to store hundreds of millions of cubic meters of air safely are necessary. Yet, commercially available CAES is currently only being developed in man-made salt caverns. In terms of geological scales these caverns are of limited size (hundreds of thousands of cubic meters). Porous Media CAES (PM-CAES) would store

air within porous rock formations named saline aquifers. Such formations are not suitable for drinking water, or oil and gas extraction, as they contain saline water called brine. Saline aquifers are readily available in the subsurface (Succar and Williams, 2008). Therefore they could provide much greater total storage volumes than artificial salt caverns. In PM-CAES, air would displace brine inside the network of μm to mm-scale pores of the aquifers.

It is hypothesised that extending current CAES technology to be used with porous rock stores, would enable significant inter-seasonal electricity storage potential to be achieved in the UK. This study will therefore focus on assessing the potential for using porous sedimentary rocks as the reservoir for CAES in the offshore of the UK.

1.4 Research Scope

Currently no consensus has been reached on the amount of energy storage which will be needed over the course of the next 25 years. A recent review has highlighted the challenges associated with such estimates including the difficulty of modelling complex energy systems influenced by socio-economic factors. It is also difficult to estimate how technology will evolve (Blanco and Faaij, 2018). This observation, was also true when this research was designed in 2014, therefore rather than trying to assess the potential for PM-CAES to reach a poorly constrained target, the choice was made to assess the overall storage potential, which could be achieved using the available UK saline aquifer resource.

Sufficient theoretical studies exist which suggests that PM-CAES would be a technically feasible technology (Allen *et al.*, 1983; Succar and Williams, 2008; Kushnir, Ullmann and Dayan, 2010, 2012; Oldenburg and Pan, 2013a; Pan and Oldenburg, 2014a). A successful field test was also performed in the 1980s showing that the theoretical calculations were in reasonable agreement with the test results, and that air could be stored and recovered in porous rocks (Allen *et al.*, 1984; EPRI, 1990). It was identified that a gap existed in that no nation scale assessment of PM-CAES had been done before in way that was easily reproducible. Most existing assessments focused on specific sites (McGrail *et al.*, 2013). It was therefore deemed important to build upon existing theoretical model to understand the PM-CAES system behaviour over the range of recommended geological and plant characteristics, and to use that understanding to develop a streamlined workflow for nation scale scoping of inter-seasonal PM-CAES storage potential.

1.5 Research Aims and Layout

The aims of this research are to:

1) Assess the electricity storage potential of offshore UK saline aquifers.

2) Provide an understanding of the PM-CAES system storage potential, based on the geology of the store, and the characteristics of the surface plant.
3) Establish and publish predictive models which can be used for other PM-CAES storage potential assessments.

The assessment will provide an estimate of:

1) The expected efficiency of a PM-CAES cycle.
2) The power capacity expected from a PM-CAES site.
3) The number of wells required to access the storage potential.
4) The geographical location of the areas offering storage potential which can be used to perform site investigation.

This will be performed by:

1) Researching existing siting criteria in the literature in order to delineate the problem and focus the modelling.
2) Building coupled numerical models representative of a PM-CAES system used for inter-seasonal electricity storage.
3) Performing sensitivity analyses of the models of step 2.
4) Developing algebraic predictive models for the energy storage capacity, the power capacity and the efficiency of the system, using the results from step 3.
5) Use the predictive models to estimate the PM-CAES potential of offshore UK formations using data from CO_2 Stored, a geological database regrouping porous rock formations of the UK.
6) Use ArcMap, a Geographical Information System (GIS), to identify areas with storage potential.

This thesis contains seven chapters. The first chapter is the introduction. The second chapter is a literature review of the various CAES technologies available, followed by the relevant theory on two-phase flow in porous media on which the finite element code OpenGeoSys (used for the store model) is based, and finally an introduction to the key thermodynamic concepts used in the turbomachinery models is provided. The third chapter regroups the geological model design, the sensitivity analysis design, the results of the sensitivity analysis and their discussion. The fourth chapter follows the same template as the third for the CAES plant model. The fifth chapter presents the predictive models derived from the sensitivity analyses results of the previous two chapters, and attempts to quantify the influence of the key parameters on the models output. The sixth chapter applies the predictive models to a database of offshore UK saline aquifers to estimate the inter-seasonal potential resource which could be achieved by using PM-CAES. The seventh chapter regroups the main conclusions of this work and suggests avenues for further work.

Chapter 2 Literature Review

This section contributes to knowledge by regrouping and introducing the key concepts and literature relevant to the assessment of porous rock resources combined to CAES. It is aimed at providing a detailed understanding of CAES. It addresses the breadth of the technology and justifies the choices made for the modelling which are presented and discussed in subsequent chapters. The first section presents and discusses various aspect of CAES, such as components of a CAES system, the variety of technologies and stores available, and CAES history and current developments. The second section provides the theory of flow in porous media. The third section presents the thermodynamic concepts necessary to understand the modelling of the turbomachinery found in the surface facilities.

2.1 Compressed Air Energy Storage

The following section will answer the following questions:

1. Why chose to model diabatic-CAES over other CAES technologies?
2. Why focus solely on modelling offshore sandstone aquifers in the UK?

The first section will present the layout of a conventional diabatic-CAES (D-CAES) plant followed by the details of the various operation phases. Alternative CAES technologies will then be introduced, and the choice for choosing D-CAES over more efficient technologies will be discussed. Metrics to assess the efficiency of CAES will then be discussed.

The second part of the literature review will present the work already undertaken concerning underground storage parameters for CAES operations. A summary of the main CAES technologies can be found in Figure 2-14 on page 31.

The last section will present where CAES technologies currently stand on the world scene, what main projects are operating or planned and what are the challenges that CAES development is currently facing.

2.1.1 Introduction to CAES operations and technologies

2.1.1.1 Diabatic CAES Plant Overview

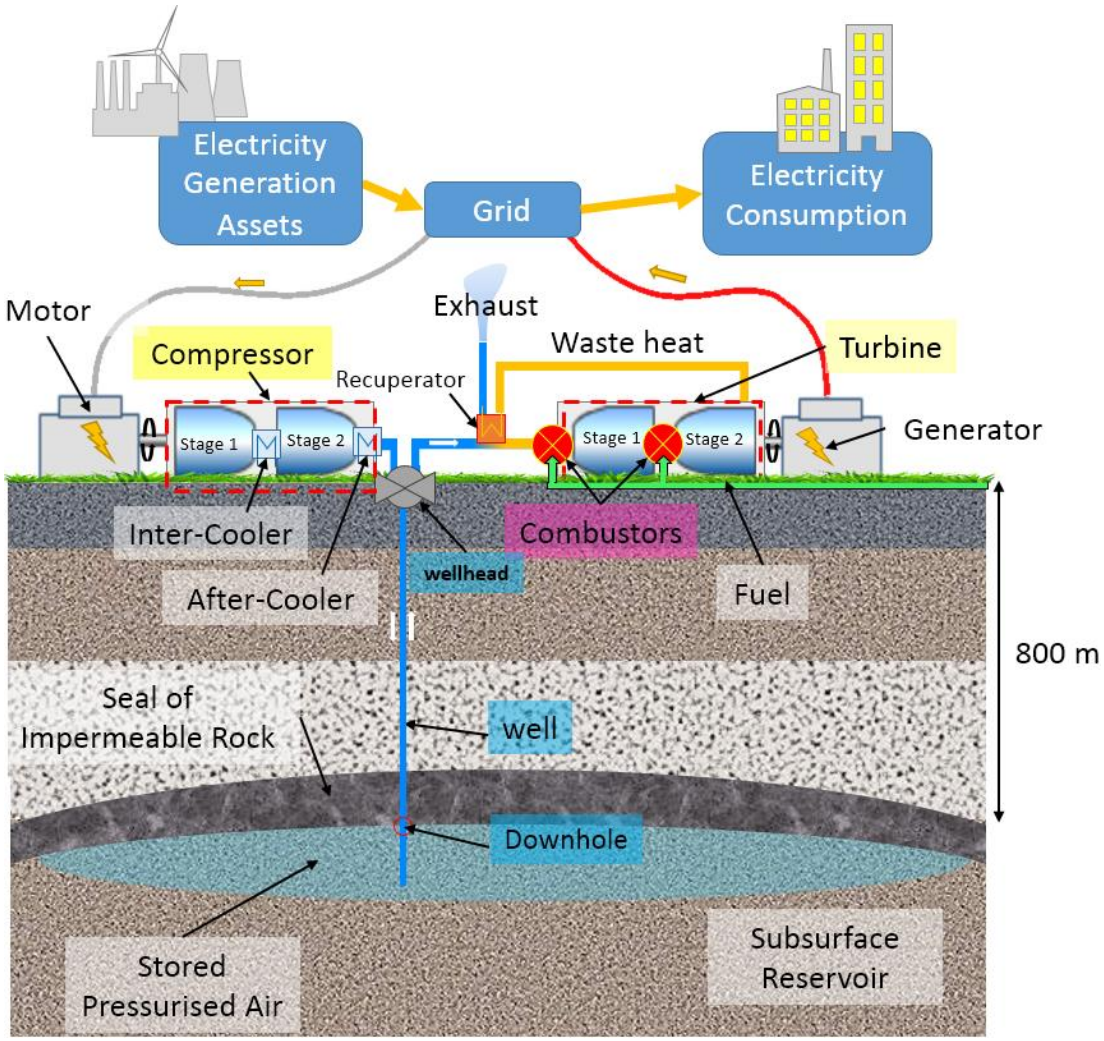

Figure 2-1: Schematic of a conventional CAES plant. The surface facilities are composed of a motor using low cost electricity during times of low demand to power a compressor compressing air from atmospheric pressure to a higher storage pressure. The compression happens in stages, and the air is cooled in between each stage using inter-coolers. After the compression the air is cooled down to the storage temperature using an after-cooler. The well is used to carry the compressed air from the surface to the subsurface storage reservoir, and back from the reservoir to the surface. During times of high demand, when the price of electricity increases, the well is opened allowing the air to flow back to the surface. Once at the surface the air is heated using fuel and waste heat before being expanded through the turbine. In this example, the expansion occurs in two stages with a reheating of the air in between each stage. The rotation of the turbine blades cause a shaft to rotate, this shaft is linked to a generator producing electricity. Adapted from (Chen *et al.*, 2009)

A schematic of a conventional diabatic CAES (D-CAES) plant is shown in Figure 2-1. A diabatic process is a thermodynamic process in which heat is exchanged between the system and the surroundings, the following section will shed light on how this definition reflects conventional CAES. The key components of CAES are (Kushnir, Ullmann and Dayan, 2012):

1. A compressor: A mechanical device used to compressed air at atmospheric pressure to the storage pressure.
2. A motor/generator: A device capable of converting electricity into a mechanical motion operating the compressor or mechanical motion from the turbine into electricity.
3. A gas turbine: A device capable of extracting energy from the expansion of a gas. It is composed of two parts, a combustor in which the incoming pressurised air is heated, and an expander, in which the heated pressurised air is causing a shaft to rotate.
4. A store: A store in which the pressurised air can be stored between its compression and expansion. It can take many forms, amongst which porous rock or a hollow cavern. The various store types are discussed in section 2.1.3.

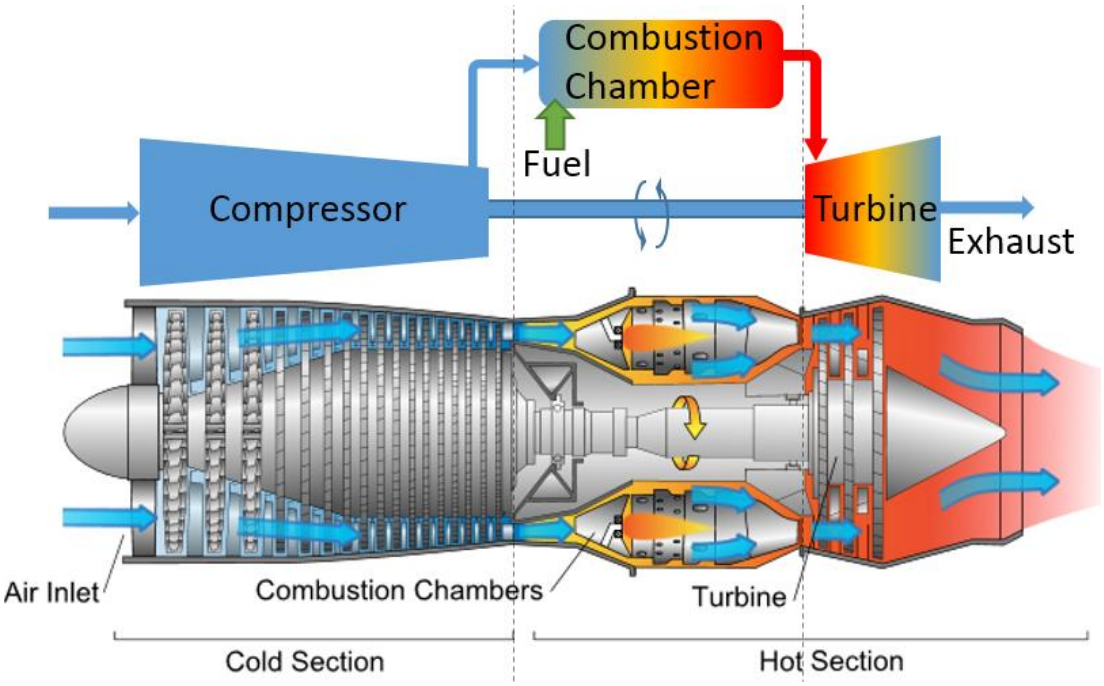

Figure 2-2: Schematic of a conventional aerodrive gas turbine, in which the key components of CAES can be identified: compressor, combustor, and turbine. The main difference with a CAES system is the lack of store in which to store the compressed air and prevents gas turbines from decoupling compression and expansion. Modified /Accessed from http://cset.mnsu.edu/engagethermo/images/gasturbineanimation.png created by Jeff Dahl (under creatives common license) on 12/02/2018.

Elmegaard & Brix (2011) propose a classification for the components of the system, see Figure 2-3, which relates to the consumption and production of electricity, and reflects the various uses a CAES facility can have. The advantage of the CAES plant operation, compared to a standard gas turbine (see Figure 2-2 for detailed schematic), is that the compression and expansion phases occur at different times. This decoupling is made possible by the addition of a store for the compressed air. The benefit of decoupling compression and expansion is that much more of the power resulting from the expansion of the gas can be converted to electricity,

whereas in conventional gas turbines up to two thirds of the energy produced is used to compress the gas (Succar and Williams, 2008). In other words, in a CAES plant since the air is already compressed when the expansion starts, more of the energy resulting from the expansion can be used to produce electricity. The motor and generator are usually encompassed in the same device and can either consume or produce electricity by using a system of clutches. When it is connected to the compressor it will consume energy and act as a motor, and when it is connected to the turbine it will generate electricity as a generator (Kushnir, Ullmann and Dayan, 2012). A CAES plant therefore offers both the possibility of being used as a conventional gas turbine plant, and as an energy storage plant.

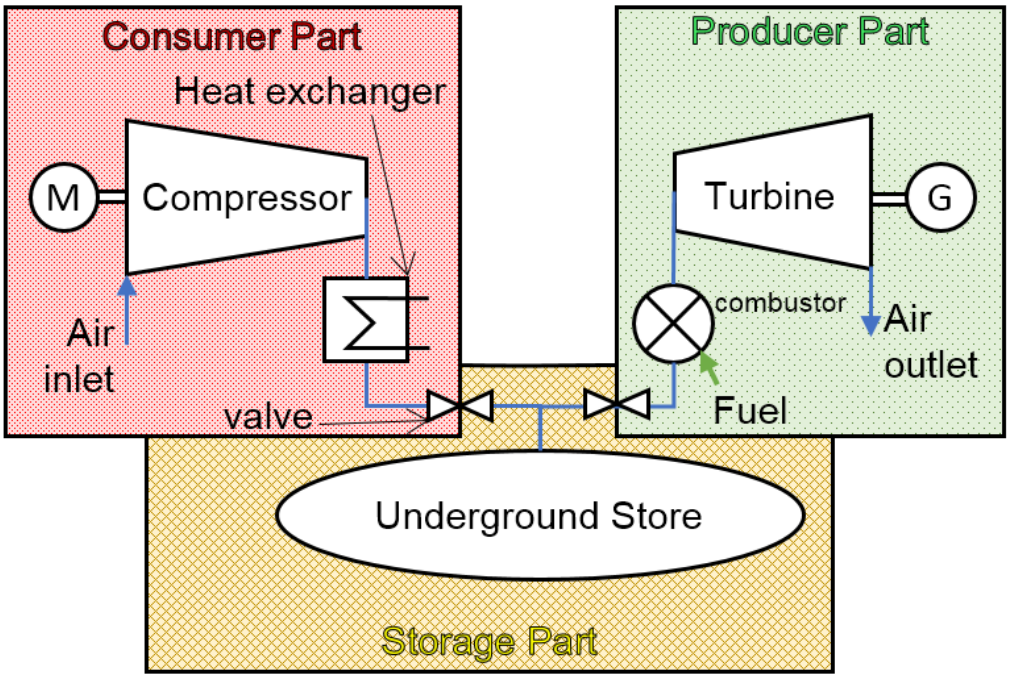

Figure 2-3: Classification of the various CAES components according to their role in the energy system. The classification distinguishes between the producer part which includes the motor, compressor and after-cooler; the storage part which contains the underground store; and finally the producer part composed of the combustor, turbine and generator. M is the motor, consuming electricity in order to compress air. G is the generator converting the rotation of the turbine shaft to electricity (Elmegaard and Brix, 2011)

2.1.1.2 CAES Operation Stages

A CAES plant can operate under three different modes: a charging mode, a storage (shut-in) mode, and a generation mode (see red, yellow and green areas in Figure 2-3 respectively) (Kushnir, Ullmann and Dayan, 2012).

2.1.1.2.1 Charging Mode

The CAES plant is run in charging mode when electricity prices are low due to low demand (i.e. off-peak periods). It consists of the motor running the compressors using low cost excess power capacity. Atmospheric air is compressed and cooled. Cooling the air during the

compression is beneficial as compressing a cool gas requires less energy than compressing a hot gas. Since compression increases the gas temperature, the compression is broken up in steps and inter-coolers are used to reduce the gas temperature at each step. Therefore the amount of energy required is reduced. After-coolers reduce the temperature of the air after the compression and before it reaches the underground store to allow for lower storage volume requirements, reduced thermal fatigue in the store, and lower air viscosity which facilitates the flow of air through the store (Kushnir, Ullmann and Dayan, 2012). Once the air has been compressed and cooled it is injected into the subsurface store for storage.

During compression of air into the store, the compressor can operate in two main ways (graphic representation in Figure 2-4):

- A constant mass-flow rate is maintained by the compressor leading to an increase in outlet pressure throughout the compression cycle.
- A constant outlet pressure is maintained by the compressor resulting in a diminishing mass-flow rate throughout the compression cycle.

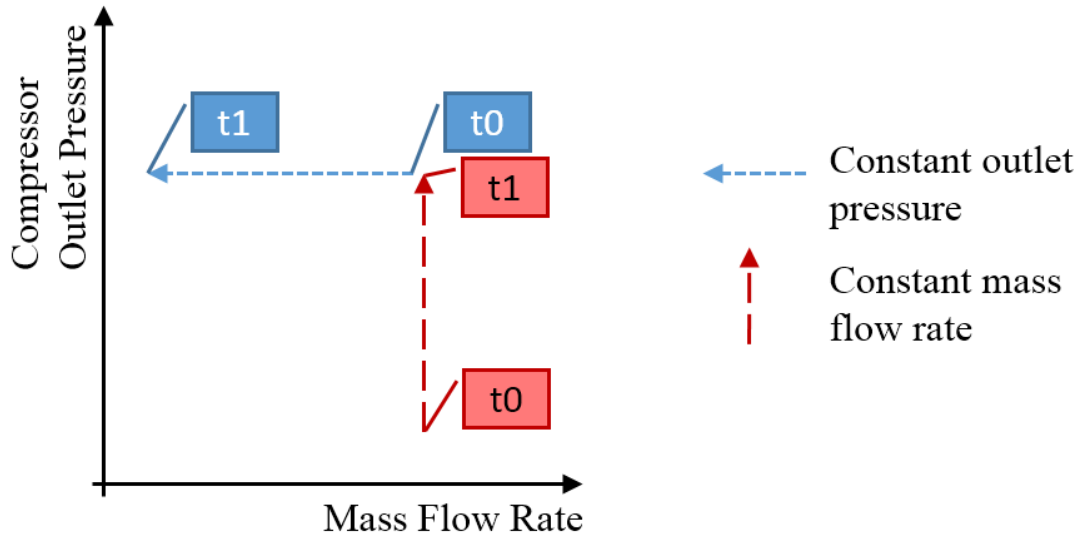

Figure 2-4: Representation of the two modes of operation for a compressor between two times, t0 and t1 where t0 < t1.

These different operation modes are dictated by the store physical properties and also apply to the discharge mode (Kushnir, Ullmann and Dayan, 2012).

2.1.1.2.2 *Shut-in Mode*

Following air injection in the underground store, the shut-in mode is initiated. It is characterised by neither compression nor expansion taking place and the pressurised air being locked into the subsurface store. This mode of operation lasts until the conditions of low electricity demand, and hence, low electricity prices encountered during the compression

mode shift to conditions of high demand and electricity prices. As such, the value of generating electricity using the stored air is maximised.

During this stage, heat and mass transport occur only in the store (Kushnir, Ullmann and Dayan, 2012). In the case of porous rock subsurface store, pressure gradients formed during charging mode, due to the resistance to flow created by the porous rock (as opposed to an empty cavern), tend to stabilise over time (see Figure 2-5) (Oldenburg and Pan, 2013a). Those pressure fluctuations are key to this research as they will determine the rate at which the air can be stored and injected into the store as explained in section 2.2.2. The modelling will aim to understand how the geology of the store affects the time it takes for those pressure gradients to form and dissipate.

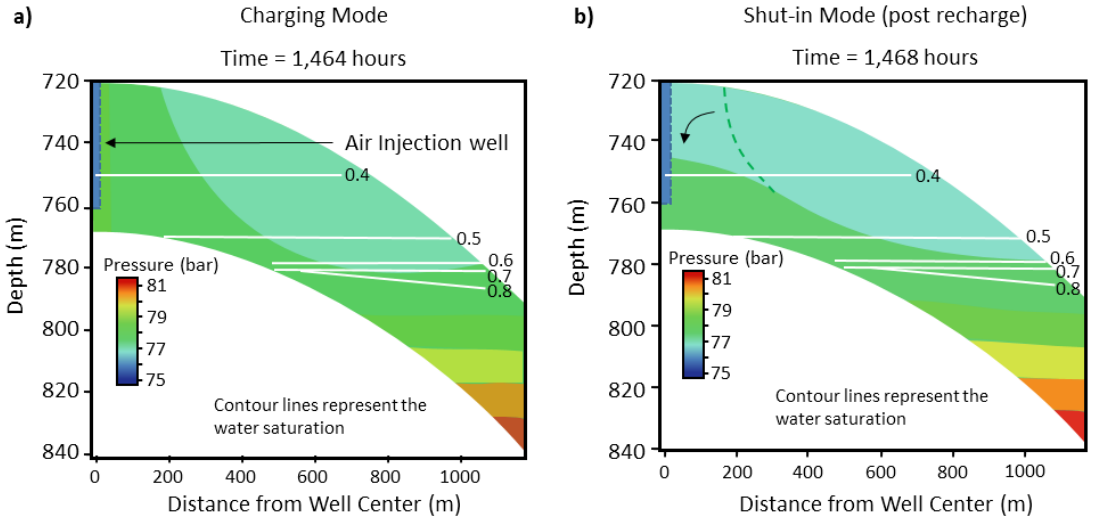

Figure 2-5: Data from Oldenburg & Pan (2013a) simulations of injection in an aquifer. (a) represents air injection, (b) shut-in period. In (b) the stabilisation of the pressure gradient is indicated by the black arrow. The portion of the well where air can be injected is represented by the blue rectangle in the top-left of each snapshot.

2.1.1.2.3 Generation Mode

During times of peak electricity demand the plant shifts from shut-in mode to generation mode. The air compressed in the store is discharged through a well, into the combustion chamber of a gas turbine where it is fired up by the addition of natural gas. The compressed hot gas resulting from the combustion then expands through the gas turbine, which runs the generator and produces electricity. A minimum store pressure after discharge is maintained to avoid any adverse consequences in the store (e.g. collapse of the pore-structure of the store). After this stage is completed another charging mode is initiated and a new storage cycle started (Kushnir, Ullmann and Dayan, 2012). However, there can be a time lag between the discharge and the subsequent charging phase. This time lag can last a few hours for daily CAES, to a few months

for seasonal CAES. This may be necessary in order to meet economically affordable conditions before operating the charging mode (Kushnir, Ullmann and Dayan, 2012). As this study focuses on storing energy on a scale of weeks and months (i.e. inter-seasonal storage), the generation mode will be followed by a shut-in mode, as it is deemed reasonable to assume that it will take a few months for the electricity prices to drop for charging to be feasible.

2.1.1.3 Alternative CAES Technologies

Following on from the description of a conventional diabatic CAES (D-CAES) plant operation, this section will review alternative CAES technologies which are currently being researched. The aim is to provide the reader with a broad understanding of the breadth of systems CAES entails. Unlike D-CAES, none of the following technologies are currently commercially mature, nonetheless, some are soon to be at demonstration scale. The concept behind each technology will be briefly introduce, then advantages and/or limitations will be discussed, finally a justification for not considering the technology within the scope of this research will be provided.

2.1.1.3.1 Adiabatic CAES with Thermal Energy Storage

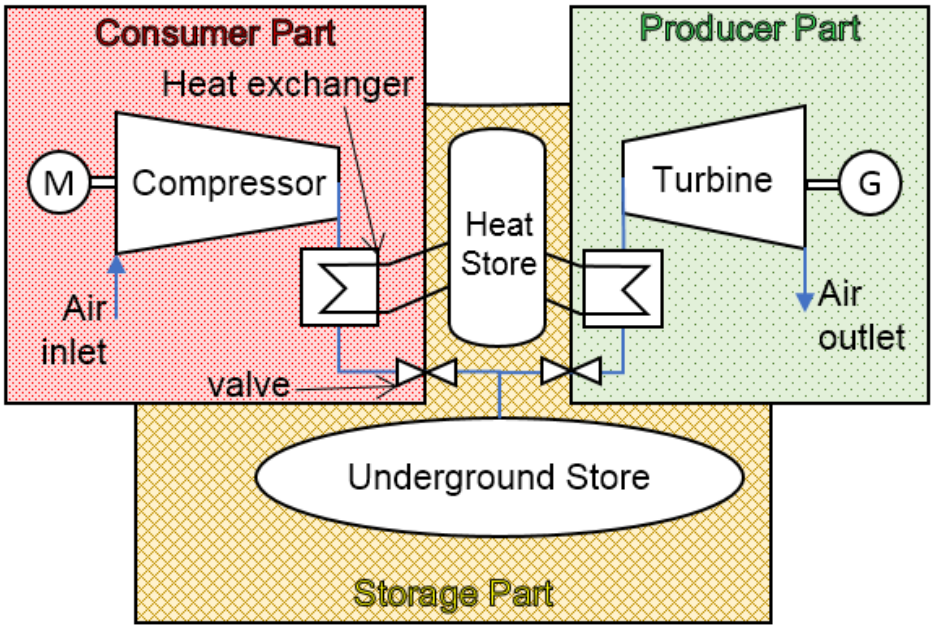

Figure 2-6: Using the schematic from Figure 2-3 a thermal store can be added to remove the need for fuel. During compression heat is stored, and this heat is returned to the air prior to it being expanded. M is the motor, consuming electricity in order to compress air. G is the generator converting the rotation of the turbine shaft to electricity (Elmegaard and Brix, 2011)

Adiabatic-CAES (A-CAES) consists in removing heat from the air stream during compression and storing that heat in a thermal energy store (Figure 2-6). During generation mode the heat is returned to the air prior to it reaching the turbine. The advantage of storing the heat is that no natural gas is needed in order to re-heat the air prior to its expansion. The turbomachinery

is still being designed and its characteristics are not available. This technology is the focus of significant research as it will save having to add natural gas to the energy mix of the plant making the storage cycle operating fully on renewable sources (Grazzini and Milazzo, 2012; Barbour *et al.*, 2015; Helsingen, 2015). Yet, developing high temperature thermal energy storage (TES) on a seasonal timescale is proving to be a very significant challenge. A detailed literature review on TES applicable to seasonal scales only yielded TES with temperatures inferior to the ones needed for CAES (up to about 200 °C). For this reason this technology will not be studied further.

2.1.1.3.2 *Adiabatic CAES without Thermal Energy Storage*

In this technology, to remove the need for an independent heat store, the heat can remain in the air stream during compression but if the heat is not removed from the air stream, then the hot air needs to be stored, and heat losses to the environment minimised. Either way, considering the high temperatures of the air after compression (around 500 °C depending on the target storage pressure), it is not feasible to store air at this temperature without high risks of subjecting the store to thermal fatigue and damage (Smith *et al.*, 1978). Furthermore, compressors have a limited operating temperature therefore, using this technology would limit the storage pressure since above a certain pressure the temperature within the compressor would be too high for it to operate safely. In addition the high temperature of the air in the compressor would increase the amount of energy needed for the compression. Further modelling would be needed to ensure that the temperature would indeed have adverse effects on the store (Stottlemyre, 1978). However, modelling water and air flow behaviour with an important temperature fluctuation component makes processes like thermal fatigue and geochemical reaction more important and the modelling more complex. Due to the wide ranging scope of the project it was deemed that such specific modelling would not be suited.

2.1.1.3.3 *Isothermal CAES*

Isothermal CAES promises to be a very efficient technology, removing the need for high temperature heat storage. These systems, like the ones patented by SustainX Inc. (www.sustainx.com) and LightSail (www.lightsail.com), consists of operating a cylinder and piston based engine utilising an electric motor (see (1) in Figure 2-7). During each stroke a water mist or light foam is sprayed in the cylinder. During compression the heat generated is continuously absorbed by the water and during expansion the heat is continuously extracted from it. This continuous heat exchange process enables the compression and expansion to occur with a temperature fluctuation close to 10 °C from ambient temperature, rather than requiring significant cooling or heating of the air at specific times via inter-coolers and combustors respectively. The temperature of the stored water would thus have to be much

lower than that of heat stores used for A-CAES, making low temperature heat storage used for building heating application sufficient. The need for the heat storage could be removed altogether if the CAES plant is located near a source of waste heat (e.g. power station). Despite isothermal CAES being still under research and development, the technology offers the potential to achieve inter-seasonal energy storage. In addition, the electrical power generated is likely to be lower than for D-CAES and A-CAES as upscaling the power output of a piston and cylinder engine to the 100s MW scale is challenging. Hence, this technology is poorly suited to porous rock store where one of the challenges will be to maximise the power capacity per well.

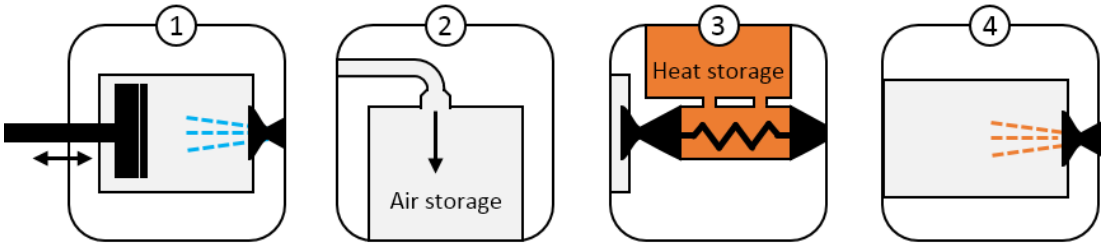

Figure 2-7: LightSail Technology I-CAES. (1) The heat generated during compression is being continuously absorbed by water being sprayed into the compression chamber. (2) The compressed air is stored in a tank. (3) The warm water is stored in a heat store at temperatures close to ambient. (4) During expansion of the air, the warm water is sprayed in the expansion chamber and the heat from the water is continuously transferred back to the air as it expands maintaining its temperature near to constant. Adapted from http://blogs.berkeley.edu/2015/02/10/the-promise-of-energy-storage/

2.1.1.3.4 Air Injection in Thermal Enhanced Oil Recovery

Although not a CAES method *per se* the use of compressed air for enhanced oil recovery should be investigated. The formal name of the method is "*in-situ* combustion" and its informal one "fireflooding". It consists in combusting a portion of the oil trapped in porous rock, in the subsurface, to allow the remaining fraction to flow towards a well, where it can be recovered. The mechanisms by which the flow of oil is increased are complex, and beyond the scope of this review, and dependent on the amount of oxygen and moisture in the air, the type of oil, and the porous rock properties (Sarathi, 1998). From an engineering point of view this method demonstrates the viability of injecting large volumes of air at high pressures underground using compressors which can be fitted on offshore platforms, where limited space is available. In terms of insight into the air flow mechanisms *in-situ* combustion can bring to PM-CAES, it is interesting to note that such method could be used to transition from a producing oil field to a PM-CAES site. In terms of the insight it can bring to developing the method in porous rocks without any hydrocarbons it is limited due to the very different temperature and chemical conditions to which the air will be exposed to.

2.1.2 Assessing CAES Efficiency

In order to compare the various CAES technologies amongst themselves as well as against other storage technologies standardised metrics need to be used. The focus of this work is on conventional diabatic CAES, which consumes energy in the form of both fuel and electricity, whilst only producing electricity as a useful product (Succar and Williams, 2008). Therefore, one way to understand the system is to use performance indices of the energy inputs which describe how performant the system is. The system performance is analysed by comparing some input to the output of the system. A number of examples and their uses are presented in Figure 2-8. The two important indices for CAES are the heat rate and the charging electricity ratio (CER) (Succar and Williams, 2008). This will make D-CAES comparable to existing power stations using fossil fuels.

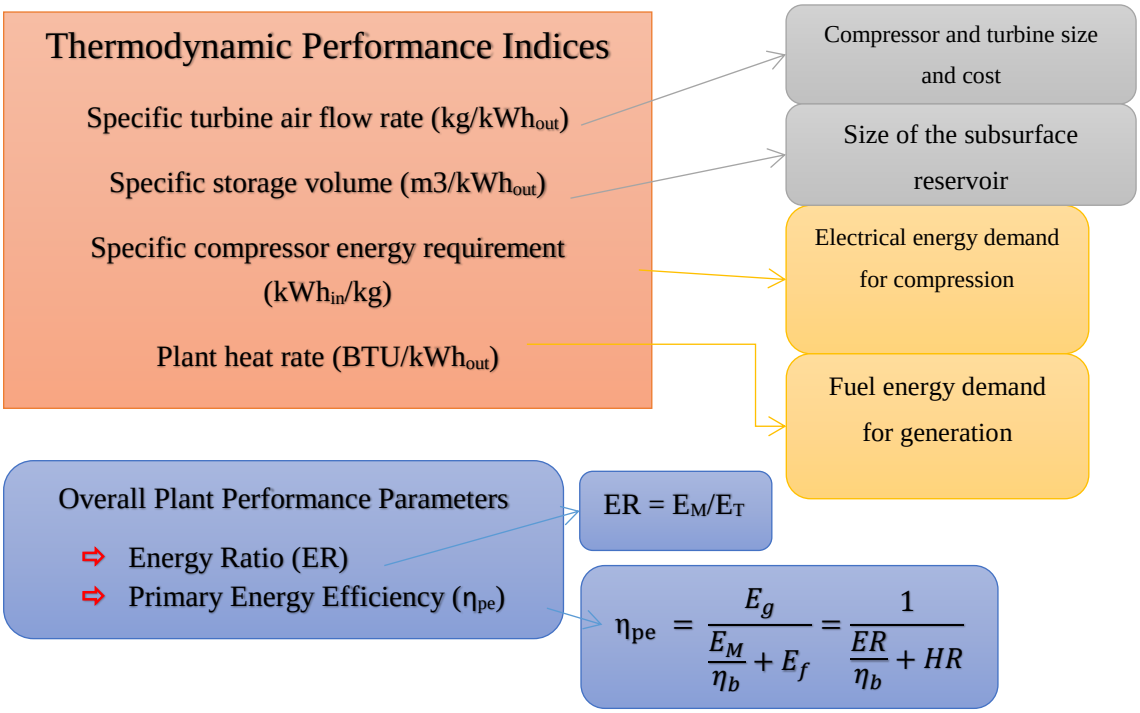

Figure 2-8: Thermodynamic Performance Indices and the Parameters they define. In grey the Component Sizing Parameters, in yellow the Energy Requirement Parameters and in Blue the Overall Plant Performance Parameters. E_M and E_T are the net overall energy exchanged with the grid during the charging and power generation phases, respectively, and E_f is the fuel energy introduced in the generating phase. The plant heat rate is HR, and η_b is an external thermal efficiency of the base load power plant that provides the power for the compression phase. BTU stands for British Thermal Unit and is equivalent to $2.93 \cdot 10^{-4}$ KWh, it is usually used to express the energetic values of fossil fuels (Kushnir, Ullmann and Dayan, 2012)**.**

2.1.2.1 The Heat Rate

The heat rate introduced in Figure 2-8 represents the amount of fuel energy necessary to produce one kWh of output electrical energy. It is valuable to determine the fuel requirements of the plant and the associated costs for the purpose of economic viability. The heat rate is markedly influenced by the design of the plant, and by how well the plant minimises the heat

and pressure losses inducing a reduction in electricity being produced by the combustion of one unit of fuel (British Thermal Unit, BTU; or J). The heat rate is greatly reduced when the waste heat left in the air stream after the turbine is being recovered and used to pre-heat the air entering the combustors, the device performing this is called a recuperator.

A low heat rate implies that the plant is efficient at converting energy from the fuel to electricity, and hence has low greenhouse gases emissions per unit of produced electricity. To put this into context the heat rate of the Huntorf CAES plant in Germany, is of 5870 kJ/kWh without a heat recuperator and the heat rate of the McIntosh CAES plant, USA, is of 4330 kJ/kWh with a recuperator. These values are lower than for a conventional gas turbine (about 9500 kJ/kWh) since, on the one hand, for a conventional gas turbine a significant portion of the power produced is used to compress the air entering the turbine. For CAES plants on the other hand, air compression is achieved using electricity rather than fuel (Succar and Williams, 2008).

2.1.2.2 The Charging Electricity Ratio

The Charging Electricity Ratio (CER) is the ratio of generator output electricity to compressor electricity input (Succar and Williams, 2008). Due to the addition of natural gas during the power generation mode, the CER for a CAES system is going to be greater than one. Typical values range from 1.2 to 1.8 kWh_{output}/kWh_{input}. CER includes air pressure and heat losses due to the air transiting through pipes at the surface and through a well to the subsurface store, as well as the efficiency of the compressor to compress air and the turbine to expand it. (Succar and Williams, 2008)

2.1.2.3 How to meaningfully assess CAES efficiency?

As previously mentioned, combining electrical and thermal (fuel derived) energy into one single equation to calculate efficiency is erroneous, albeit common, since there are significant differences between the usefulness of thermal and electrical energy (Succar and Williams, 2008; Garvey and Pimm, 2016). Therefore, the first step to providing a meaningful efficiency measure for CAES is to express thermal energy and electricity using an equivalent basis. This can either be achieved by converting thermal energy into a corresponding quantity of electrical energy or *vice versa*. The resulting efficiencies are referred to as roundtrip efficiency and primary energy efficiency respectively. Efficiency values using different efficiency calculations are summarised in Table 2-1. For the purpose of this work the roundtrip efficiency defined by Eq. 2-1 will be used, in order to provide a measure of efficiency in terms of electricity only. This will ensure results are comparable to other electricity storage and electricity generation technologies.

Table 2-1: CAES efficiency values from the literature, with E_M and E_T are the net overall energy exchanged with the grid during the charging and power generation phases, respectively, and E_f is the fuel energy introduced in the generating phase. η_T the efficiency with which a power plant converts fuel energy to electrical energy. η_{NG} the efficiency with which the amount of energy contained in natural gas can be converted to electricity. Values from Succar & Williams (2008).

Efficiency	Formula	Reported Value	
		No Recuperator	With Heat Recuperator
Primary Energy Efficiency	$\eta_{PE} = \frac{E_T}{E_M/\eta_T + E_f}$	CAES Charged from Nuclear Power (η_T = 33%)	
		24.5%	29.7%
		Charged from Fossil Fuel Power Plant (η_T = 42%)	
		28.2%	34.4%
		Charged from Combined Heat and Power Plant (η_T =35%)	
			35.1 to 41.8%
		Charged from Grid-averaged Baseload Power (η_T = 35%)	
			42 to 47%
Roundtrip Efficiency	$\eta_{RT} = \frac{E_T}{E_M + E_f \times \eta_{NG}}$	4220 kj LHV/kWh, CER = 1.5, η_{NG} = 47.6%	
			81.7%

The important message one can draw from the variety of efficiency calculations available is that thermal and electrical energy cannot be combined, and therefore, the relevant expression to be used depends upon what one is looking to understand from an efficiency calculation (Succar and Williams, 2008).

$$\eta_{RT} = \frac{E_T}{E_M + E_f \times \eta_{NG}} \qquad 2\text{-}1$$

Where, η_{RT} is the Roundtrip efficiency of the CAES plant, E_T the electrical output of the plant, E_M the electrical input to the motor, E_f the thermal energy input from the fuel and η_{NG} the efficiency with which the thermal energy is converted to electrical energy in conventional gas turbine.

2.1.2.4 Storage System Efficiency

In the literature, considerable attention has also been drawn to the storage system efficiency which is not well represented by the overall CAES performance efficiencies in Table 2-1. Oldenburg & Pan (2013a) have been extending the traditional energy difference between energy stored and energy produced from the storage by modelling a coupled well-reservoir system to account for energy losses occurring both in the reservoir and the well. The reservoir refers to a subsurface porous rock store. By calculating these losses they can analyse the

storage efficiency of a PM-CAES system. The key findings of their work, providing encouraging conclusions to study PM-CAES further, are explored next.

They have demonstrated that porous rock reservoirs were very efficient at storing energy and air. They calculated an air mass loss of 3.5% per cycle, which is within the 4% acceptable limit proposed by Giramonti *et al*. (1978) and the same as the losses occurring at Huntorf CAES power plant in Germany (Oldenburg and Pan, 2013a).

The energy losses due to the well appear to be only due to heat losses to the well's surroundings. These losses reduce as the well temperature equilibrates with the surrounding rock over time (Oldenburg and Pan, 2013a).

Further encouraging conclusions from their work address the deliverability (ability to inject and extract the air from the porous rock reservoir) limitations which could be imposed by high or low pressure diffusivity within the reservoir. They found that low pressure diffusivity in the reservoir was not limiting injection, and that the limiting factor for flow rate was the contact area between the well and the reservoir rock. As for large pressure diffusivity, if the reservoir is bounded by an effective cap rock seal then the risk of pressure diffusion is limited.

They state that the pressure gradients forming in the porous reservoir are highly reversible on daily cycles. This study will explore the pressure gradient stabilisation on inter-seasonal cycles.

Their work offers an understanding of how a PM-CAES reservoir will react to air storage when the pore spaces of the reservoir rock are connected and allow fluid flow and pressure diffusion well beyond the zone in which the air is stored. Such systems are known as open systems. There is therefore much uncertainty as to how exactly a porous reservoir would behave under CAES operation, in the case of a compartmentalised system isolated from the far field by some geological feature (such as sealing faults).

2.1.3 Underground Air Stores

This section will present the various types of subsurface air stores that can be used for CAES. The specificity of each will be introduced and the reasons for focusing exclusively on saline aquifers, which are brine bearing porous rocks, will be discussed.

There is a wide variety of stores that can be used for CAES. They are subdivided in two categories: surface and subsurface stores. These categories are self-explanatory and this section will only focus in introducing the subsurface stores, because the aim of this research is to provide large scale, bulk inter-seasonal storage, which can only be achieved using geological subsurface stores. At such scales, surface stores would have to be at a high storage pressure in order to compensate for the smaller volumes, hence more expensive turbomachinery (i.e. compressor and turbine), and greater safety concerns. This would significantly increases the costs of CAES, making it uncompetitive (Grazzini and Milazzo, 2012). The various types of underground stores which can be used for compressed air storage are subdivided as follow (Kushnir, Ullmann and Dayan, 2012):

- Porous Rock Reservoirs: The air is stored in the pore network of the rock matrix.
  - Aquifers: The pores are initially saturated with water or brine.
  - Depleted Gas Reservoirs: The pores initially contain a mixture of natural gas and brine.
- Caverns: The air is stored in hollow cavities
  - Salt Caverns
  - Hard Rock Caverns

Each of these categories is discussed hereafter. A significant emphasis will be placed upon the two types of porous rock reservoirs.

2.1.3.1 Porous Rock Reservoirs

The geological terminology for an underground porous rock in which air can be stored and recovered is a ‘reservoir’. In order for a reservoir to be used as an underground storage for CAES, it needs to be overlaid by a cap-rock layer impermeable to air flow (see Figure 2-9). Furthermore, the storage complex composed of the reservoir and the cap-rock, should have a trapping structure under which the air can accumulate (Allen *et al.*, 1983; Succar and Williams, 2008; Kushnir, Ullmann and Dayan, 2012). Such structures are known as structural traps and are similar to those that formgas and oil reservoirs. If these conditions are met the risk of vertical or horizontal air leakage outside the storage complex is greatly reduced (Kushnir,

Ullmann and Dayan, 2012). The recommended depth range to the top of the reservoir, for it to be used for CAES, is about 200 to 1,500 m based on Allen *et al.* (1983). The presence of faults and other geological structural features in the area might enhance or reduce the risk of leakage; this is why a detailed knowledge of the geology of the area is required before taking any PM-CAES project further. Any PM-CAES project requires site specific models and since this is not possible to do for every potential site in the UK, a new approach had to be developed to tackle the assessment of PM-CAES on a nationwide scale.

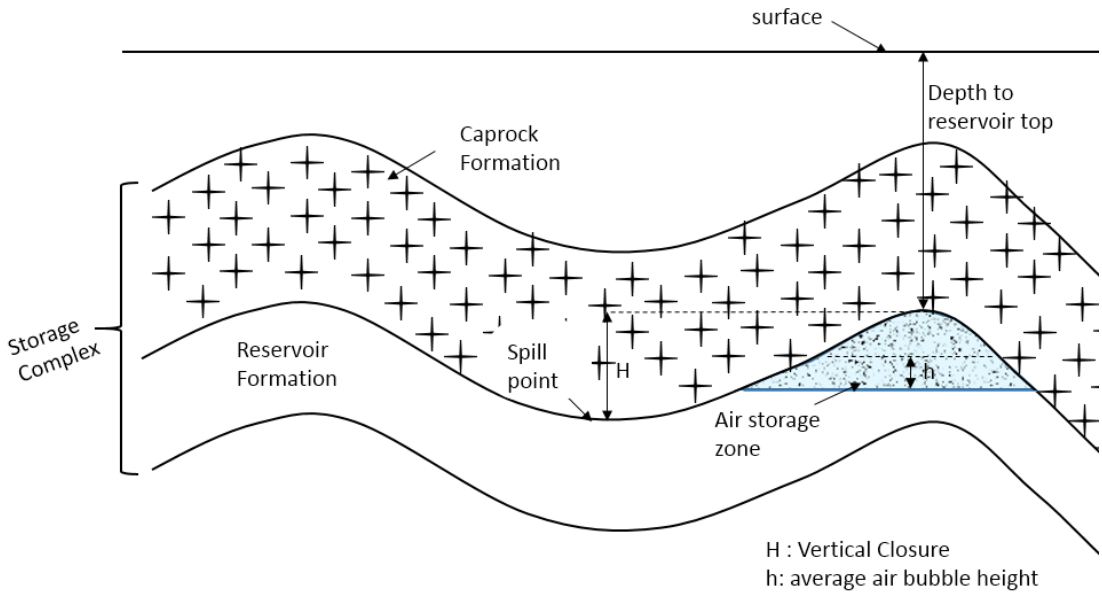

Figure 2-9: Schematic of a cross-section through a potential CAES storage site (without the well and surface facilities) and the associated terminology used in Table 2-2. The location of the air storage zone is located in a structural trap, other types of traps can exist. This shows that only a small fraction of the overall formation will actually be used to store the air.

This approach focuses on establishing the key geological parameters that affect a porous CAES reservoir using the literature and testing how the PM-CAES plant reacts to changes in those parameters. The key characteristics used in determining if a porous rock reservoir is suitable for PM-CAES are its: depth, areal extent, thickness, porosity and permeability. These characteristics enable calculation of the reservoir volume available for air storage, as well as the rate at which air can be compressed or released. This is important as it will enable an estimate of how many wells are required to achieve a power output target (Kushnir, Ullmann and Dayan, 2012). A large research campaign on CAES in the 1980s led to the establishment of siting criteria to determine the suitability of a geological reservoir to be used as a CAES store (Smith *et al.*, 1978; Stottlemyre, 1978; Allen, Doherty and Thoms, 1982; Allen *et al.*, 1983, 1984). Those siting criteria proved to be a very sound basis, underlined by multidisciplinary research, and will thus be used in this study. This study will focus on the

formations which fall within the siting criteria published. Furthermore a method to estimate the storage potential quantitatively based on the siting criteria will be developed. Some uncertainty still remains around the storage pressure range criterion. Ranges reported in the literature include: 2-15 MPa (Allen *et al.*, 1983), 2-7 MPa (Succar and Williams, 2008) or 1.9-12.2 MPa (Stottlemyre, 1978). This uncertainty highlights the need for the work carried out in this study to be performed. A summary of the key geological & geophysical parameters, and their values, can be found in Table 2-2. Figure 2-9 presents the terms used in the table using a cross section schematic. Further discussion on the selection of the parameter ranges will take place in section 3.3.5 to incorporate how new research and technological improvements in turbomachinery allow for more optimistic ranges for some parameters.

Table 2-2: Values for different criteria used to determine if a porous rock reservoir can be used for CAES. In green values from (Succar and Williams, 2008)**, in orange from** (Allen *et al.*, 1983)**, in blue from** (Oldenburg and Pan, 2013a)**, and in purple from** (Kushnir, Ullmann and Dayan, 2010)**. * With Vr the total void volume of the aquifer above the spill point contour, Vs the volume needed for CAES operation. ** h_a the air bubble thickness, h_f the total thickness of the formation. (Continues onto next page)**

Reservoir Quality	Units	Unusable	Marginal	OK	Good	Excellent
Permeability	mD	< 100	100-200	200-300	300-500	> 500
	mD	< 100 or > 5000				
	mD					1013
Permeability to gas	mD	< 300				
Porosity	%	< 7	7-10	10-13	13-16	> 16
	%			> 10		
	%	< 5 or > 35				
	%					20
Total Reservoir Volume	Vr/Vs*	< 0.5		0.5-0.8 or > 3.0	0.8 - 1.0 or 1.2-3.0	1.0-1.2
Total Closure Rating	h_a/h_f**	< 0.5		0.5-0.75	0.75-0.95	0.95-1.0
Centerpoint thickness	m			>10		
Vertical closure	m			> 10		
Depth to Top Reservoir	m	< 137 or >760	140-170	170-260 or 670-760	260-430 or 550-670	430-550
	m			200-1500		
	m			720		
Reservoir pressure	bar	< 13 or > 69	13-15	15-23 or 61-69	23-39 or 50-61	39-50
Type of Reservoir		Highly Discontinuous	Moderately vulgar limestone & dolomite	Reefs, highly vulgar limestone & dolomite	Channel sandstones	Blanket sands
Residual Hydrocarbons	%	> 5		1-5		<1

Caprock leakage		Leakage evident	No data available	Pumping test shows no leakage		
Caprock Permeability	mD			$> 10^{-5}$	$< 10^{-5}$	
Caprock Threshold Pressure	bar			21-55	> 55	
Caprock Thickness	m			< 6		> 6
	m			10		
Injection Temperature	°C			> than ambient reservoir temperature but < 250		
	°C			50 for an initial ambient temperature of 40		
	°C	< 26.85 or > 126.85				
Injection Pressure	bar			not above the discovery pressure by more than 0.16 bar per meter of the caprock to avoid fracture		

2.1.3.1.1 *Saline Aquifers*

Aquifers, as shown in Figure 2-10, are rock formations characterised by the natural presence of water in their pore space. This work will focus on saline aquifers which contain water with a significant amount of dissolved solids. The percentage of dissolved solids used in this work will be discussed in section 3.3.7.1. The reason for focusing on saline aquifers is that they are readily available and it is therefore expected that more storage could be found in them as opposed to depleted gas fields, introduced later. Furthermore, the lack of residual hydrocarbons will make predicting the nature of the fluid mixture to model easier, reducing uncertainty. Another characteristic of aquifers is the rock type. Saline aquifers are formed by two main rock types shown in Figure 2-11: limestone and sandstone. The nature of fluid flow in either varies greatly. In sandstone the flow happens through the pore space in between the grains of the rock (i.e. matrix), whilst in limestone it happens preferentially in fractures and secondary permeability resulting from dissolution. This makes the assumption of a homogenous media, which was used in the modelling, primarily relevant to sandstone aquifers.

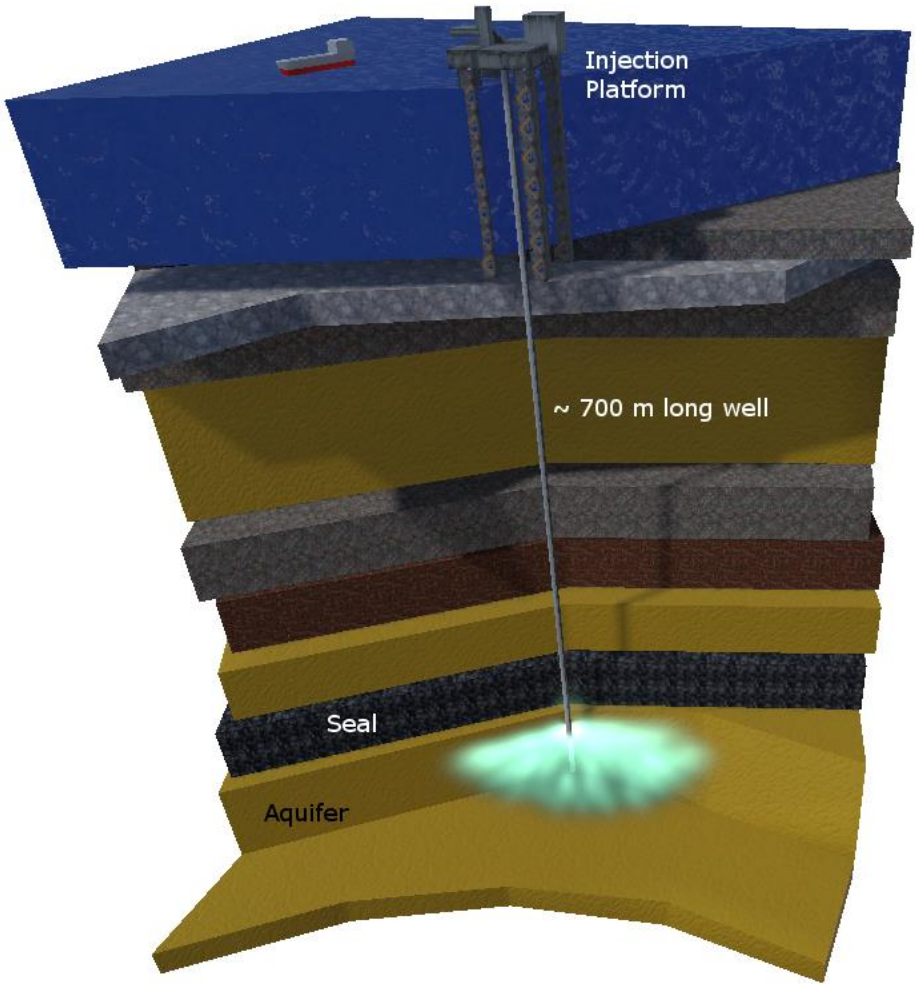

Figure 2-10: 3D Diagram of air storage in an offshore saline aquifer.

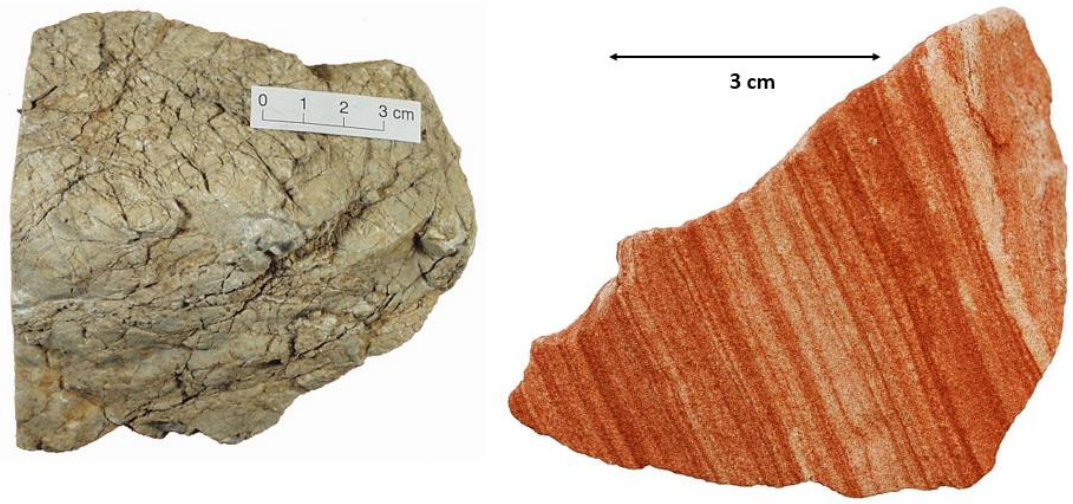

Figure 2-11: Limestone (left) and sandstone (right) samples. In limestones, the main travel pathways for fluids are the fractures and cavities of the rock, in sandstone fluid travels through the interconnected pore space network in between the grains. Source: Limestone image accessed form https://www.earth.ox.ac.uk/~oesis/nws/nws-a98-kc2.html permission to reproduce granted by David Waters, Sandstone image from http://www.sandatlas.org/sandstone/ permission to reproduce granted by Siim Sepp.

The first step in assessing if an aquifer would be suited for PM-CAES is to proceed to a site characterisation using a variety of monitoring techniques: e.g. seismic surveys, sampling of formation fluids, or existing literature data as a less expensive preliminary step. If the site characterisation has provided satisfactory results the next step is to develop the reservoir and make it ready for cyclic air storage. This is achieved by injecting air continuously inside the reservoir for a few weeks or months, in order to displace the brine originally in the pore space and partially replace it with air. This will lead to the formation of an air "bubble" (Stottlemyre, 1978; Succar and Williams, 2008; Kushnir, Ullmann and Dayan, 2012). It is important to note that not all the air injected will be recovered at each cycle. This leads to the concept of total working capacity (TWC) and cushion gas requirement (CGR). The TWC is the portioned of the air being cycled in and out of the reservoir whilst the CGR is the portion of gas that constantly remains within the reservoir to ensure that the air saturation remains high. The total volume of gas (TVG) in the reservoir when the reservoir has reach its maximum storage capacity is $TVG = TWC + CGR$ (Amid, 2013). Once the air bubble is large enough to prevent water coning (i.e. the suction of brine into the well during production) the TWC is injected and the CAES operation can start.

Alternatives to using air as the cushion gas have been proposed (Oldenburg and Pan, 2013b). Oldenburg & Pan (2013b) suggested using CO_2 since the density of CO_2 increases much faster than that of air with increasing pressure, using CO_2 as a cushion gas would result in a more important "spring effect" during the discharge phase. The challenge being to balance the

distance between the air and CO_2 boundary and the well in order to maximise the benefits of using CO_2 without any CO_2 breakthrough at the well (i.e. unwanted recovery of an injected fluid inside a producing well). This idea, however will not be investigated further here.

This work will help provide information on the likelihood of water conning for inter-seasonal PM-CAES. Water coning is characterised by the presence of water with gas in the well during the generation phase when the gas pressure is decreased below hydrostatic pressure (Allen *et al.*, 1983; Kushnir, Ullmann and Dayan, 2012). Water coning must be avoided to prevent severe damage to the gas turbine (Allen *et al.*, 1983; Braester and Bear, 1984; Azin, Nasiri and Entezari, 2008). To be avoided the wells should be partially penetrating, that is, not extending all the way to the base of the reservoir (Figure 2-12), and the distance between the gas/water interface and the well face should be important enough. In sandstones, since horizontal permeability tends to be higher than vertical permeability the lateral distance between the well face and the gas/water interface should be greater than the vertical one. Conclusions diverge about the importance of water coning. According to Kushnir *et al.* (2012) and Kushnir *et al.* (2010) water coning is a key limiting factor for the discharge gas flow rate. For Allen *et al.* (1983) however, the likelihood of water coning appears to be limited and greatly site dependent. This work addresses this question for inter-seasonal storage.

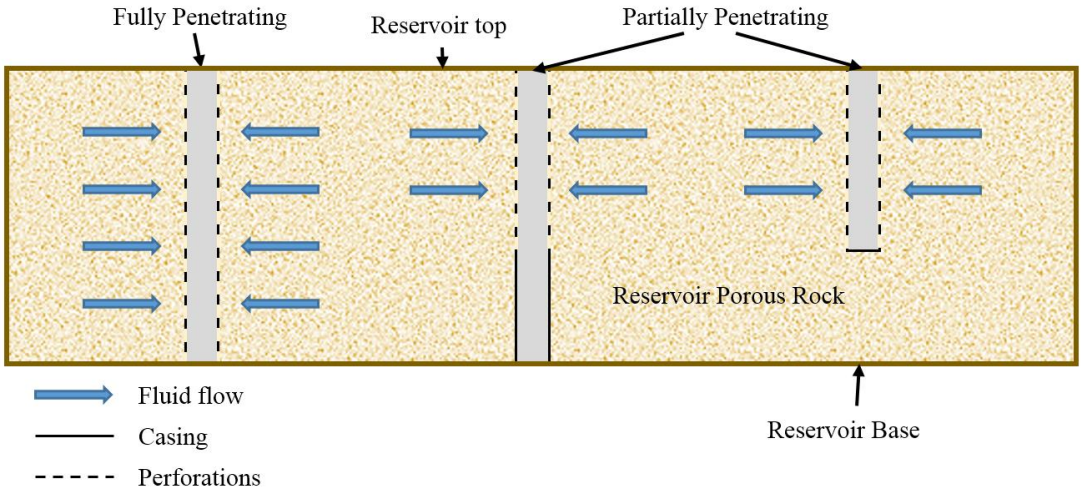

Figure 2-12: Full and partial well penetration concepts. The penetration of the well can be defined as the portion of the well length exposed to the reservoir. This section either has perforations through the casing, or a screen (mesh), both allow the flow of fluids to/from the reservoir.

2.1.3.1.2 *Depleted Gas Reservoirs*

Depleted gas reservoirs are geological formations which used to contain natural gas that has now been partially extracted. Using depleted gas reservoirs presents both advantages and disadvantages compared to saline aquifers. Two of the advantages of using depleted gas reservoirs over saline aquifers, are that more data is available on the formation since it had to

be studied for the purpose of gas extraction, and also that it is able to naturally hold a gas at high pressure over millions of years. However,such benefits come at a cost, the gas remaining in the reservoir after commercial production has stopped can lead to potentially flammable mixtures with uncertain compositions making them hardly usable in carefully designed turbines, and creating an uncontrolled ignition risk in high temperature reservoirs, both within the reservoir and within the surface facility, leading to a safety risk. In order to avoid flammable mixtures a reservoir sweep, consisting in the injection of a fluid into the reservoir to displace another, can be performed, or barriers formed of inert gas inserted to separate the air from the remaining natural gas. These measures are no substitute to a properly designed field development (Allen *et al.,* 1984). It is clear that those challenges make it harder to find a general case model for depleted gas reservoir. Furthermore, since a wealth of geological information and operation data history is available over field scales, specific site models are more appropriate to estimate the potential of depleted gas reservoirs. It was deemed that it was more important to assess the potential for aquifers, for which less data is available, in order to inform whether it would be worth investigating them further as an option for large scale inter-seasonal CAES.

The development phase of a depleted gas reservoir is very similar to that of a saline aquifer, since usually, it is filled by a mixture of brine and residual natural gas following natural gas depletion. When a reservoir is known as "dry", that is to say that it has an impermeable bottom seal rock instead of a water contact, wells can fully penetrate the air zone, as shown in Figure 2-12, which allows for operations to take place at a much wider range of pressures. This is due to water coning being a very low risk in dry reservoirs. The only pressure restriction which applies to a dry reservoir is that the reservoir pressure should not exceed the threshold pressure which would cause the reservoir rock to fracture (Kushnir, Ullmann and Dayan, 2012).

2.1.3.2 Cavern Stores

A cavern is ordinarily a manmade store. It can either be developed in low permeability hard rock or underground salt deposits. Salt caverns can be developed using a process known as solution mining which requires a well reaching the salt formation in which warm water is being pumped in and out in order to dissolve a cavern out (Figure 2-13).

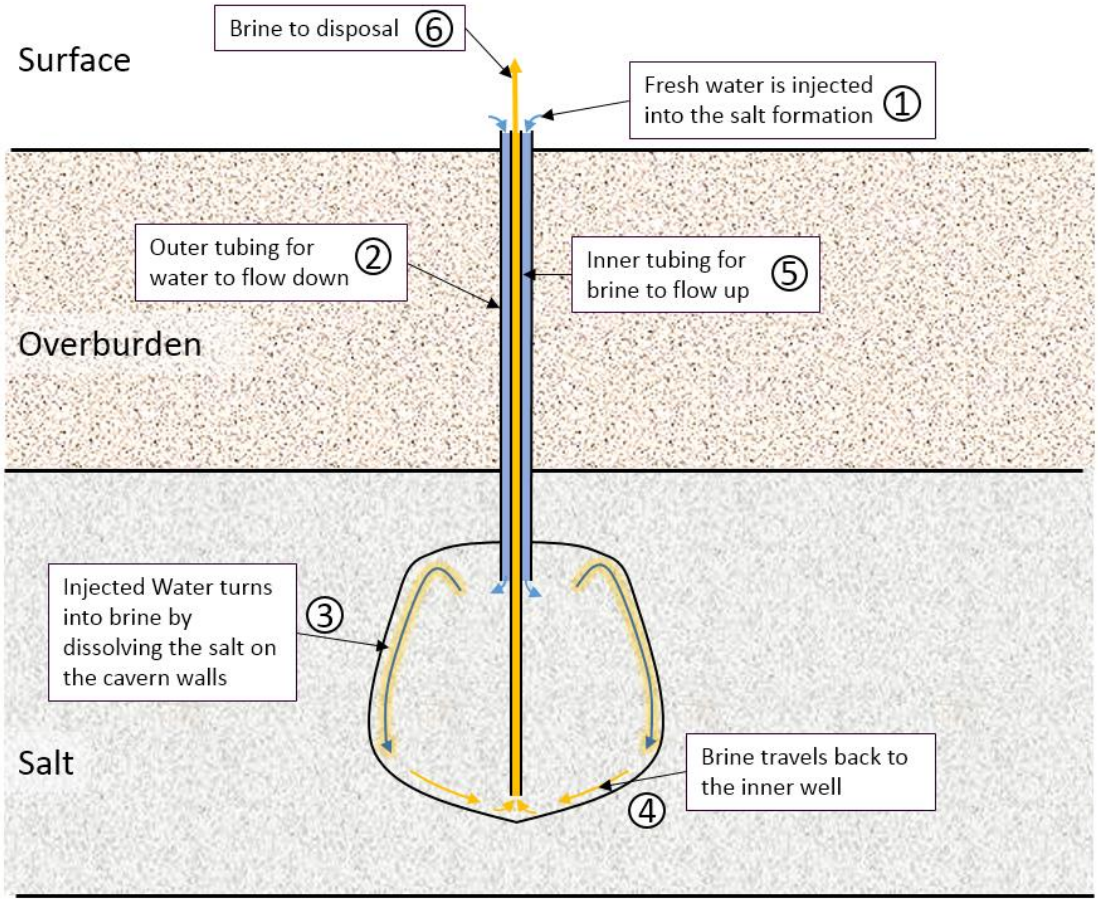

Figure 2-13: Solution mining process schematic. Solution mining is performed by circulating water through the salt formation using a well. The water is injected into the formation (1 and 2) and dissolves the surrounding salt (3) before being forced back to the well (4) and to the surface (5) where it can be treated or disposed off (6). Once the process is finished a layer of sludge has formed at the base of the cavern and some of the brine will be impossible to recover. This needs to be taken into account when working out the cavern volume.

Using a cavern over a porous rock reservoir has advantages. Firstly, caverns are readily available and can be made in almost any location since many rock types can be used (e.g. salt, granite although more expensive than salt). Secondly, there are no issues linked to pressure gradients and water coning in a cavern due to the fact that the store is hollow rather than porous. This means that deliverability rates and storage rates are much more flexible than in porous rock reservoirs. The maximum storage pressure should not exceed ~160 bar/km of depth for caverns (Kreid and McKinnon, 1978).

However, some limitations are also significant. The volume of air in the caverns is insufficient to undertake inter-seasonal storage. Huntorf and McIntosh CAES plants use caverns and operate on daily or so cycles (Crotogino, Mohmeyer and Scharf, 2001; Chen *et al.*, 2009). Hard rock caverns are expensive to create and using pre-existing mines or other caverns removes the ability to choose the location and depth (Kushnir, Ullmann and Dayan, 2012).

Similarly, pre-existing caverns might not have been made to handle cyclic pressure variations and are therefore at risk of limiting the deliverability and storage rates. Building a cavern is also time consuming. Salt caverns are relatively low cost to mine but might end up being limited if CAES develops (Oldenburg and Pan, 2013a).

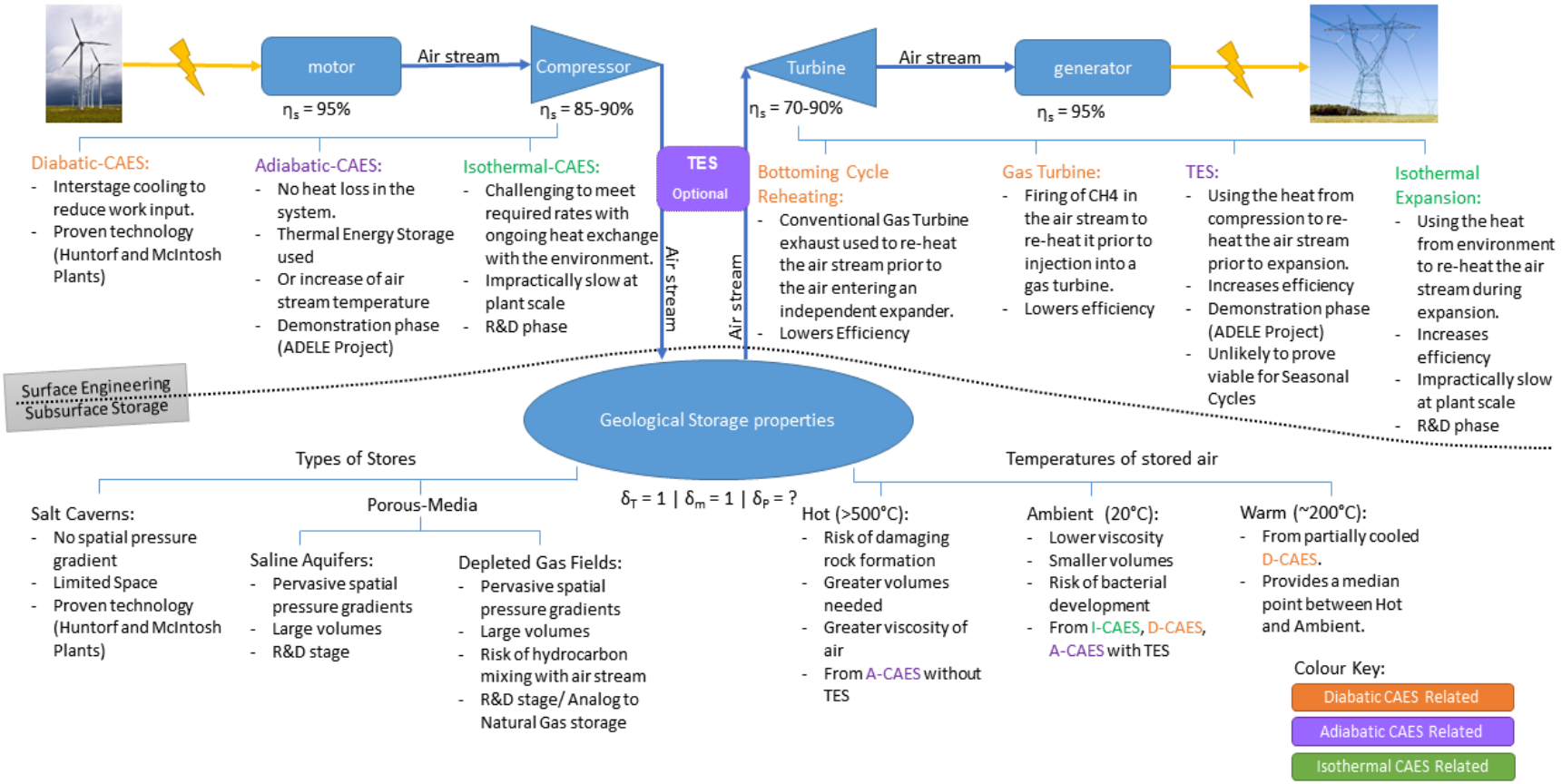

Figure 2-14: Overview of CAES technologies and store types. η_s represents the isentropic efficiency which accounts for losses between an ideal process with no losses and real process with losses. δ represents the changes in temperature (T), air mass (M) and pressure (P) occurring inside the store as a ratio between the start and finish of the shut-in phases.

2.1.4 Developments and Challenges of CAES

Following on from the introduction to the variety of CAES technologies, this section will introduce the two existing CAES plants, referred to numerously throughout this study, as well as current major CAES projects worldwide to provide an understanding of where the technology currently stands.

2.1.4.1 Reference CAES Plants

This section presents the two CAES plants currently in operation in the world, both of which are D-CAES. The Huntorf plant will later be used to calibrate the combustion efficiency of the model. Furthermore, both plants illustrate well what services and operational reliability CAES has to offer.

2.1.4.1.1 Huntorf

The Huntof CAES Plant, located near Bremen in Germany, started operating in late 1978. The plant was initially designed and built to provide up to two hours of storage at 290 MW by Asea Brown Boveri Ltd. This plant's purpose was to provide enough energy to nuclear power plants to operate a restart in case of a complete grid outage (i.e. black-start services) as well as providing power to meet sharp, but short, increases in demand (i.e. peak shaving services). The plant has operated successfully for almost four decades being available 90% of the time and a starting up with a reliability of 99%. The plant has been modified to accommodate up to three hours of storage at 321 MW, enabling it to be used to provide balancing services to the wind generation in Germany (Hoffeins, 1994; Crotogino, Mohmeyer and Scharf, 2001; Succar and Williams, 2008; Kushnir, Ullmann and Dayan, 2012).

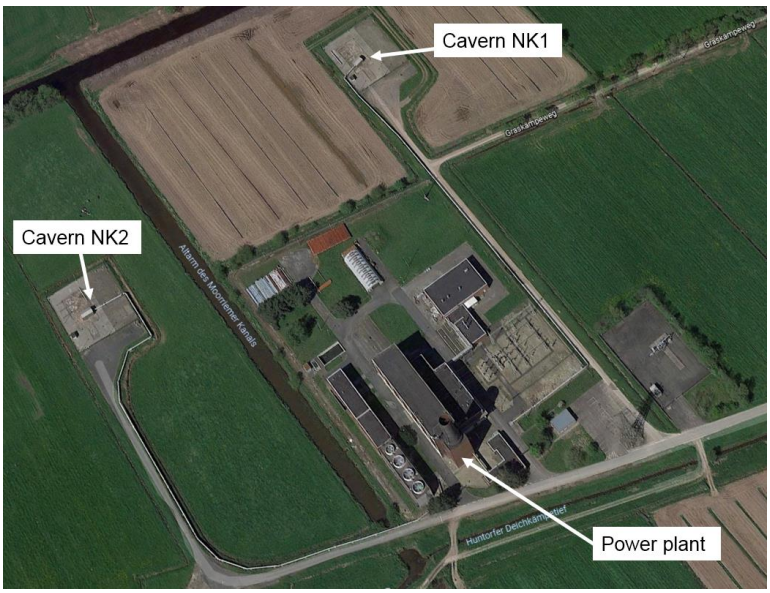

Figure 2-15: Aerial view of the Huntorf CAES plant site depicting the surface footprint a CAES plant might have (Edited from Google GeoBasis-DE/BKG (©2009)) (Crotogino, Mohmeyer and Scharf, 2001).

The underground stores used at Huntorf comprise of two salt caverns with a total combined volume of 310,000 m^3 and a pressure operability range of 48 to 66 bar. The compressors operate at a mass flow rate of 108 kg/s whilst the expander operates at rate of 417 kg/s. The compression and expansion both occur over two stages. No heat recuperators are used at Huntorf to minimise the start-up time of the plant (Succar and Williams, 2008).

2.1.4.1.2 *McIntosh*

In 1991, thirteen years after Huntorf started operating in Europe, a second CAES plant was commissioned in Alabama, USA. Built by the Alabama Electric Cooperative the 110 MW McIntosh plant was designed to operate at full power for 26 hours. Unlike Huntorf, it uses a single salt cavern of 560,000 m^3 as the air store, with an operating pressure range of 45 to 74 bar. The project was developed by Dresser-Rand, which was involved on the Larne CAES project in Northern Ireland (Gaelectric, 2017). One of the key additions to the Huntorf design was the addition of a heat recuperator which reduces fuel consumption by 22%, hence lowering the heat-rate of the plant. Despite initial complications addressed by changes to the combustors, the plant has now been in operation for over 15 years. The average starting reliability and average running reliability of the generation cycle are 91.2% and 96.8% respectively, and of 92.1% and 99.5% for the compression cycle (Succar and Williams, 2008).

2.1.4.2 CAES Projects

A few other projects have been commissioned since the beginning of the 21st century. It is important to note that the proposal for new projects shifted from an average of once a decade or so, prior to the year 2000, to once a year since. The Department of Energy of the USA have put together a database of the energy storage projects taking place worldwide (http://www.energystorageexchange.org/). Out of the other 19 projects in the database, the most relevant are introduced thereafter. Adiabatic-CAES is currently being tested by the ALACAES project in Switzerland; it uses an abandoned tunnel as the air store. A project in Gaines, Texas USA, was commissioned in 2012 and operates a near-isothermal CAES technology integrated to wind power. SustainX has another 1.5 MW near-isothermal demonstration project in the USA. In Europe, Gaelectric Energy Storage had announced a 330 MW D-CAES, due to be built in Larne, Northern Ireland in 2019, but the funding was pulled out in early 2018. Many more CAES related projects are in the early phases of development and the early 2020s should see demonstration plants' commissioning.

2.1.4.3 Technical Obstacles & Limitations to CAES Development

There are many reasons why only a very limited number of CAES projects are planned or undergoing, most of which have been introduced over the past two chapters. Here, those limitations will be summarised within the context of the research undertaken in this study.

One of the challenges is the difficulty of locating adequate and economically viable geological formations enabling storage under CAES operation (Kushnir, Ullmann and Dayan, 2012). The most widespread formations adequate for CAES are aquifers, however, they are also the ones with the least data available (Succar and Williams, 2008). This study will provide further information on those issues by informing on where the potential geology of interest lies in the offshore UK, as well as which geological parameters are key and need to be constrained first. To properly design a CAES plant, the geological reservoir characteristics need to be known, and the associated variations in pressure and temperature during operation accurately predicted and modelled (Kushnir, Ullmann and Dayan, 2012). This is essential as it is needed to establish the number of wells needed to inject/extract air from a saline aquifer. It will also guarantee that the reservoir is operated within a safe range of pressures and temperature. This study will provide an assessment of the pressure fluctuations associated with an inter-seasonal CAES cycle in porous rock for compartmentalised reservoirs. Furthermore, predicting pressure variations in the reservoir enables the surface turbomachinery to be selected according to reservoir operating requirements. That is to say that the compressor unit must be able to meet the maximum storage pressure at the well top, and that during discharge the pressure and temperature in the reservoir dictate the inlet pressure of the gas turbine, as well as the fuel required for firing the discharged air. In addition to these considerations, further economic, political and environmental concerns are likely to slow down the investment in CAES projects (Kushnir, Ullmann and Dayan, 2012). This project will not address those issues in detail, only introduce them in the discussions when they are relevant to understanding the technical feasibility of PM-CAES in the UK.

2.2 Theory of Isothermal Two-Phase Flow in Porous Media

2.2.1 Conceptual Modelling of Fundamental Principles

This section introduces the key concepts relevant to understanding flow in porous media, in particular two-phase flow involving liquid and gas. It provides the knowledge needed to understand how micro-scale processes taking place on a pore level can be approximated to model flow in subsurface reservoir on the macro-scale.

2.2.1.1 Phases and Saturation

A given control volume within a porous medium subjected to two-phase flow (in the case of PM-CAES a gas and a liquid) can either have one of the two phases present, or both. On the macro-scale the rock is conceptualised as a homogeneous material, where at a micro-scale the rock would contain pore space (i.e. void) and rock. That porosity within the rock which is able to contain either phase because the pores are interconnected is referred to as the *effective*

porosity. When a single liquid phase is being considered, the proportion of effective porosity occupied by the liquid is called *saturation*. When in two-phase flow, the proportion of the phases relative to each other within the effective porosity can be quantified using saturation. Under two-phase flow, if only one phase is present it has a phase saturation of 1, and the absent phase of 0. In a two phase system the saturation of any phase lies between 0 and 1 (Helmig, 1997). The concepts of saturation and porosity are illustrated in Figure 2-16.

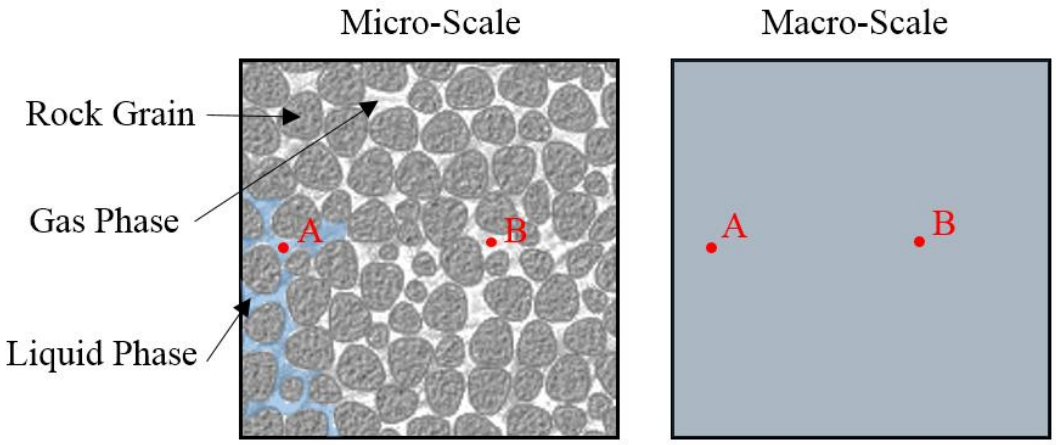

Figure 2-16: Representation of the porous media on micro and macro scales. At a micro scale the concepts of saturation and porosity are non-existent (left image), yet they are a useful approximation of the porous media at a macro scale where the microscopic features are not depicted individually (see right image). This can be illustrated by taking two discrete points A and B and considering where they fall on either scales. On a micro-scale each point is either located in pore space or rock grain, and similarly, either in the fluid phase or the gas phase. On the contrary, on the macro-scale point A and B both have a liquid phase saturation of about 25% and a porosity of 40%. This illustrated how, at a macro-scale, having two distinct points becomes irrelevant as both A and B share the same characteristics. Hence, the macro-scale can be seen as a continuum.

2.2.1.2 Capillarity

The interactions between the various phases (solid, fluid, gas) in a two phase system are characterised by the surface forces at the interfaces between them. The molecular cohesion of those phases as well as adhesion effects between them are the cause of those forces. The various forces will usually lead to a curved interface between the two fluids as shown in Figure 2-17. These forces between the phases are known as the surface tensions (interfacial tension for σ_{12} in the figure) and the angle between the interface of the two fluids and the solid's surface is the contact angle. The fluid with an acute boundary angle is the wetting-fluid, the other is known as the non-wetting fluid (Helmig, 1997).

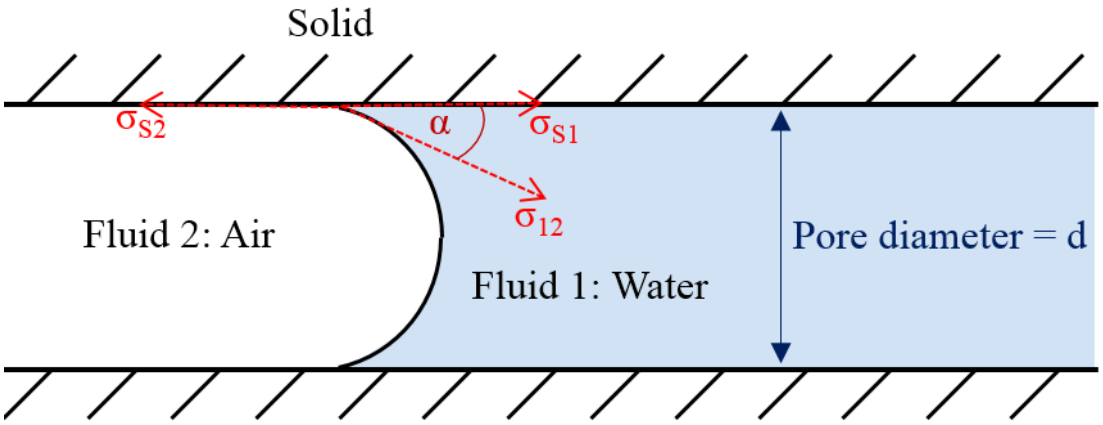

Figure 2-17: Interfacial tensions, σ, contact angle θ, and pore diameter represented for a three phase system composed of a solid capillary tube, and two fluid phases: air and water. Here, water is the wetting phase and air the non-wetting phase.

A discontinuity in pressure occurs across this curved interface between the two fluid phases. It is called the capillary pressure, p_c, and can be seen as how much pressure will have to be exerted to replace the fluid in the pore space.

$$p_{c12} = p_2 - p_1 \qquad 2\text{-}2$$

The capillary pressure is expressed by the Laplace pressure equation:

$$p_{c12} = \frac{4\sigma_{12}\cos\theta}{d} \qquad 2\text{-}3$$

With σ_{12} the interfacial tension between the two fluid phases, θ the contact angle between the fluid interface and the solid surface, d the pore throat diameter, the subscripts 1 and 2 refer to the water and gas phase respectively.

In terms of relationship to saturation of the phases, one can understand from equation 2-3 that as the diameter of the pore throat increases the capillary pressure decreases. This means that when draining a porous rock the wetting phase will recede to smaller pores. Similarly, when more wetting phase is added to the medium (imbibition), it will move to larger pores (Helmig, 1997). This relationship between capillary pressure and saturation is represented graphically in Figure 2-18. These observations have macroscale implications in terms of capillary pressure and saturation. Indeed, since low saturation implies that the wetting phase is exclusively present in the small pores of the rock (the ones with a small pore throat), and that a relationships exists between the pore throat size and the capillary pressure through equation 2-3 then, on the macroscale there is a relationship between the capillary pressure and the saturation (Helmig, 1997).

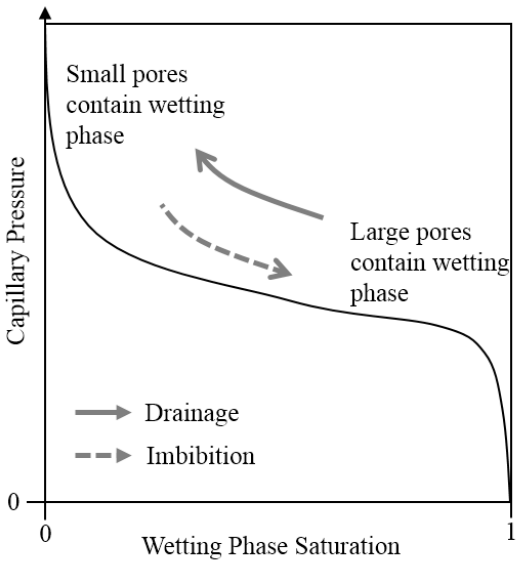

Figure 2-18: Curve illustrating the idealised relationship between capillary pressures and wetting phase saturation. When the wetting phase saturation is high large pores are occupied and the capillary pressure is low since a slight increase in pressure of the gas phase will be enough to remove the wetting phase from large pores. As the water recedes to smaller and smaller pores more and more pressure is needed to displace it out therefore the capillary pressure increases. In reality this relationship might evolve over time, this concept, known as hysteresis is explored further later on.

This relationship can be derived from experimental measurements or empirical models. The choice and details of the approach taken to represent the capillary pressure – phase saturation relationship will be discussed in section 3.3.6.1.

2.2.1.3 Darcy's Law

Flow in a porous media can be represented macroscopically by Darcy's law (Darcy, 1856). Darcy's law is useful as it relates porous media and fluids properties to fluid flow induced by a given pressure gradient. Darcy's experiment, described in his volume about the fountains of the city of Dijon, France, and the resulting empirical observation and law where derived under the following assumptions (Freeze and Cherry, 1979):

1. Laminar-flow
2. Saturated porous media
3. Steady-state flow
4. Homogeneous, isothermal and incompressible fluid
5. Neglecting kinetic energy

The fundamental assumption to use Darcy's law is that the flow has to be laminar. That is, when it is dominated by viscous forces as opposed to inertial forces. This is the case when the flow is slow and parallel. This is usually the case when modelling underground aquifers or oil and gas reservoirs. However, near the wellbore, the flow can happen to be turbulent and

dominated by inertial forces, leading to errors when modelling the well vicinity using Darcy's law (Fetter, 2001).

The Reynolds number is the ratio of inertial to viscous forces and can therefore be used to decide whether a scenario involving flow in porous media can be modelled using Darcy's law. According to Bear (1972) and Hassanizadeh & Gray (1987) laminar flow can be assumed when the Reynolds number is less than 10.

Darcy's law provides a relationship between the fluid flow, Q (m^3/s), the flow area A (m^2), the hydraulic conductivity of the porous medium with respect to the fluid, K (m/s), and the hydraulic gradient, i (-), representing the pressure gradient driving the fluid.

$$Q = AKi \tag{2-4}$$

Or the specific discharge, **v** ($m^3/s\ m^2$):

$$\frac{Q}{A} = \mathbf{v} = Ki \tag{2-5}$$

Darcy's law expresses the flow rate as a linear function of the pressure gradient. Where non laminar flow occurs this relationship is no longer linear. However several authors have shown that Darcy's law can easily be adapted to account for this by including a non-linear pressure term (Kolditz, 1997; McCraw *et al.*, 2015).

2.2.1.4 Permeability

The hydraulic conductivity, K, is a constant of proportionality between the specific discharge and the pressure gradient driving the flow. Hence, as noted by (Hubbert, 1956), K is both dependent on the media and the fluid. This can be visualised by imagining an experiment where the gradient and the media are kept the same, and where water is replaced by oil. One can then easily conceive that the specific discharge of oil, which is more viscous than water, will be lower than the specific discharge of water. Hence that the term K will be reduced despite the fact that the media has remained unchanged. This led to the notion of *specific* or *intrinsic permeability* which captures the ability of the porous media to allow fluid to flow independently of the fluid itself. The hydraulic conductivity is equal to the product of the intrinsic permeability of the media, *k*, thereafter referred to as permeability, the density of the fluid, ρ, and the acceleration due to gravity, g, all divided by the fluid viscosity, μ.

$$K = \frac{k\rho g}{\mu} \tag{2-6}$$

It is important to note that this relationship is only true for single phase flow. Indeed, when a two-phase flow is being considered the fluids will impede each other's flow. This means that

if only permeability is used then the impedance of fluids on one another will not be accounted for. To represent the permeability (k) of a phase (α) a common parameter is used: the *relative permeability, krel*$_\alpha$.

$$k_\alpha = k_{rel,\alpha} k \qquad 2\text{-}7$$

Considering the fact that the saturation of the phases might change in a two-phase flow system, it is important to note that when one phase is absent then the relative permeability of that phase must be 0. Therefore relative permeability of a fluid will vary as a function of the fluids saturation (Helmig, 1997).

The phase permeability is often referred to as the *effective permeability* (k_α) and is defined as the product of the intrinsic and relative permeability.

The two most common models used to represent the relationship between relative permeability and saturation are the Brooks-Corey (Brooks and Corey, 1966) and van Genuchten (van Genuchten, 1980) models. The Brooks-Corey model will be used in this work. The model is described, and its choice discussed in section 3.3.6.2.

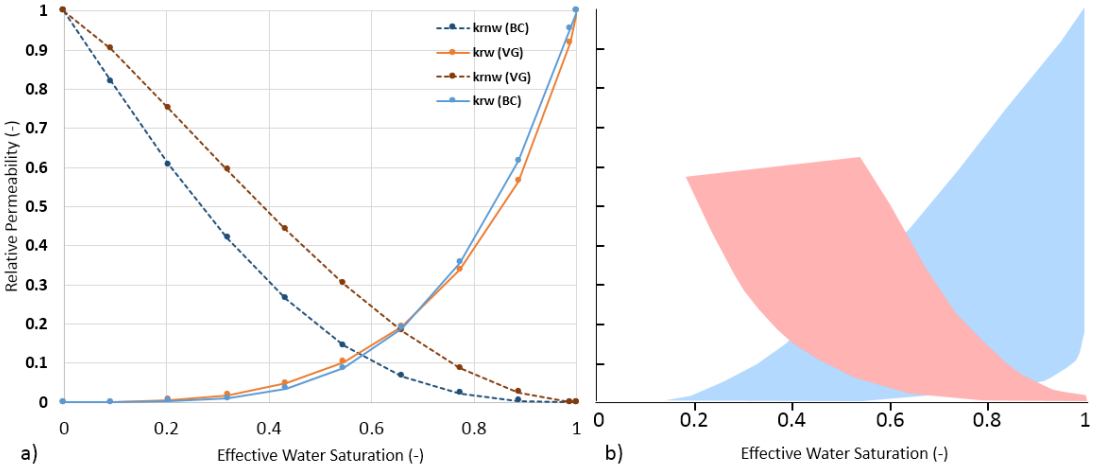

Figure 2-19: Relative Permeability – Saturation Relationships. a) Using the models from Brooks-Corey (1966) and Van Genuchten (1980). b) Areas covered by published data for CO_2 and Brine showing the variability of the relationship. Figure data from (Benson *et al.*, 2013)**.**

The general trend of either models however is that low saturations are characterised by low relative permeabilities since at low saturations the phase is confined to small pores in which the molecular forces of the fluid make flow much harder (Helmig, 1997). The curvature of the relationships are controlled by the heterogeneity of the medium. High curvature is characteristic of heterogeneous medium in which a small addition in non-wetting phase is characterised by an important drop in relative permeability of the wetting phase. This drop is

caused by some of the pores, now occupied by the non-wetting phase, acting as a bottleneck obstructing the flow of the wetting phase into a larger array of pores.

2.2.1.5 Hysteresis

Hysteresis can be defined as the dependence of the current state of a system on its previous states. In two-phase flow in porous media, hysteresis can be found in the capillary pressure-saturation (Figure 2-20) and relative permeability-saturation relationships (Lenhard and Parker, 1987; Furati, 1997).

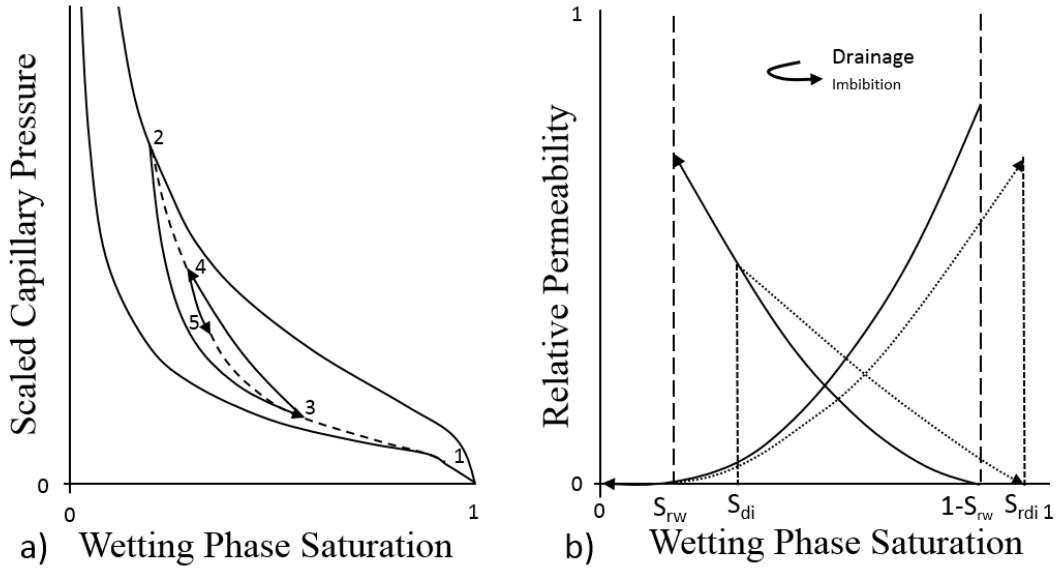

Figure 2-20: Hysteresis effects in porous media under two-phase flow cycles. a) Hypothetical hysteresis in capillary pressure - saturation curve. Redrawn using (Lenhard and Parker, 1987) **showing how for each imbibition and drainage phase the relationship changes. b) Relative permeability-Saturation relationship during a single, drainage-imbibition cycle. Redrawn using** (Furati, 1997)**.**

The hysteresis of the capillary pressure-saturation relationship can be understood by assessing how the parameters of Laplace equation 2-3 might change over multiple drainage and imbibition cycles of the wetting phase. The first effect is that the contact angle between the fluid interface and the solid varies depending if the interface is advancing or receding, consequently leading to a different capillary pressure at the same point in the system for drainage and imbibition. The second effect is due to the variable geometry of a pore throat leading to a shift in the fluid interface position within the pore throat. The final, and most important point for the porous rock system under consideration is the residual saturation (Helmig, 1997). Residual saturation is the amount of fluid that will "always" remain in the pore space once it has been emplaced. Imagine a fully water saturated system in which gas is injected, at the onset of injecting the saturation of water is 1 and that of gas is 0. Gas is injected until the saturation reaches 0.5 for both phases. Then water is injected to flush the gas out,

however, no matter how much water is injected and regardless of how high the capillary pressure between the two fluid phases is raised, the gas saturation will not drop below 0.2 for example. This is therefore a critical effect to incorporate in order to model the development of a CAES porous reservoir. The implementation of this effect will be discussed in detail in the geological modelling Chapter 3.

The hysteresis in the relative permeability-saturation relationship can be assumed reversible after a cycle of drainage followed by imbibition has been achieved, as long as the previous maximum non-wetting phase saturation is not exceeded (Furati, 1997). This assumption will be used in this work since a developed site will be assumed in the initial conditions, this will be discussed further in Chapter 3.

2.2.2 Mathematical Model

2.2.2.1 General Mass Balance

The mechanical motion of fluids in a porous reservoir, is represented by a mass and momentum equation, accompanied by constitutive equations representing fluids' and material's properties, as well as boundary conditions representing how the modelled system interacts with the surroundings (Helmig, 1997).

The general continuity equation for mass in a control volume, V, which remains constant in space and time is given by equation 2-8. This assumes that the diffusive part of the flux is not accounted for since the advective flux is much larger than the diffusive effects.

$$\frac{\partial(\phi\rho)}{\partial t} + \mathrm{div}(\phi\rho\mathbf{v}_a) - \rho Q = 0 \text{ in V} \qquad 2\text{-}8$$

With $\mathbf{v}_a$ the average fluid velocity, and ρQ the mass flux source term.

Scheidegger (1974) has shown that the Darcy velocity of each phase present in the porous medium can be described by the generalised Darcy's law to:

$$\mathbf{v}_{\boldsymbol{\alpha}} = -\frac{1}{\mu_\alpha} k_\alpha \cdot (\mathbf{grad} p_\alpha - \rho_\alpha g) \qquad 2\text{-}9$$

This expression will also be used to extend the relationship to two phase flow.

It is now necessary to relate the continuity equation to the material properties of the porous medium as well as the fluid characteristics. For fluid flow in porous media this can be achieved using Darcy's law (Bear, 1972; Helmig, 1997). The following section details how Darcy's findings can be related to the continuity equation through the average fluid velocity term.

The average velocity, $\mathbf{v}_a$, in the continuity equation is inversely proportional to the porosity of the medium (see equation 2-11). Hence, combining equation 2-8 and 2-9, the single phase flow equation is obtained:

$$\frac{\partial(\phi\rho)}{\partial t} + \text{div}\left(\rho\frac{k}{\mu}\cdot(\mathbf{grad}\, p - \rho g)\right) - \rho Q = 0 \text{ in V} \quad \text{2-10}$$

With:

$$\mathbf{v_a} = -\frac{\mathbf{v_\alpha}}{\phi} \quad \text{2-11}$$

2.2.2.2 Two-Phase Flow

The mass balance equation 2-10 can then be extended to represent two-phase behaviour in porous media, which is the focus of this study. The mass balance for a fluid phase α which totally saturates the system is:

$$\frac{\partial(\phi_\alpha\rho_\alpha)}{\partial t} + \text{div}\left(\rho_\alpha\frac{k_\alpha}{\mu_\alpha}\cdot(\mathbf{grad}\, p_\alpha - \rho_\alpha g)\right) - \rho_\alpha Q_\alpha = 0 \text{ in V} \quad \text{2-12}$$

The saturation of a phase (S_α), represents the amount of pore space occupied by one phase (ϕ_α) relative to the total porosity (ϕ):

$$S_\alpha = \frac{\phi_\alpha}{\phi} \quad \text{2-13}$$

Therefore, using the notion of relative permeability explored earlier, the mass balance equation for a single phase in an unsaturated system is found by combining equations 2-7 and 2-13 to equation 2-12:

$$\frac{\partial(S_\alpha\phi\rho_\alpha)}{\partial t} + \text{div}\left(\rho_\alpha\frac{k_{rel,\alpha}k}{\mu_\alpha}\cdot(\mathbf{grad}\, p_\alpha - \rho_\alpha g)\right) - \rho_\alpha Q_\alpha = 0 \text{ in V} \quad \text{2-14}$$

Additional constraints are necessary for this relationship to be true, firstly the sum of the saturation of all the phases must be equal to one, and secondly a relationship between the capillary pressure between the phases and the phases' saturation must exist.

The two phase system in this study would be composed of two components, air and water, and two fluid phases, liquid and gas. No phase change will be considered, hence the mention of gas or air as well as liquid or water will be equivalent.

The mass balance of water can be expressed as:

$$\frac{\partial(S_w \phi \rho_w)}{\partial t} + \text{div}\left(\rho_w \frac{k_{rel,w} k}{\mu_w} \cdot (\mathbf{grad}\, p_w - \rho_w g)\right) - \rho_w Q_w = 0 \text{ in V} \qquad 2\text{-}15$$

Assuming a constant liquid density, and a fixed rock matrix, as well as expressing the pressure of the water in terms of gas and capillary pressure, p_c, equation 2-15 can be rewritten as equation 2-16 (Kolditz, Görke, *et al.*, 2012).

$$\frac{\phi \rho_w \partial(S_w)}{\partial p_c} \dot{p_c} + \text{div}\left(\rho_w \frac{k_{rel,w} k}{\mu_w} \cdot (-\mathbf{grad}\, p_a + \mathbf{grad}\, p_c - \rho_w g)\right) - \rho_w Q_w = 0 \text{ in V} \qquad 2\text{-}16$$

The mass balance for air can also be formulated using gas capillary pressure and water saturation as variables (Kolditz, Görke, *et al.*, 2012).

$$-\frac{\phi \rho_a \partial(S_w)}{\partial p_c} \dot{p_c} + \phi(1 - S_w)\left(\frac{\partial \rho_a}{\partial p_a} \dot{p_a} + \frac{\partial \rho_a}{\partial p_c} \dot{p_c}\right) + \text{div}\left(\rho_a \frac{k_{rel,a} k}{\mu_a} \cdot (-\mathbf{grad}\, p_a + \rho_a g)\right) - \rho_a Q_a = 0 \text{ in V} \qquad 2\text{-}17$$

In the two equations above the saturation (red) and advective flux terms (blue) are included since it is assumed that the rock matrix is incompressible and that the advective regime is dominant over the diffusive regime. These are reasonable assumptions to make since 1) this study considers a clean sandstone with good reservoir qualities and 2) operating at 'reasonable pressures'. To the contrary, in clays swelling related to changes in pressure and saturations are likely, and diffusion is more prevalent. The air mass balance equation also includes a gas compressibility term (yellow), which introduces a relationship between the gas and capillary pressure and gas density. Both the saturation and compressibility terms can be considered storage terms.

These last two equations are the fundamental equations used in the modelling performed in this study. The numerical method used to solve those equation numerically are addressed in section 3.2.1.

2.3 Thermodynamic Introduction

This section will introduce the fundamental thermodynamic concepts needed to understand a CAES system and the modelling of the compressor and turbine components of the CAES system presented in Chapter 4. Further information and the detailed derivation of the equations presented here can be found in (Çengel, 2004; Barbour, 2013). The definition of the terms work, and energy are reminded here for convenience:

Energy is the ability to cause changes. With respect to work it is the capacity to do work. With respect to heat it is the capacity to heat up an object. Its units are the Joule (Çengel, 2004).

Work is a form of energy involving a force and a movement in a given direction. It is expressed in force multiplied by distance with the units of Newton-meter, which is equivalent to Joules (Çengel, 2004).

2.3.1 First Law of Thermodynamics

The First Law of Thermodynamics expresses the conservation of energy principle: the total energy within an isolated system remains constant, and internal energy is a thermodynamic property, i.e. it describes the state of the system. In a closed system, where no mass flow occurs across the boundaries, any change in energy is due to heat or work, and represented by the relationship:

$$\Delta E_{sys} = \Delta U + \Delta KE + \Delta PE = (Q_{in} - Q_{out}) + (W_{in} - W_{out}) \qquad 2\text{-}18$$

Where ΔE_{sys} is the change in total energy of a system, ΔU the change in internal energy and ΔKE and ΔPE the change in kinetic and potential energy respectively, Q and W the heat and work transferred across system boundaries respectively. The subscripts "*in*" and "*out*" refer to the quantities transferred inside and outside of the system boundary during the process respectively.

An open system is defined as a system allowing mass flow across its boundaries. When considering an open system, any change in the system energy has to be equivalent to the energy transferred across its boundaries, either as heat and work or through mass flow (Çengel, 2004). This principle is expressed by relation 2-19.

$$\Delta E_{sys} = E_{in} - E_{out} = (Q_{in} - Q_{out}) + (W_{in} - W_{out}) + \left(E_{mass,in} - E_{mass,out}\right) \qquad 2\text{-}19$$

The right-hand side of the equation deals only with positive quantities. The direction of the energy transfer is represented by the subscripts "*in*" and "*out*" (Çengel, 2004). The principles

illustrated here will be the basis for the mathematical model of the compressor and turbine described in Chapter 4.

The work in equation 2-19 can be divided into the work performed by the fluid at the inlet and outlet of the system and all remaining forms of work. This, combined to the definition of change in energy of a closed system leads to the energy balance for an open system (Barbour, 2013):

$$\frac{dE_{sys}}{dt} = \dot{Q}_{sys} - \dot{W}_{sys} + \dot{m}(\bar{u}_{in} + p_{in}\bar{v}_{in} + KE_{in} + PE_{in}) - \dot{m}(\bar{u}_{out} + p_{out}\bar{v}_{out} + KE_{out} + PE_{out}) \quad 2\text{-}20$$

With the subscript "*sys*" referring to the control volume (in the practical case considered here the volume of the compressor or turbine), "*in*" and "*out*" the states at the inlet and outlet respectively, $\dot{W}_{sys}$ the work flow rate out of the control volume, $\dot{Q}_{sys}$ is the rate of heat input, $\bar{u}$ is the specific internal energy of the gas, *p* and $\bar{v}$ are the pressure and specific volume of the states, $\dot{m}$ is the mass flow rate of gas (Barbour, 2013).

When studying CAES turbomachinery it is reasonable to assume that there is no net gain or loss of energy within the control volume, and that the kinetic and potential energy changes across the compressor or turbine can be neglected (Çengel, 2004; Barbour, 2013; Barbour *et al.*, 2015). Grazzini & Milazzo (2012) suggest that, when studying a CAES system the changes in kinetic energy are two to three order of magnitude lower than the changes in the enthalpy of air, and hence can be neglected.

Under these assumptions, and using the definition of the specific enthalpy of the gas ($h = \bar{u} + p\bar{v}$) equation 2-20 becomes:

$$\frac{\dot{W}_{sys}}{\dot{m}} - \frac{\dot{Q}_{sys}}{\dot{m}} = h_{in} - h_{out} \quad 2\text{-}21$$

It can now be seen that when considering a process, with no heat transfer (i.e. $\dot{Q}_{sys} = 0$), the difference in enthalpy is equal to work.

2.3.2 Second Law of Thermodynamics

The second law of thermodynamics dictates the direction of transfer of energy in a process, and the evolution of the quality of this energy. A process cannot occur unless it meets the requirements of both the first and second laws of thermodynamics as necessary (though not always sufficient) prerequisites (Çengel, 2004). There are several equivalent formulations of the second law, one of which is known as the Clausius Statement:

It is impossible to construct a device that operates in a cycle and produces no effect other than the transfer of heat from a lower-temperature body to higher-temperature body. (Clausius, 1854)

A simple analogy would be that a cup of coffee at 45 °C will not increase its temperature further when left unattended in a room at 18 °C.

If the cup is to heat up further then another effect is necessarily needed in order to fulfil the second law of thermodynamics, for example adding energy via a micro-wave.

The second law can be represented and verified rigorously using a thermodynamic quantity known as entropy, which is discussed in the next section.

2.3.3 Entropy, and its Role in Reversible and Irreversible Processes

Entropy is a measure of the quality of the energy of a system, in the sense that it describes the breadth of distribution of energy levels amongst the discrete components of a system. A low entropy would correspond to a narrow distribution of energy levels amongst the population of system components, as illustrated in Figure 2-21 and Figure 2-22. Entropy plays a critical role in the formulation of the second law of thermodynamics. It also is a fundamental agent in the concepts of reversibility and irreversibility that are critical when discussing the applications of the second law.

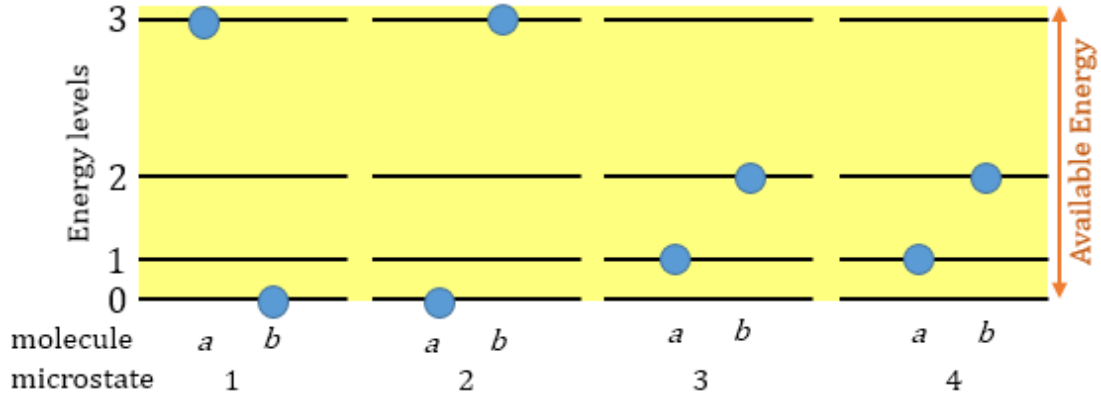

Figure 2-21: Schematic of a thermodynamic system containing two molecules, each molecule has access to four levels of energy (it is important that in this example energy is discretised). A molecule at any given level will "have" the corresponding amount of energy. For example a molecule on the first level will have zero energy whilst a molecule on the fourth level will have three energy. The system can be arranged in any way as long as the sum of all the molecules' energy is equal to the amount of available energy (i.e. three). The two molecules can therefore be arranged into four combinations called microstates, each equally probable. Entropy is positively correlated to the number of equivalent microstates possible in a system. From the schematic it can therefore be deduced that the entropy of a system is increased by either increasing the number of energy level available or by increasing the amount of molecules in the system, since either will increase the maximum number of equivalent microstates. The number of available energy levels can be increased by either increasing the temperature of the system which is akin to increasing the amount of available energy, or by increasing the volume or by decreasing the pressure of the system which reduces the gap between energy levels.

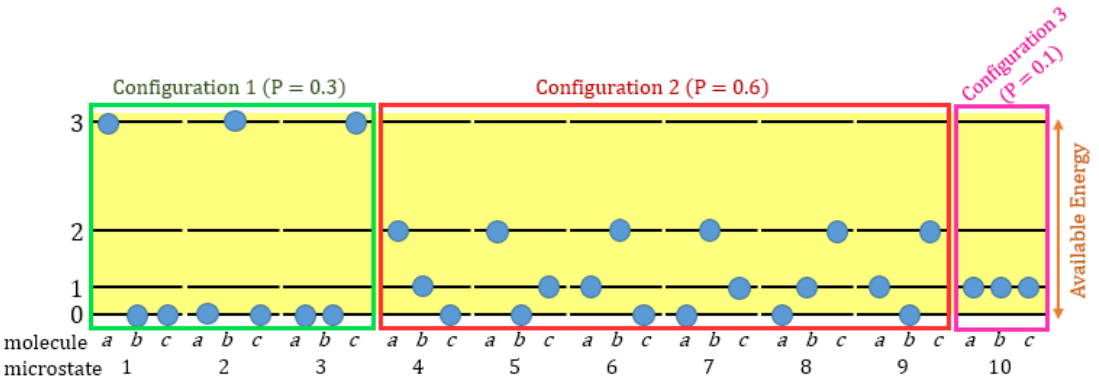

Figure 2-22: Building on the notions from Figure 2-21, if another molecule is added to the system the number of possible microstates in the system increases to 10. It is now interesting to see that the microstates can be grouped in configurations based on the energy level repartition. All the microstates in a configuration are equivalent to one another. In this example, molecules a, b and c are identical, and move from one microstate to another randomly, hence the probability of a microstate of configuration 2 occurring in the system is of 0.6 whereas the probability of the configuration 3 occurring is only of 0.1. If the number of molecule in the system is important, then the amount of microstates increases exponentially and the probability of occurrence of a microstate which is not within the main configuration become negligible. The configuration of any system which contains a large enough amount of molecules can therefore be predicted. It should also be noted that the configuration with the dominant probability will always be the one containing microstates where most of the energy level are occupied (i.e. the widest distribution in energy level).

Mathematically, a change in entropy is characterised by equation 2-22:

$$dS = \frac{\delta Q}{T_b} + S_{gen} \qquad 2\text{-}22$$

A process is said to be reversible if both the system and the surroundings can be returned to their initial states at the end of the process, while overall exchange of energy at the end of the reversal would be nil (Çengel, 2004). If only the system can be reverted to its initial state however, then, changes to the surroundings have occurred (such as work or heat) to restore the system's initial state. A process resulting in that outcome would be described as irreversible. (Çengel, 2004).

If the second Law of Thermodynamics is expressed using entropy, it states that a process can only occur if the sum of the change in entropy within the system, and its surrounding, is equal or greater to zero. This is why a reversible process is associated with no change in entropy within the system, and why entropy is a good property to represent the second law of thermodynamics and the quality of energy (Çengel, 2004). A process which leads to no change in entropy is referred to as isentropic.

2.3.4 Isentropic Efficiencies

Isentropic efficiencies provide a quantification of the difference between a real and an isentropic (ideal) process. For the study of CAES, they can be used to assess the performance

of the compressor and turbine. Equation 2-23 describes isentropic efficiency for steady-state turbines used in CAES, it is defined as the ratio of real (actual) work to isentropic (ideal) work (Çengel, 2004).

$$\eta_{is} = \frac{W_{real}}{W_{is}} = \frac{\left(\dot{W}/\dot{m}\right)_{real}}{\left(\dot{W}/\dot{m}\right)_{is}} \quad 2\text{-}23$$

And equation 2-24 for steady-state compressors:

$$\eta_{is} = \frac{-W_{is}}{-W_{real}} = \frac{\left(-\dot{W}/\dot{m}\right)_{is}}{\left(-\dot{W}/\dot{m}\right)_{real}} \quad 2\text{-}24$$

2.3.5 Ideal Gas

An ideal gas, as defined by the ideal gas law, is a gas for which its temperature (*T*), pressure (*P*), specific gas constant (*R*) and specific molar volume (*v*) are related by:

$$Pv = RT \quad 2\text{-}25$$

As demonstrated experimentally by Joule (1843), a gas can be considered ideal when its pressure is small with respect to its critical pressure and when its temperature is high with respect to its critical temperature (Çengel, 2004). In these conditions, individual gas molecules are expected to interact little with each other, except through elastic collisions, and the space between each molecule is vast compared to their dimensions (which can be neglected when calculating the macroscopic properties of the gas).

Considerable simplifications arise from the application of equation 2-25, in particular for an ideal gas it can be shown that the internal energy is a function of temperature alone. Since enthalpy is derived from internal energy by addition of the product *Pv*, application of 2-25 also implies that enthalpy is a function of temperature alone for an ideal gas.

2.3.5.1 Specific heats of an ideal gas

The specific heat indicates the amount of heat needed to raise the temperature of a unit mass of gas by one degree Celsius. Two definitions are widely used, one relating to heat addition taking place at constant volume, c_v, and the other one referring to heat addition at constant pressure, c_p. Understanding how those specific heat varies is essential to predicting the work output of turbines and compressors in a CAES system (Çengel, 2004).

Defining the specific heats in terms of other thermodynamic quantities yields:

$$c_v = \left(\frac{\partial u}{\partial T}\right)_v \quad \text{2-26}$$

$$c_p = \left(\frac{\partial h}{\partial T}\right)_p \quad \text{2-27}$$

Therefore, since the internal energy, *u*, and enthalpy, *h*, of an ideal gas are only dependent on temperature, so are the specific heats (Çengel, 2004).

The specific heat ratio of an ideal gas is:

$$k = \frac{c_p(T)}{c_v(T)} \quad \text{2-28}$$

It can be shown that an isentropic process is described by the relationship $pv^k = constant$ for an ideal gas with constant specific heats (i.e. a perfect gas) (Çengel, 2004).

An isentropic process between two states can be expressed by:

$$p_1 v_1^k = p_2 v_2^k \quad \text{2-29}$$

Which can be rearranged to:

$$\frac{p_2}{p_1} = \left(\frac{v_1}{v_2}\right)^k \quad \text{2-30}$$

If an ideal gas is assumed then:

$$p_1 v = RT_1 \text{ and } p_2 v = RT_2 \quad \text{2-31}$$

Which gives:

$$\frac{p_2}{p_1} = \left(\frac{RT_1/p_1}{RT_2/p_2}\right)^k = \left(\frac{T_1 p_2}{T_2 p_1}\right)^k = \left(\frac{p_2}{p_1}\right)^k \left(\frac{T_1}{T_2}\right)^k \quad \text{2-32}$$

Or:

$$\frac{T_2}{T_1} = \left(\frac{p_2}{p_1}\right)^{\frac{k-1}{k}} \quad \text{2-33}$$

2.3.6 Polytropic Process and Efficiency

So far mostly reversible processes have been discussed for ideal gases. However, in order to model reality more accurately it is important to account for the irreversibilities occurring in

real processes. As of yet, only isentropic efficiency has been proposed to account for those irreversibilitities. Another alternative, building upon the notions presented above and better suited to CAES turbomachinery is presented thereafter.

A polytropic process is a process which includes some heat transfer to the environment. When applied to CAES it can be used to account for the heat transfers through the turbomachinery boundaries which are not perfectly insulated.

A polytropic process is described by the relationship:

$$pv^n = constant \tag{2-34}$$

In which n is a constant specific to the process studied. A polytropic process between to states can be expressed by:

$$p_1 v_1^n = p_2 v_2^n \tag{2-35}$$

Which can be rearranged to:

$$\frac{p_2}{p_1} = \left(\frac{v_1}{v_2}\right)^n \tag{2-36}$$

If an ideal gas is assumed then:

$$\frac{T_2}{T_1} = \left(\frac{p_2}{p_1}\right)^{\frac{n-1}{n}} \tag{2-37}$$

Therefore there exists a relationship, to express a polytropic process using an isentropic formulation, with the ratio in the exponent being corrected by a value known as the polytropic efficiency defined by equations 2-38 and 2-39 for a compressor and turbine respectively.

$$\eta_{pol,c} = \frac{n}{n-1}\frac{k-1}{k} \tag{2-38}$$

$$\eta_{pol,t} = \frac{n-1}{n}\frac{k}{k-1} \tag{2-39}$$

The polytropic efficiency is independent from the compression ratio (Barbour, 2013). This makes it a more appropriate way to account for irreversibilities in the system, since mass flow rates are constant, but pressure ratios variable throughout the compression and expansion time periods.

In the literature most of the efficiencies provided for the turbomachinery are given as isentropic efficiencies. Therefore a conversion from isentropic to polytropic efficiency is necessary. This can be achieved by assuming that the polytropic process is representative of the real work, which is reasonable since the polytropic exponent accounts for heat transfer.

From the following reminder on the relationship between isentropic efficiency and work, enthalpy and temperature:

$$\eta_{is,c} = \frac{W_{is}}{W_{pol}} = \frac{h_{out,is} - h_{in}}{h_{out,pol} - h_{in}} = \frac{T_{out,is} - T_{in}}{T_{out,pol} - T_{in}} \quad \text{2-40}$$

Which gives, when replacing the temperature difference by the relationship to pressure ratios given by equation 2-33 and 2-37:

$$\eta_{is,c} = \frac{{P_{out}/P_{in}}^{\frac{k-1}{k}} - 1}{{P_{out}/P_{in}}^{\frac{n-1}{n}} - 1} \quad \text{2-41}$$

And when replacing the polytropic exponent by the ratio of specific heat corrected by the polytropic efficiency as indicated in 2-39, a relationship between both efficiencies solely dependent on the pressure ratio can be established:

$$\eta_{is,c} = \frac{{P_{out}/P_{in}}^{\frac{k-1}{k}} - 1}{{P_{out}/P_{in}}^{\frac{k-1}{k\,\eta_{pol,c}}} - 1} \quad \text{2-42}$$

2.3.7 Visualising CAES technologies

Isentropic and polytropic processes, can be visualised on a pressure- volume diagram in Figure 2-23. Another process type not yet introduced in term of polytropic exponent is an isothermal process, in that case n = 1. The area to the left of the curves in the figure show the integral of VdP, that is the work necessary for compression (Çengel, 2004). One can see that the compression requiring the least work is isothermal, and the one requiring the maximum work is isentropic. The same would be true for expansion where isothermal expansion would produce the least amount of work, and adiabatic the most amount of work. If both expansion

and compression path can be matched to one another then the system becomes highly efficient, hence why a considerable amount of research is being undertaken in adiabatic and isothermal CAES. One should note however, that although isothermal CAES might be able to offer high efficiencies, the amount of work that can be extracted per mass unit of air is lower than with adiabatic CAES making it potentially less attractive. The derivation of the work for multi-stage expansion and compression are presented in section 4.2.1.2 which describes the plant model built for this study.

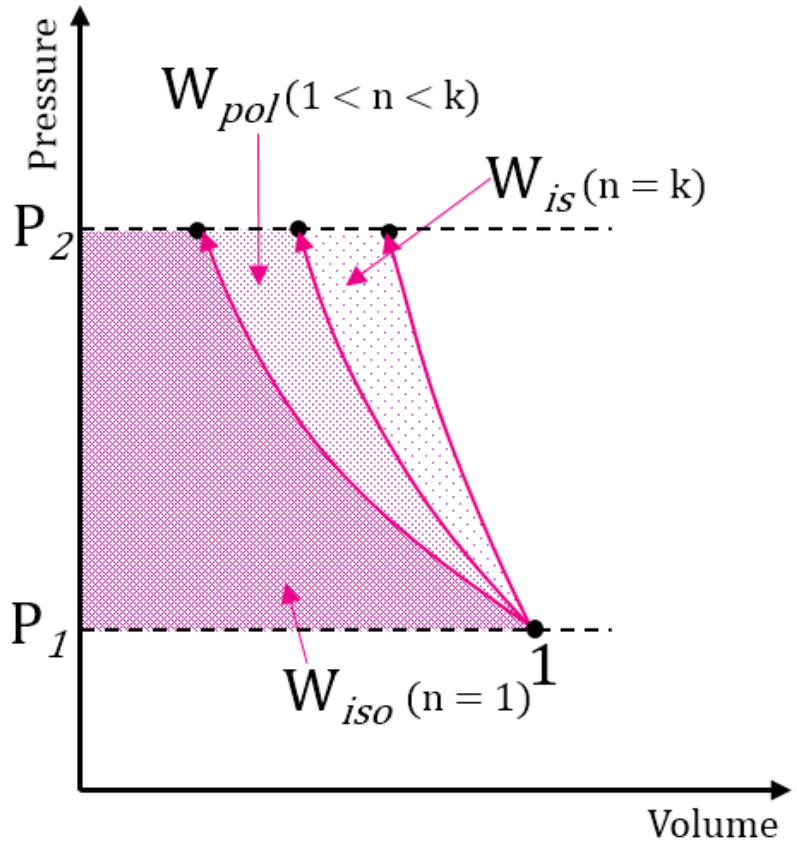

Figure 2-23: Pressure-specific volume diagram of isentropic, polytropic and isothermal compression from a pressure 1 to a pressure 2. The superimposed dotted area to the left of each of the curve represents the amount of work needed to perform the compression. Reproduced from (Çengel, 2004)**.**

2.4 Conclusions

The literature review undertaken in this chapter has shown that diabatic or conventional CAES plant technology is the most suited to address the challenge of deploying the technology to address the need for inter-seasonal energy storage. The two main reasons for this choice are that conventional CAES has a proven track record of over 40 years of successful operation at Huntorf, Germany and 20 at McIntosh, USA; the second most important reason is that the well-researched Adiabatic-CAES technology is unusable because no thermal energy storage temperature technology exists which can store heat at high temperatures on the timescales required for inter-seasonal storage.

Another key finding from the literature review which underpin this research is that porous rock, and in particular saline aquifers, would offer the large storage volume necessary to achieve inter-seasonal CAES. The main drawback identified was the lack of high resolution spatial geological data which would enable site specific modelling and investigation to be performed, leading to the need to develop a methodology capable of addressing this limitation. This method is presented in the following Chapter 3. This limitation is also the reason why depleted gas fields are not being considered in this study. Both because higher quality data is available, and the presence of residual hydrocarbons would lead to a more complex system, making a site specific approach better suited to assessing the CAES potential of those fields.

The challenges of quantifying the efficiency of a CAES system in a way that is comparable to other generation and storage technologies had also been highlighted. Various metrics where discussed, such as the CAES plant heat rate and the charging electricity ratio, both of which provide insights in how to optimise and design the CAES system. However, round-trip efficiency has been identified as the one metric that makes the technology comparable to others. This is because it accounts for the fact that part of the energy input to a PM-CAES system used for inter-seasonal storage will be in the form of thermal energy.

The final findings from the literature review, are more technical in nature and were aimed at providing readers with the required knowledge to understand the significance of the work carried out in the following chapters. Nonetheless a note should be made that the flow of air and water inside the store will be handled using a software package implementing Darcy's Law. The compressor and turbines will be modelled as reversible systems with losses accounted for using polytropic efficiency. It is important to stress that a relationship between the commonly reported isentropic efficiency of compressors and turbines and the pressure ratio independent polytropic efficiency used here, has been established.

Chapter 3 Modelling the Geological Store

3.1 Introduction

The previous chapters introduced the rational for considering PM-CAES as an inter-seasonal energy storage technology and for assessing its potential in the UK, along with its associated challenges. The assessment of PM-CAES requires a method to assess the storage capacity and efficiency from geological parameters, this is performed using numerical and analytical models. The five separate models address the following parts of the PM-CAES system:

1. The subsurface reservoir
2. The well
3. The compressor
4. The combustor
5. The turbine (expander)

This chapter focuses on the reservoir modelling. The aim of the reservoir model was to estimate the pressure response which might be expected using a reservoir for PM-CAES, rather than to attempt to replicate the detailed reservoir geometry of individual PM-CAES sites. The reason for this choice being that the variability in geology offshore UK would have made the results of a complex model no more transferable to other sites than the one modelled. In addition, for some formations only scarce data is available. A more modular approach was preferred where the reservoir was idealised and a sensitivity analysis performed on key parameters identified in the literature, which can be determined, at least approximately, using geophysical monitoring techniques. The advantage of this method is that it allows the quantification of uncertainties resulting from scare geological data.

This chapter presents:

1) The development of the geological model using the OpenGeoSys modelling software.
2) How the sensitivity analysis of this model was designed based on the offshore UK saline aquifer geology.
3) The results of the sensitivity analysis.
4) What the results indicate about predicting pressure fluctuations in a porous media store during a PM-CAES cycle, and how the limitations of the modelling might affect the results.

3.2 Geological Model Using OpenGeoSys

This section presents the structure of the OpenGeoSys software and the assumptions underlying the modelling of the reservoir. The two phase flow theory implemented in the software package is detailed in section 2.2.

3.2.1 OpenGeoSys

The OpenGeoSys project is aimed at providing an open-source numerical simulation tool for thermo-hydro-mechanical-chemical (THMC) processes in porous media. OpenGeoSys is based on an object-oriented implementation of the Finite Element Method (FEM) which allows to solve multiscale field problems numerically. The code evolved from the pioneering RockFlow modules in the mid-eighties in Fortran, to RockFlow-C in C and GeoSys/RockFlow in C++ , and finally the latest version 5.5.7 of OpenGeoSys in C++ (Kolditz, Bauer, *et al.*, 2012). The object oriented code allows for a flexible coupling of THMC processes and the associated constitutive models.

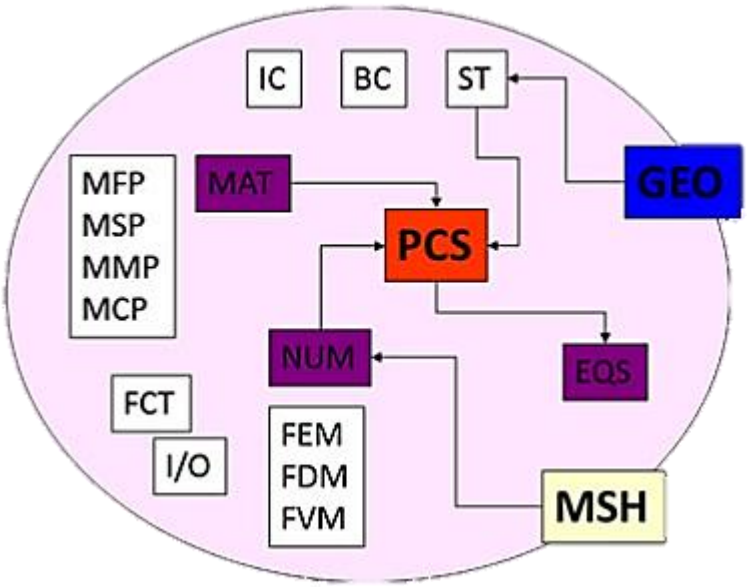

Figure 3-1: OpenGeoSys Object Oriented Structure, for explanation and the meaning of the acronyms, see text below (Kolditz, Bauer, *et al.*, 2012)

The structure of OpenGeoSys is presented in Figure 3-1 (Kolditz, Bauer, *et al.*, 2012). The object oriented approach allows the inputs needed to solve the governing equations, associated with the THMC processes, to be provided in individual files. Each of the file types discussed below take the form of essentially text files, where each file type is referred to by the corresponding 3 letter extension shown in Figure 3-1 (e.g. mymodel.msh and mymodel.geo). The MSH file contains the finite element mesh representing the space discretisation in the form of nodes and elements (see Figure 3-2), over which the governing equations are solved. The geometry object (GEO) is used to assign names to individual nodes or groups of nodes. The names in the GEO object can then be used to assign the boundary conditions (BC), initial conditions (IC) and source terms (ST) needed to solve the governing equations and define the problem. Outputs can also be requested at any node named within the GEO object. In the

reservoir simulations performed in this study the data is extracted at the well node located at the top of the reservoir. The fluid equations of state (e.g. for density and viscosity) are specified in the material fluid properties object (MFP). The material properties (e.g. capillary pressure – saturation relationship, porosity and permeability) are specified in the material medium properties object (MMP). Both MMP and MFP are required for two-phase flow processes considered in this study. Other objects such as the chemical and solid properties (MCP and MSP respectively) are needed for mass or reactive transport and mechanical processes, none of which are modelled in this study. The accuracy of the equation solvers are specified in the numeric object (NUM) and the settings of the time step increment in the time object (TIM). The process class (PCS) manages the coupling method of the THMC processes simulated (Kolditz, Bauer, *et al.*, 2012).

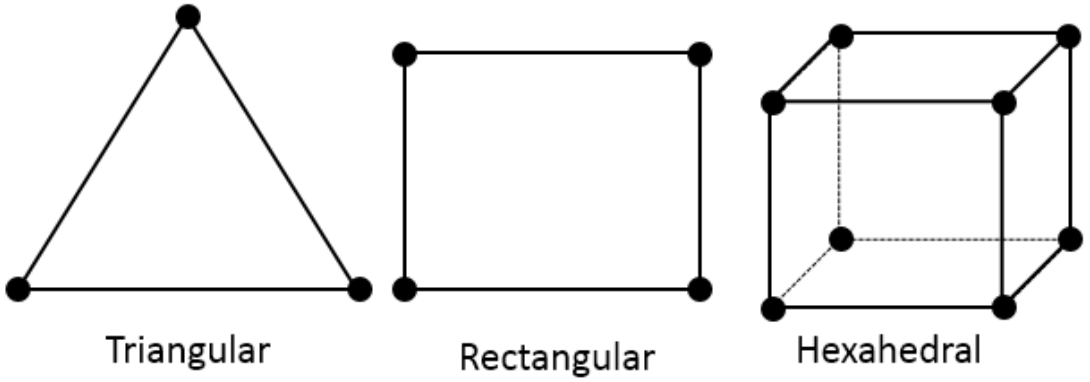

Figure 3-2: Example of elements used to discretise the domain over which the equations are to be solved by the FEM. Depending on the nature of the problem the elements can either be 3D or 2D. A mesh is composed of several elements. Shapes and sizes of elements may vary within a single mesh.

3.2.2 Numerical Finite Element Method

In order to numerically evaluate the solution of the mathematical model presented in section 2.2.2, the Finite Element Method, implemented in OpenGeoSys, was used (Kolditz, Bauer, *et al.*, 2012). Following on from the spatial discretisation of the problem into a mesh of 2D rectangular elements, the governing equations need to be discretised. This is achieved using the integral form of the governing equations. OpenGeoSys implements the method of weighted residuals, which is frequently used to solve hydraulic problems (Helmig, 1997).

The method of weighted residuals consists in using shape functions to estimate the solution for each element. This approximation results in a residual error at each node of the element. It is those residual errors from the other nodes and linked elements, which are then weighted by shape functions. The resulting weighted average is forced to equal zero (Istok, 1989). A weighting function often used in finite element discretisation of multiphase flow problems is the *Bubnov-Galerkin* method (Helmig, 1997). It has the particularity that the weighting

function used to weight the residual errors, and the shape function used to estimate the primary variables over the element, are the same (Istok, 1989; Helmig, 1997).

3.2.2.1 Galerkin Finite Element Method

The general balance equation for multiphase flow problem with unknown u is given as:

$$\frac{\partial}{\partial t}u + div\,\mathbf{F}(u) = r \text{ in G} \qquad 3\text{-}1$$

Where F is equal to the convective flux and diffusive flux into the domain G, minus the flux out, plus any source or sink terms.

The boundary of the domain G is defined as $\Gamma = \Gamma_D\, U\, \Gamma_N$. Therefore the initial conditions over the domain are given by:

$$u(x,0)\; u_0(x) \qquad \text{for t = 0} \quad x \in G \qquad 3\text{-}2$$

$$u(x,t) = u_D(x,t) \qquad \text{for t} \geq 0 \quad x \in \Gamma_D \text{ (Dirichlet boundary conditions)} \qquad 3\text{-}3$$

$$\mathbf{F}(u)\cdot\mathbf{n} = \mathbf{F}_n \qquad \text{for t} \geq 0 \quad x \in \Gamma_N \text{ (Neumann boundary conditions)} \qquad 3\text{-}4$$

Where **n** is the vector normal to the boundary Γ_N.

Therefore the integral form of the Eq. 3-1 if constant boundary conditions are equal to zero and Gauss' integral theorem is applied:

$$\int_G W\frac{\partial \tilde{u}}{\partial t}\,dG - \int_G \mathbf{grad}\,W\cdot(\mathbf{v}\,\tilde{u})\,dG + \int_{\Gamma_N} W\left(\tilde{\mathbf{F}}_n\cdot\mathbf{n}\right)\,d\Gamma = \int_G W\,r\,dG \qquad 3\text{-}5$$

Where, W is the weighting function used to weight the residual error from the approximation of u, $\tilde{u}$ denotes the approximation of u and $\tilde{\mathbf{F}}_n$ denotes approximation of the flux $\mathbf{F}_n$. The first term on the left hand side represents the time dependence of u, the second term on the left hand side the distribution of u over the domain, the third term on the left hand side the flux across the domain boundary, and the term on the right hand side the sources and sinks.

Setting the shape function Nj, the approximation of u over an element with j nodes is given by:

$$\tilde{u} = \sum_j \hat{u}_j N_j \qquad 3\text{-}6$$

The Standard Galerkin method for which the shape and weighting functions are the same ($W_i = N_i$) can be used to express Eq. 3-5 as follows:

$$\sum_j \frac{d\hat{u}_j}{t} \int_G N_i N_j \; dG - \sum_j \hat{u}_j \int_G \mathbf{v} \cdot \mathbf{grad}\, N_i N_j \; dG + \int_{\Gamma_N} N_i \left(\tilde{\mathbf{F}}_n \cdot \mathbf{n}\right) \; d\Gamma \quad 3\text{-}7$$

$$- \int_G N_i \, r_i \; dG = 0$$

Where $\hat{u}_j$ represents the discrete nodal value of u. The sources and sink term r is replaced by its discrete value at node i, r_i.

The integral of the first term on the left hand side of Eq. 3-7, can be written in matrix form, and is known as the *mass matrix* (Helmig, 1997):

$$\mathbf{M} = \int_G N_i N_j \; dG \quad 3\text{-}8$$

Similarly, the following flux terms can be included in the *coefficient matrix* defined as (Helmig, 1997):

$$\mathbf{A} = \int_G \mathbf{v} \cdot \mathbf{grad}\, N_i N_j \; dG \quad 3\text{-}9$$

If the remaining terms, which encompass the fluxes across the boundary and sources and sinks inside the domain, are referred to as **R**, the Eq. 3-7 can be rewritten:

$$\mathbf{M}\left[\frac{d\hat{u}_j}{dt}\right] + \mathbf{A}\left[\hat{u}_j\right] = \mathbf{R} \quad 3\text{-}10$$

3.2.2.2 Time Discretisation

As is shown in Eq. 3-10 the two phase flow problem under consideration in this study requires the discretisation of the primary variables in time as well as space. The time discretisation is achieved using a finite difference scheme in OpenGeoSys (Kolditz, Görke, *et al.*, 2012). The time dependence of u takes the form:

$$\frac{\partial u}{\partial t} = f(u) \quad 3\text{-}11$$

Considering a fixed time step size, Δt, a finite difference scheme can be applied to Eq. 3-11 to define f_m as:

$$\frac{u_{n+1} - u_n}{\Delta t} = f(u_m) \quad 3\text{-}12$$

A *Forward Difference Method* results from m = n, and a *Backwards Difference Method* from m = n + 1. A parameter w can be introduced to weight between those two end members, such that:

$$u_{n+1} = u_n + \Delta t\,(\omega f_{n+1} + (1-\omega) f_n) \quad 3\text{-}13$$

Or:

$$\frac{u_{n+1} - u_n}{\Delta t} = \omega f_{n+1} + (1-\omega) f_n \quad 3\text{-}14$$

The main finite difference schemes are:

- The Forward Difference Method uses the known values at time t, hence ω = 0
- The Crank-Nicholson Method uses mid-way value of the time interval, hence ω = ½
- The Backwards Difference Method uses the value at $t+\Delta t$ of the time interval, hence ω = 1

The finite difference method can then be applied to the rearranged form of Eq. 3-10 given as:

$$\frac{d\hat{u}}{dt} = \mathbf{M}^{-1}(\mathbf{R} - \mathbf{A}\,\hat{u}) \quad 3\text{-}15$$

In this form, the right hand side is equivalent to *f* in Eq. 3-11. Therefore using the equivalence in Eqs. 3-12 and 3-14 discretisation of u with respect to time is given by:

$$\frac{u_{n+1} - u_n}{\Delta t} = \omega[\mathbf{M}^{-1}(\mathbf{R} - \mathbf{A}\,\hat{u})]_{n+1} + (1-\omega)[\mathbf{M}^{-1}(\mathbf{R} - \mathbf{A}\,\hat{u})]_n \quad 3\text{-}16$$

Since the $\mathbf{M}$, $\mathbf{A}$ and $\mathbf{R}$ are all independent of u as shown in Eq. 3-7, approximation in time of u_{n+1} is given by:

$$\left(\frac{1}{\Delta t}\mathbf{M} + \omega\,\mathbf{A}\right) u_{n+1} = \left(\frac{1}{\Delta t}\mathbf{M} - (1-\omega)\,\mathbf{A}\right) u_n + \mathbf{R} \quad 3\text{-}17$$

Although the discretisation method described in this section is applied to a generic multiphase flow equation, it describes the key components of the OpenGeoSys software used in this study. Further information on more advanced optimisation of the method described here can be found in (Kolditz, 2002).

3.2.3 OpenGeoSys Two-Phase Flow Simulation Assumptions

For simplicity all the modelling assumptions made for the reservoir model are listed thereafter. Some assumptions are discussed further in the chapter.

1. Assume the material is a continuum: This assumption is needed to be able to differentiate continuous functions representative of the material and fluids modelled mathematically.

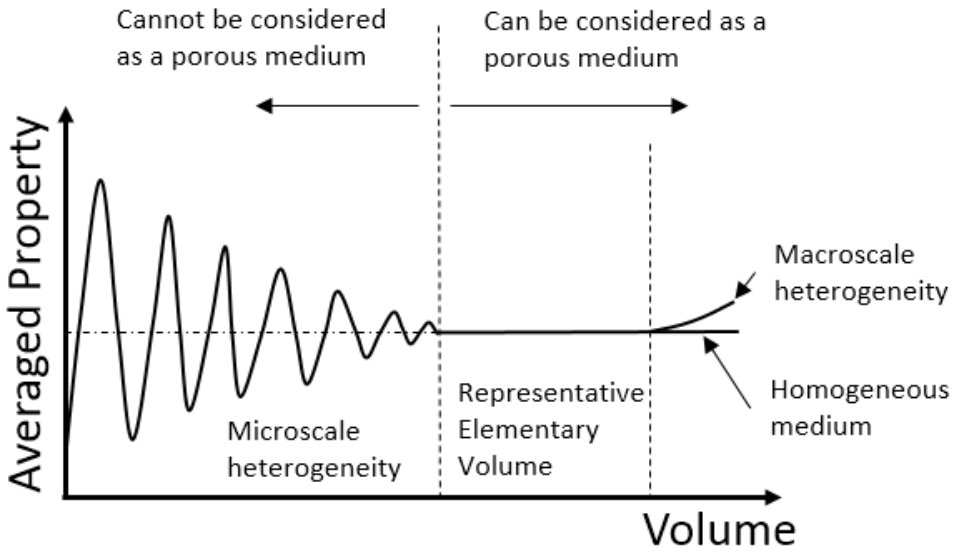

Figure 3-3: Concept of Representative Elementary Volume (REV) represents the volume at which a measured property can be assumed constant. An example applicable to the modelling of porous rock would be the saturation of the pore space. (Illustration of concept from (Bear, 1972)**).**

2. A macroscopic representation of the system is considered, with properties and laws suited to describe the physical processes occurring at a microscopic scale from a macroscopic perspective. Such laws include Darcy's Law, and Saturation, for example (Helmig, 1997).
3. Isothermal Flow: In reality temperature is likely to vary in the vicinity of the borehole. This would have an effect on the gas viscosity and density. It is also likely to cause dehydration of a approximately 5 m zone around the wellbore, as well as chemical reactions (Allen *et al.*, 1983). This means that the results of the modelling will not provide accurate measurements of water flooding due to dehydration. The knowledge that the wellbore vicinity will be dehydrated is represented by a fixed air saturation boundary condition at the well. This assumption is discussed further in section 3.3.6.4.
4. No Geochemical reactions: The modelling ignores potential geochemical reactions that might be induced by the processes modelled. Most of those reactions are likely to occur during the development of the site which is not modelled in this work, as discussed in section 3.3.10, and result from temperature greater than 90 °C (Smith *et al.*, 1978) .
5. No biological reactions: The modelling ignores potential biological development that might be induced by the processes modelled, as well as its impact on the system. Information can be found at (Succar and Williams, 2008; Bauer *et al.*, 2013).
6. No Mechanical deformation of the reservoir: No mechanical deformation of the reservoir is being modelled. Cycling swelling of the reservoir seems to occur in

underground gas storage inter-seasonal scenarios (Castelletto *et al.*, 2010). However, continuous cycling does not seem to prove unmanageable in terms of well integrity over the life span of a potential CAES project (Watson and Jones, 2010). To ensure that unrealistic results are not misinterpreted, an analytical model for rock collapse and fracture, discussed in section 3.4.1, was used to filter out the results (Aadnoy, 1991). Furthermore, after a potential reduction in reservoir quality due to initial depletion, an elastic response is to be expected (Figure 3-4) (Dornhof *et al.*, 2006). The compressibility of the matrix acts to reduce the pressure differentials between the air injection phases and the productions phases making the system modelled the worst case scenario.

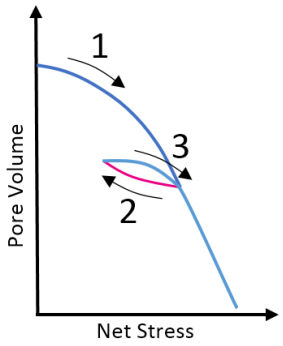

Figure 3-4: Hysteresis of compaction. The initial depletion (1) leads to increase stress, unloading the material (2) not all the pore volume is recovered, further loading of the material (3) initially leads to a quasi-elastic response. Redrawn (Dornhof *et al.*, 2006)

7. No Seal Fracturing Modelling: potential fracturing was not modelled and a maximum threshold pressure was chosen from the literature instead. A value of 0.181 bar/m depth of injection pressure was proposed as a rule of thumb by (Allen and Gutknecht, 1980), which agrees with the threshold used in this study of about 77% of the lithostatic stress, based on UK North Sea data (Moss *et al.*, 2003).
8. Using brine: The density of the liquid phase was selected to represent a brine, rather than pure water. Values for brine viscosity and density at reservoir conditions where estimated from (McCain, 1991) and (Spivey and Mccain, 2004) respectively.
9. Capillary pressure curves were derived directly from pore throat radius measurements on sandstones (Nabawy *et al.*, 2009) and verified to be applicable to the PM-CAES system using relationships developed by Pittman (1992).
10. Air density and viscosity are interpolated from tables Stephan *et al.* (2013) based on the equations of states proposed by Lemmon & Jacobsen (2004) and Lemmon, Jacobsen, Penoncello, & Friend (2000).
11. No skin effect around wellbore. Skin effects are known to either increase or reduce predicted pressure at the well-reservoir interface. Since the modelling in this study is

not site specific and not enough geological information is available to predict the skin effects, they were ignored. Furthermore, remediation technics known as "stimulation technics", including acid treatment can be put in place to mitigate the skin effect (Tronvoll, Larsen and Li, 2004).

12. The wellbore space is not modelled jointly with the reservoir. It is simulated as a boundary condition for saturation and as a source term for gas injection and production.
13. No hysteresis in capillary pressure – saturation and relative permeability – saturation curves; only one set of curve is being used. This is limiting in the sense that the residual water saturation will always remain greater than it should be. This also prevents the modelling of site development since air would be able to leave previously saturated areas leading to unrealistic results. In the case of cycling however, a slight movement of the interface between the water and air zone might be observed but the remaining cushion gas will prevent full depletion of the reservoir and hence preserve the flow characteristics of the reservoir (Oldenburg and Pan, 2013a). Discussed in section 3.3.10.
14. 2D axi-symmetric model centred on vertical well axis. Discussed in section 3.3.3.
15. Homogeneous porous media. Discussed in section 3.6.5.
16. Isotropic permeability. Discussed in section 3.3.6.3.
17. Dry air is used. Discussed in section 3.3.7.2.1.
18. No air dissolution in the brine, nor air humidification taken into account. It is assumed that most of the dissolution would occur in the development of the site. Losses due to dissolution after 300 hours of cycling, spread over 60 days, have been reported to be of less than 2% of the cycled air mass (McGrail *et al.*, 2013) which is within the recommended limit of 4% air mass loss per cycle proposed by (Giramonti *et al.*, 1978)
19. Seal is modelled as top and bottom boundaries closed to air and water flow. Discussed in section 3.3.3.
20. The far edge of the model is closed to flow as it is assumed the simulation space is located in an array of wells, this point is discussed later. Discussed in section 3.3.3.

3.3 Reservoir Model

This section reviews the parameters required by the model and how they were selected to be applicable to the offshore UK aquifer geology. The specific parameter combinations modelled can be found in appendix 8.1.

3.3.1 Project Aim and Applicability of Sensitivity Analysis

The aim of the project is to estimate the potential of PM-CAES using the offshore UK saline aquifer resource. Hence, understanding the uncertainty associated with that resource is necessary, before attempting to model it. This section contains the study of the CO_2 Stored database which contains geological information on the offshore UK saline aquifer resource, see Table 3-1 for the parameters contained in the database (Bentham *et al.*, 2014). This study showed the diversity of the resource with respect to some parameters (permeability, porosity, etc…) influencing fluid flow in porous media. It was deduced that the values of these parameters were highly variable from formation to formation. Understanding how they affected the roundtrip efficiency and the power capacity of the PM-CAES system, introduced in Chapter 2, was essential to reduce the uncertainty and to be able to quantify the potential of the technology in the UK.

Table 3-1: List of geological information contained in the CO2 Stored database. Not all the information is provided for each formation. The complete database is available online and a free licence is available on request (www.co2stored.co.uk) (Bentham *et al.*, 2014)**.**

Parameter	Example (where appropriate)
Unit Type	Saline Aquifer, Depleted Gas Field
Stratigraphic Age	Upper Jurassic
Stratigraphic Group	Humber Group
Stratigraphic Formation	Bunter Sandstone Formation
Stratigraphic Member	Burns Sandstone Member
Geographic Area	Central North Sea
Description/Reference	Burns_013_21
Coordinates (lat,lon)	
Storage Type	Confined (closed box)
Gross Thickness	
Surface Area	
Porosity	
Pore Volume	
Temperature	
Fracture Pressure	
Shallowest Depth	
Mean Depth	
Salinity	
Permeability	
Irreducible Water Saturation	0.25
Brine Viscosity	

The characteristics of the surface plant also contribute significantly to uncertainty and are discussed in Chapter 4.

3.3.2 Sensitivity Analysis Definition and Design

In the wider field of uncertainty analysis, the study of uncertainty in mathematical model outputs related to a change in a model parameter is called sensitivity analysis (Saltelli, 2002). Many approaches can be chosen to undertake a sensitivity analysis. For this project, due to time and computational limitations, a partly probabilistic and partly deterministic multiple scenario approach was preferred (Ringrose and Bentley, 2015). This approach is limited to *circa* two hundred models, each designed to represent a likely encountered scenario (Heijden, 1996). The scenarios to model were generated in two steps:

1) Determining some parameters randomly (e.g. reservoir depth)
2) Ensuring that parameters dependent on theses random parameters (e.g. temperature) where suited to the random value. The relationship between the random parameters and the dependent parameters was deterministic.

This approach allows for a more realistic study of uncertainty as it filters out any unrealistic scenarios which would be included using solely a probabilistic approach.

As shown in Figure 3-5, the geological reservoir two-phase flow simulation yielded the injection and production pressure at the bottom of the well which were used as inputs to the wellbore model to study the sensitivity of the PM-CAES system to changes in plant parameters.

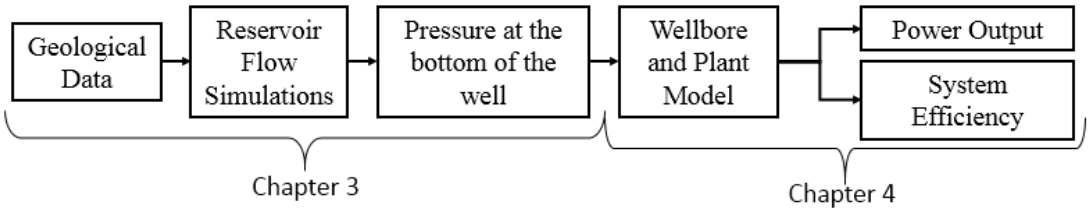

Figure 3-5: Modelling workflow followed to achieve a relationship between geological data with power output and system efficiency.

In order to perform a sensitivity analysis, random parameters had to be varied. To ensure the research outcomes of the project can easily be used, the parameter chosen as random variables for the sensitivity analysis were:

1. Reservoir Thickness
2. Reservoir Depth
3. Reservoir Permeability
4. Reservoir Porosity

These parameters are selected as they can either be constrained using geophysical surveys or relationships with depth exist (Schenectady, 1976; Allen *et al.*, 1983). Thus, they are likely to

be available or estimated in the early stages of a screening process. The subsequent section investigate how a PM-CAES is most likely to be developed and which deterministic rules can be used to establish the reservoir model geometry based on the value of the random parameters.

3.3.3 Conceptual Model Geometry

The approach selected for the sensitivity analysis of the fluid flow simulations in the reservoir raised a few challenges. One of them was that each conceptual scenario had to be carefully designed based on the knowledge available on how a PM-CAES site might be operated and how large it would be. Since there are no commercial PM-CAES sites in operation, this challenge was addressed by using the literature and knowledge relevant to underground gas storage. In most cases underground gas storage pertains to natural gas storage.

Table 3-2: Comparison of underground gas storage sites in France with Rough, the main facility in the UK, showing the number of wells. from (Storengy, 2017)**. The energy, was calculated using $E = volume \times LVH$, with LVH, the methane low heating value of 0.0085 MWh/m^3. Storage capacities are reported as billions or millions of cubic meters.**

Country	Field Name/Location	Reservoir Type	Capacity (at std. cond.)	Energy (TWh)	Operation Wells	Depth (m)
UK	Rough	Depleted Gas Field	4.25 Bm^3 WG 9.49 Bm^3 CG	36	29	2,700
France	Chémery	Saline Aquifer	7 Bm^3	59	67	1,085
France	Soings-en-Sologne	Saline Aquifer	1,138 Mm^3	7	10	820
France	Beynes	Saline Aquifer	1,185 Mm^3	10	36	430 and 740
France	Céré-la-Ronde	Saline Aquifer	1,200 Mm^3	10	13	910
France	Cerville	Saline Aquifer	1,500 Mm^3	13	38	450
France	Trois-Fontaines l'Abbaye	Depleted Gas Reservoir	2,080 Mm^3	18	5	1,700
France	Germigny-sous-Coulombs	Saline Aquifer	2,800	24	22	848
France	Saint-Clair-sur-Epte	Saline Aquifer	1,700 Mm^3	14	20	702 and 743

It emerged from the study of the underground gas storage literature, summarised in Table 3-2, that the UK has the peculiarity that it is reliant on one large offshore underground gas storage facility, the Rough Underground Gas Storage operated by Centrica Energy (Centrica, 2015).

In comparison the USA has 391 facilities and Germany 42 (Fernando and Raman, 2009). With a capacity of 36,117 GWh, Rough's energy storage capacity is more than ten times greater than any other underground gas storage projects in the UK (Fernando and Raman, 2009). Since the aim of this work is to assess large scale inter-seasonal storage, facilities similar to Rough are to be expected.

Preliminary calculations based on the Huntorf's 290 MW turbine with a flow rate of 417 kg/s, have shown that approximately 1,100 wells would be needed to store an amount of energy equivalent to the Rough facility and deliver it, as electricity, over 2 winter months (see box below). That is about 40 facilities the size of Rough, both in terms of working gas volume and well numbers.

Huntorf Turbine flow rate = 417 kg/s

Huntof Turbine Power Rating = 290 MW

Storage Time Target = 2 months

Rough's Storage Capacity = 36.1 TWh (thermal) × 0.47 (fuel to electricity efficiency) = 16.9 TWh (electric)

2 months of Huntorf turbine's production:

$$290\ \text{MW} \times 10^{-6} \times 24\ \text{hours} \times 30.5\ \text{days} \times 2 = 0.42\ \text{TWh}$$

Hence, $\frac{16.9\ \text{TWh}}{0.42\ \text{TWh}} = 40\ \text{turbines}$,

40 turbines would be needed to deliver 16.9 TWh to the grid over two months.

That is: $2\ \text{months} \times 417\ \text{kg/s} \times 40$ = 106 Billion kg of working gas of air which would require about 1100 wells producing air at 15 kg/s.

These calculations, combined to the amount of wells per site as shown in Table 3-2, indicate that modelling PM-CAES bulk storage sites requires the modelling of multiple wells per site. This proved to be the next significant challenge, since modelling multiple wells would require 3D models of hypothetical sites. 3D models would have added considerable mesh complexity, increasing computational time. Yet, the lack of accurate geological data meant that the uncertainty in the parameters and results would not have been reduced.

Therefore 2D radially symmetric reservoir models were used to simulate how most of the wells at a site would behave as part of a uniform well array. The concept behind this modelling approach is to model only a single well which belongs to an array (see Figure 3-6). Because the well is part of an array, the far edge of the model can be set to a no flow boundary since at

that distance from the well the pressure effect of the next well in the array will be equivalent, in opposite direction, to that of the modelled well (see Figure 3-7).

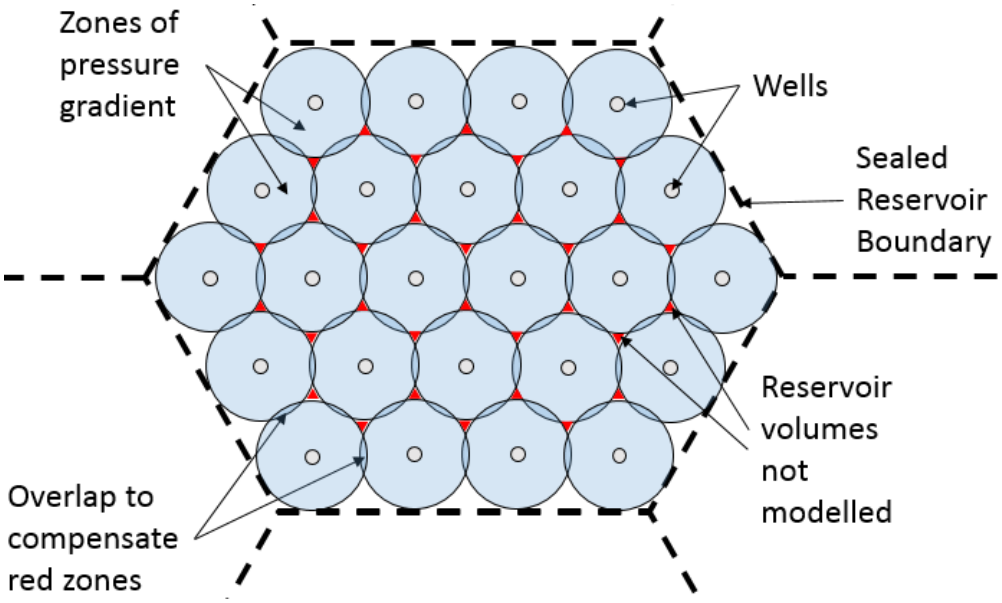

Figure 3-6: Map view of a well array simulated by the model (not to scale). The reason for the overlap is to account for the radial-symmetry. The areas in red cannot be represented by the model and therefore the pressures in the simulation would be higher than the ones expected in reality, since less volume is available to for it to dissipate. To minimise this effect it can be imagined that a hexagonal array of well is being modelled and that the true radius of the project would be slightly less than that of the one used in the simulation. This means that the overlapping volumes "cancel out" the volume represented by the red triangles. Since the pressure is sampled at the well/reservoir interface, the effect is negligible.

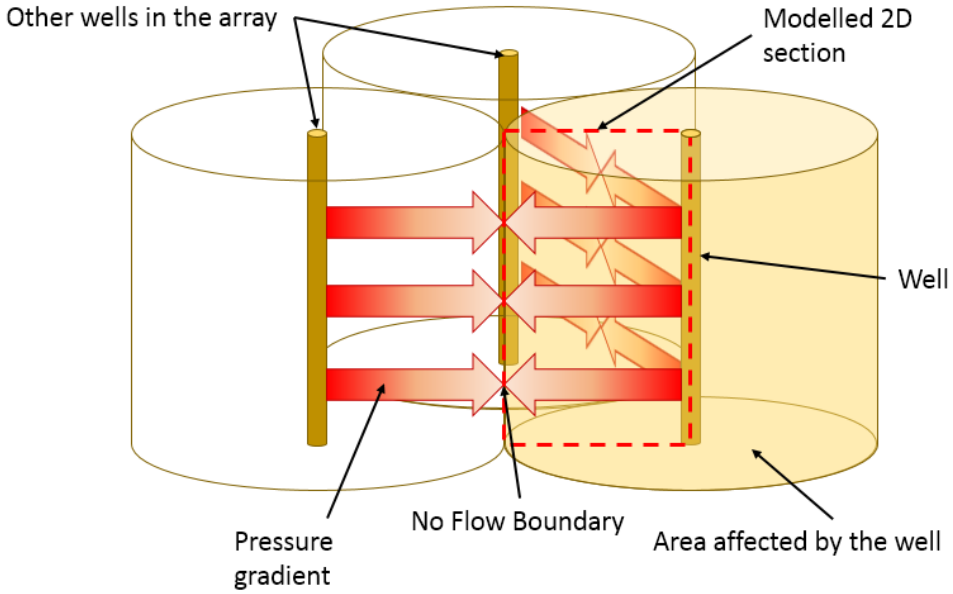

Figure 3-7: Schematic of the concept of no flow boundary which enables the modelling of 3D vertical well arrays using 2D radial symmetry. At each point along the boundary of the area affected by a well the pressure gradient starts to reverse, therefore no fluid can cross the boundary. This theoretical concept is what allows the modelling of well arrays to be completed by modelling the dotted 2D section using radial symmetry.

3.3.4 Model Radius and Well Penetration Lengths

The scenario based approach used implies that for each scenario, the difference in porosity, permeability, depth and thickness of the reservoir will lead to a different PM-CAES well array setup. The setup is understood as the adjustment of well spacing and the air saturated zone, to reflect how different scenarios would be best exploited by an operator. Such an example is shown in Figure 3-8 where thin reservoirs are operated using fully penetrating wells and thicker reservoir using partially penetrating wells. This optimisation is incorporated in the model by adjusting the mesh density and radius to account for the change in well spacing, and by adjusting the boundary conditions and source terms used to reflect the change in air layer thickness and in well screen length. Equation 3-18 was used to calculate the model radius.

$$radius = \sqrt{\frac{m_{TGV}}{\rho_a \phi S_a h_a \pi}} \qquad 3\text{-}18$$

Where, m_{TGV}, the total mass of air to store; ρ_a, the air density at the maximum storage pressure and reservoir temperature; ϕ, the porosity of the rock; S_a, the average air saturation in the air saturated zone = 0.58; h_a, the height of the air saturated zone, taken as 75% of the reservoir thickness, except for thin reservoirs less than 50 m, for which the reservoir thickness was used.

The radius of the well was set to 26 cm. Although optimistic, this radius was used in previous PM-CAES modelling studies (Oldenburg and Pan, 2013a; Pan and Oldenburg, 2014a). The well was assumed to fully penetrate reservoir less than 50 m thick and penetrate 50% of the thickness otherwise.

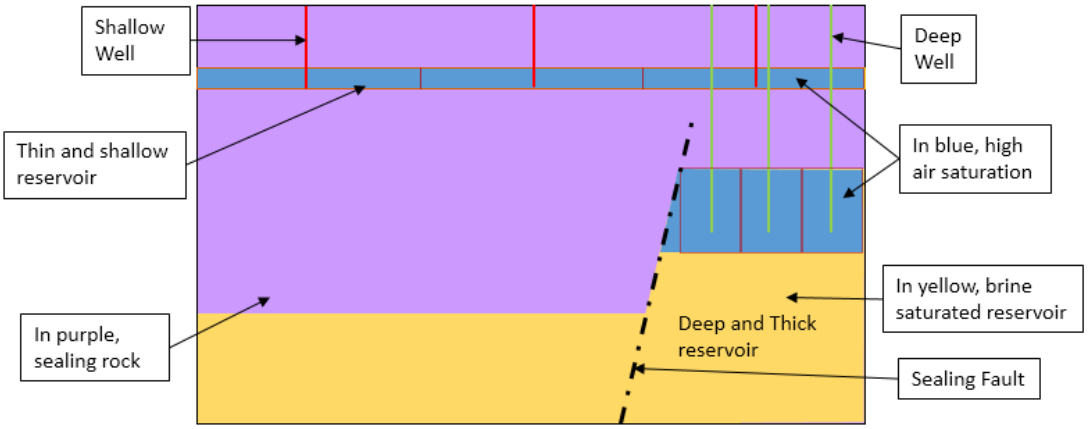

Figure 3-8: Example of different site optimisation for a deep and shallow reservoir. In the shallow and thin reservoir the operator will be looking at more widely spread well and will fully saturate the reservoir with air to prevent water conning. In the deeper scenario, the thickness of the reservoir would make the full saturation of air unmanageable and uneconomical, yet the well screen lengths could be deeper and the well closer to one another.

3.3.5 Random Reservoir Parameters: A Choice Tailored to the UK

Once an understanding of the geometry of a PM-CAES site was developed, and the deterministic rules to model it established, the parameter ranges over which the random parameters would be sampled had to be determined. To do so, the geological parameter selection was made based on the 574 entries from the CO_2 Stored database. The CO_2 Stored database, is an online database initially developed over 2 years by a consortium of public and private sector organisations, it contains information pertaining to the offshore saline aquifer and oil and gas fields of the UK (Bentham *et al.*, 2014). The database was studied to ensure that the model was applicable to the variation in geological characteristics of offshore UK saline aquifers. At this point a note should be made that compartmentalised reservoirs systems are common in the Central North Sea according to many studies, including : (Gaarenstroom *et al.*, 1993; Holm, 1998; Noy *et al.*, 2012), this makes the reservoir geometrical approached discussed earlier even more relevant to a UK case study.

3.3.5.1 Study of the CO_2 Stored Database

The blue data in the histograms in Figure 3-9 highlights the variability in geological parameters which can be encountered in the offshore UK saline aquifer resource. Out of the 574 entries documented in the database only 484 have information on aquifer geological characteristics. The scenario based approach which was chosen had to account for this variability. In order to achieve this, siting criteria from the PM-CAES literature were compiled (Table 2-2 in section 2.1.3.1). From this compilation it was concluded that in order to have flow rates permitting PM-CAES on an economical basis, the permeability of the reservoir had to be of 100 mD or more (Succar and Williams, 2008; Kushnir, Ullmann and Dayan, 2010). Hence, this value was set as the lower permeability threshold, and the 140 entries from the CO_2 Stored database with a permeability of less than 100 mD were filtered out (see greyed out data in Figure 3-9). The literature also states that a trapping mechanism for the air is required in order to ensure that the stored air does not flow away from the well during the shut-in periods (Giramonti *et al.*, 1978; Smith *et al.*, 1978; Allen and Gutknecht, 1980; Succar and Williams, 2008). Therefore, the 45 formations which were not reported to display any kind of trapping mechanism were removed from the potential targets. These two stages of filtering left 185 potential entries, describing 27 formations, which could be used for CAES (shown in orange in Figure 3-9). It were those 185 entries which were used to determine the ranges over which the random parameters were sampled for the sensitivity analysis.

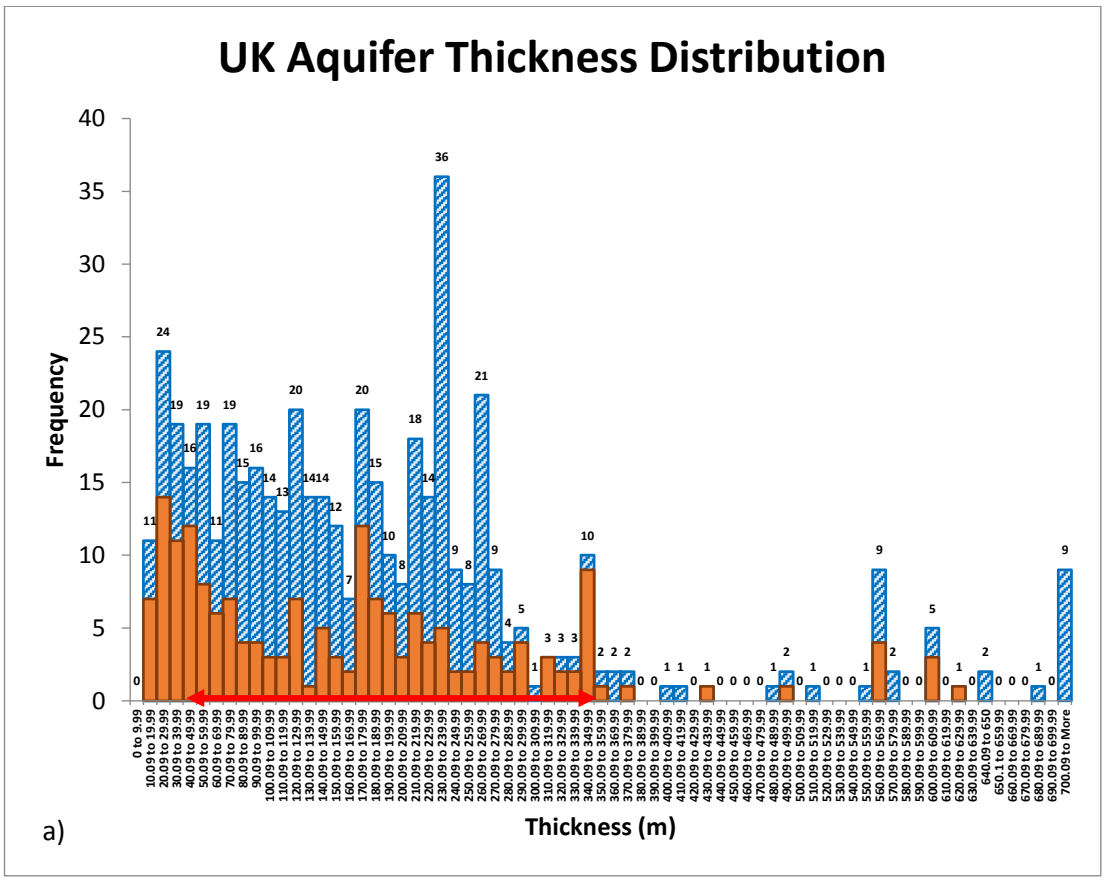
UK Aquifer Thickness Distribution
Frequency
Thickness (m)
a)

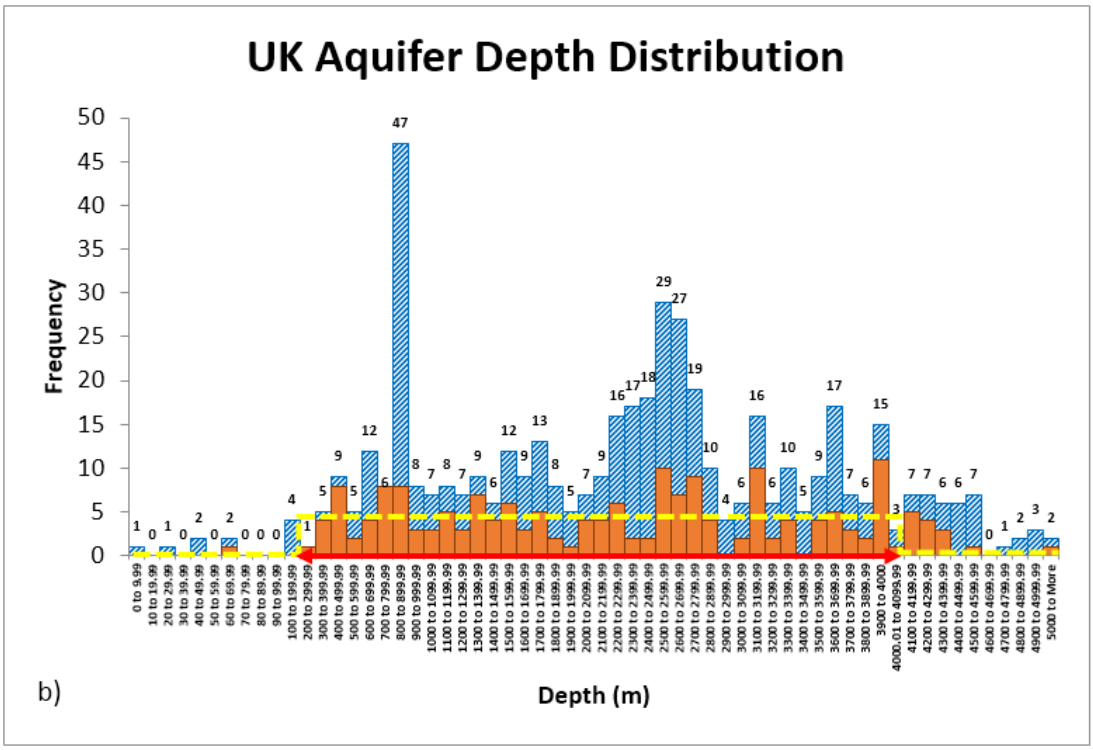
UK Aquifer Depth Distribution
Frequency
Depth (m)
b)

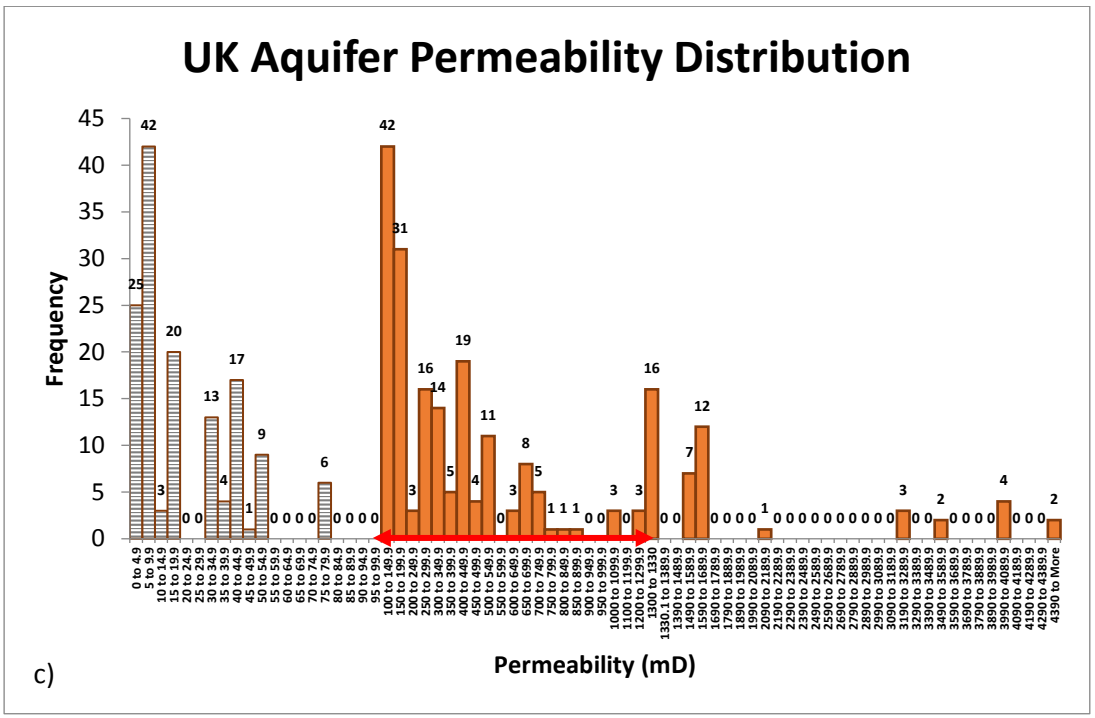

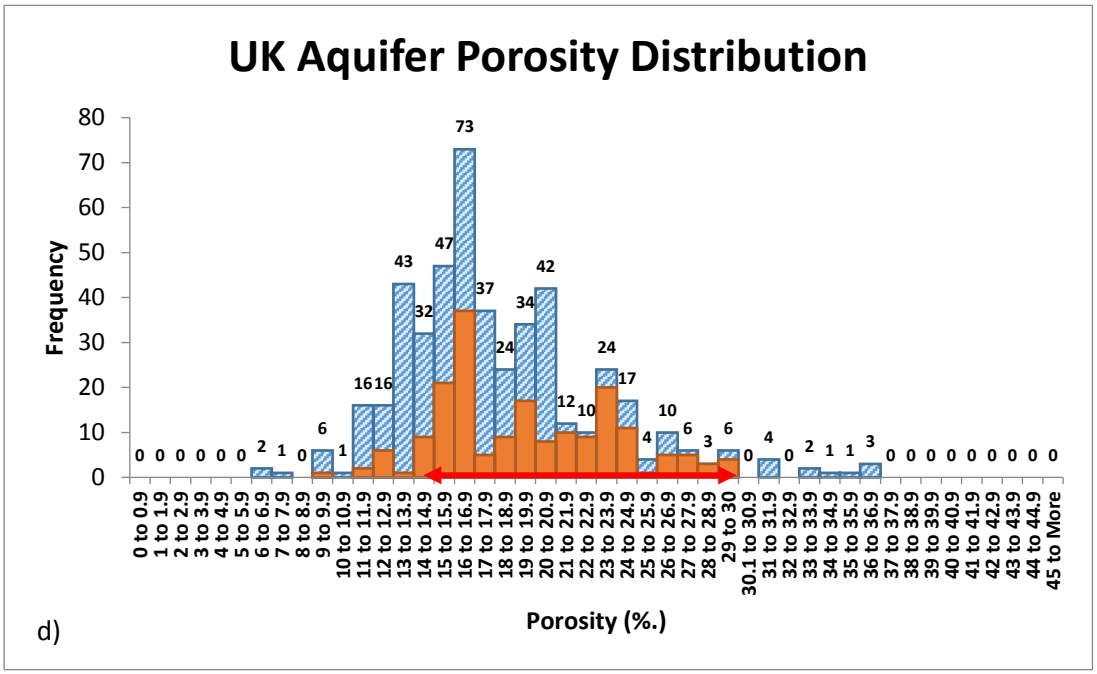

Figure 3-9: Distributions for aquifer thickness (a), permeability (b), shallowest depth (c) and porosity (c) in the offshore UK, based on the CO_2 Stored database. The initial 484 formations with geological data are given in stripped blue. The 185 remaining formations after filtering out formation with less than 100 mD and/or no trapping mechanism are shown in filled orange. The greyed horizontally stripped data in the permeability distribution represents the data filtered out. All data is from the CO_2 Stored Database. The red arrows indicate the selected parameter ranges. The yellow dashed line on the depth distribution (c) indicates the uniform nature of that distribution from 200 to 4,500 m depth.

The selection of the values used in the sensitivity analysis was completed in order to encompass as much of the database entries as possible. An upper and lower bound value were selected for permeability, porosity and reservoir thickness. Indeed, since the frequency

distribution for those three parameters could be fitted to a unimodal or bimodal distribution, a near-minimum and near-maximum value could be selected. The values selected are displayed in Table 3-3. Rather than selecting exactly the P10 and P90 values, the minimum and maximum value were arbitrarily selected to encompass as much as possible of the range, whilst avoiding values which could cause the models to become unstable due to the well mass flow rate being kept constant accross all simulations. The well rate will be discussed in section 3.3.8.

For the shallowest depth, the probability distribution was closest to a rectangular distribution than to a multimodal one, and the depths ranged from 7.93 m to 5.5 km. The shallowest depth value was selected to be 200 m in order to allow enough pressure for PM-CAES to be economically viable according to Allen *et al.* (1983). The depth siting criterion upper limit of 760 m available in the literature was not used because most of the limitations due to depth and pressure were imposed by the turbomachinery technology of the 1980s (Succar & Williams, 2008; conference talk from Gaelectric UKES 2015). The recent CAES Larne project by Gaelectric (Commission, 2016; Gaelectric, 2017) is exploiting geology at a depth greater than 1.4 km, which exceeds the 760 m presented as the maximum depth by Allen *et al.* (1983). For this reason the modelling in this research proposes to explore depths up to 4 km to take into account formations which could be exploited using current and future turbomachinery technology (more details in section 4.2.2). The pressure drop caused by wellbore effects, as the air travels from a reservoir at 4 km depth to an expander at the surface, leads to a ~250 bar pressure at the entry of the expander. 250 bars corresponds to the maximum inlet pressure for CAES turbo-expanders on the market (Dresser-Rand, 2017).

In order to explore as much as the ranges as possible, the ranges were randomly sampled using a uniform distribution to create unique parameter combinations on which statistical test could be run.

Table 3-3: Selected parameters from which parameter combinations used in the sensitivity analysis will be derived. The min, mid-range and max columns indicate the parameters selected for the sensitivity analysis. The modal value represents the value occurring the most in the filtered formations. And the final column indicates how many database entries fall within the min to max ranges selected.

Parameter	*Min*	*Max*	*Entries within range (%)*
Reservoir Thickness (m)	*40*	*350*	*77*
Reservoir Shallowest Depth (m)	*200*	*4,000*	*91*
Reservoir Porosity (-)	*0.15*	*0.30*	*94*
Reservoir Permeability (mD)	*100*	*1,330*	*84*

3.3.5.2 Selecting a Maximum Storage Pressure

The storage pressure is defined as the pressure at the top of the reservoir when the store is fully charged. It is expected that the storage pressure will be between the hydrostatic pressure and the fracture pressure of the reservoir. This will dependend on multiple factors such as whether or not the reservoir can be depleted of some of its water before air injection starts. Therefore the sensitivity analysis will be conducted on three sets of models:

1) One "end member" set, which encompass all possible combination of reservoir depth, permeability, thickness and porosity reported in Table 3-3. Modelled for a hydrostatic storage pressure. This set of scenarios are refered to as the 'deterministic' scenarios in the results section 3.5.1.
2) A set of models with randomly sampled reservoir depth, permeability, thickness and porosity operated with a storage pressure equal to hydrosatatic. Refered to as the 'hydrostatic stochastic' scenarios in the results section 3.5.2.
3) Another with randomly sampled reservoir depth, permeability, thickness and porosity operated with a storage pressure close to fracture pressue. Refered to as the 'stochastic scenarios at 77% of the lithostatic pressure' in the results section 3.5.2.

Based on fracture data from the north sea, the arithmetic average fracture pressure for aquifer reservoirs is of 77% of the lithostatic pressure from depths ranging from 200 to 4,000 m (Moss *et al.*, 2003). This value was used to determine the higher end of the storage pressure range.

3.3.6 Deterministic Reservoir Parameters: Modelling of the Porous Medium

Following on the choice of ranges over which the reservoir depth, porosity and permeability and thickness would be sampled it was necessary to select appropriate models to describe such a porous medium.

3.3.6.1 Capillary Pressure-Saturation Relationship

The next step in describing the reservoir medium used in the modelling is to assign a 'capillary pressure – saturation relationship' as introduced in section 2.2.1.2. The capillary pressure curve informs on how much pressure is needed to "push" a fluid through a pore throat based on the saturation of the fluids.

3.3.6.1.1 Inferring Capillary Pressure – Saturation Curve from Experimental Data

The capillary pressure between two fluids in a porous rock can be described by the *Laplace* equation 2-3. The selection of the parameters of that equation are presented here, as well as the calculation of the capillary pressure curve. In the PM-CAES system the wetting phase is the brine which is *in-situ* and coating the rock, and the non-wetting phase is the air being cycled in the reservoir.

The contact angle between brine and quartz is assumed to be near 0° (taken as 3°) to represent the initial wetting condition of the reservoir (Vavra, Kaldi and Sneider, 1992). The contact angle has indeed been reported to be near zero for air-water-silica systems (Davis, 1994; Bradford and Leij, 1995).

Since no values of interfacial tension for air and brine could be found at reservoir condition a fixed value of 72 dynes/cm, representative of the interfacial tension of methane and brine, was used (Vavra, Kaldi and Sneider, 1992). Interfacial tension decreases drastically for air as temperature and pressure increases (Duchateau and Broseta, 2012) yet it increases with salinity which balances the effect (Argaud, 1992). Furthermore laboratory experiments conducted on methane, CO_2 and N_2 mixtures at reservoir conditions, show that the higher the amount of N_2 in the mixture, the lower the drop in interfacial tension (Rushing *et al.*, 2008). In addition, the change in interfacial tension is caused predominantly by temperature and to a lesser extent by pressure (Rushing *et al.*, 2008). Therefore the assumption that the interfacial tension will not fluctuate significantly during a PM-CAES cycle can be made, since air is composed of 79% of N_2 and the reservoir temperature is near isothermal during a PM-CAES cycle (Oldenburg and Pan, 2013a). A reduction in interfacial tension leads to a reduction in capillary pressure, allowing air to flow more easily, which would be beneficial to CAES-PM operations. Hence, using a value of 72 dynes/cm is conservative.

The pore-throat radii distribution from (Nabawy *et al.*, 2009) offered pore throat distributions for clean sandstones with good reservoir properties, likely to be analogous to PM-CAES target reservoirs. The pore throat radii are correlated to saturation as explained in section 2.2.1.2. It was then possible to calculate capillary pressure curves using the *Laplace* equation.

3.3.6.1.2 *Smoothing and Validation*

Since the distribution of pore throat radii was calculated experimentally the data had to be smoothed in order to avoid generating instability during the numerical simulation (Figure 3-10). Indeed, it was found that sharp gradients changes in the initial curve led to instability which required unmanageably small time-steps. This smoothing was performed using a two point moving average. The capillary curve obtained with the smoothed data is compared to the one obtained for the raw data in Figure 3-11. The end effect on the model was to allow larger time steps to be used for similar results (plumes of similar extent and saturations but without extreme values caused by instability).

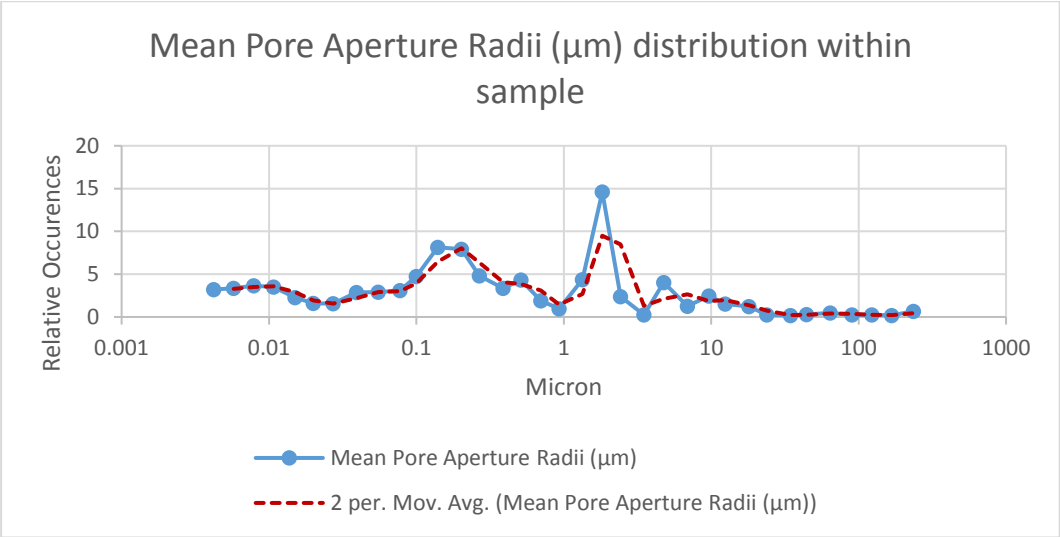

Figure 3-10: Pore throat aperture distribution in the sandstone sample from Nabawy *et al.* (2009) used to produce the 'capillary pressure – saturation' curve. The red curve represent the 2 point moving average used to smooth out the distribution.

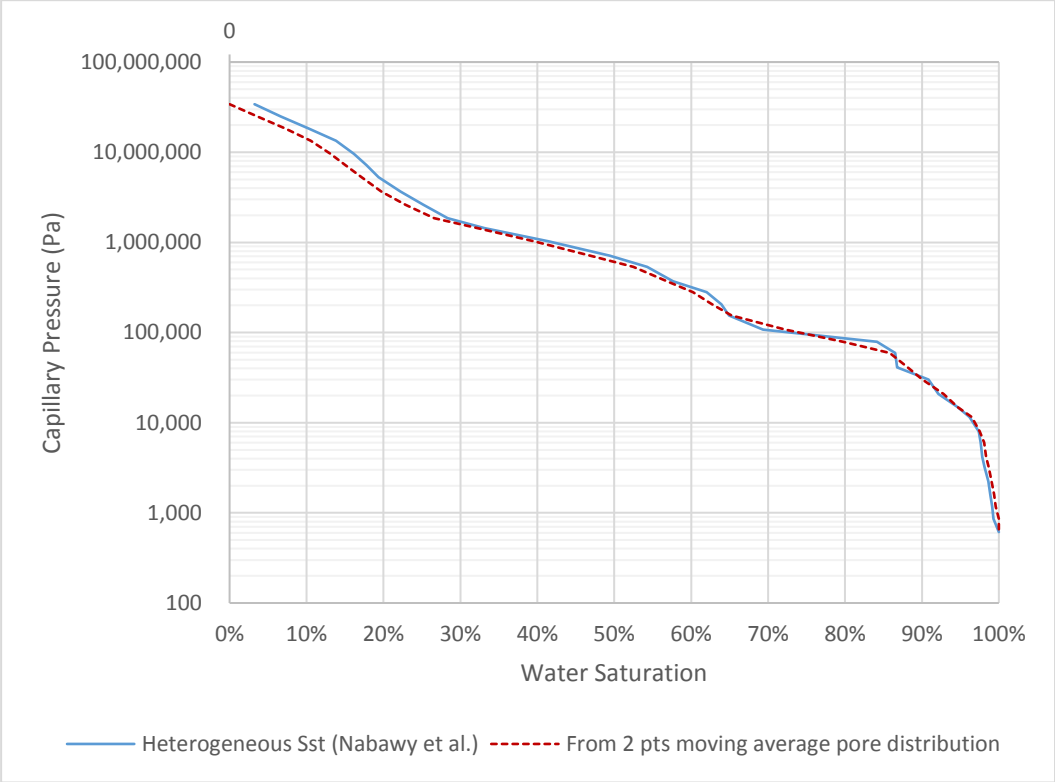

Figure 3-11: Sandstone curves derived from Nabawy *et al.* (2009) high porosity (25 to 35%) sandstones and a heterogeneous porethroat distribution on the microscale. The blue line is dervied using the Laplace equation, an interfacial tension of 72 dynes/cm and a contact angle of 3° and the raw pore-throat data. The dotted line uses the smoothed data.

To ensure that the experimental pore throat radius was appropriate to the PM-CAES system the pore throat radius can be empirically related to the rock permeability and porosity. Two of the most used empirical relationships have been derived by Pittman (1992) and Winland

(1976). Most of the work relates the mercury saturation of a rock to the pore throat radius. This allows the verification that the sandstones studied by Nabawy *et al.* (2009) are indeed suited for PM-CAES as shown in Figure 3-12.

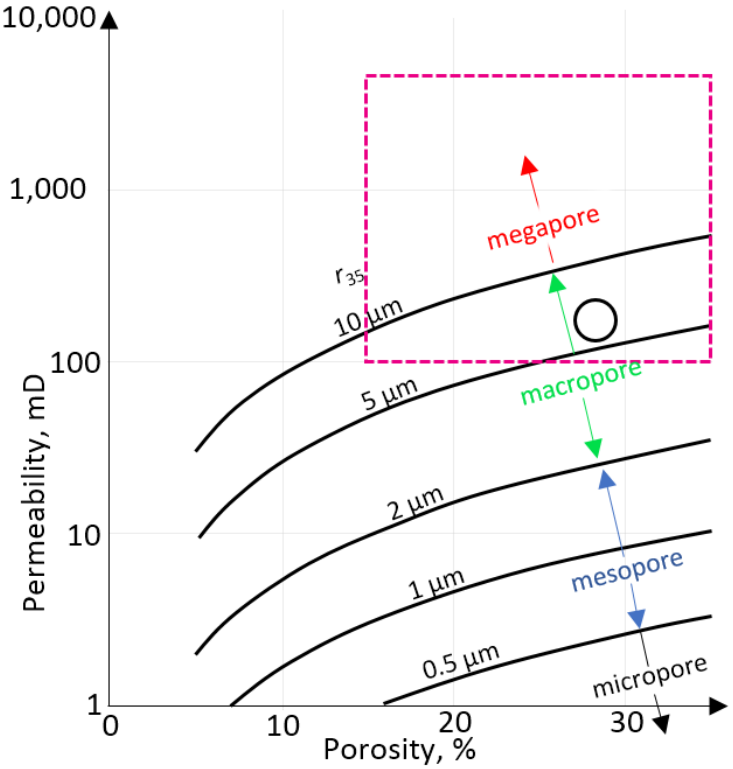

Figure 3-12: Empirical model based on regression attributed to Winland (1976), from (Kolodzie, 1980)**. Labels for four ranges of pore throat radius at 35% mercury saturation (r35) are taken from** (Martin, Solomon and Hartmann, 1997)**. Mercury is usually used in laboratory experiments as it makes it easier to perform measurements. The red box represents the area of sandstones likely to function with PM-CAES. And the black circle represents the sandstone selected from** (Nabawy *et al.*, 2009)**.**

Using experimental data led to a capillary pressure curve with a gradient steeper than those from existing models such as the *Van Genuchten* model (van Genuchten, 1980). This is essential since a fundamental numerical limitation of pressure-pressure formulations is that near zero $\frac{\delta p_c}{\delta S_w}$ leads to high instability in the model since even a small error in the capillary pressure will be reflected by a large one in wetting phase saturation. Furthermore, steeper gradients lead to a smeared water-air interface which is likely to be more problematic to PM-CAES. A more conservative scenario is therefore being modelled. To some extent, this choice can also be seen as representing some of the natural heterogeneity of the rock which leads to a smearing of the air-brine interface and compensates the assumption that the rock is homogenous.

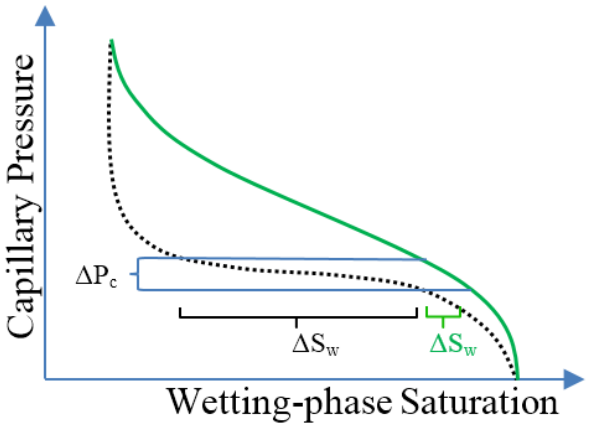

Figure 3-13: Diagram of curves describing two porous media systems, one with strong capillarity (in green) and one with weak capillarity (in dashed black). The system modelled is approximated using strong capillarity. This is found to be adequate based on the pore space geometry of a rock analogous to the ones used for PM-CAES using the work of Winland (1976).

3.3.6.2 Relative Permeability Curves

Finally, the relative permeability curves are used to represent the impedance one fluid phase causes to the other, and has been introduced in section 2.2.1.4. It is represented by a correction factor to the permeability value of the porous media.

The relative permeability curves were derived from the empirical model by R. H. Brooks & Corey (1966) due to the lack of existing data concerning relative permeability of air and brine at reservoir conditions. This widely used model was selected in order to provide results easier to replicate and compare with published PM-CAES modelling studies such as Oldenburg & Pan (2013a) and Pan & Oldenburg (2014a). This model is based on the pore size distribution index (λ) and the effective saturation of the porous medium. That is to say that the geometry of the rock, accounted for by λ, as well as how much of each fluid is present, influences how much impedance to flow is caused by one fluid on the other.

To remain consistent with the heterogeneous nature of the pore distribution from the capillary curve the Brooks-Corey shape parameter was chosen to be of λ = 0.3, representing a rock with a range of pore throat sizes.

The Brooks-Corey model is mathematically described by:

$$k_{rw} = S_e^{\frac{2+3\lambda}{\lambda}} \qquad 3\text{-}19$$

$$k_{rnw} = (1 - S_e)^2 \left(1 - S_e^{\frac{2+\lambda}{\lambda}}\right) \qquad 3\text{-}20$$

Where, k_{rw} is the relative permeability of the wetting phase, and k_{rnw} is the permeability of the non-wetting phase. And S_e the effective saturation defined by:

$$S_e = \frac{S_w - S_{rw}}{1 - S_{rw} - S_{rnw}} \qquad 3\text{-}21$$

Where S_w is the wetting phase saturation, S_{rw} the residual wetting phase saturation (the minimum amount of wetting phase left in the porous media after drainage), S_{rnw} the residual non-wetting phase saturation (the minimum amount of non-wetting phase left in the porous media after imbibition).

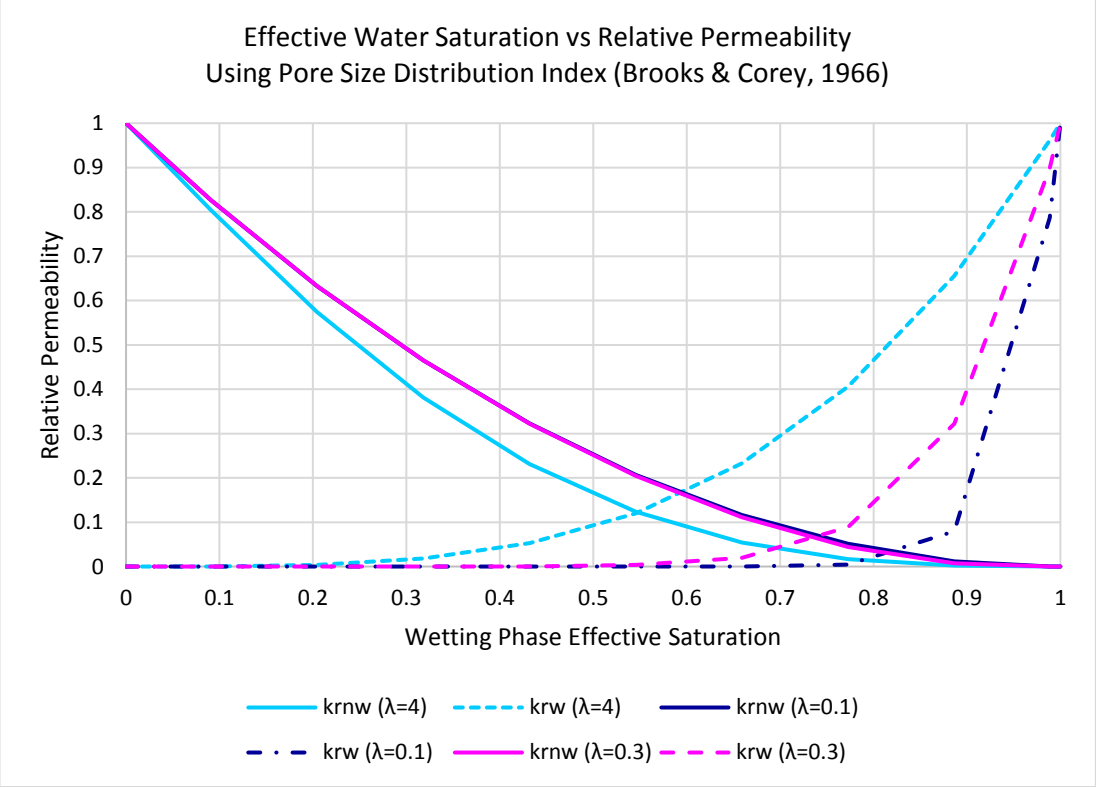

Figure 3-14: Effective wetting-phase saturation against relative permeability for various pore size geometries and sorting. λ=4 for unifrom, λ=0.3 for fairly wide , λ=0.1 for extremely wide range of pore sizes. The value used in the model is of 0.3 which is representative of a heterogeneous range.

The pore size distribution index (λ) is theoretically any positive number. It affects the relative permeability and water saturation relationship in a non-linear fashion, hence a λ value of 0.5 represents a rock with medium range of pore sizes, whereas a λ value of 4 represents a uniform range of pore size and a value of 0.1 an extremely wide range of pore size (Bloomfield *et al.*, 2001). This is reflected in Figure 3-14 where the blue dotted curve (λ=0.1) illustrates that a

reduction in wetting phase saturation from 1 to 0.9 leads to a ~90% drop in permeability for that phase. However the non-wetting phase relative permeability also remains low, therefore this represents a porous media that is heterogeneous in pore size which leads to major impedance in the fluid flow. Another way of looking at it, is that a small addition of non-wetting phase into the medium greatly reduces the relative permeability of both phases. One can imagine that, in a heterogeneous rock, a single bubble of gas lodged in a large pore can prevent water from flowing through this pore to the pores connected to it (Figure 3-16). Whereas, in a homogenous media the water can just as easily travel around the gas filled pore since all pores are of similar sizes (Figure 3-15).

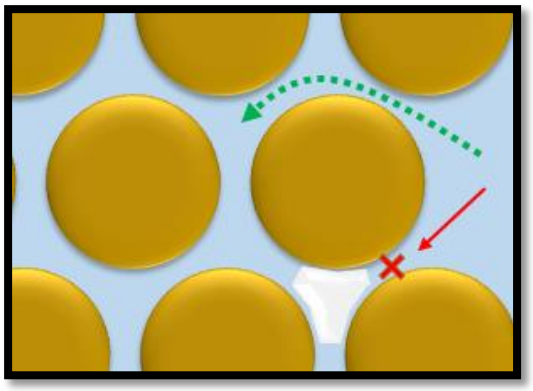

Figure 3-15: Rock with a high pore size distribution index value. The pores being of similar sizes the wetting phase can still flow through the porous media even when a small amount of non-wetting phase is present. Crosses represent no flow pathways.

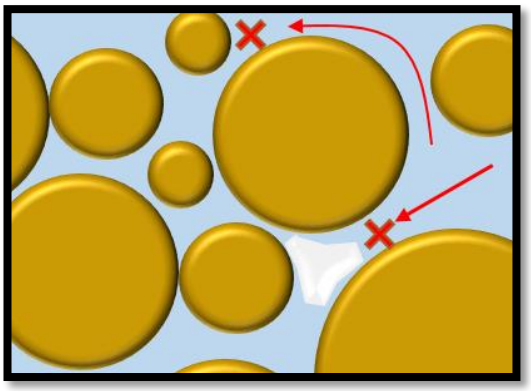

Figure 3-16: Rock with a low pore size distribution index value. The pores having different sizes, once a small amount of non-wetting phase has lodged itself in a large pore it can prevent flow of the wetting phase through the medium if the capillary pressure remains constant.

3.3.6.3 Note on Permeability Anisotropy

Rocks generally display some degree of anisotropy (i.e. directional dependency) between the vertical and horizontal permeability. Although many reasons can lead to anisotropy in a rock's permeability, it is usually found that compaction and diagenesis leads to horizontal permeability being greater than vertical permeability. Questioning whether this anisotropy in permeability will have a significant effect on the reservoir simulation results is essential. One model was tested with and without permeability anisotropy (Figure 3-17). In the anisotropic case the ratio of vertical to horizontal permeability was set to 0.5. The difference in average storage pressure over the entire reservoir, after 8 cycles of one year each, never exceeded ~2 bars. The average ratio of injection pressure to production pressure, from the 8 cycles, remained the same. Based on this result, the conceptual nature of the model, and the three reasons below, the decision to use an isotropic permeability was made:

1) Considering the single phase flow Darcy Flow equation $\mathbf{v} = \frac{-k}{\mu}\nabla(P)$, where $\mathbf{v}$ is the fluid velocity, k the permeability, μ the fluid viscosity and ∇P the pressure gradient, The constant of proportionality between the pressure gradient and the fluid velocity is given by $\frac{-k}{\mu}$. Therefore the lower the viscosity the less the pressure gradient will influence the fluid velocity. Hence, when modelling a PM-CAES reservoir with a total gas volume already in place, the lower viscosity of the gas compared to that of brine makes the gas flow velocity less sensitive to pressure changes (Ringrose and Bentley, 2015).
2) Using an isotropic system also increases the vertical flow of brine. This means that using an isotropic permeability for the reservoir is a conservative approach with respect to water conning (i.e. water suction through the base of the well).
3) Following from point (1) three orders of magnitude change in permeability or more would justify modelling an anisotropic permeability. Since a very simple geological and rock model is being used, it would not be justified to add permeability contrast. (Ringrose and Bentley, 2015)

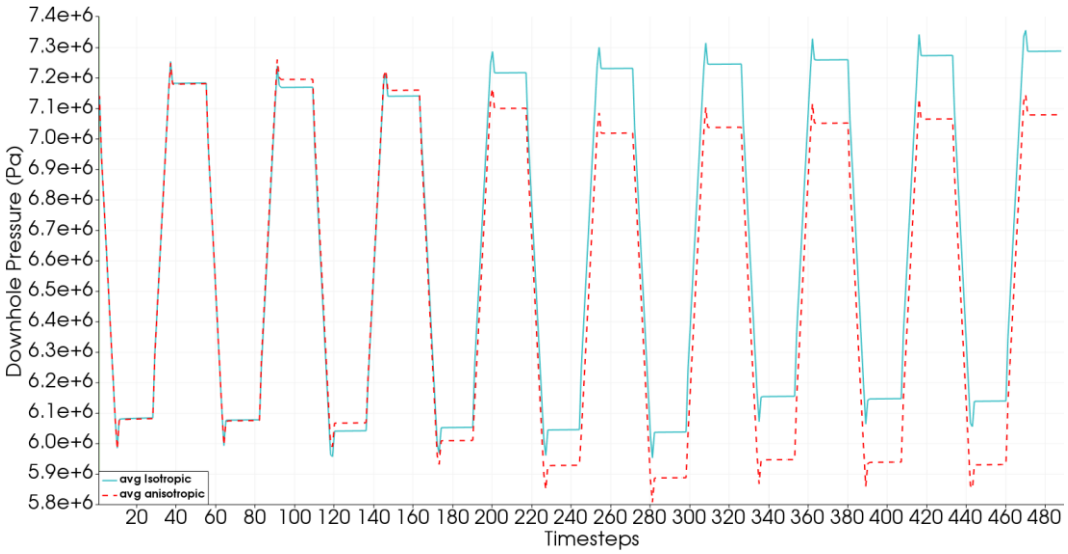

Figure 3-17: Downhole pressure extracted from a store model where an isotropic and anisotropic permeability were used. One time step is about a week. The store depth is of 700 m and the horizontal permeability of 1 D. For the anisotropic simulation the vertical permeability was reduced to 500 mD. The results indicate that after 10 inter-seasonal cycle of one year each the maximum pressure difference is of approximately **2 bar. This corresponds to a variation of about 3% of the mean pressure recorded during a cycle (about 66 bar).**

3.3.6.4 Selecting a geothermal gradient

Reservoir temperature is a regional model parameter. The technology used in this work is diabatic-CAES, in which the cooling of the air after the compression can be controlled to ensure the gas reaches the reservoir at reservoir temperature. It was necessary to specify a

geothermal gradient to refer to in order to determine the temperature conditions in the different scenarios.

A geothermal gradient of 34 °C/km was derived from the data provided in the CO_2 Stored database for formations with a permeability of 100 mD or more. This gradient is within the 20 to 40 °C/km range reported for the North Sea by (Carstens and Jepsen, 1981). Furthermore, the scatter of the temperature data, shown in Figure 3-18, is low (R^2=0.96), which allows the use of a single geothermal gradient, as opposed to testing a few values.

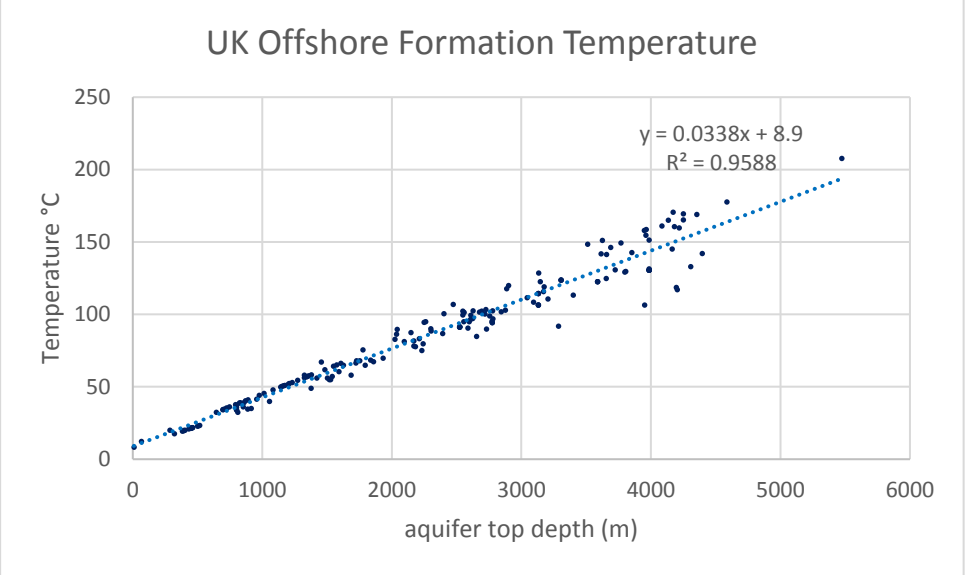

Figure 3-18: Offshore UK saline aquifer temperature as a function of top depth. The data was taken from the CO_2 Stored Database for formations with a permeability of at least 100 mD. The geothermal gradient is 33.8 °C/km with a seafloor temperature of 8.9 °C (intercept of the line).

In order to simplify the modelling and reduce computational time the reservoir temperature in the simulations were fixed to the temperature at the reservoir top depth. Therefore, any temperature dependent parameter was replaced by a constant. This choice was made based on the findings of (Oldenburg and Pan, 2013a) which show small variations in reservoir temperature during a diabatic or adiabatic PM-CAES cycle where, after compression, the cooling temperature of the injected air is set so that it reaches the reservoir at the *in situ* temperature. Indeed, the reservoir temperature exhibits a variation of less than 3 °C at all times during the cycle, except at the onset of injection close to the well. Because at the onset of injection, cold air within the pipes from the previous cycle, is pushed into the reservoir leading to a drop in temperature of slightly less than 10 °C for a few minutes. Two test models were run using both end member temperatures found in Oldenburg and Pan (2013), 18 and 44 °C. The results are shown in Figure 3-19, which highlight that the changes caused by the temperature difference at the onset of injection are negligible.

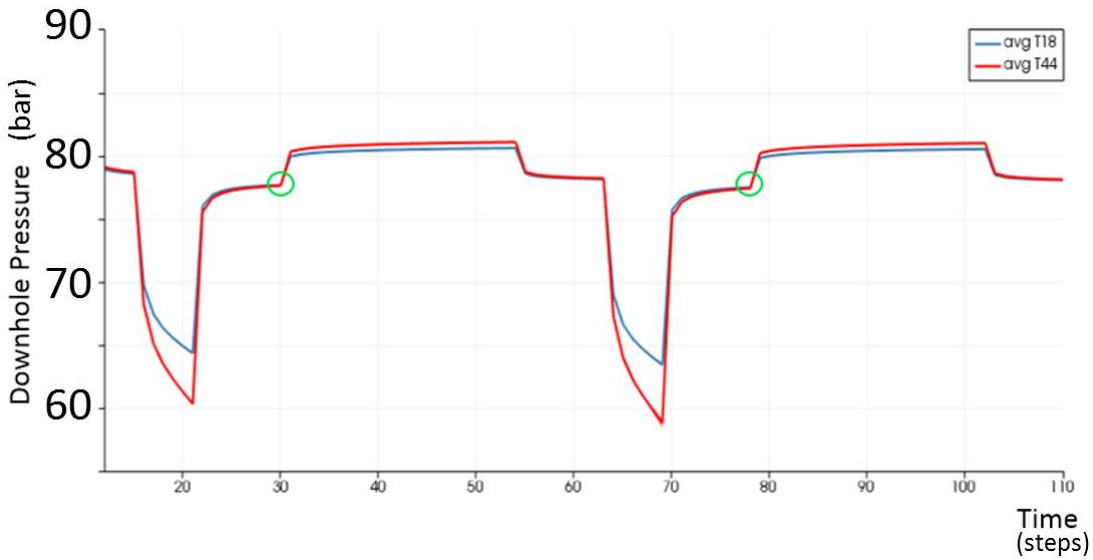

Figure 3-19: Temperature Sensitivity Testing showing that the important temperature change at the onset of injection (green circles) has a negligible effect on the pressure response at the well.

3.3.7 Representing Fluids

Following on from the porous media model, the modelling parameters describing the air and brine must be discussed. Once the fluids have been described, it will be possible to establish injection and production flow rates.

3.3.7.1 Wetting-fluid Properties

The next step in designing the model is to select properties for the wetting-phase of the two-phase flow system. Since the reservoir is composed of hydrophilic sandstone and is initially saturated with brine, it is assumed that the wetting fluid is the brine and the non-wetting fluid the air (Szymkiewicz, 2013; Jarvis, 2015).

3.3.7.1.1 Brine Density

The brine density was calculated using the most likely salinity value based on the study of the saline aquifers from the offshore UK CO_2 Stored database (Figure 3-20).

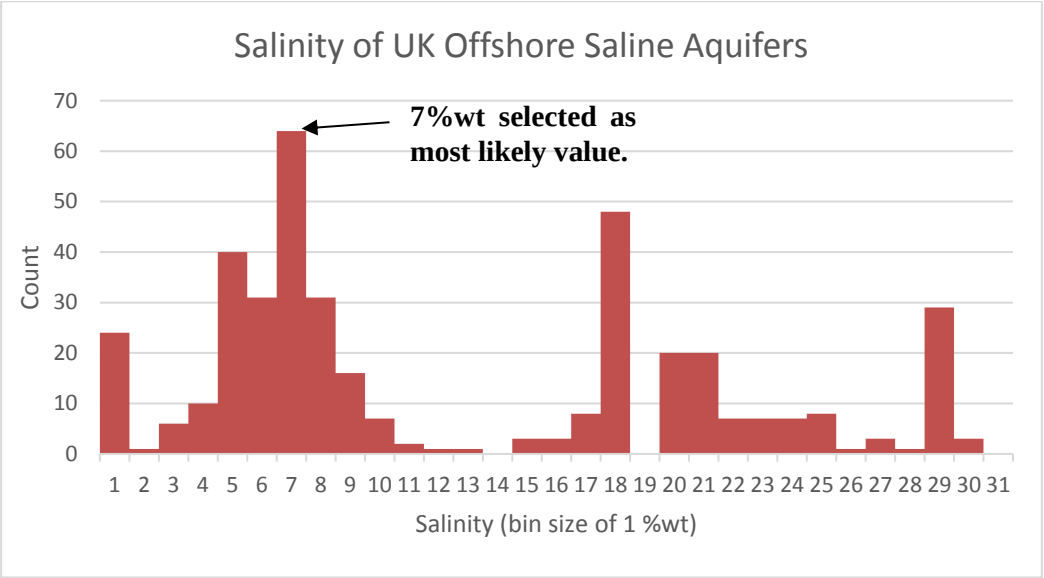

Figure 3-20: Brine salinity of UK saline aquifers. Bin sizes set to unity. The most likely value is 7%wt.

Due to the correlation between depth of the reservoir and reservoir temperature, the temperature used to calculalte brine density was chosen to be the reservoir temperature. Therefore, the brine density is depth dependent.

Spivey & Mccain (2004) present correlations between brine density and its pressure, temperature, and salinity, based on experimental work for brine density. Their work is well suited to the scenarios in this study as it covers the range of temperature and pressures encountered over the depth range of the models. The pressure at reservoir depth is approximated using the brine density at a reference depth of 2 km which is between the surface and the maximum reservoir top depth of 4 km. This reference was set to 1,023 kg/m^3. Trials where made for reference densities of 1,050 and 1,000 kg/m^3 but the change observed in the brine density was of less than 1 kg/m^3.

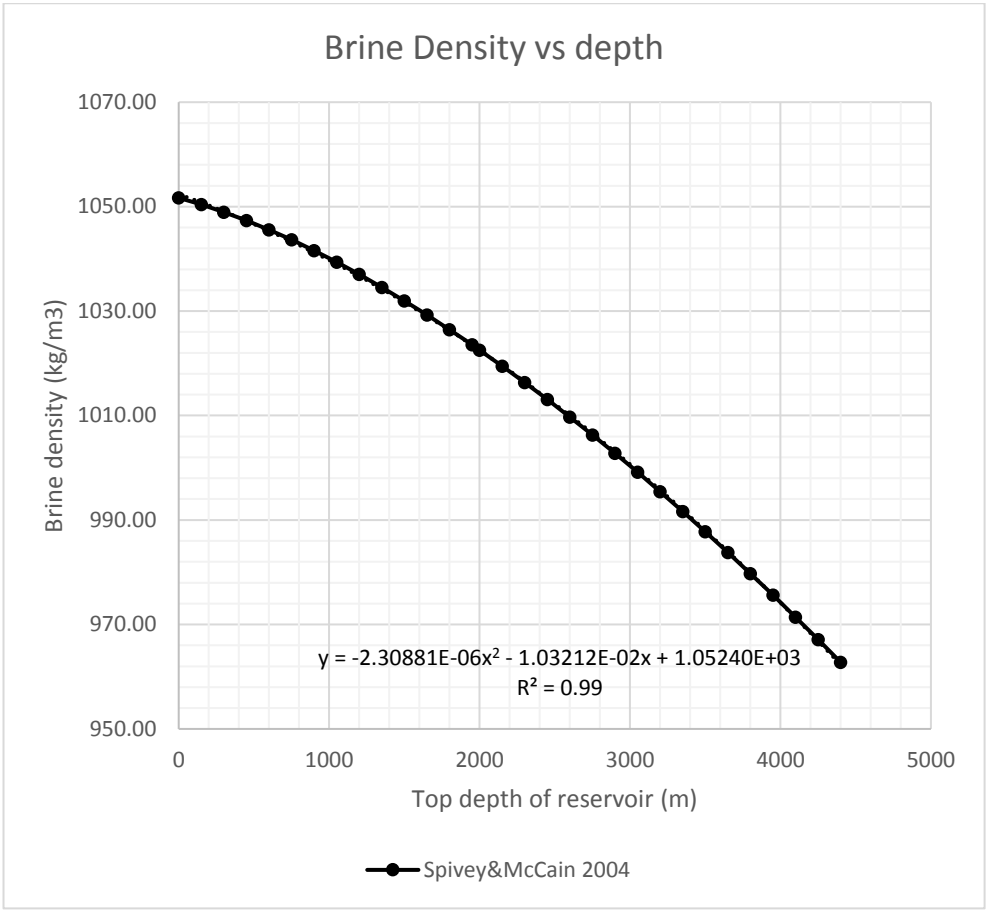

Figure 3-21: Brine density against the top depth of the reservoir from Spivey & McCain (2004) correlations.

3.3.7.1.2 *Brine Viscosity*

The brine salinity is assumed constant at 7%wt and so is the temperature in each scenario, hence, the brine viscosity is taken as a constant from the (Matthews and Russell, 1967) correlations.

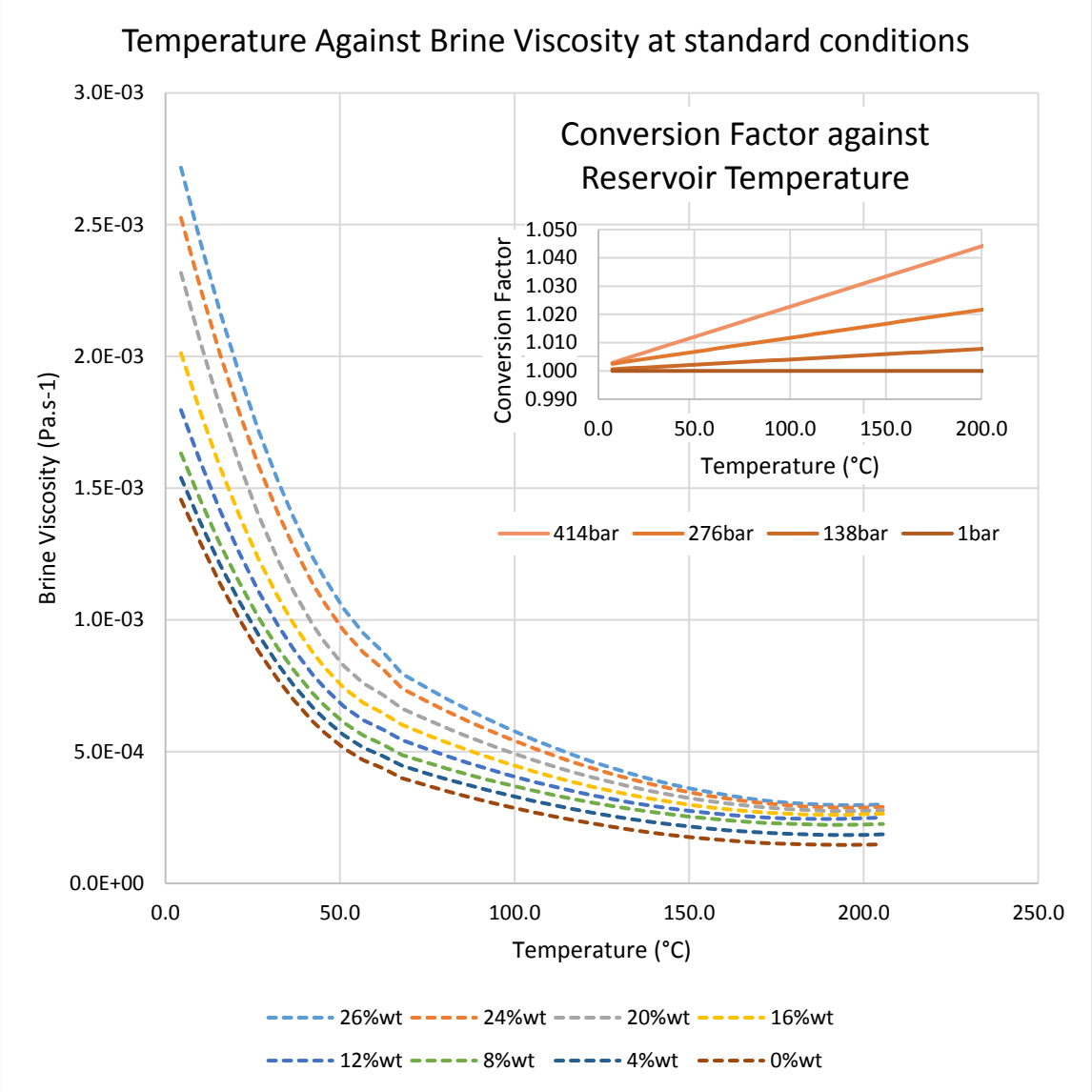

Figure 3-22: Brine viscosity taken from (Matthews and Russell, 1967) **for different brine salinities (%wt). The conversion is to be applied to the brine viscosity value at standard condition to convert it to reservoir temperature. Reported error in viscosity at standard conditions from 0 to 49 °C is 1%, from 49 to 100 °C is 5% and from 100 to 210 °C is 10%. The error in the correction factor is 5%.**

3.3.7.2 Non-Wetting fluid Properties

3.3.7.2.1 *Air Density*

Dry air was chosen as it simplifies the modelling and previous modelling from the Pittsfield field test experiment also uses dry air viscosity demonstrating it was sufficient to provide well performance predictions (EPRI, 1990). Furthermore, the water present in the atmospheric air

will condense in the inter-coolers during the compression. As will be discussed in section 3.3.10, since the cycling of the air rather than site development and the injection of the cushion gas is being modelled, the air is likely to remain dry in the reservoir.

OpenGeoSys allows a variety of density models to be used for the non-wetting fluid density, yet for isothermal conditions the only available density models are linear functions of pressure. It was therefore necessary to determine the linear approximation most closely related to the operating conditions expected for each scenario. The density data used to derive the relationships (in yellow in Table 3-4) was taken from tables published in (Stephan *et al.*, 2013) based on the work from (Lemmon *et al.*, 2000).

Using this data it was possible to extrapolate the linear relationship needed as an input for OpenGeoSys in two steps:

1) Establishing the quadratic functions for the change in air density against temperature at isobaric conditions (Figure 3-23 a.)
2) Establishing the linear functions for the change in air density against pressure at isothermal conditions over the pressure range likely to be encountered in the scenario (Figure 3-23 b.).

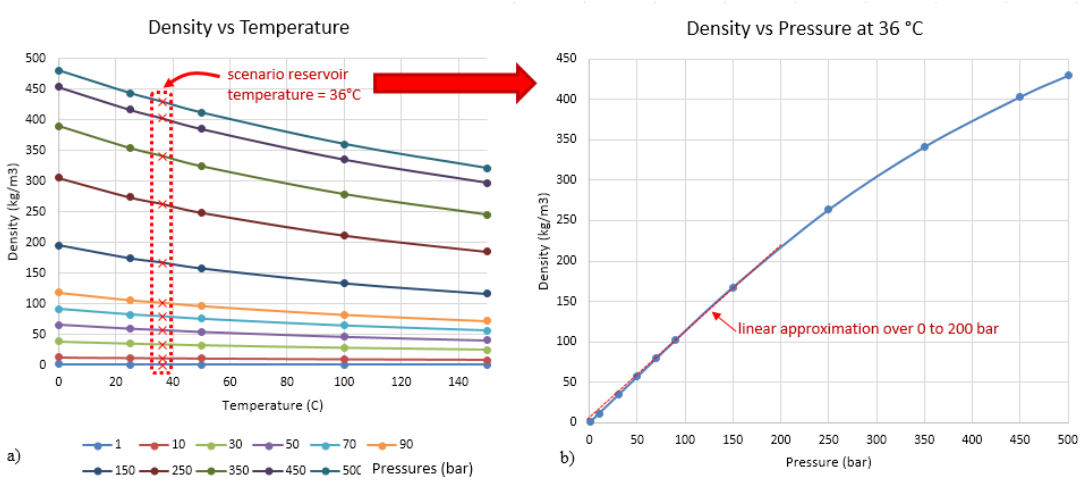

Figure 3-23: Graphical representation of air density approximation. a) First, the quadratic relationship between density and temperature is established. Then the specific density for a given temperature (here, 36 °C) at each of the pressures for which a quadratic relationship was developed can be estimated. b) Then those density values at specific pressures can be used to estimate the quadratic relationship between density and pressure at 36 °C. A linear approximation can then be determined over the pressure range likely to occur during the reservoir simulation.

A hypothetical example of this procedure is provided in Table 3-4. The fit of the linear functions inputted in OpenGeoSys to the published data is of $R^2 \geq 0.99$.

Table 3-4: Example of calculations used to determine the dry air density function to input into OpenGeoSys. Columns in yellow are from (Stephan *et al.*, 2013) **based on** (Lemmon *et al.*, 2000; Lemmon and Jacobsen, 2004)**. The blue column, represents a scenario with a reservoir temperature of 36 °C. a) The procedure in which, the missing density values at 36 °C are derived using quadratic functions of the form $\rho = aT^2 + bT + c$ for each line (non-isothermal and isobaric). b) The red box, highlights the density values which can be approximated using an isothermal linear relationship, here this model is only valid for a scenario where the pressure would always remain between 1 and 60 bar.**

P bar/ T °C	0	25	36	50	75
1	1.3	1.2	?	1.1	1.0
5	6.4	5.9	?	5.4	5.0
10	12.8	11.7	?	10.8	10.0
20	25.8	23.5	?	21.6	20.0
30	38.8	35.3	?	32.4	30.0
40	52.0	47.1	?	43.2	39.9
50	65.2	59.0	?	54.0	49.8
60	78.5	70.8	?	64.7	59.6
70	91.7	82.7	?	75.4	69.4
80	105.0	94.4	?	86.0	79.2

a)

P bar/ T °C	0	25	36	50	75
1	1.3	1.2	1.1	1.1	1.0
5	6.4	5.9	5.7	5.4	5.0
10	12.8	11.7	11.3	10.8	10.0
20	25.8	23.5	22.7	21.6	20.0
30	38.8	35.3	34.1	32.4	30.0
40	52.0	47.1	45.5	43.2	39.9
50	65.2	59.0	56.9	54.0	49.8
60	78.5	70.8	68.3	64.7	59.6
70	91.7	82.7	79.7	75.4	69.4
80	105.0	94.4	91.0	86.0	79.2

b)

3.3.7.2.2 *Air Viscosity*

The air viscosity used in the models was derived from the same dataset from which the air density was selected (Stephan *et al.*, 2013). The tabulated data was subjected to the same procedure as described above, whereby, the viscosity values for reservoir temperatures were inferred using quadratic equations. The OpenGeoSys software was able to take quadratic expressions to solve for viscosity, so there was no need here to select pressure ranges of interest and convert the quadratic expressions to linear ones as was performed for the air density.

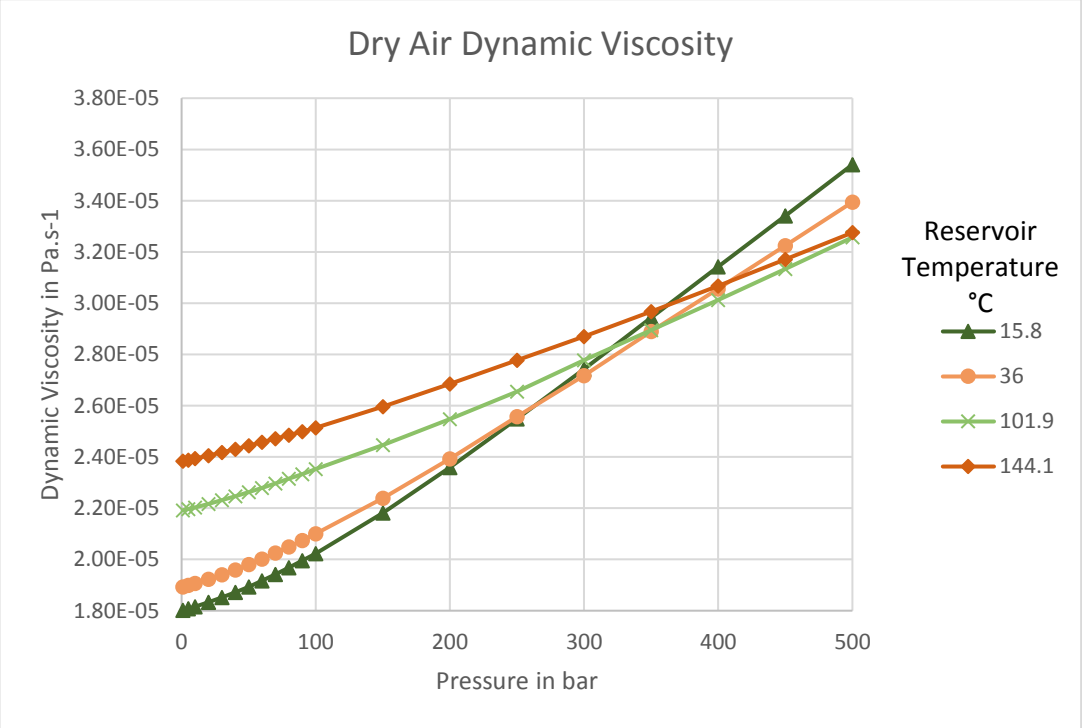

Figure 3-24: Dry air viscosity model derived from (Lemmon and Jacobsen, 2004; Stephan *et al.*, 2013) **implemented in OpenGeoSys. All $R^2 > 0.99$.**

3.3.8 Selecting a Maximum Production Rate

Now that the porous medium has been constrained, and the equations of states for the fluids in that medium have been established, it is necessary to estimate how much air flow can be expected through this medium.

In order to ensure that the modelling exercise was successful and representative of how a PM-CAES project might be developed it was essential to estimate a realistic well deliverability. Deliverability was estimated at 15 kg/s using published well data from the natural gas industry in offshore UK gas fields. A Monte Carlo simulation was performed on the ranges of parameters selected in section 3.3.5.1 to estimate flowrates in high quality reservoirs used for PM-CAES. 15 kg/s was found to correspond to a likely flowrate. Finally each scenario was subjected to an individual flowrate estimation to ensure that it would be stable and that the assumption of laminar flow needed to utilise Darcy's Law was verified. The results are tabulated in the appendix 8.1.

3.3.8.1 Existing Production Data

The UK government Oil and Gas Authority (OGA) has made production data for UK gas fields available (BERR, 2007). The data presents the monthly production of dry gas, condensate and production water per well up to the year 2000. Using the time of production, and the amount produced, it was possible to estimate the deliverability of each well in the offshore UK gas

fields. The average flow rate for each gas producing well in offshore UK fields is plotted in Figure 3-25.

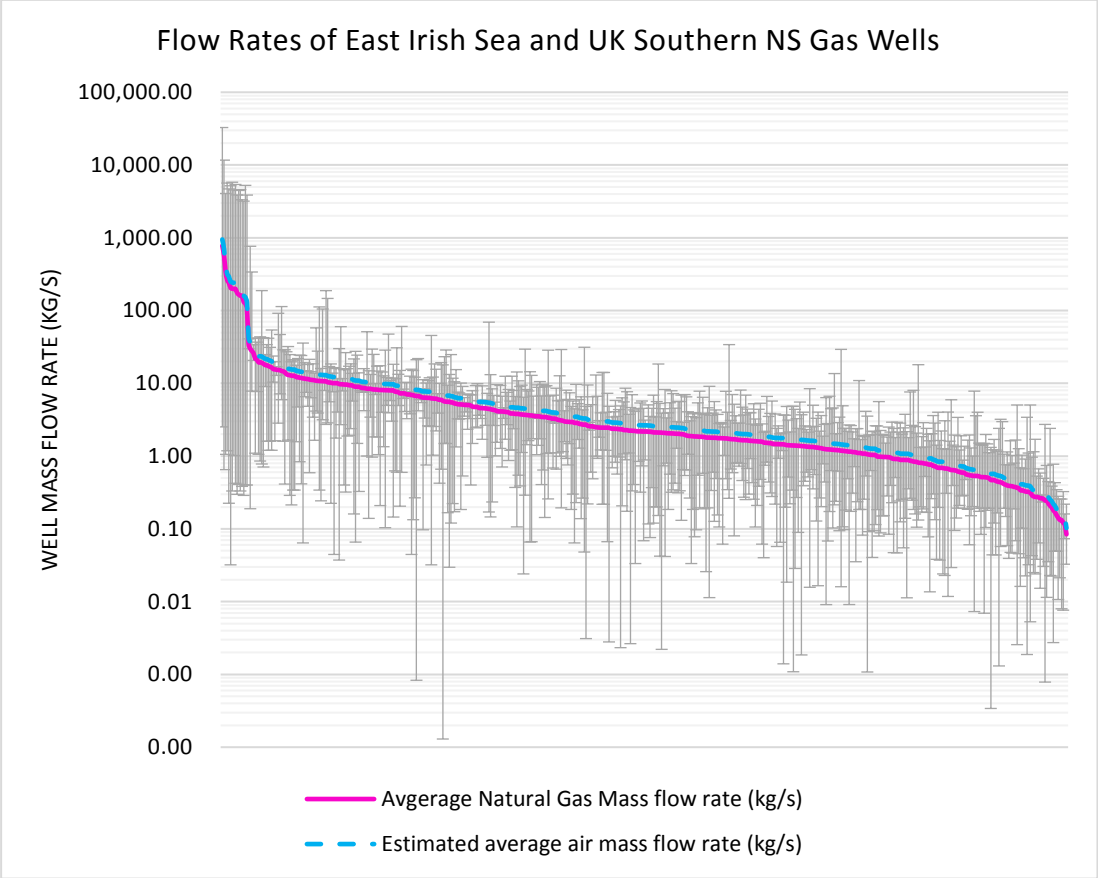

Figure 3-25: Average flow rate of gas of the offshore UK gas fields, the names of the wells have been omitted from the x-axis as it was impossible to display over 500 well names. The magenta line shows the flow rate for natural gas and the dotted line the estimated air mass flow rates. The error bars represent the range of flow rates greater than 0 encountered in the dataset of each well. Although the logarithmic scaling of the y-axis exacerbates the size of the error bars, it can be noted that the majority of the wells have a maximum mass flow rate which never exceeded 20 kg/s .Data from (BERR, 2007)**(data provided in digital supplementary information).**

A cumulative percentage count of well flow rates is shown in Figure 3-26. More than half the offshore UK gas wells have a flow rate of less than 3 kg/s. This is not encouraging as such flow rates would require many wells to meet the turbine mass inlet flow rate (e.g. 417 kg/s at Huntorf) significantly increasing the capital costs associated with drilling and pressure losses due to friction in pipes. This implies that the sites where PM-CAES might be developed would be niche. A gas well rate of 15 kg/s was chosen as 90% of the wells have a flow rate of less than that (P_{10}). This value is thought to be high enough to make PM-CAES economically viable, whilst having a reasonable, 10% chance, of being encountered if the conditions are right. Amongst such conditions can be included a permeability of more than 100 mD discussed in section 3.3.5.1.

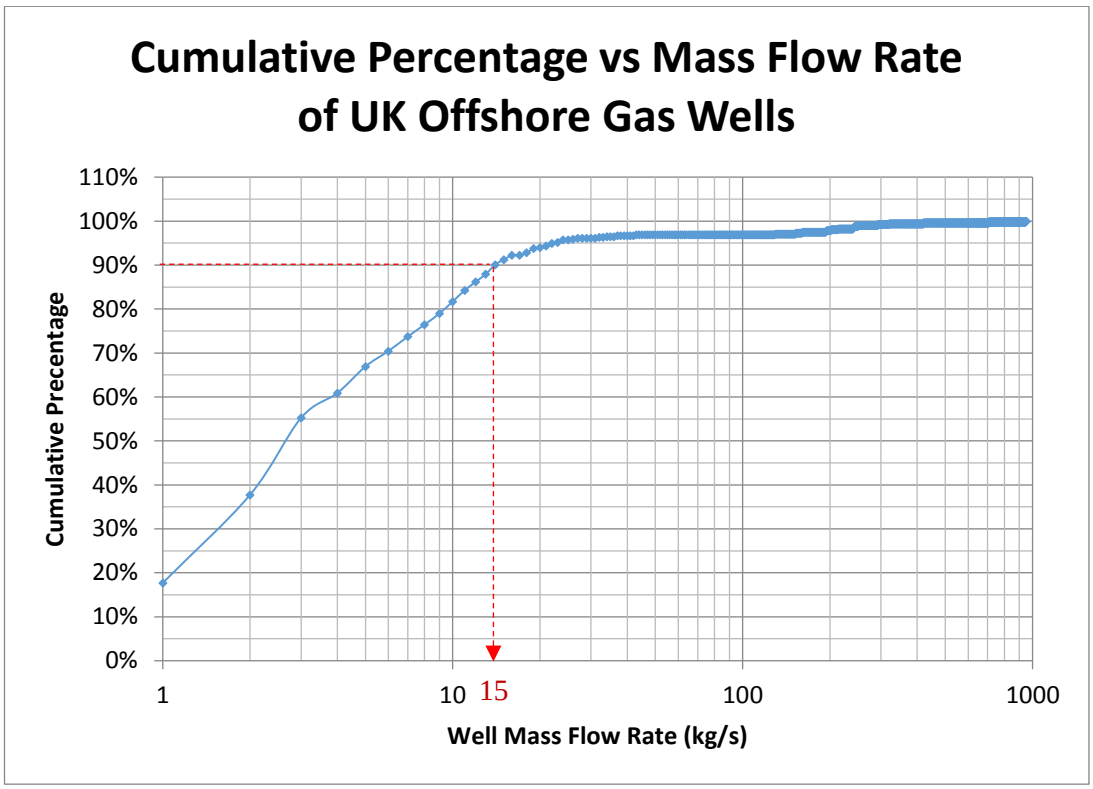

Figure 3-26: Cumulative percentage count of well flow rates converted to air mass flow rates. The percentages on the Y-axis represents the percentage of wells with a mass flow corresponding to the value on the X-axis or less. More than 50% of wells produce at 3 kg/s or less, whilst 90% produce at ~15 kg/s or less.

Another consideration when interpreting the UK gas field production data was that the PM-CAES system involves air as the stored fluid rather than natural gas. An attempt to quantify the expected change in flow rate for the same reservoir and operating conditions was undertaken. Using the analytical solution for single-phase compressible flow in porous media (Eq. 3-22), and modifying the viscosity, density, and compressibility factor values to represent either natural gas (assumed to be 100% methane) or air, it was found that for a fixed set of parameters, independent from fluid characteristics, the mass flow rate of air was up to 30% higher than that of methane. The exact ratios for different scenarios are reported in Table 3-5. This calculation was undertaken assuming the same relative permeability value for both air and methane, because little data exists for relative permeability of air under reservoir conditions. This finding is encouraging since underground gas storage of natural gas is widespread around the world and would indicate that, in terms of delivery, PM-CAES could perform better than natural gas storage.

$$q_{sc} = -10^{10} \frac{\pi\, T_{sc} k_{eff}\, h_a\, \rho_{sc}\, (p_F^2 - p_S^2)}{\mu\, P_{sc} T\, Z \ln\left({}^{r_F}/_{r_W}\right)} \qquad 3\text{-}22$$

Where: q_{sc} the mass flow rate of air at the well; r_w being the well radius in m; r_F being the formation radius in m; p_s being the pressure at the wellbore (bar); p_F being the pressure at the formation edge (bar); h_a being the air saturated zone thickness; assumed equivalent to formation height, in m; k_{eff} being the effective permeability (the relative permeability factored by absolute permeability) in m^2; T_{sc} and P_{sc} surface temperature and pressure respectively; Z being the compressibility factor of air; T being the reservoir temperature in degrees Kelvin; μ being the air viscosity in Pa.s; ρ_{sc} being the density of air at standard condition (*c.* 1.2 kg/m^3).

Table 3-5: Results of the assessment of divergence in mass flow rates, for a pressure difference of 10 bar between the well and the opposite model edge, when using air instead of methane as the stored fluid. On average the mass of methane flowing to the well is 8% lower than the mass flow of air under the same conditions. For an air thickness of 100 m, a relative permeability of 0.3, a permeability of 500 mD, and a pressure delta of 5 bars, and a reservoir and well radius of 250 and 0.26 m respectively.

Fluid	Viscosity (Pa.s)	Compressibility Factor	Temperature (C)	Average Pressure (bar)	Mass Flow Rate (kg/s)	Mass Flow Rate Ratio (m_{air}/ m_{CH4})
CH_4	1.95e-5	0.967	100	245	45.1	1.27
Air	2.66e-5	1.035	100	245	57.5	
CH_4	2.37e-5	1.092	141	400	48.4	1.30
Air	3.06e-5	1.21	141	400	62.9	
CH_4	1.12e-5	0.96	16	20	8.3	1.11
Air	1.83e-5	0.99	16	20	9.2	
CH_4	1.33e-5	0.89	35	80	28.4	1.10
Air	2.03e-5	0.99	35	80	31.1	

3.3.8.2 Validation of the Mass Flow rate using Monte Carlo Simulation

At this stage a Monte Carlo analysis of the expected flow rates achievable using an analytical solution was performed to ensure that the selected mass flow rate of 15 kg/s was likely to occur in high-quality reservoirs.

The analytical solution used is that of steady-state, single-phase radial and laminar flow in a porous media (Eq. 3-22). The assumptions underlying this equation are discussed below. A complete derivation of the equation can be found in Katz & Lady (1976) and Succar & Williams (2008).

Steady-state Assumption: The cylindrical models used to simulate a well array had closed boundaries, see section 3.3.3. Therefore, reaching steady state conditions within the reservoir was impossible, as the pressure across the entire model decreased throughout the air production period. This transient behaviour is due to the pressure at the edge of the model not being set to a hydrostatic pressure (i.e. no water flowed into the model to sustain the pressure). This means that the estimates had to be undertaken for a given time and a given pressure difference between the well and the model edge. Preliminary simulations of a few models showed that the pressure difference between the well screen and the opposite model edge was in the order of 5-10 bars during periods of air production or injection.

Single Phase Flow Assumption: Single phase flow was approximated by representing the impedance of water on the air flow by a constant factor. This was completed by using the effective permeability, k_{eff}, which is the product of the abosulte permeability of the medium, k, and the relative permeability factor (here chosen to be 0.2 which is representative of the, assumed, 47% air saturation in the reservoir) (Figure 3-27). The implications of this implementation are that the brine saturation remains constant through space and time, implying no brine flows through the medium. The water impedance to air flow was factored into the permeability of the porous medium itself.

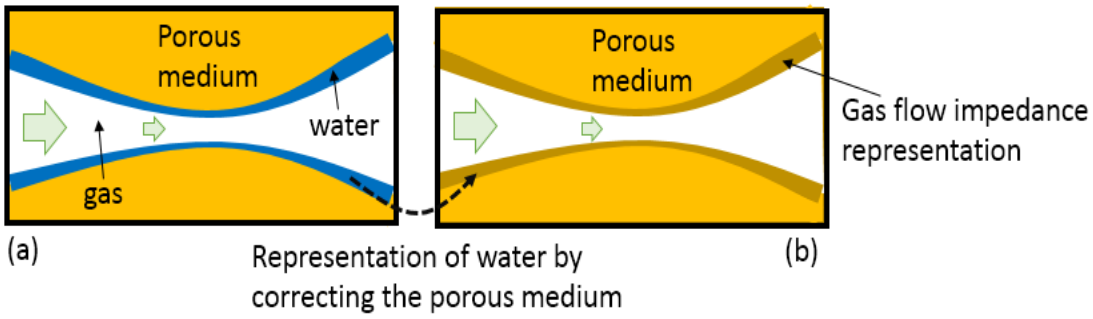

Figure 3-27: Green arrows represents air flow direction. (a) Representation of the two-fluid medium with water and gas. (b) Single phase (gas) approximation by representing the water impedance on air flow by some porous medium. One can imagine that the reduction in pore throat diameter due to the water can be represented as a pore throat reduced by the same amount. This suppose that the water does not flow.

Laminar Flow Assumption: Ensuring that the flow was laminar, making the third assumption valid, was verified by calculating the Reynolds Number in each scenario. This dimensionless number is representative of the ratio of inertial to viscous forces acting upon the fluid in motion (Sommerfeld, 1908). It indicates whether the fluid flow will behave in a laminar fashion, making it valid to be modelled using Darcy's law, or in a turbulent one. Fluid flow with Reynolds values of up to 10 can be represented using Darcy's law (Bear, 1972; Hassanizadeh, S. M. & Gray, 1987).

Results and Discussion: The Monte Carlo Simulation results, displayed in Figure 3-28, show that the most likely mass flow rates appear to be ranging from ~ 5 to 25 kg/s. It is important to note that this analysis was performed using the chosen conservative parameter ranges, hence the deliverabilities are skewed towards higher values than the ones observed UK wide for offshore gas wells. This preliminary analysis provided confidence that the choice of a mass flow rate of 15 kg/s in the simulation was both likely to be sustained for the duration of the simulations, as well as existing in approximately 10% of the offshore UK gas production wells.

The results highlight that higher flow rates could be achieved. The choice of 15 kg/s is considered a safer, most likely alternative. It is indeed unlikely that all the wells in an array of a large site could operate at flowrates of 100 kg/s reliably for many years of cycling.

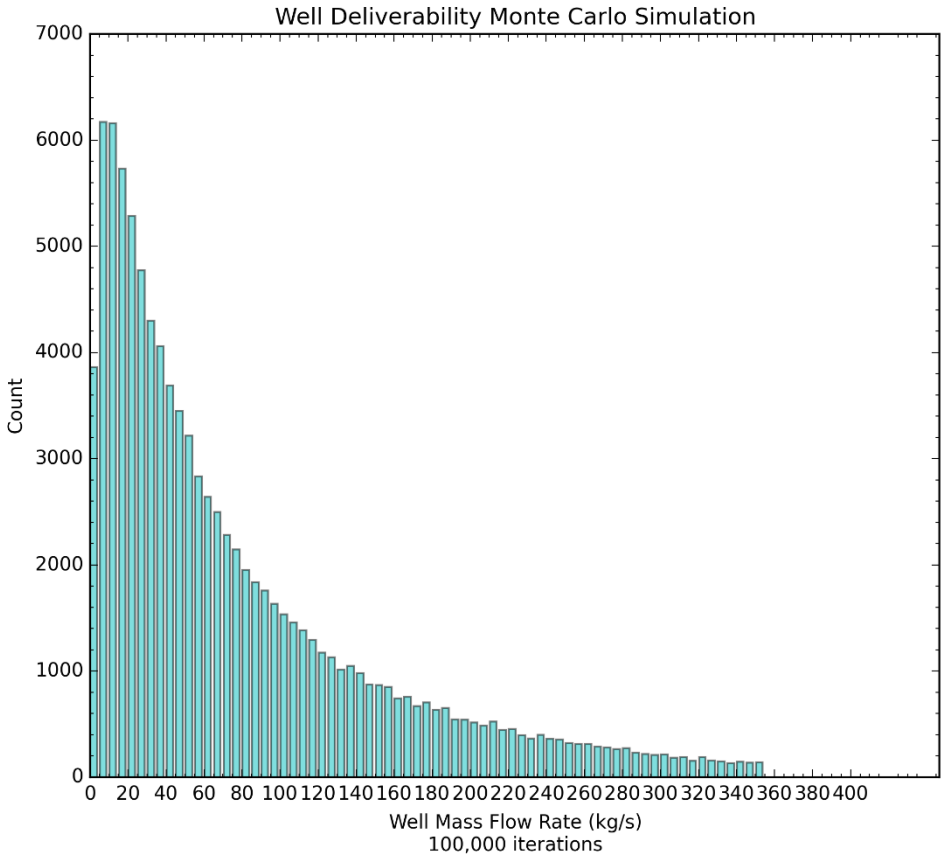

Figure 3-28: Results of the Monte Carlo well deliverability analysis for a 0.5 – 10.0 bar well to opposite model edge difference, assuming a constant average gas saturation of 47% over the reservoir leading to an approximate relative permeability of 0.2 for air. The equations of state used to describe air are described previously.

3.3.9 Seasonal Cycling Schedule

It was then important to define the schedule determining when the air will be cycled in and out of the reservoir. This was essential to couple the plant simulations to the reservoir ones. It was also needed to calculate the mass of air which should be stored. This was readily

performed since the mass flow rate of 15 kg/s was set and the amount of cushion gas known. For the modelling in this research the cushion gas will account for 50% of the total gas in the reservoir. This ratio of cushion gas falls within the values proposed by Flanigan (1995).

To decide which schedule should be used for the cycling of the air the following questions were considered:

1) When is energy needed?
2) How long will it be needed for?
3) How can the benefits of compression and expansion decoupling be used?
4) How feasible are seasonal cycles?

The first question can be answered by looking both at past, present and predicted demand and generation data for the UK. Indeed, the energy demand has been, and is, higher in the winter than in the summer. As discussed in section 1.4 of the introduction, the prediction on the proportion of future energy demand to be met by electricity varies greatly. Yet, addressing this question is beyond the scope of this project and significant work has been completed to show that an increase in electricity demand over the winter month due to electrification of the heating is a likely scenario (Figure 3-29) which should be considered (Ecf, 2011; NationalGrid, 2011; Partnership Energy Research, 2011; Strbac *et al.*, 2012; UK Department of Energy and Climate Change, 2013; The Electricity Storage Network Ltd, 2014).

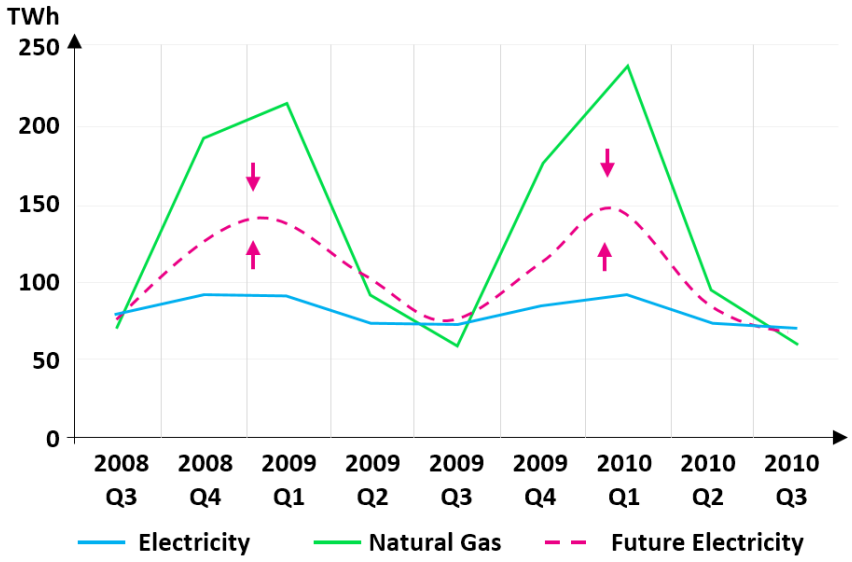

Figure 3-29: Final energy consumption in TWh for gas, petroleum products and electricity. The dotted line represents the effect that electrification is likely to have on the future electricity energy consumption. Data from (Partnership Energy Research, 2011)

From Figure 3-29, the demand seems to remain high for the entire winter quarters. However this research also aims to address the decoupling benefits of the technology, which enables to

inject air for longer at a lower rate, reducing the energy needed for compression per unit mass as well as the risk of fracturing the seal in the geological reservoir. Therefore the schedule was fixed to a 4 months injection period from May to August included, and a 2 month production period in January and February, with shut-in periods in-between the two.

The feasibility of those cycles where established using experience from the underground gas storage. According to Grappe (2008) typical injection for underground gas storage lasts for 100 to 200 days and production for 50 to 100 days. The proposed schedule fall within these ranges.

The cycles were fixed for all the runs in the sensitivity analysis, since the demand would be independent from the storage site geological characteristics. Furthermore, the aim of the study is to assess if the geological resource of the UK can be adapted to the electricity demand.

3.3.10 Approximating Reservoir Development

The first step in developing a CAES cycle using porous rock is to develop the site. That is, inject some cushion gas into the brine saturated reservoir, in order to displace the brine away from the well and the storage area. This cushion gas will remain underground and will not be recovered. Once enough air has been injected in the reservoir and stable conditions have been reached, the cycles can start.

It was noted that residual trapping was not accounted for in the OpenGeoSys solution used. This makes the modelling of site development impossible. Since the effective permeability is a function of air saturation, the lack of residual saturation fails to capture the air flow behaviour in areas of the reservoir where residual saturation should normally be observed. Therefore the pressures and gas saturation patterns which would be observed during site development cannot be replicated by the model.

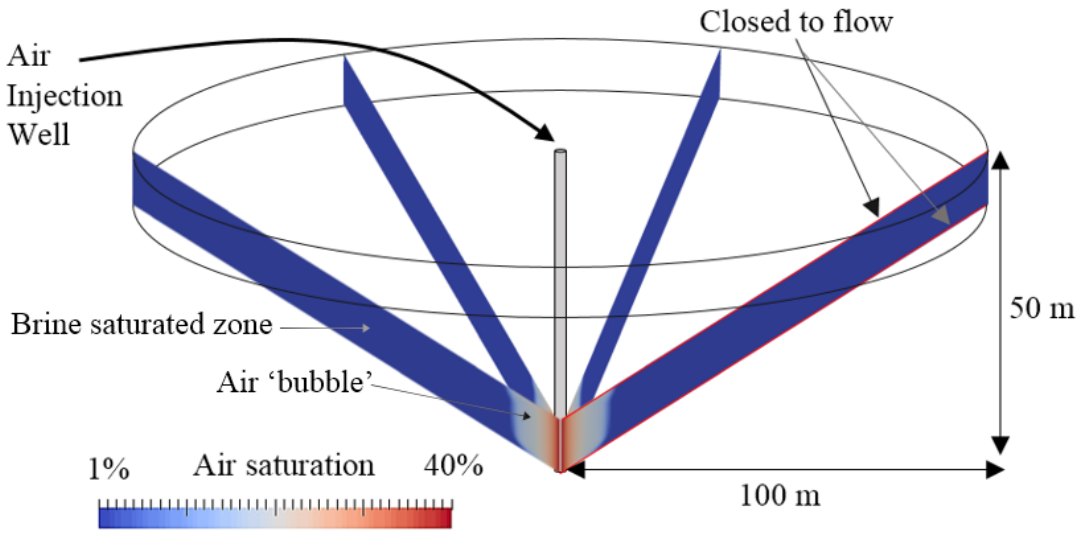

Figure 3-30: Inverted cone model used to test if the residual trapping of air was implemented.

This was tested using an axisymmetric inverted cone (Figure 3-30) saturated with brine, in which air was injected. The injection was then stopped and the air allowed to migrate up the cone towards the surface. In Figure 3-31, the progression of the red patch shows the air (in red) migrating upward after the injection has stopped and it is visible that the vicinity of the well gets re-flooded by the brine (in blue). This indicates that the residual trapping is non-existent. In the case where cycling is modelled, that limitation can be worked around by applying a new capillary pressure – saturation curve to the areas of the model already containing air. The new curve is set to have a minimum gas saturation equal to the residual gas saturation so that when the gas is removed from the system, its saturation will not be reduced below the residual saturation. Finally, it is suggested that a comparison with an industry standard simulator be made to assess the impact of missing residual saturation on site development should it be modelled in future research.

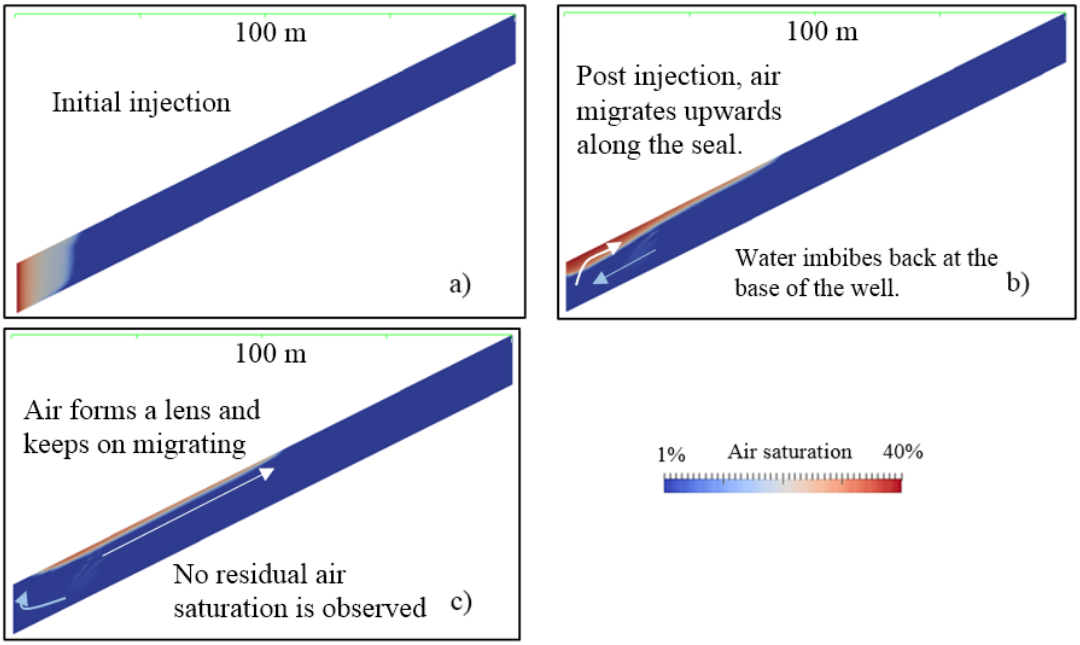

Figure 3-31: Cross section results from the residual trapping test using the inverted cone depicted in Figure 3-30. a) shows the initial injection of air. b) air injection has stopped and the air (red patch) injected migrates upwards whilst brine imbibes in the well vicinity. c) the air continue to migrate upwards displacing brine at the top front and being replaced by it at the base front.

Accounting for site development has been achieved by creating a model with two zones and running it to steady state. An upper zone which was set to a uniform air saturation, which was assumed to have been already injected. And a lower zone set to a 99% water saturation (this value was elected to allow the solver to perform fast enough whilst minimising the effect on the solution).

The gas density was then approximated using the depth and temperature conditions at the top of the reservoir. Using this density the radius of the air saturated zone could be determined. A first simulation did not include air injection and production cycles enabling it to run to steady state for each model. A hydrostatic pressure boundary was applied to the top boundary (Figure 3-32). This first simulation resulted in an air loss of less than approximately 0.2% of the total mass of stored air. This loss was deemed to be within what might be encountered during the development of a real site.

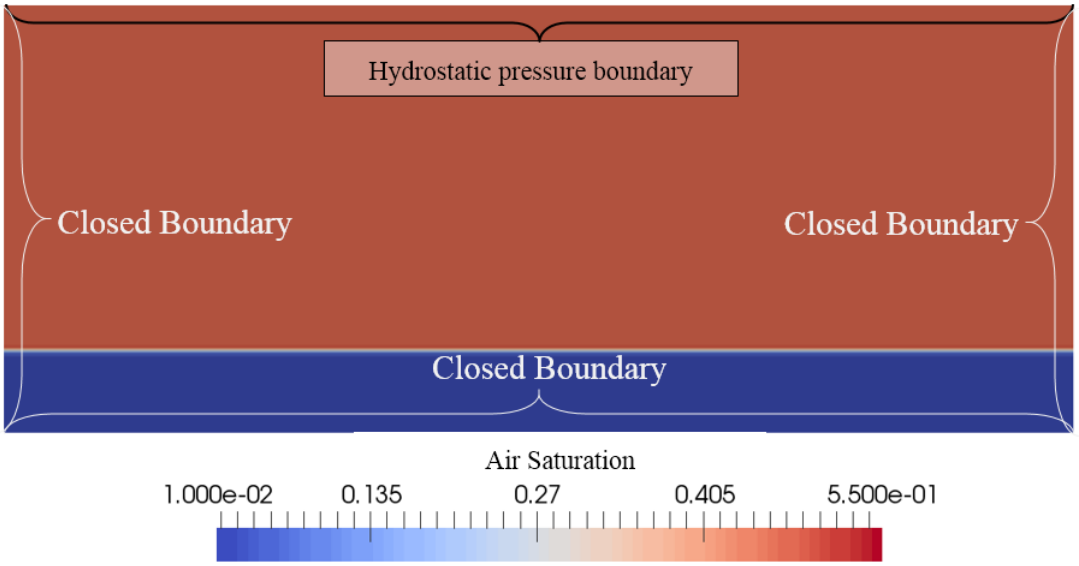

Figure 3-32: Initial pressure boundary conditions for the steady state models.

3.3.11 Two-Phase Isothermal Fluid Flow Modelling of PM-CAES Cycles

Once a replica of what a reservoir might look like after site development was obtained, the simulation of the cycling of air were performed. The gas and capillary pressure outputs of the site development simulations were used as initial conditions for the cycle simulations. In order to represent the simultaneous operation of an array of well, the boundary conditions for pressure were adjusted. The boundaries at the top and base of the model were closed to represent the impermeable caprock. The boundaries to the left and the right of the model were also closed, with the exception of the well-reservoir interface where injection and production would take place (see Figure 3-33).

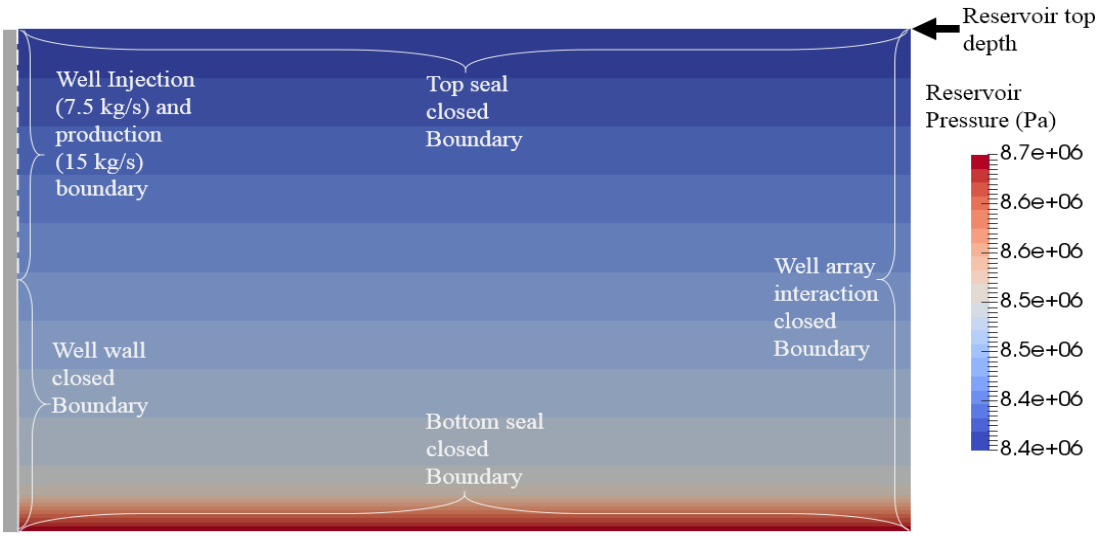

Figure 3-33: Boundary conditions and source term applied to the pseudo-steady state model outputs in order to perform cycle simulations.

3.4 Testing the Validity of Geological Model Outputs

In order to ensure that the pressure outputs from the OpenGeoSys models were valid and could be used in the plant model sensitivity analysis to follow, three checks where implemented, each looking to answer one of the following questions:

1. Has the simulation remained stable for at least a full cycle.
2. Was the minimum production pressure at least 10 bars.
3. Has the minimum production pressure remained high enough to prevent geomechanical damage to the reservoir?

The reasons behind each of those question were:

1. At least one cycle is necessary to correctly perform the plant simulations.
2. A minimum pressure of at least 10 bars was deemed necessary to ensure that enough power could be generated from a single well. This value however, is probably optimistic as it was taken from a report from 1980, based on the minimum inlet pressure of the turbomachinery (McCafferty, 1980). A full economic analysis would be necessary to predict the minimum power output per well.
3. If mechanical damage is sustained then modelling fluid flow alone is no longer valid and a geo-mechanical model should be coupled to the flow simulation to account for mechanical effects.

The first two checks were easily performed by filtering out simulations which did not last at least 1 full cycle or had a minimum production pressure of less than 10 bars. The following section will present the model used to test whether geomechanical effects susceptible of causing adverse effects to the injection and delivery of air to and from the reservoir had to be considered.

3.4.1 Wellbore Collapse and Sand Production

The extraction or injection of fluids from and into the subsurface will have geomechanical repercussions on the reservoir and the wellbore linking it to the surface. Such repercussions include, sand production, wellbore collapse, reservoir compaction, wellbore fracturing and formation damage (Zoback *et al.*, 1985; Tronvoll, Larsen and Li, 2004).

Some of those processes are associated with the depletion of fluids from the reservoir and the associated drop in pore pressure, others are linked to the recharge of the reservoir and the associated increase in pore pressure. It is only necessary to test whether depletion causes damage as the maximum storage pressure is constrained to not exceed the fracture pressure of the reservoir, set at 77% of the lithostatic pressure.

Wellbore collapse and sand production are processes by which the wellbore becomes unstable and starts to fail leading to sand and rock chunks to break off the wellbore walls. The causes of the instability can be low wellbore pressure or/and high flow rates leading to increased

stress on the borehole. Being able to predict such behaviour is important to reduce the risk of having sand damaging the wellbore and the surface turbomachinery as well as ensuring that the well life is extended. To assess the likelihood of this behaviour, selection of an appropriate failure criterion is needed. It will predict when the rock will fail.

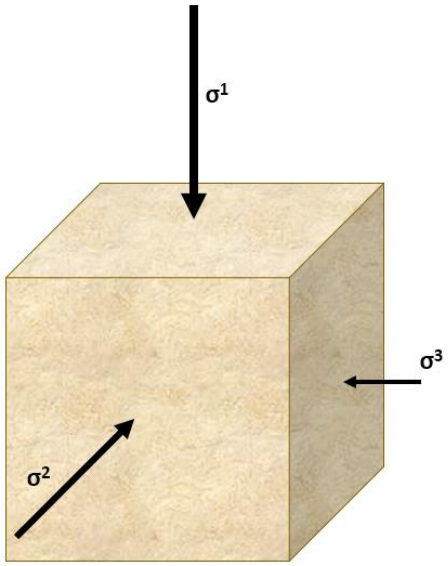

Figure 3-34: Cube of rock with arrows depicting the three principal stresses applied to it. σ^1 is the maximum principal stress (here taken to be the vertical principal stress), σ^2 is the intermediate principal stress and σ^3 is the minimum principal stress. σ^2 and σ^3 are also the principal horizontal stresses.

The Mohr-Coulomb failure criterion is well suited for idealised scenarios, like the one of a vertical well aligned to a vertical principal stress caused by the overlying rock. Under such a scenario, which is representative of the one used in the modelling from this work, the principal horizontal stresses are equal to one another, as the reservoir is homogenous. When the horizontal stresses are greater than the vertical stress the system is in a triaxial extension state. If the vertical stress is greater than the horizontal stresses it is in a triaxial compression state. Under a triaxial compression state, all the information needed is how the depletion of the reservoir (i.e change in pore pressure) will influence those stresses in order to predict failure. To do so B. Aadnoy (1991) derived a simple compaction model relating the changes in pore pressure to changes in horizontal stresses. Using this model combined to the Mohr-Coulomb criterion the wellbore collapse or failure pressures for a given drop in pore pressure can be predicted using Eqs. 3-23 and 3-24 from B. S. Aadnoy & Kaarstad (2010) (see Figure 3-35).

$$P_{wc} = \frac{1}{2}(3\sigma_{max} - \sigma_{min}) - \frac{\cos\phi}{1-\sin\phi}\tau_0 \qquad 3\text{-}23$$

$$P_{wc}^{*} = P_{wc} - \frac{1-2\nu}{1-\nu}(P_0 - P_0^{*}) \qquad 3\text{-}24$$

Where P_{wc} is the well collapse pressure for the initial pore pressure condition, P_0; * indicates the condition after air production. The parameters used in Eqs. 3-23 and 3-24 used to determine the collapse pressure are presented in Table 3-6.

When this is performed it is possible to estimate whether or not the drawdown model would have resulted in wellbore failure, making the scenario unsuitable for PM-CAES usage. The stress values used to implement the check prior to the simulation are based on the stress ratios published by B. S. Aadnoy & Kaarstad (2010).

Table 3-6: Parameters used to predict wellbore failure analytically. It was assumed that the failure was most likely at the wellbore since that is where the greatest pressure swing will occur. The Poisson ratio, is at the high end of the predicted values for sandstone in order for the result to be conservative (Austin, 1995; Dvorkin, 2008)**. The rock friction angle was taken towards the lower end of the likely encountered angles according to relationships from** (Weingarten and Perkins, 1995; Chang, Zoback and Khaksar, 2006)**. Lower friction angle lead to a higher threshold for collapse pressure, making this choice a conservative one.**

Parameter	Equation / Constants
Cohesive rock strength, τ_0 (bar)	= $3{,}846.15 \cdot 10^{-5}$ × store depth
Horizontal stress, $\sigma_{max}=\sigma_{min}$ (bar)	= $14{,}519.23 \cdot 10^{-5}$ × store depth
Initial pore pressure, P_0 (bar)	= $10{,}000.00 \cdot 10^{-5}$ × store depth
Depleted pore pressure, P_0^{*} (bar)	= minimum production pressure modelled
Poisson ratio, ν	= 0.25
Rock friction angle, ϕ (°/rad)	= 27/0.47

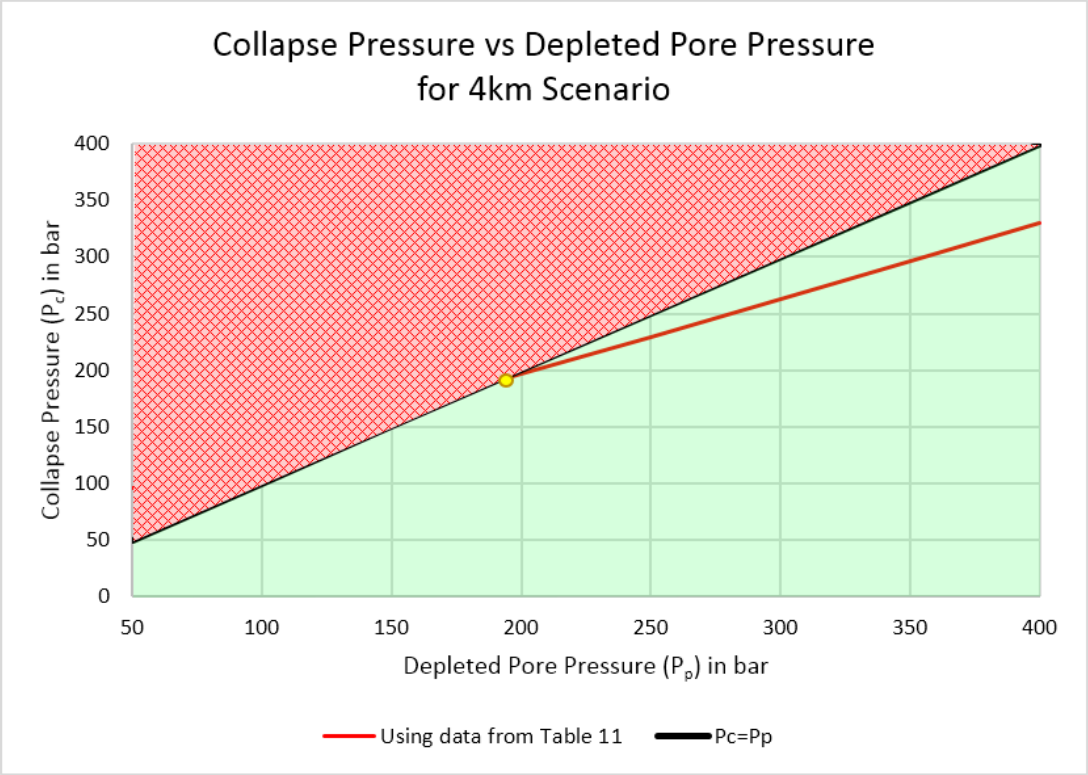

Figure 3-35: Graphical representation of the wellbore collapse model used in this study (Aadnoy and Kaarstad, 2010)**. The scenario modelled here uses a reference overburden pressure corresponding to a 4km deep reservoir. The red line shows the collapse pressure corresponding to a given pore pressure. The black line divides the red patterned area were the collapse pressure is greater than the pore pressure and the green area were the pore pressure is greater than the collapse pressure. Since the collapse occurs when the pore pressure becomes lower than the collapse pressure, the black line is the failure line. The red line represent the dropping pore pressure from the 4 km example as air production occurs. The yellow marker indicates that the well will collapse when the pressure at the well-reservoir interface reaches** approximately **190 bars. For each model the same can be done, the collapse pressure can be determined from the modelled depleted pore pressure at the end of production and test if that collapse pressure is lower than the modelled pressure.**

3.5 Geological Sensitivity Analysis Results

3.5.1 Geological Deterministic Sensitivity Analysis Results

The aim of this sensitivity analysis was to study how the reservoir pressure varied during injection and production for each extreme geological scenario. The following observations can be made:

1. Downhole pressures remain fairly un-sensitive to permeability changes in the reservoir over the ranges of permeability considered (Figure 3-36).
2. The deeper the reservoir depth, the greater the maximum injection pressure and minimum production pressure are for reservoirs thicker greater than 40 m (Figure 3-37).
3. Permeability has a significant impact on the numerical stability of the simulation. Low permeability models failed much more than high permeability models for models with

a depth of 200 m. This is directly linked to the fact that higher permeability allows greater flow rates to be produced from the reservoir.

4. The reservoir pressure fluctuations are un-sensitive to porosity changes (Figure 3-38).
5. Reservoir thicknesses greater than 40 m do not seem to affect the reservoir pressure (Figure 3-39).
6. Reservoir thickness of 40 m can leads to a decrease in minimum production pressure at depths of 2,750m and 4 km (Figure 3-37).
7. 8 out of the 108 simulations failed to stabilize. All of which had been predicted to be unstable using the analytical solution (Eq. 3-22) in section 3.3.8.1.

These results are in accordance with the siting criteria proposed by Allen *et al.* (1983) and Stottlemyre (1979) reported in section 2.1.3.1. The results of this work also provide insights for depth up to 4 km which is outside the ranges proposed by Allen *et al.* (1983) due to limitations of turbomachinery at the time.

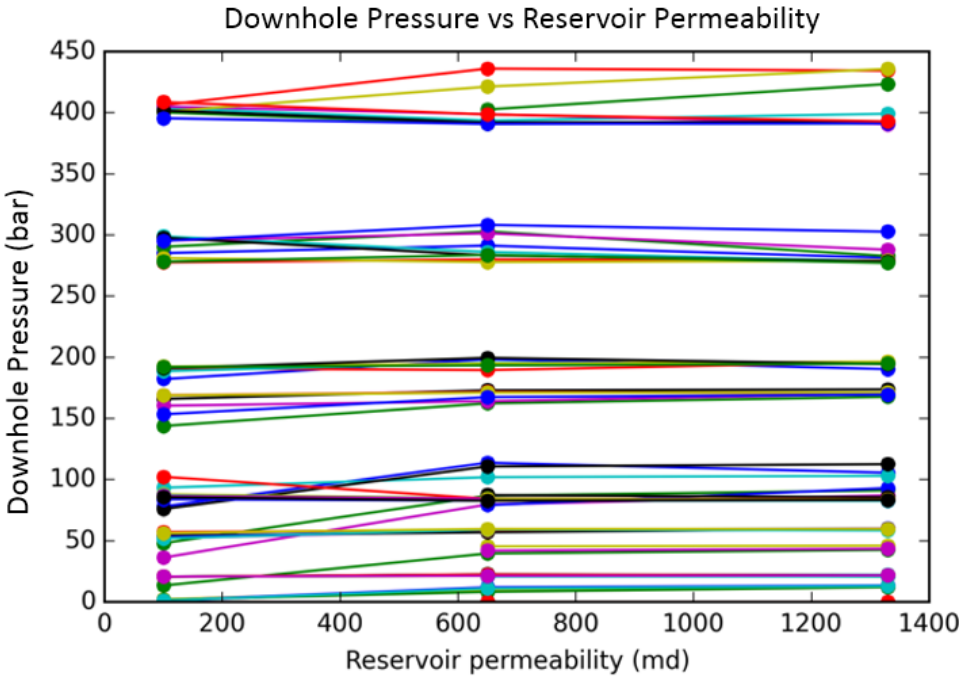

Figure 3-36: The colour code used indicates sets of models which share common parameter settings. For example, three models linked by a red line represents, models which share the same porosity, reservoir thickness and depth, but a different permeability. The results indicate that the downhole pressure response is mostly insensitive to the reservoir permeability. Lower permeability seem to have a slighter greater effect than higher permeability.

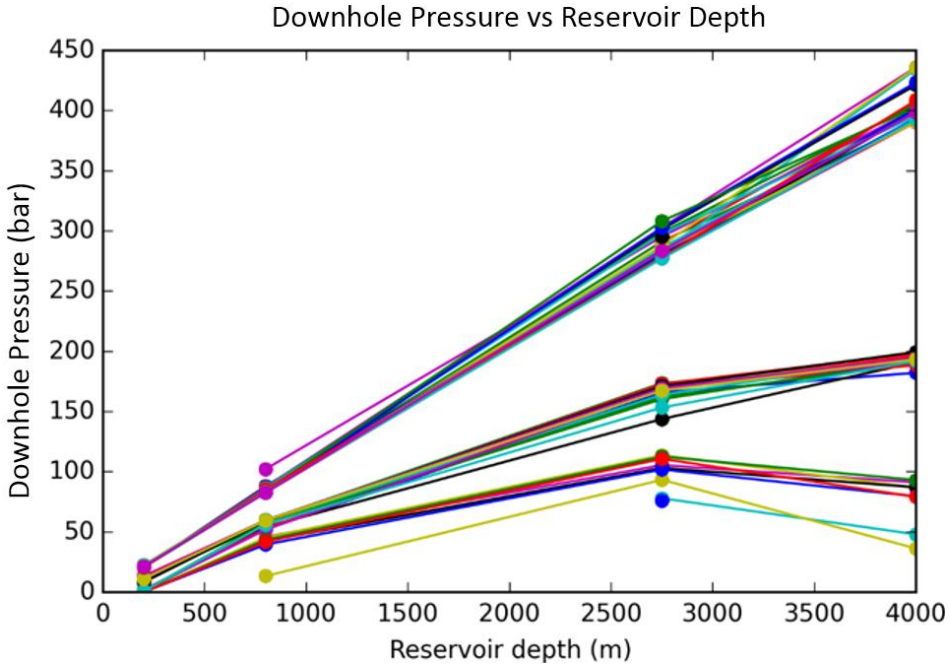

Figure 3-37: Depth is the parameter which seems to have the greatest impact on the average minimum production pressure. For most models they are related via a linear relationship. Models at a depth of 2750 m and 4000 m with a thickness of 40 m lead to a drastic reduction in the production pressure.

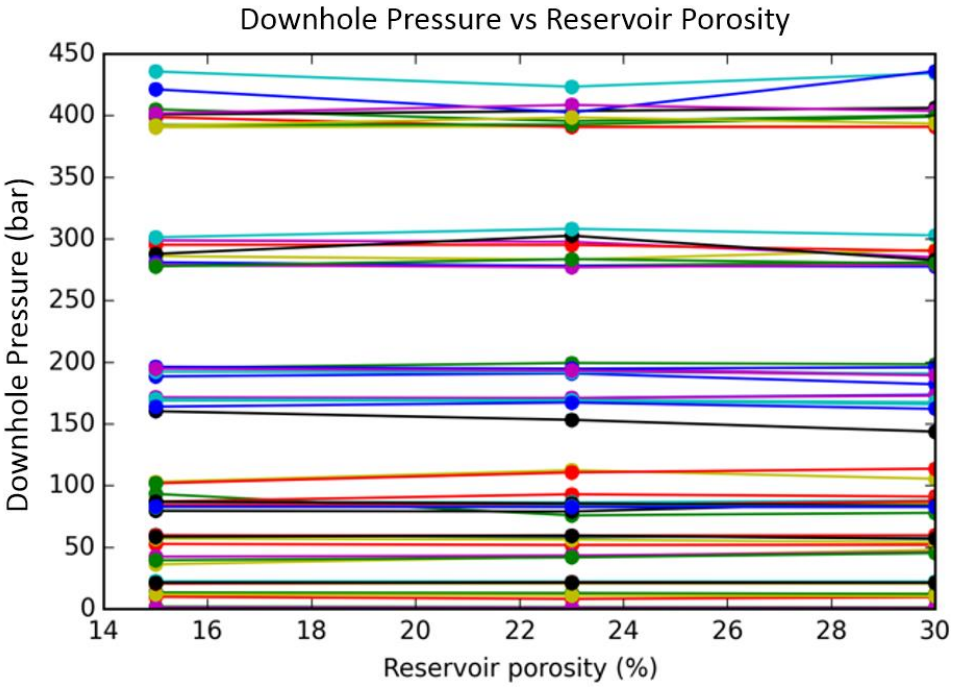

Figure 3-38: The effects of porosity on the average minimum production pressure are essentially non-existent.

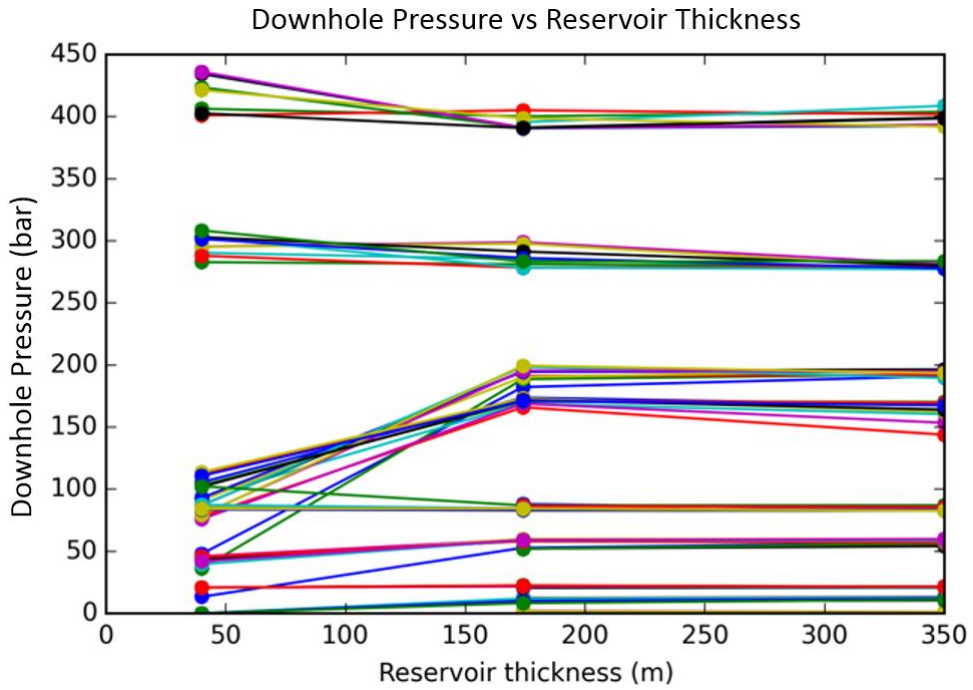

Figure 3-39: This figure shows the average minimum production pressure achieved during the cycles of each simulation. The production pressure is mostly un-sensitive to the reservoir thickness, as the slope of most sets of models are close to zero. However, for some models with a depth of 40 m the production pressure is significantly lower than for the models with the same set of parameters, but greater thicknesses.

3.5.2 Geological Stochastic Sensitivity Analysis Results

As indicated in section 3.3.5.2, once the end member scenarios had been modelled, it was deemed preferable to run a set of 50 random hydrostatic models with parameter values selected within the ranges considered previously in order to allow more values to be fitted to future regressions. Further simulations were run using a storage pressure set at 77% of the lithostatic pressure. All the values reported in the following figures were averaged over 5 to 10 cycles, depending on whether or not the simulation could be completed within the 12 hours of allotted computing time per simulation.

The results are shown below in Figure 3-40, Figure 3-41, Figure 3-42 and Figure 3-43. The lack of correlation between the maximum injection pressure (i.e. storage pressure) and minimum production pressure, and geological parameters other than reservoir depth (over the ranges of criteria deemed suitable for PM-CAES) has not been reported before in the literature and is discussed in the following section.

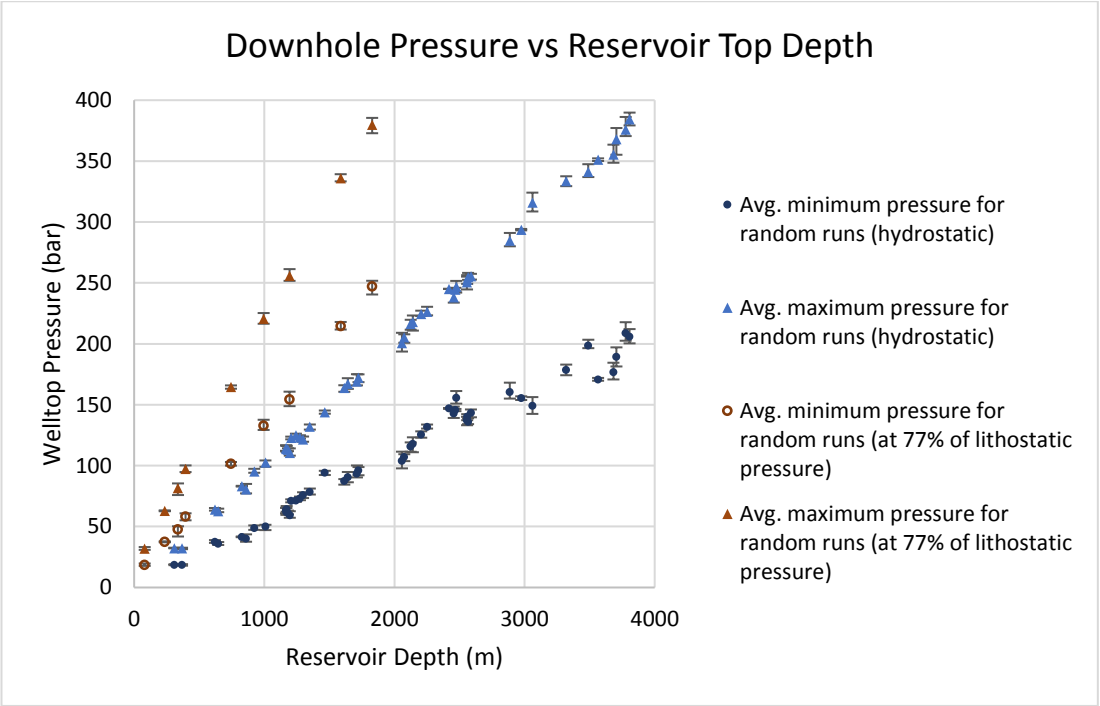

Figure 3-40: Maximum injection pressure and minimum production pressure at the well bottom vs reservoir top depth. The data was extracted from the simulation output files at the point where the well enters the reservoir. The arithmetic average of the minimum/maximum of each cycle is reported. The error bars indicate the maximum and minimum pressure.

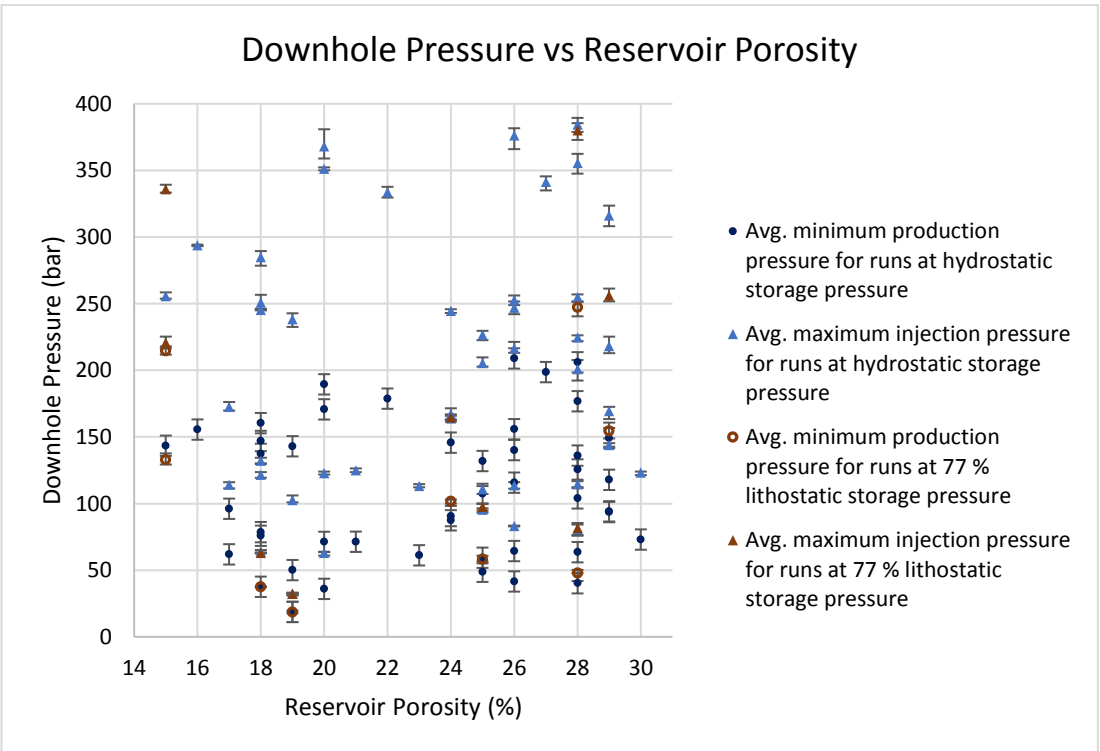

Figure 3-41: Reservoir porosity against maximum injection pressure and minimum production pressure at the well bottom. No clear correlation between reservoir porosity and downhole pressure can be found over the ranges modelled. The error bars indicate the maximum and minimum downhole pressure of the simulation.

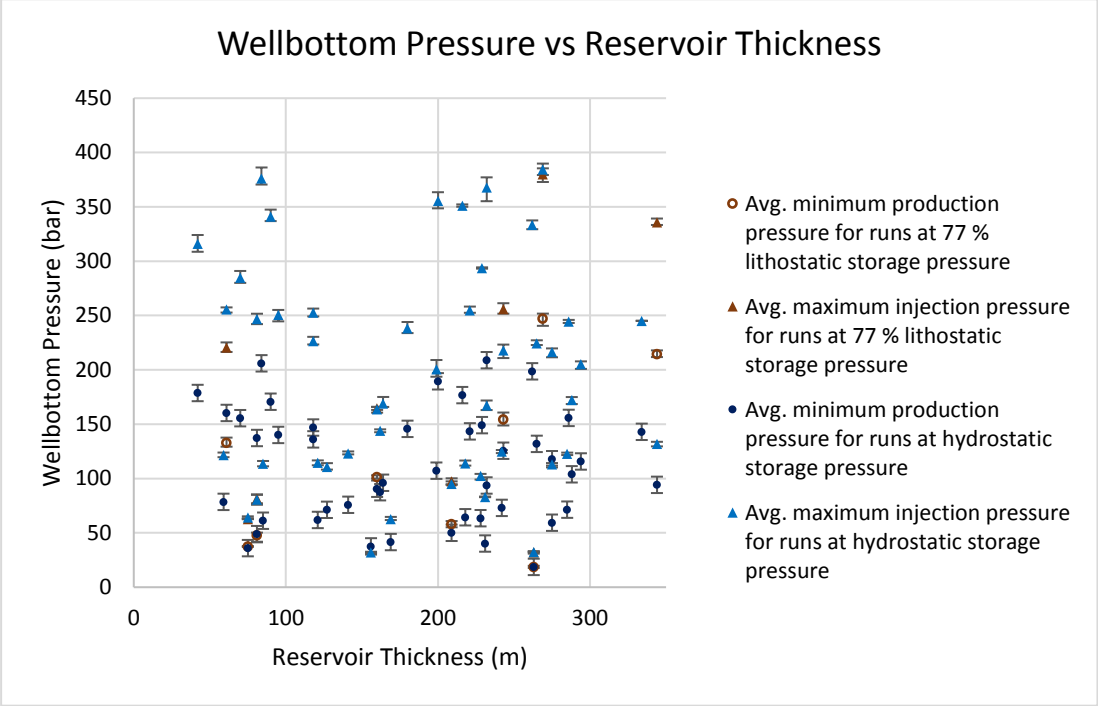

Figure 3-42: Reservoir thickness against maximum injection pressure and minimum production pressure at the downhole. The stochastic results concur with the deterministic ones. No clear correlation between reservoir thickness and downhole pressure can be found over the ranges modelled. The error bars indicate the maximum and minimum downhole pressure of the simulation.

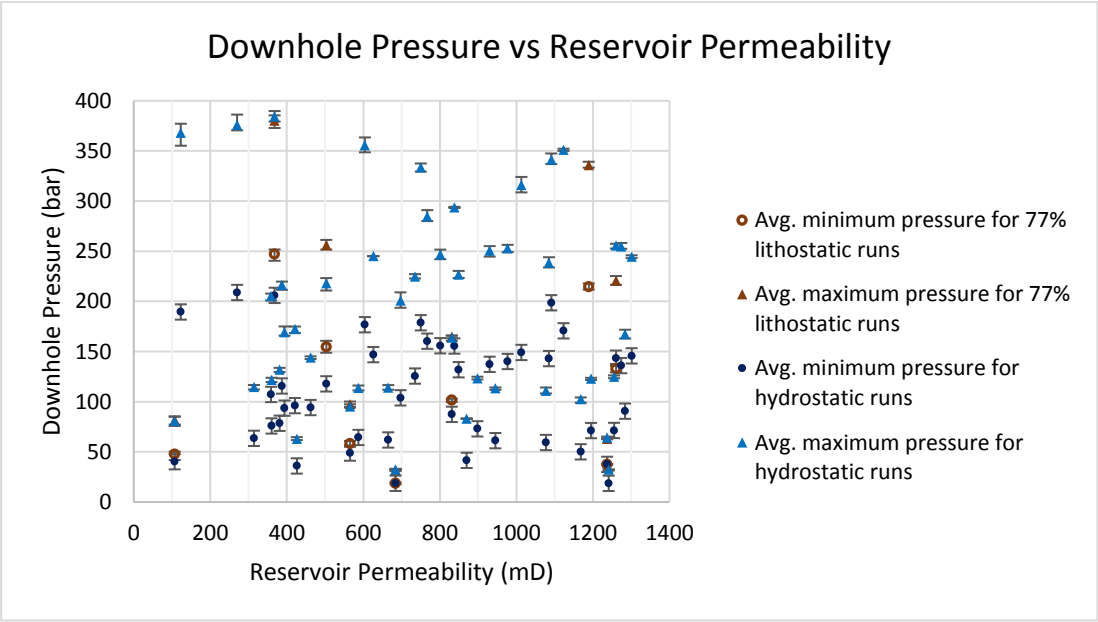

Figure 3-43: Reservoir permeability against maximum injection pressure and minimum production pressure at the downhole. The stochastic results concur with the deterministic ones. No clear correlation between reservoir permeability and downhole pressure can be found over the ranges modelled. The error bars indicate the maximum and minimum downhole pressure of the simulation.

3.6 Discussion and Limitations

This section will discuss the trends observed in the results, what can be inferred from them concerning the PM-CAES system and how the assumptions of the modelling are reflected in them, and the resulting uncertainty.

3.6.1 Geomechanical Effects

Some minimum production pressures lie outside the linear trends between depth and downhole pressure (both stochastic and deterministic simulation results summarised in Figure 3-44). The models yielding those values failed the analytical verification for wellbore collapse. This means that the geomechanical effects induced by such a downhole pressure drop during air production are important, and since they are not modelled those results are not representative and should not be used to establish correlations between geology and downhole pressure. However, these results are used to refine the parameter ranges over which PM-CAES reservoirs can be selected.

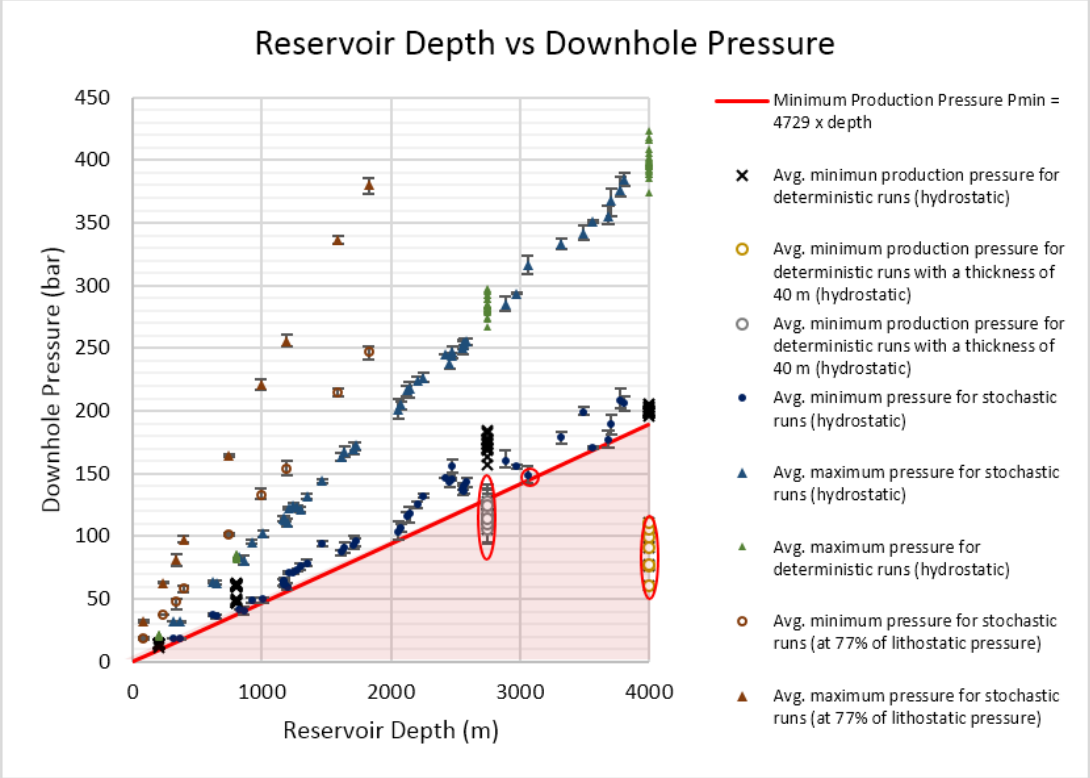

Figure 3-44: Maximum injection pressure and minimum production pressure at the downhole vs reservoir shallowest depth. The term "deterministic" refers to the simulations run using the end members of the parameter ranges. The term "stochastic" indicates simulations performed on parameter values randomly sampled within the parameter ranges (section 3.3.5.2). The deterministic production data shows the simulations in which the reservoir thickness was set at 40 m (hollow symbols). Analytical solutions from Aadnoy and Kaarstad (2010) have shown that the simulations at 4 km depth with 40 m thickness all resulted in mechanical collapse of the wellbore (i.e. below the Minimum Production Pressure line). This means that mechanical effects in the reservoir are significant. Since they have not been modelled, these minimum production pressure values where considered to be unrepresentative of the natural (continues on next page)

response of the system. The variability in the wellbore collapse pressures is explained by its dependence on the minimum production pressure at the well-reservoir interface. In essence, the collapse pressure diminishes proportionally to the downhole pressure. Initially the collapse pressure is much lower than the downhole pressure but there is a crossover threshold where the downhole pressure will be lower than the collapse pressure. This effect is depicted in Figure 3-35.

In Figure 3-44, the models circled in red which lie outside of the linear trends all have in common a 40 meter thickness. Which implies that for models at depth greater than 2.75 km, a thickness of 40 meters is too small to accommodate the 15 kg/s mass flow rate of air during an entire PM-CAES cycle without inducing significant geomechanical effects. The stochastic simulations show the same thing: the one model which has a thickness of 42 m at a depth of about 3 km failed to pass the mechanical test; whilst another with the same thickness at a depth of 2 km passed it. This indicates that reservoir operation with a maximum storage pressure close to hydrostatic pressure could lead to collapse of the reservoir. Therefore the minimum reservoir thickness was increased to 50 m, since all simulations with reservoir thickness above this threshold were successful. In contrast, the models simulating reservoir operation with a storage pressure close to the fracture pressure passed the geomechanical test, as indicated by the brown hollow circles in Figure 3-44. Hence, to minimise the risks of either fracture or collapse the reservoir should be operated at an intermediate storage pressure between the hydrostatic and fracture pressure.

3.6.2 Using Proven Ranges of Operability

PM-CAES was shown to be technically feasible when using values for model parameters within ranges derived from literature and updated to fit modern technology (Allen *et al.*, 1983; Succar and Williams, 2008; Kushnir, Ullmann and Dayan, 2010; Oldenburg and Pan, 2013a). The results confirm that most of the parameter ranges selected for the sensitivity analysis in section 3.3.5.1 are suitable for PM-CAES. At depths of 200 m a few simulations failed to sustain the mass flow rate required for inter-seasonal storage (see models labelled “i” in appendix 8.1). This research therefore informs that the minimum reservoir top depth should be increased to 260 m, which is the threshold specified by Succar & Williams (2008) for “good reservoirs” allowing PM-CAES. The ranges are therefore compatible with the closed compartmentalised reservoir modelled in which the greatest downhole pressure swings occur. Table 3-7 summarises the published ranges and the ones used. As noted before the minimum reservoir thickness was adjusted to 50 m.

Table 3-7: Parameter ranges used in this study based on previous literature. It was found that a minimum reservoir thickness of 50 m and a minimum depth of 260 m were needed to ensure a 15 kg/s flow rate could be sustained during the 2 months of air production.

Parameter	Published Range Extremes	Used Range
Reservoir Intrinsic Permeability (mD)	100 +	100 – 1,330
Reservoir Porosity (%)	5 - 35	15 - 30
Reservoir Thickness (m)	10 +	40(50) - 350
Reservoir Minimum Depth (m)	137 – 1,500	200(260) – 4,000

It is important to recall that the parameter ranges used led to discarding about 70% of the formations contained in the CO_2 Stored database. A minority of high quality reservoirs are therefore being considered here.

Another consequence of choosing conservative ranges is that reservoir depth is the only parameter correlated to the injection and production pressures. Of course, if extreme values such as permeabilities of a couple of tens of millidarcies, or thicknesses less than a meter where tested it is highly likely that those parameters would have a significant influence on the downhole pressure response.

This work did not intend to prove the feasibility of PM-CAES, but rather, design a method to be able to assess the storage potential achievable from known geological data on a nationwide scale as opposed to a site scale. A number of successful scenarios have been identified and modelled, from which downhole pressure response can be estimated using a linear approximation.

Depth Controls on the System

If depth is the key parameter affecting the downhole pressure response, it is important to consider what conditions change with depth in the model. Pressure and temperature of the reservoir have been defined by depth. Indeed, the maximum storage pressure was set using either a hydrostatic pressure gradient or one equal to 77% of the lithostatic pressure (c. in Figure 3-45). The reservoir temperature was set using a geothermal gradient of 34 °C/km applicable to the North Sea. Therefore, by using depth as a variable, which makes sense from a geological point of view, both reservoir temperature and pressure are coupled which makes it impossible to distinguish which one is controlling the reservoir pressure response, or if the interaction between the two is important in quantifying that response. Therefore, a few of the models were run just by changing the reservoir pressure whilst maintaining the reservoir temperature and *vice versa*. (model outputs provided in digital supplementary information).

As expected, since the fluid properties are dependent on both reservoir pressure and temperature, the reservoir pressure response was impacted in both cases. However, a detailed quantification of those responses in order to use the maximum reservoir pressure and reservoir temperature as predictors of the downhole pressure would really be useful on a field scale basis. Since this assessment takes a more holistic approach, and that reservoir pressure and temperature are often correlated in reality, it is reasonable to use depth as the predictor for the downhole pressure variations.

3.6.3 Minimising Storage Pressure in Compartmentalised Reservoirs

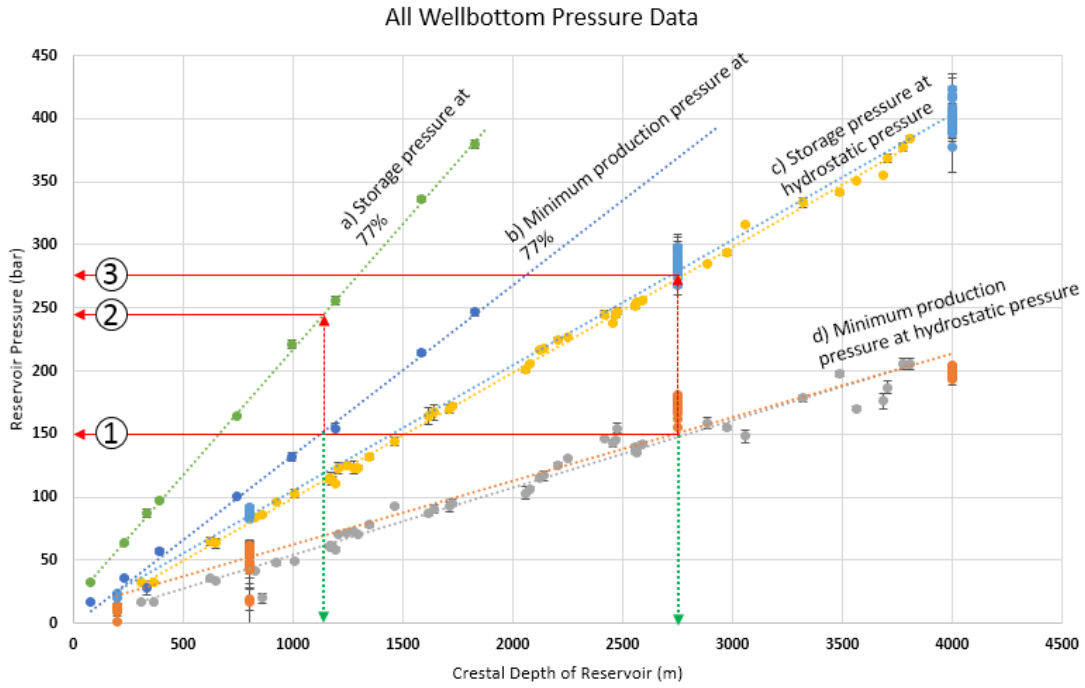

Figure 3-45: Annotated graph of the average maximum injection (storage) reservoir pressure and minimum production pressure occurring during the modelled scenarios. The number of cycles in each simulation varies between 5 and 10 depending on whether or not the simulation could be completed within the allocated 12h of computing time. Data a) represents scenarios in which the target storage pressure is set at 77% of the lithostatic pressure (fracture pressure). Data b) represents the minimum production pressure resulting from the production of air from the reservoir over two months for the scenarios represented in a). Data c) represents scenarios in which the target storage pressure is set at hydrostatic pressure, and d) the minimum production pressure resulting from 2 months of production. Data a) and c) do not fall on perfect lines because of the fact that the input storage pressure varied slightly for each cycle. The annotation indicate that storing as close as possible to the fracture pressure leads to a lower storage pressure for the same minimum production pressure. Even though the storage pressure was set in the models, the example in this graph assumes a "set" production pressure as such pressure would in reality be imposed by the turbine and electricity demand. In the example depicted here the set minimum production pressure is of 150 bars (1), to achieve this the two end member possibilities are either to operate a store at 2,750 m depth at a storage pressure of 275 bars (3) or a 1,100 m depth store at a storage pressure of 245 bars (2). Operating a store at 1.1 km close to fracture pressure could yields benefits such as cheaper well drilling costs, however the risk of fracturing the reservoir would need to be carefully evaluated.

Having modelled the two end members of the possible storage pressure range under which a given store can operated, which are either an operation close to hydrostatic pressure or one at

77% of the lithostatic pressure, it appears that operating a reservoir as close as possible to the fracture pressure (data a. in Figure 3-45) would lead to substantial advantages if the risk of fracture can be well understood and mitigated. Such an advantage would be to achieve a minimum production pressure for shallower reservoirs equivalent to that of deeper reservoirs operated with a storage pressure close to hydrostatic pressure. Assuming that the production pressure throughout the cycle is throttled to the minimum production pressure to match the turbine inlet pressure, then, for a shorter well, power output equivalent to that of a deeper well, could be achieved. Therefore a reduction in well drilling costs for an equivalent power output can be achieved when operating a reservoir closer to the fracture pressure.

Figure 3-45 illustrates those benefits by fixing a target minimum production pressure and comparing what storage pressure and reservoir depth would be needed to achieve it for a store operated near fracture pressure, and for a store operated at hydrostatic pressure. These examples conclude that for a minimum production pressure of 150 bars, the maximum injection pressure could be reduced by around 30 bars by operating a 1,100 m deep store close to fracture pressure, as opposed to a 2,750 m store at hydrostatic pressure.

Another benefit of operating stores as close as possible to fracture pressure, would be that the rate of downhole pressure fluctuations and the associated mechanical fatigue are reduced as illustrated in Figure 3-46. Because the difference between the maximum and minimum storage pressure will be lower than when operated at hydrostatic pressure. Furthermore a lower reservoir pressure fluctuation means a steadier power output, less throttling to the turbine inlet pressure of the air.

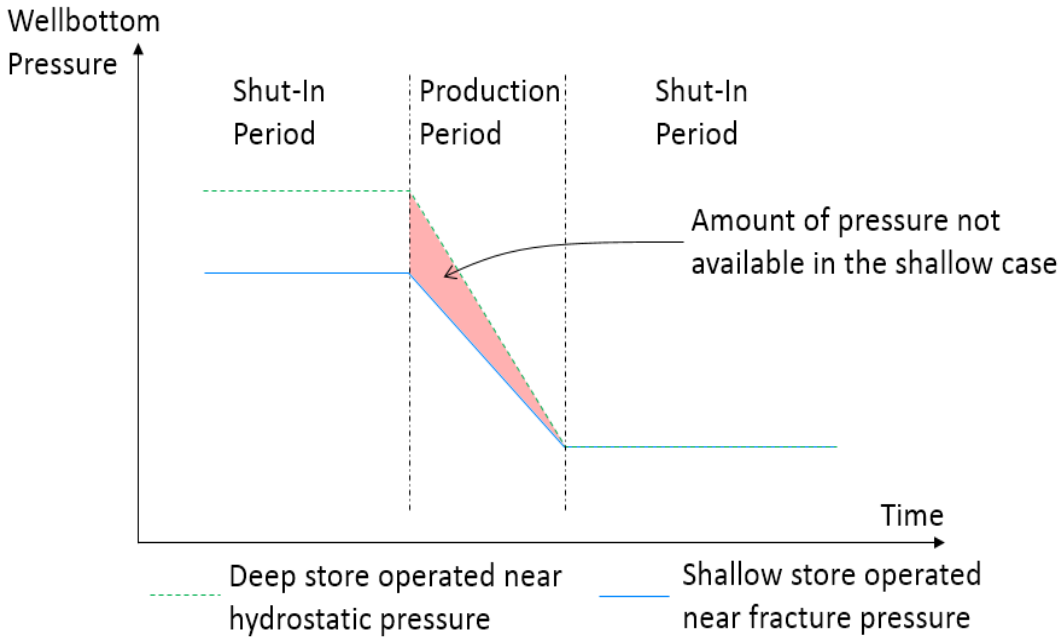

Figure 3-46: Illustration of the downhole pressure fluctuations for two stores. A deep store, operated near hydrostatic pressure which is associated with a faster drop in downhole pressure during the production period than a shallow store operated closer the fracture pressure. This reduction in downhole pressure drop rate might be beneficial to minimise stresses in the reservoir, yet it is also the consequence of less pressure being available to do work in the turbine.

3.6.4 Aquifer Connectivity

Due to the single well, 2D radial-symmetric approach, the pressure connectivity between the PM-CAES site and the rest of the aquifer was not modelled. The system is therefore modelled as a closed pressure container. The key consequence of this assumption in the modelling results was to lead to injection pressure and production pressures which are higher and lower respectively to those encountered in a connected aquifer. Hence, a connected aquifer would absorb some of the pressure changes occurring at the site and lead to a smaller pressure difference between injection and production than a closed system. This smaller pressure difference would result in higher efficiencies, as less compressor work would be needed to reach the injection pressure and more work could be extracted from the turbine due to higher production pressures. Hence, a closed system can be seen as a worst case approximation of the PM-CAES store in terms of pressure fluctuations.

Due to the fact that the average pressure differential over the model at any given time was relatively low (10 bars at most) the deliverability of the reservoir was reduced compared to an open system aquifer where greater pressure differentials can be formed at a given time step. Kushnir *et al*. (2010) and Kushnir *et al*. (2012) found that water conning was likely to be critical if the gas deliverability was high enough. Their conclusions holds true for the open

system they modelled, yet the results from this study suggest that the effects of water conning in closed reservoir are of limited importance. This results from the fact that lower well flow rates can be sustained, and that those flow rates are below the threshold likely to cause water conning. Furthermore in a closed aquifer system no brine can enter the system as the pressure drops. This conclusion is supported by the statement from (Allen *et al.*, 1983) which implies that the significance of water conning for PM-CAES is greatly site dependent.

Oldenburg & Pan (2013) modelled a daily PM-CAES scenario consisting of a single well injecting into a homogenous sandstone anticline connected to an open aquifer. They observed that the saturation of the air within the reservoir did not show significant variation during the cycle, and that the pressure gradients caused by the injection and production of the gas stabilised rapidly during the shut-in (storage) phases. The same observations are made in this study, the zone saturated with air does not vary significantly throughout the cycle. In addition the pressure gradient forming between the well and the edge of the model during production and injection stabilises rapidly (within a few hours) during the shut-in phases.

3.6.5 Heterogeneity Impacts

The lack of heterogeneity is likely to impact the model predictions. Heterogeneity has been shown to have a significant impact on fluid flow in the subsurface (Giordano, Salter and Mohanty, 1985; Lu *et al.*, 2012; Szymkiewicz, 2013; Reynolds and Krevor, 2015; Ringrose and Bentley, 2015). However, the modelling tool's Pressure-Pressure formulation does not enable the study of heterogeneity (Helmig, 1997). Furthermore, since the project aims to scope multiple different formations and geologies it is unlikely that a heterogeneity suitable for all formations in the study could be chosen. Especially as variations in the features of the formation related to the environment in which it originated leads to different heterogeneity patterns. Modelling heterogeneity is key when modelling specific sites but this is not the purpose of this study. The over-predictions in storage volume inside the models due to the lack of heterogeneity are accounted for by applying a storage volume efficiency similar to the one proposed for Carbon Capture and Storage predictions (Haszeldine, 2009). This efficiency represents the reality that only a small portion of a formation volume will eventually be infilled by air making large volumes occupied by heterogeneities partially accounted for. A remaining limitation is that the effects on heterogeneity on reservoir pressure and air saturation in the reservoir are unaccounted for. It is proposed that rather than modelling uncertain heterogeneity in this scoping assessment study, further work would be needed to do site specific models of a few sites. Those sites would be located within a few formations identified in Chapter 6.

It would then be possible to see how the predictions from this study and the estimations from the site studies compare, and if a trend can be found between the two that would enable the predictions of this study to be applied to heterogeneous formations. The advantage of this method is that it would enable the reduction in the uncertainties of both the scoping study and the site specific study. That is to say that the impact of the missing heterogeneity in the scoping study could be determined as well as the impact of not modelling the entire formation in the site specific study. This would enable quantification of uncertainties which cannot be achieved in each respective study.

3.6.6 Conclusion

It has been shown in this chapter that the reservoir depth, porosity, thickness and permeability are essential in distinguishing between formations that have potential to contain suitable PM-CAES sites and those who do not. Indeed, the ranges for those parameters indicated in the literature had to be adjusted to account for the availability of better turbine and compressor technology. In addition, the modelling has shown that the minimum thickness of the reservoir had to be adjusted to 50 m, and the minimum depth to 260 m to ensure that any combination of values from within the parameter ranges established would ensure a formation to be suitable for PM-CAES. It is important to note that specific combinations outside those ranges might prove successful, yet consistently successful PM-CAES inter-seasonal cycling outside the ranges established in this chapter cannot be observed. These ranges can therefore be considered appropriate to perform a scoping exercise of inter-seasonal PM-CAES at a national scale.

The second important conclusion which can be drawn from this modelling exercise of a complex system is that, assuming that the chosen formation has a depth, permeability, porosity and thickness which fall within the proposed ranges, then the injection and production pressures can be estimated using the reservoir depth. Only the reservoir depth is needed to reach an approximation of the injection and production pressures likely to be encountered during the PM-CAES operation. This observation has not been documented in previous literature and is due to the parameter ranges successfully describing a system with good air flow characteristics required for inter-seasonal PM-CAES.

Chapter 4 Modelling the Wellbore and Surface Facilities

4.1 Introduction

To estimate the storage potential achievable using PM-CAES, the plant needs to be modelled. It includes the compressor, combustor and turbine. The well allowing air to flow between the plant and the porous rock store, also needs to be modelled. Modelling the CAES plant and the well allows the power output and consumption of the system to be estimated. This estimate reflects both the plant characteristics, and the geological store characteristics, because the reservoir model and the plant and wellbore models are coupled. A sensitivity analysis of the PM-CAES model was performed by varying the compressor and turbine efficiencies.

In section 4.2.1 the analytical models, implemented in Python 2.7 programming language, for the compressor and turbine are described. In section 4.2.2 the well model is presented and in section 4.2.3 the combustor model is introduced. In section 4.2.4 the model assumptions are summarised. In section 4.2.5 the testing and calibration of the Python code is detailed. In section 4.3 sensitivity analysis of the plant and wellbore model is presented. Section 4.4 and 4.5 report the results from the test model and the sensitivity analysis respectively. The conclusions and discussion of the results and what the light they shed on the PM-CAES system is done in section 4.6.

For convenience the diagram of a conventional PM-CAES system is presented again here, more information on a PM-CAES cycle and plant operation can be found in section 2.1.1.

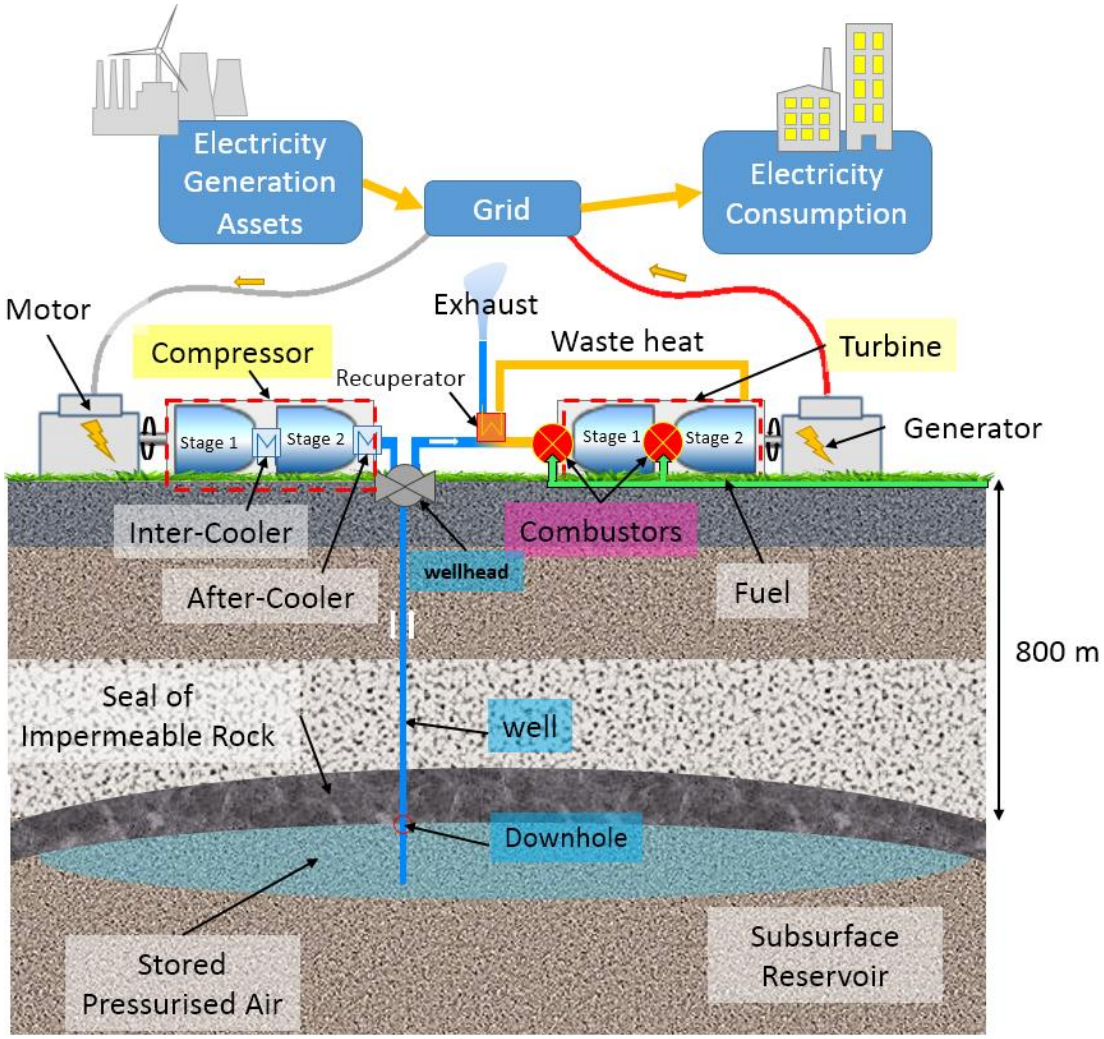

Figure 4-1: Schematic of a conventional CAES plant. The surface facilities are composed of a motor using low cost electricity during times of low demand to power a compressor compressing air from atmospheric pressure to a higher storage pressure. The compression happens in stages, and the air is cooled in between each stage using inter-cooler. After the compression the air is cooled down to the storage temperature using an after-cooler. The well is used to carry the compressed air from the surface to the subsurface storage reservoir, and back from the reservoir to the surface. During times of high demand, when the price of electricity increases, the wellhead is opened allowing the air to flow back to the surface. Once at the surface the air is heated using fuel and waste heat before being expanded through the turbine. In this example, the expansion occurs in two stages with a reheating of the air in between. A schematic of the compressor and turbine is provided in Figure 4-2. The rotation of the turbine blades cause a shaft to rotate, this shaft is linked to a generator producing electricity. Adapted from (Chen *et al.*, 2009)

4.2 Plant and Well Models

4.2.1 Diabatic-CAES Turbine and Compressor Model

Conventional Diabatic-CAES is a proven commercial technology. Indeed, it has been used for over 40 years successfully at the Huntorf plant in Germany, as well as at the McIntosh plant in Alabama, USA. Although not the most efficient CAES technology, it can be used as a meaningful way to compare PM-CAES with existing CAES plants using salt caverns. The use of Diabatic-CAES as an analogy allows the reduction of some of the uncertainties of

turbomachinery characteristics. This section therefore describes the analytical models used to represent the two key components of a diabatic CAES plant: 1) the compressor and 2) the turbine. In particular, the models used to represent the multiple stages within the compressor and turbine used in conventional CAES systems are introduced (see yellow coloured labels in Figure 4-1). The well and combustor are introduced in following sections. The models' implementation in Python 2.7 is provided in appendix 8.2. Figure 4-2 provides a schematic of a multi-stage compressor and turbine to serve as reference throughout this section.

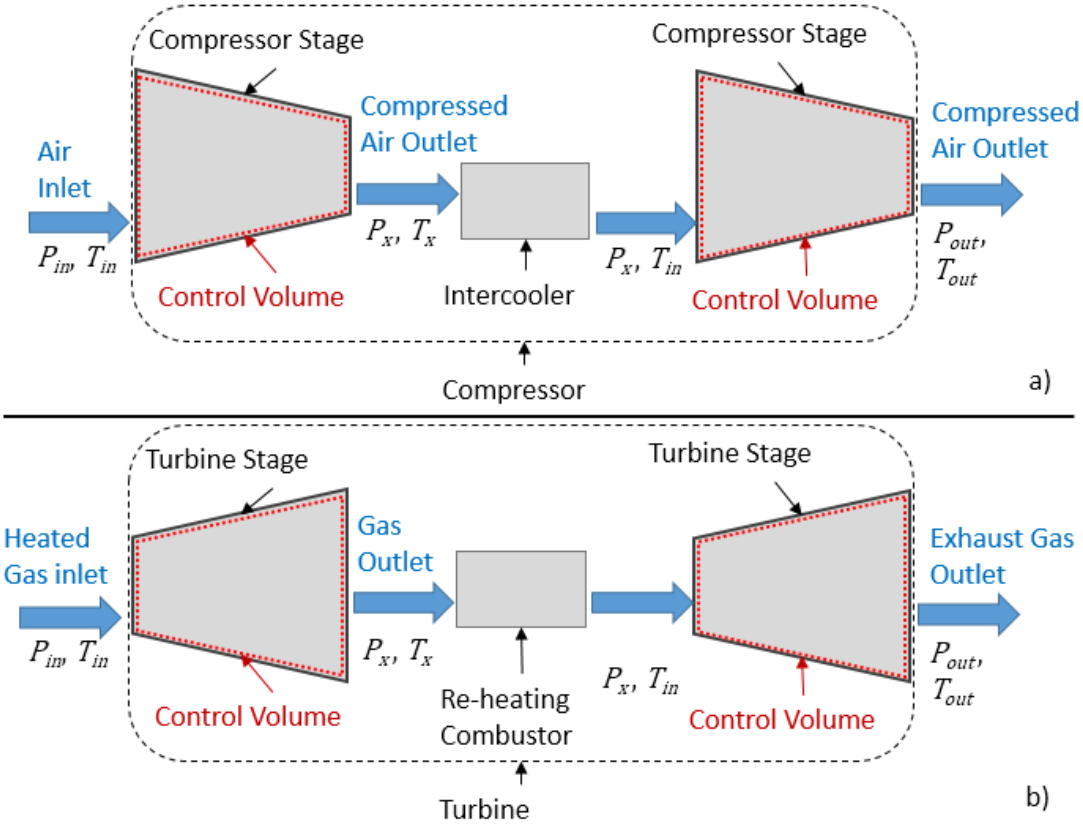

Figure 4-2: Schematic diagram of a compressor (a.) and a turbine (b.). The pressure (P) and temperature (T) at the inlet and outlet of the turbine and compressor are referred to by the subscripts in and out respectively. The subscript x denotes the unknown intermediate pressure between two stages. Note that in both case the inlet temperature to the second stage is equal to the temperature at the inlet of the compressor or turbine. This is achieved by the use of an intercooler for the compressor, and of a combustor for the turbine. The control volumes, over which the integration is performed in order to determine the work required by the compressor and done by the turbine, are indicated in red dotted lines.

4.2.1.1 Work approximation of single stage reversible process

Building upon concepts introduced in section 2.3, analytical models are introduced in this section. They are used to determine the work required to compress the air, as well as the work produced from its expansion. Initially, an isentropic compression or expansion is considered, assuming it is an ***internally reversible process*** with ***air behaving as an ideal gas*** with ***constant specific heats***.

The first assumption that the process is internally reversible implies that losses in heat and pressure occurring in a real process are disregarded. This leads to a crude approximation of the work input to the compressor and output from the turbine. To account for those heat and pressure losses (i.e. irreversibilities) a polytropic efficiency term, explained in section 2.3.6, is included.

The air can be considered an ideal gas at the pressures and temperatures encountered in CAES turbomachinery (see Table 4-1 and section 2.3.5 for more details). It can therefore be used in the analytical models.

Table 4-1: Table showing the pressure (in bar) and temperature (in K) conditions of the gas under which the gas can be assumed to behave as an ideal gas. This is true at high reduced temperatures (> 2) as long as the reduced pressure is much greater than 1 (Çengel, 2004)**. The table was designed assuming air was being expanded and the critical pressure and temperature of air were chosen to be 37.25 bars and 132.41 K respectively. Ranges of operability encountered during conventional-CAES operations are shown as blue shading.**

P (bar)\T(K)	273.15	373.15	573.15	673.15	873.15	973.15	1273.15	1773.15	2273.15
1	Ideal Gas	Ideal Gas	Ideal Gas	Ideal Gas	Ideal Gas	Ideal Gas	Ideal Gas	Ideal Gas	Ideal Gas
50	Ideal Gas	Ideal Gas	Ideal Gas	Ideal Gas	Ideal Gas	Ideal Gas	Ideal Gas	Ideal Gas	Ideal Gas
100	Ideal Gas	Ideal Gas	Ideal Gas	Ideal Gas	Ideal Gas	Ideal Gas	Ideal Gas	Ideal Gas	Ideal Gas
150	Ideal Gas	Ideal Gas	Ideal Gas	Ideal Gas	Ideal Gas	Ideal Gas	Ideal Gas	Ideal Gas	Ideal Gas
200	Ideal Gas	Ideal Gas	Ideal Gas	Ideal Gas	Ideal Gas	Ideal Gas	Ideal Gas	Ideal Gas	Ideal Gas
250	Ideal Gas	Ideal Gas	Ideal Gas	Ideal Gas	Ideal Gas	Ideal Gas	Ideal Gas	Ideal Gas	Ideal Gas
350	Ideal Gas	Ideal Gas	Ideal Gas	Ideal Gas	Ideal Gas	Ideal Gas	Ideal Gas	Ideal Gas	Ideal Gas
400	Non-ideal Gas	Non-ideal Gas	Non-ideal Gas	Non-ideal Gas	Non-ideal Gas	Non-ideal Gas	Non-ideal Gas	Non-ideal Gas	Non-ideal Gas

Assuming constant specific heat leads to an uncertainty of ± 3% in the work output from the turbine, or consumed by the compressor (Figure 4-3). This uncertainty was estimated from the change in work output observed over the range of ratios of specific heats, for extreme pressure ratios and a minimum of 2 compression stages (Figure 4-2);. This change in work output is proportional to both the difference in inlet and outlet pressure of each stage, and the number of compression/expansion stages. The sensitivity of work to the ratio of specific heats is evaluated over the 288 K to 973.15 K temperature range encountered in the CAES turbomachinery throughout a cycle. Therefore, it is unlikely that the actual deviation will reach ± 3% since the compression and expansion processes modelled do not occur over the entire temperature range.

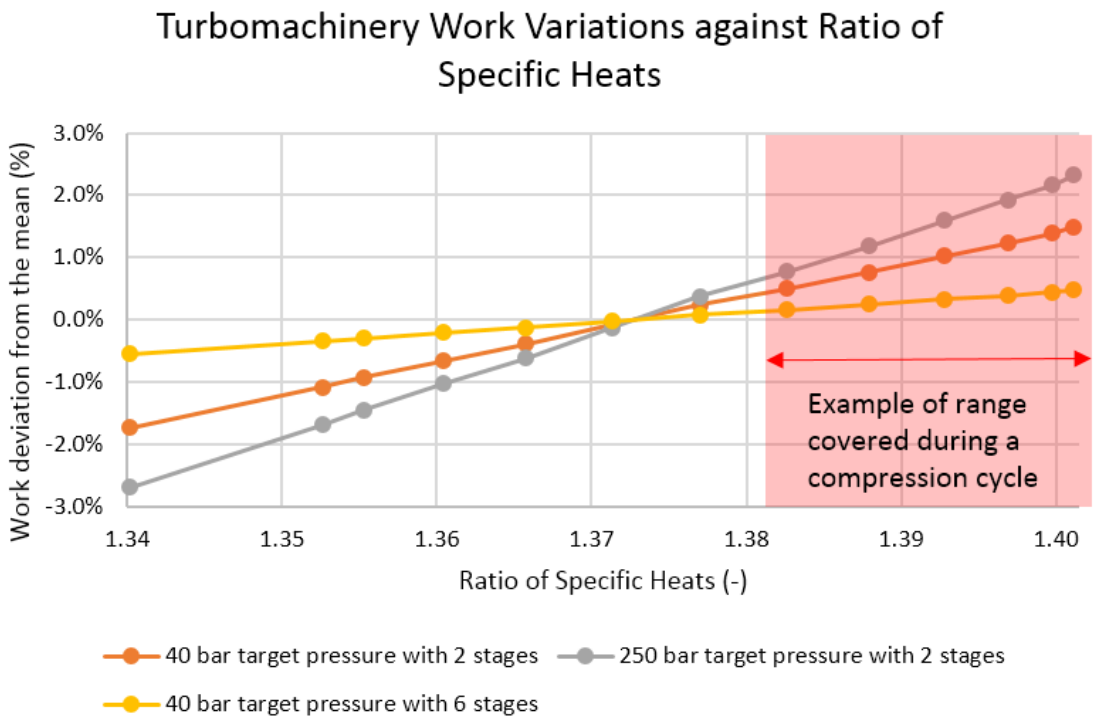

Figure 4-3: The calculation of the work resulting from the compression/expansion of air to or from the target pressure to/from atmospheric pressure is presented here. The value of the specific heat is varied over the range 288 to 973.15 K. The mean value of work over that range for each of the three curves is calculated and the deviation from it computed. Assuming that the specific heat ratio remains constant causes an error in the range of ± 3%. However, as shown by the red shaded area, it is unlikely that the processes will occur over the entire temperature range due to the multi stage processes, the error will likely be smaller than that. The range of temperature over which the ratio of specific heats were determined is 288 K to 973.15 K.

Following on from the verification of the underlying assumptions, the work from a single stage, reversible process, is given by the integration of the pressure change over the control volume of the stage (Figure 4-2):

$$W_{rev} = \int_{in}^{out} V dP \qquad 4\text{-}1$$

Integrating using the ideal gas law introduced in the section 2.3.5, leads to:

$$W_{rev} = \frac{kR(T_{in} - T_{out})}{k-1} = \frac{kRT_{in}}{k-1}\left[\left(\frac{P_{out}}{P_{in}}\right)^{k-1/k} - 1\right] \qquad 4\text{-}2$$

Where: W is the work done by the compressor (positive) or the turbine (negative) per unit mass, k the ratio of specific heats (for air, k is 1.4). R is the specific gas constant. V the volume of the stage, P the pressure of the gas. The subscripts *in* and *out* indicate the inlet and outlet

conditions of the compressor/turbine. *rev* indicates that the process does not account for losses as it is reversible.

4.2.1.2 Extending to Multiple Stage Turbomachinery

In order to achieve more representative results, comparable to existing CAES plants, multi-stage compression and expansion capabilities were added to the code (Xing and Jihong, 2013; Liu, Liu, *et al.*, 2014; Kaiser and Efzn, 2015). For the case of a two stage compression, as illustrated in Figure 4-2 a), the total work done can be defined as the sum of the work done at each stage (Eq. 4-3). The work done in the first compression stage is the work done on the gas, from the known inlet pressure (P_{in}) to an unknown intermediate pressure (P_x). Likewise, the work done in the second stage is the work done from compressing the gas from the intermediate pressure to the known storage pressure (P_{out}).

$$W_{total,rev} = W_{I,rev} + W_{II,rev} \tag{4-3}$$

Where the subscripts *I* and *II* refer to the first and second compression stages respectively.

Therefore substituting the work from a single stage as described by Eq. 4-2 in Eq. 4-3 gives:

$$W_{total,rev} = \frac{kRT_{in}}{k-1}\left[\left(\frac{P_x}{P_{in}}\right)^{k-1/k} - 1\right] + \frac{kRT_{in}}{k-1}\left[\left(\frac{P_{out}}{P_x}\right)^{k-1/k} - 1\right] \tag{4-4}$$

The value of intermediate pressure (P_x), illustrated in Figure 4-2 a), which minimises the total work can be found by differentiating the equation above with respect to P_x and setting the ensuing equation equal to zero. By doing so, the value of P_x lead to an equal compression ratio at each stage. The intermediate pressure is given by Eq. 4-5.

$$P_x = (P_{in}P_{out})^{1/2} \tag{4-5}$$

The total work for a two stage compression is then given by Eq. 4-6.

$$W_{total,rev} = 2W_{I,rev} \tag{4-6}$$

For a number of stages (*s*), the intermediate pressure is given by the generic form of Eq. 4-5:

$$P_x = \left(P_{in}{}^{s-1} P_{out}\right)^{1/s} \quad \text{4-7}$$

This leads to a generic equation for s stages:

$$W_{rev} = s\frac{kRT_{in}}{k-1}\left[\left(\frac{P_{out}}{P_{in}}\right)^{k-1/sk} - 1\right] \quad \text{4-8}$$

The same is true for multistage expansion, except that the value of the work will be negative.

4.2.1.3 Accounting for Irreversibilities

The Eq. 4-8 above was derived for a reversible compression process, it needs to be corrected to account for irreversibilites occurring in real turbines and compressors (e.g. heat transfer through insulation, friction losses and turbulences). As discussed in section 2.3.6, a polytropic efficiency (η_{pol}) can account for compression and expansion not being truly reversible processes. Equations 4-9 and 4-10 characterise the work needed to compress the gas and the work recovered from its expansion respectively. These equations are used in this study.

$$W_c = s\frac{kRT_{in}}{k-1}\left[\left(\frac{P_{out}}{P_{in}}\right)^{k-1/\eta_{pol}sk} - 1\right] \quad \text{4-9}$$

$$W_t = s\frac{kRT_{in}}{k-1}\left[\left(\frac{P_{out}}{P_{in}}\right)^{\eta_{pol}(k-1)/sk} - 1\right] \quad \text{4-10}$$

Determining the outlet temperature of the expansion stages was done by rearranging the work from Barbour *et al.* (2015) for multiple stages:

$$T_{out} = T_{in} \times \left(\frac{P_{out}}{P_{in}}\right)^{\eta_{pol}(k-1)/sk} \quad \text{4-11}$$

4.2.2 Well Model

The well is an essential part of the PM-CAES system (see blue label in Figure 4-1) and its effects on the air pressure needs to be modelled, because the transfer of air through a well, to or from the storage reservoir, results in pressure changes. These changes need to be quantified to ensure that the outlet pressure in the compressor model and the inlet pressure in the turbine model are representative of the pressure expected at the top of the well (i.e. at the wellhead). The well model is important as it will allow the reservoir model to be coupled to the compressor and turbine models. In other words, the pressure outputs from the reservoir model

can be corrected using the well model to determine the outlet pressure of the compressor and the inlet pressure of the combustor and turbine.

The well effects on the wellhead (see Figure 4-1) pressure were determined using an analytical approximation. The solution was tested against numerical simulations of PM-CAES systems from the literature to ensure its accuracy (Oldenburg and Pan, 2013a; Pan and Oldenburg, 2014a). It is worth noting that in the hydrocarbon industry, vertical flow performance tables, which relate the well flow rate to the bottom hole and wellhead pressure, are used to investigate the effect of different wellbore diameters and optimise the well design. Industry software like the VFPi ancillary program from ECLIPSE, or PIPESIM, can generate those tables (accessible at https://www.software.slb.com/products). For PM-CAES site specific investigation, using such tables would be ideal to estimate the optimal well diameter and orientation. The analytical solution used and the testing workflow are detailed below.

4.2.2.1 Smith's Equation

In 1950 Smith presented the theoretical background for calculations involving the flow of gas in wells (Smith, 1950). His focus was on quantifying the friction effects in a gas well by determining a friction factor. The equations he derived can be re-arranged to determine the pressure at the wellhead and downhole during the injection and production phases of the PM-CAES cycle. His work was subsequently used as the basis for further work in the gas industry and proved to be a reliable approximation (Cullender and Smith, 1956; Lee and Wattenbarger, 1996; Brill and Mukherjee, 1999).

The derivation of the equation assumes that both the temperature and the compressibility factor of the gas are fixed throughout the well. Since air is being used, the assumption that the compressibility factor is constant is reasonable since it does not vary by more than approximately 5% over the range of pressures encountered in the wellbore for any one scenario.

The assumption of a constant temperature is not as easily defendable and this is why Smith's equation was verified against numerical simulations accounting for temperature variations. The results of these tests are presented later, in section 4.2.2.3.

The final assumption made by Smith was that the change in kinetic energy is negligible. This assumption is justified for flow rates used in gas well tests (Smith, 1950).

Smith's Equation, as presented in his original work from 1950:

$$Q = 61.75 \times \left(\frac{1.8\,T_{sc} - 459.67}{ZP_{sc}(1.8T - 459.67)}\right)\sqrt{\frac{d^5}{f_f}\left(\frac{P_s^2 - e^S P_w^2}{e^S - 1}\right)} \quad 4\text{-}12$$

where Q is the volumetric flow rate in m^3/s; Z is the dimensionless effective compressibility factor of the gas; T is the effective flowing temperature of the gas, (K); f_f is the dimensionless fanning friction coefficient; d is the inside diameter of the well (m); P_s is the upstream pressure with respect to direction of the flow (bar); P_w is the downstream pressure with respect to direction of the flow (bar); S is the exponent defined by $0.123045GL/[(1.8T-459.67)Z]$; G is the specific gravity of the gas, which is unity for air; L is the length of the well with respect to flow direction in meters (negative during injection); T_{sc} and P_{sc} are the atmospheric temperature and pressure respectively (P_{sc} = 1 bar and T_{sc} = 289 K).

This equation was rearranged to determine the unknown wellhead pressures of interest in this study rather than the flow rate, which is already known and fixed to 15 kg/s. In the implementation of the model used in this study, the air flowing temperature was fixed to the average between the downhole reservoir temperature, which is the temperature of the stored air entering the well, and an approximation of the wellhead temperature. The wellhead temperature was determined using research from Horne & Shinohara (1979), Kutun, Tureyen, & Satman (2015) and Ramey Jr. (1962). These studies present analytical formulations to account for the heat losses occurring between the air stream inside the well and the surrounding rock formation, summarised here for convenience as Eqs. 4-13, 4-14 and 4-15. The transient heat transfer from the well to the surrounding rock as expressed in Eq. 4-13 assumes that the flow rate is sustained for over 30 days, which is the case for both the 4 months of injections and 2 months of production modelled.

$$f(t) \approx -\ln\left(\frac{r_w}{2\sqrt{\kappa t}}\right) - 0.29 \quad 4\text{-}13$$

$$A = \frac{qcf(t)}{2\pi\kappa} \quad 4\text{-}14$$

$$F_t = \Delta T q C_p \left[L + A(e^{-L/A} - 1)\right] \quad 4\text{-}15$$

Where: $f(t)$ is a dimensionless time function of the transient heat transfer to the rock surrounding the well, q is the mass flow rate of air, C_p is the specific heat capacity of the air and is assumed constant, κ is the thermal conductivity of the rock surrounding the well, and

ΔT the geothermal gradient. r_w is the radius of the casing, and L the total well depth (i.e. length). F_t is the total heat loss rate from the well.

Re-arranging the equation for the production phase where the known pressure provided by the reservoir numerical simulation detailed in the previous chapter is the upstream pressure (P_s), the wellhead pressure is given by:

$$P_w = \sqrt{\frac{P_s{}^2 - \left(\frac{QZTP_0}{548.58\,T_0}\right)^2 \frac{f_f(e^s - 1)}{d^5}}{e^s}} \qquad 4\text{-}16$$

And for injection, because the flow is reversed, the known pressure is P_w.

$$P_s = \sqrt{e^s P_w^2 - \left(\frac{QZTP_0}{548.58\,T_0}\right)^2 \frac{f_f(e^s - 1)}{d^5}} \qquad 4\text{-}17$$

It is important to note that for injection, the well length used to calculate the exponent s is negative. Therefore Eqs. 4-16 and 4-17 are equivalent.

4.2.2.2 The Well Pressure Data

Here the data used to verify that Smith's model is applicable to PM-CAES when assuming the air is flowing at constant temperature, between the surface and the reservoir, is presented. The literature contains some modelled well pressure profile over time reflecting the pressure fluctuations during a PM-CAES cycle both at the wellhead and downhole. Such data has been published by Oldenburg & Pan (2013a) and Pan & Oldenburg (2014a).

They obtained the data using a well-reservoir coupled model. The well domain was approximated using a drift-flux model to represent the two-phase flow behaviour and pressure changes expected in the well during a PM-CAES cycle.

The drift-flux model is based on a relationship between the gas velocity, the volumetric flux of the mixture flowing through the well and the drift velocity of the gas, to determine the pressure changes in the well (Figure 4-4) (Pan and Oldenburg, 2014a). The drift velocity of the gas can be defined as the velocity of the gas with respect to volume centre of the gas mixture (Ishii, 1977).

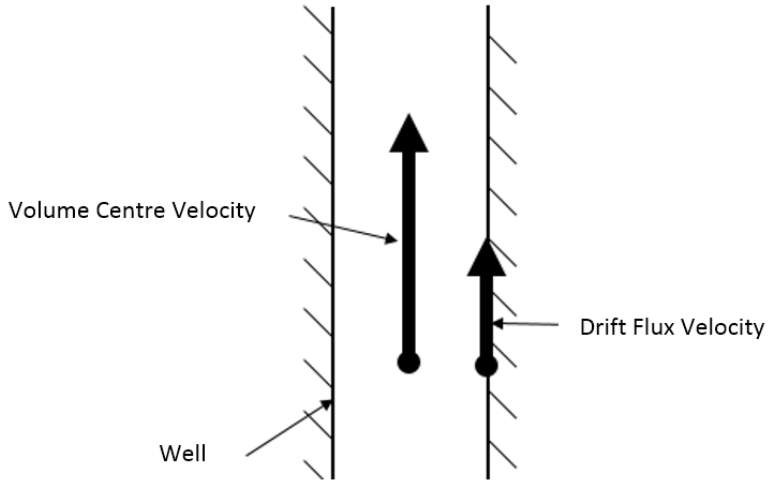

Figure 4-4: Drift flux model diagram, illustrating the key velocity concepts of the centre velocity and the drift flux velocity. The drift flux velocity differs from the centre velocity due to the interaction between the gas and the well walls.

The well roughness was set to $2.4 \cdot 10^{-5}$ m based on the benchmark for two-phase flow air and water through a 1,000 m long pipe proposed in Pan & Oldenburg (2014b). This well roughness is close to the $2.5 \cdot 10^{-5}$ m reported for steel (Kleiber, 2016). Using this value yielded a Fanning friction coefficient of 0.003 within rounding error of the same value reported by Smith (1950) for a 762 m long well. The values used to test whether or not Smith's equation was applicable to the PM-CAES system are found in Table 4-2.

Table 4-2: Parameter values used to test Smith equation's applicability to PM-CAES problems. The mass flow rates used to derive the pressure data was of 54 kg/s during injection and 209 kg/s during production, the same as the ones used by Pan and Oldenburg. However it does not affect the Fanning friction coefficient significantly (by less than $2.0 \cdot 10^{-7}$).

Parameters	Injection Values	Production Values
$\frac{1}{\sqrt{f_f}}$ = well friction factor	17.36	17.36
ε = well absolute roughness (m)	$2.4 \cdot 10^{-5}$	$2.4 \cdot 10^{-5}$
Re = Reynolds Number	$1.08 \cdot 10^{8}$	$4.17 \cdot 10^{8}$
ρ_a (kg/m3) air density	80	55
Fluid velocity (m/s)	53.03	298.54
μ_a (Pa.s) air viscosity	$2.10 \cdot 10^{-5}$	$2.10 \cdot 10^{-5}$
Well mass flow rate (kg/s)	54	209
Flowing Temperature (K)	573	573
f_f = Fanning friction coefficient	0.003	0.003

4.2.2.3 Results of Testing Smith's Equations vs Published PM-CAES Data

The comparison between values obtained using Eqs. 4-16 and 4-17 against those from downhole pressure profiles during a PM-CAES cycle is presented here (Oldenburg and Pan, 2013a; Pan and Oldenburg, 2014a). The results show a good match between the values obtained using the methodology of this study and the published data as indicated by the overlap of the blue and purple dotted lines in Figure 4-5 and Figure 4-6.

The average error, represented by the red curves in Figure 4-5 and Figure 4-6, was estimated at less than 3%. Spikes in the error value are due to the graphical extraction of the published data. For some time values (x-axis) pressure data was only extracted for either the downhole or wellhead. If this mismatch happened close to a change in PM-CAES operation phase (e.g. production to shut-in), then the closest pressure value used for comparison might have been extracted on the opposite side of the sharp change in pressure cause by the operational phase change. For the purpose of the comparison the published literature downhole and wellhead pressure data was extracted automatically by the Engauge.exe software.

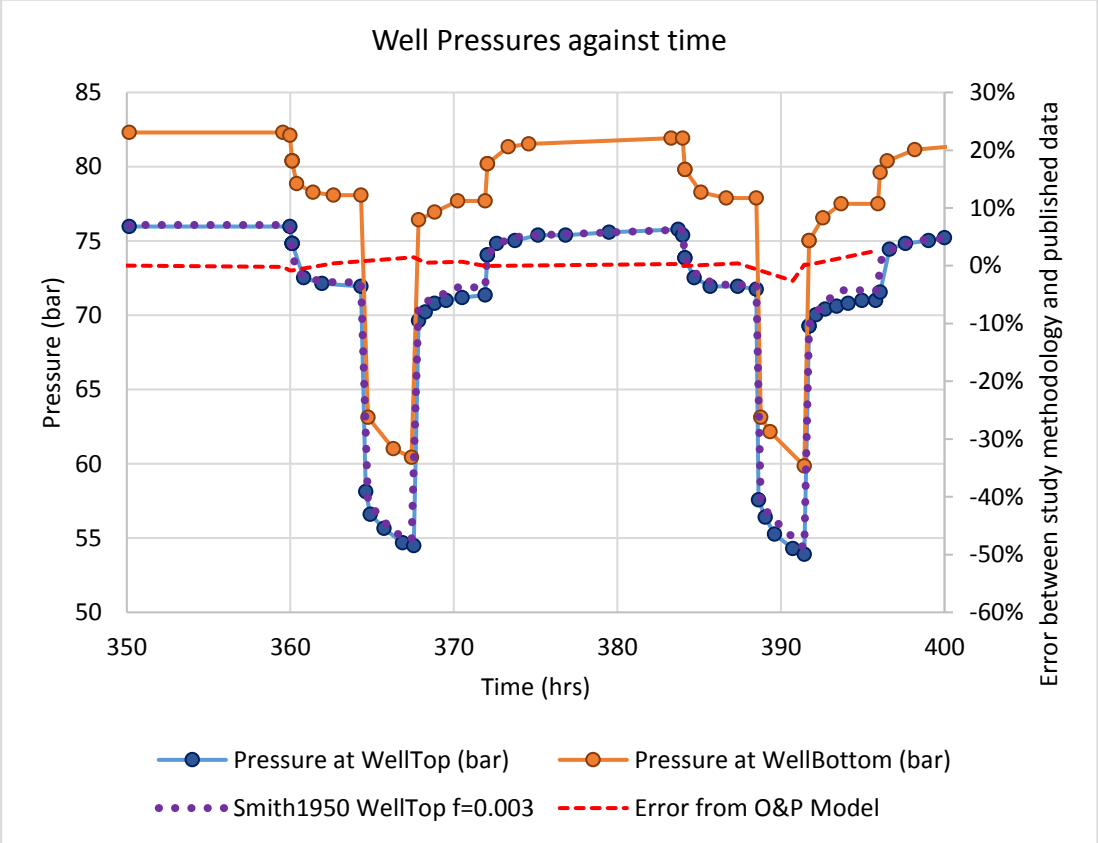

Figure 4-5: Comparison of well pressure simulation data from Pan & Oldenburg (2014a) and the analytical solution from Smith (1950) using inputs parameters from Table 4-2. The orange and blue lines represent the published data for the downhole and wellhead pressures respectively. The dotted purple line the represents the wellhead pressure estimated using Smith's equation and a Fanning friction coefficient of 0.003. The red dashed line represents the error between the values calculated using the implementation of Smith's equation used in this study and the published data.

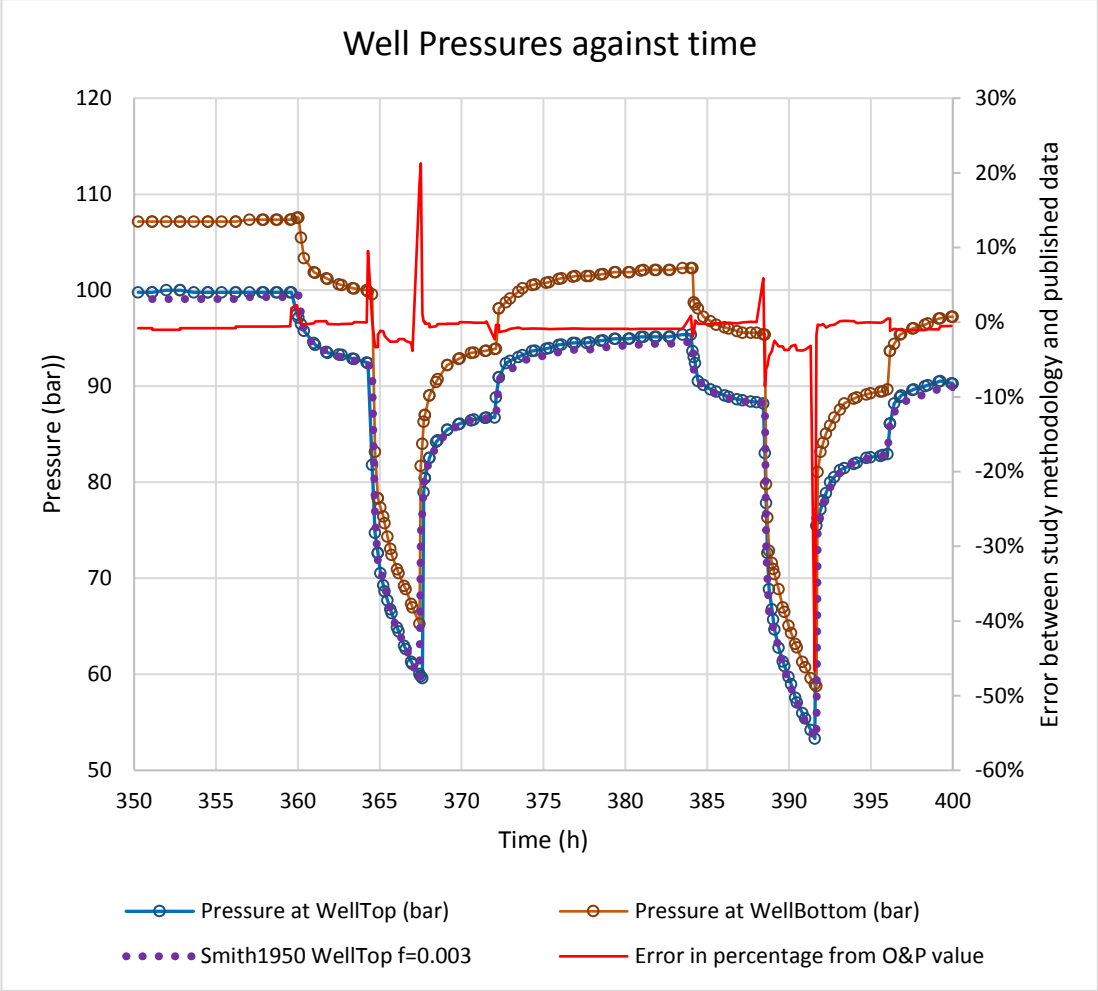

Figure 4-6: Comparison of well pressure simulation data from Oldenburg & Pan (2013a) and the analytical solution from Smith (1950) using inputs parameters from Table 4-2. The orange and blue lines represent the published data for the downhole and wellhead pressures respectively. The dotted purple line the represents the wellhead pressure estimated using Smith's equation and a Fanning friction coefficient of 0.003. The red dashed line represents the error between the values calculated using the implementation of Smith's equation used in this study and the published data.

4.2.3 Combustor Model

In the Diabatic-CAES cycle, the air is cooled prior to being injected in the underground store. Hence, during the production phase, the air needs to be re-heated before being expanded in the turbine. If air is not reheated the cooling caused by the expansion of the gas in the turbine can lead to operational hazards such as ice forming inside the turbine. The heating of the air has been analytically modelled by assuming that natural gas was added to the air stream and burnt inside a combustor. The energy losses due to the compression of the methane were ignored since the mass flow rate of methane was approximately 1% of total mass flow rate. Constant pressure and specific heat capacity was assumed during the combustion. Those assumption can be responsible for inaccuracies in predicted heat rates so calibration of the combustor efficiency was performed (Kreid and McKinnon, 1978). A pressure drop across a combustor

can reach up to 2 to 10% of the inlet pressure (Kiameh, 2002). However, this drop is usually included in the overall turbine efficiency.

The heat addition in the first expansion stage was solved analytically in order to establish the optimum ratio of air (assumed to be 21% of oxygen and 79% nitrogen) to methane in the flow rate of 15 kg/s. The combustion was assumed to be complete. For each additional subsequent stage of expansion, the amount of gas from the previous stage was assumed to be transferred in totality, with more methane added and combusted at that point. Methane was then added to the gas from the previous stage. In between stages, the mass of condensed water vapour, if any, was calculated and removed from the mass balance equation (this mass was determined simply by comparing the partial pressure of water vapour with its vapour pressure at the operating temperature). Finally, the analytical combustion model was calibrated to the Huntorf plant using a combustor efficiency factor, to correct the heat input calculated.

4.2.3.1 1st Stage Calculations:

The calculations performed to estimate the amount of methane needed in the first stage, and implemented in the code, are presented below. The amount of heat resulting from the combustion of a molar flow rate of methane is given by Eq. 4-18.

$$\sum_i P_i C_{p_i}(T_{out} - T_{in}) = \Delta H_{combustion} F_{CH_4} \qquad 4\text{-}18$$

With P_i and Cp_i the molar flow rate and specific heat capacity of species i respectively. T_{out} and T_{in} are the temperature of the gas mixture after and prior to combustion respectively. $\Delta H_{combustion}$ is the heat produced by one mole of methane, and F_{CH4} is the feed molar flow rate of methane to the combustion chamber. For each store scenario, the inlet temperature of the combustion chamber (i.e. the temperature of the air reaching the combustion chamber) was determined using the store's temperature and the works from Horne & Shinohara (1979), Kutun et al. (2015) and Ramey Jr. (1962) presented in section 4.2.2.1. These work present analytical formulation to account for the heat losses occurring between the air stream inside the well and the surrounding rock formation. The outlet temperature was fixed to 400 K above the inlet temperature. This choice was made to minimise the influence of natural gas combustion on the efficiency variations.

With $(T_{out} - T_{in}) = \Delta T$, the feed of methane, in moles, needed to increase the temperature of air by ΔT is given by:

$$F_{CH_4} = \frac{\Delta T\left(P_{CO_2}C_{P_{CO2}} + P_{H_2O}C_{P_{H2O}} + P_{N_2}C_{P_{N2}} + P_{O_2}C_{P_{O2}}\right)}{\Delta H_{combustion}} \quad 4\text{-}19$$

Assuming that the combustion of methane (CH_4) with oxygen (O_2) is complete, it yields carbon dioxide (CO_2) and water (H_2O):

$$CH_4 + 2O_2 \rightarrow CO_2 + 2H_2O \quad 4\text{-}20$$

Therefore, for the first stage of the turbine, the products (P) of the combustion can be expressed in terms of methane, oxygen and nitrogen (N_2) molar feed (F_i) entering the combustor:

$$P_{CO_2} = F_{CH_4} \quad 4\text{-}21$$

$$P_{H_2O} = 2F_{CH_4} \quad 4\text{-}22$$

$$P_{O_2} = F_{O_2} - 2F_{CH_4} \quad 4\text{-}23$$

$$P_{N_2} = F_{N_2} \quad 4\text{-}24$$

Therefore Eq. 4-19 describing the molar feed of methane can be rewritten as:

$$F_{CH_4} = \frac{\Delta T\left(F_{CH_4}C_{P_{CO2}} + 2F_{CH_4}C_{P_{H2O}} + F_{N_2}C_{P_{N2}} + \left(F_{O_2} - 2F_{CH_4}\right)C_{P_{O2}}\right)}{\Delta H_{combustion}} \quad 4\text{-}25$$

Which simplifies to:

$$F_{CH_4} = \frac{\Delta T\left(F_{N_2}C_{P_{N2}} + F_{O_2}C_{P_{O2}}\right)}{\Delta H_{combustion} - \Delta T\left(C_{P_{CO2}} + 2C_{P_{H2O}} - 2C_{P_{O2}}\right)} \quad 4\text{-}26$$

To find the mass flow rate of methane an arbitrary equivalence ratio between the mass flow rates of methane and oxygen was used. Then, Eq. 4-26 can be expressed as a function of oxygen mass flow rate (Eq. 4-34). The process to achieve this is described below:

The total mass flow rate through the turbine (m_T) for the first stage is:

$$m_T = \left(m_{CH_4} + m_{O_2} + m_{N_2}\right)_{in} = \left(m_{CO_2} + m_{H_2O} + m_{O_2} + m_{N_2}\right)_{out} \quad 4\text{-}27$$

Where m_i is the mass flow rate of the specie *i*.

Assuming a composition of air of 21% O_2 and 79% N_2 entering the first stage, then:

$$m_{O_2} = \frac{21}{79} m_{N_2} \quad 4\text{-}28$$

Setting the equivalence ratio *x* as: $x = \frac{2F_{CH_4}}{F_{O_2}}$.

It follows that, dividing the mass flow rates of methane and oxygen by their respective molar masses yields:

$$x = \frac{\frac{2m_{CH_4}}{16}}{\frac{m_{O_2}}{32}} \quad 4\text{-}29$$

$$x = \frac{4m_{CH_4}}{m_{O_2}} \quad 4\text{-}30$$

Expressing the total mass flow rate (m_T) from Eq. 4-27, in terms of m_{O2} therefore yields:

$$m_T = \left(m_{CH_4} + m_{O_2} + m_{N_2}\right)_{in} = \left(\frac{x}{4} m_{O_2} + m_{O_2} + \frac{79}{21} m_{O_2}\right)_{out} \quad 4\text{-}31$$

Which simplifies to:

$$m_T = \left(\frac{x}{4} + 1 + \frac{79}{21}\right) m_{O_2} \quad 4\text{-}32$$

Dividing Eq. 4-26 through by the molar masses, the molar feed of methane is converted to mass flow rates:

$$\frac{m_{CH_4}}{16} = \frac{\Delta T\left(\frac{m_{N_2}}{28} C_{P_{N2}} + \frac{m_{O_2}}{32} C_{P_{O2}}\right)}{\Delta H_{combustion} - \Delta T\left(C_{P_{CO2}} + 2C_{P_{H2O}} - 2C_{P_{O2}}\right)} \quad 4\text{-}33$$

Then, using the relationships between the mass flow rate of nitrogen and oxygen $m_{N_2} = \frac{79}{21} m_{O_2}$ from Eq. 4-31. The mass flow rate of methane can be expressed in terms of mass flow rate of oxygen:

$$m_{CH_4} = \frac{16\Delta T\left(\frac{79}{21 \times 28} C_{P_{N2}} + \frac{C_{P_{O2}}}{32}\right) m_{O_2}}{\Delta H_{combustion} - \Delta T\left(C_{P_{CO2}} + 2C_{P_{H2O}} - 2C_{P_{O2}}\right)} \quad 4\text{-}34$$

This yields a system of four equations which allows to find the mass flow rates of oxygen, nitrogen, and methane to be added to the combustion chamber to reach the turbine inlet pressure (here defined as T_{out} since the combustion chamber is being considered).

These equations are:

$$\begin{cases} x = \dfrac{16 \times 4(T_{out} - T_{in})\left(\frac{79}{21 \times 28} C_{P_{N2}} + \frac{C_{P_{O2}}}{32}\right)}{\Delta H_{combustion} - (T_{out} - T_{in})\left(C_{P_{CO2}} + 2C_{P_{H2O}} - 2C_{P_{O2}}\right)} & 4\text{-}35 \\ m_{O_2} = \dfrac{m_T}{\frac{x}{4} + 1 + \frac{79}{21}} & 4\text{-}36 \\ m_{CH_4} = \dfrac{x}{4} m_{O_2} & 4\text{-}37 \\ m_{N_2} = \dfrac{79}{21} m_{O_2} & 4\text{-}38 \end{cases}$$

The rate at which heat is added to the system by the methane can then be calculated using:

$$Q_{in} = m_{CH_4} \times LHV \times \eta_c \quad \text{4-39}$$

Where LHV is the low heating value of methane in J/kg, and η_c the combustor efficiency. This efficiency incorporates the combustion efficiency which is close to 100% in modern combustors (Kiameh, 2002), as well as inaccuracies due to the assumption of constant specific heats. It would also account for the efficiency gain should a heat recuperator be used to preheat the air using the heat from the exhaust gas before it enters the combustor.

Multiplying Q_{in} with by the production time yield the total amount of energy added by the combustion of methane during the production phase and can be used to work out the efficiency of the CAES system as described by the roundtrip efficiency introduced in section 2.1.2.3.

4.2.3.2 Condensation Calculations

As the hot air stream cools during the expansion inside the turbine an assessment of whether or not condensation of water would occur, and if so how much, was undertaken. This step is important since the fast rotating blades of turbines may get damaged by the impact of liquid droplets in the working fluid. It will also avoid including the effect of water droplet evaporation in the estimate of temperature change as pressure decreases.

The first step to determine the amount of condensing water, was to calculate the maximum (absolute) water vapour content the gas could hold at the exhaust pressure and temperature condition of the stage.

The ratio of the partial water vapour pressure to the total pressure of the gas is equal to the ratio of the number of moles of water vapour in the gas to the total number of moles of gas:

$$\frac{P_{water}}{P_{gas}} = \frac{n_{water}}{n_{gas}} \quad \text{4-40}$$

From this equation the partial pressure of the gas can be determined since the molar quantity of each product in the exhaust gas is known.

The saturation pressure P_{sat} can be calculated using *Antoine's Equation* and the coefficients found in Table 4-3 (Antoine, 1888):

$$\log_{10} P_{sat} = A - \frac{B}{C + T} \quad 4\text{-}41$$

With T being the temperature of the gas in Celsius, and P_{sat} is given in bar.

Table 4-3: Antoine's Equation coefficients for water were used in this study. The coefficients were calculated from the referenced author's data by National Institute of Standards and Technology of the U.S. Department of Commerce. The gap between 373 and 379 K is covered by linear interpolation in the code.

A	B	C	Tmin, K	Tmax, K	Reference
5.40221	1838.675	-31.737	273	303	(Bridgeman and Aldrich, 1964)
5.20389	1733.926	-39.485	304	333	(Bridgeman and Aldrich, 1964)
5.0768	1659.793	-45.854	334	363	(Bridgeman and Aldrich, 1964)
5.08354	1663.125	-45.622	344	373	(Bridgeman and Aldrich, 1964)
3.55959	643.748	-198.043	379	573	(Liu and Lindsay, 1970)

The ratio of the partial pressure of water vapour to the saturation pressure is called the relative humidity:

$$RH = \frac{P_{water}}{P_{sat}} \quad 4\text{-}42$$

Using this definition of relative humidity and the relationship of partial water vapour pressure the maximum theoretic water content of air, at a given temperature and pressure, can be determined. This is the particular case where the air is saturated with air (i.e. RH = 1).

Therefore:

$$n_{water,max} = \frac{1 \times P_{sat} \times n_{gas}}{P_{gas}} \quad 4\text{-}43$$

The difference between $n_{water,\,max}$ and n_{water} gives the amount of water in excess, which the gas cannot hold in vapour form. This can then be converted to the mass of condensed water using the molar mass of water. This mass of water is then removed from the system.

4.2.3.3 Second Stage Calculation:

For the subsequent stages of expansion, the excess water in the gas was removed from the final gas content and the rate at which heat is needed to heat up the remaining mass of gas was determined using:

$$Q_{in} = \sum_{i}^{s} c_{p,i} \times \Delta T \times m_i \times \eta_c \quad 4\text{-}44$$

Where c_p is the specific heat capacity of the specie *i*, ΔT the temperature increase needed, and m_i the mass flow rate of specie *i,* s the number of stages, and η_c the combustor efficiency. ΔT is determined using the turbine stages inlet pressure and the outlet temperature from the previous stage using Eq. 4-11.

Then the amount of methane to be added can be estimated using the amount of heat required and the Low Heating Value (LHV) of methane:

$$m_{CH4} = \frac{Q_{in}}{LHV} \quad 4\text{-}45$$

It follows that the quantity of methane in moles can be derived by dividing m_{CH4} by the molar mass of methane.

From which the products of the combustion for the given stage can be determined. *p* and f expressed the mass flow rate of product and feed into the combustor. Since complete combustion is assumed, then the following can be written, for stage *n*:

$$pO_{2,n} = pO_{2,n-1} - 2fCH_{4,n} \quad 4\text{-}46$$

$$pCO_{2,n} = pCO_{2,n-1} - fCH_{4,n} \quad 4\text{-}47$$

$$pH_2O_n = pH_2O_{n-1} - 2fCH_{4,n} \quad 4\text{-}48$$

$$pN_{2,n} = pN_{2,n-1} \quad 4\text{-}49$$

From Eqs. 4-46, 4-47, 4-48, 4-49, and the pressure and temperature condition at the exit of the current stage a new condensation calculation can be performed. Then, the mass of water vapour can be adjusted and the heat addition for the subsequent stage performed.

A note should be made that although the procedure followed for the subsequent stages (all stages but the first) seem to be heavily approximated, the ratio of methane added to the total gas is <1%. Therefore it is reasonable to assume that the addition of the methane on top of the existing mass of gas will remain within the turbine's operability range (some water product may also be removed between stages, partly compensating for the addition of methane).

4.2.4 Plant Model Assumption Summary

The assumptions used in the compressor, turbine and combustor models discussed previously are summarised here for convenience:

1. Air is assumed to behave as a perfect gas
2. Constant specific heat capacity of methane is assumed during combustion.
3. Uses polytropic efficiency to account for irreversibilities and losses in the system.
4. Work output at each stage is equal based on an optimal pressure ratio.
5. Assume dry air for heat addition calculations.
6. Assume a constant heating value of 0.0139 $MWh_{thermal}$/kg for CH_4
7. Specific heat ratio of 1.4 is assumed constant for air during compression and expansion.
8. No throttling of the air stream during the expansion process is assumed to take place in the calculations.

4.2.5 Testing and Calibration Using Huntorf Data

The next step was the validation of the Python program using existing data from the Huntorf plant. This test was performed by editing the code to ensure that each compression and expansion stage was representative of the turbomachinery used at Huntorf. This did not involve a fundamental change in the program structure and the equations described in this chapter were used. This section will review the design of the Huntorf plant and present the key components of the test model. The comparison of the results of the test simulation with existing Huntorf data is reported in section 4.4.

4.2.5.1 The Huntorf Plant

The Huntorf Plant, introduced in section 2.1.4.1.1, is located in Germany, it has been operating since 1978 (Crotogino, Mohmeyer and Scharf, 2001). The plant has a capacity of 290 MW for 3 hours (870 MWh). The store used at this plant is a salt cavern. The simple design of the

Huntorf Plant allows the plant model developed to be tested and calibrate the combustor efficiency to it. The Huntorf plant uses a low-pressure and a high-pressure compressor, with 4 compression stages in total (Figure 4-7 elements 7 and 9), with an intercooler (8) and an aftercooler (10). The expansion is undertaken in two stages in a high-pressure and low-pressure turbine, with a combustion chamber for each stage.

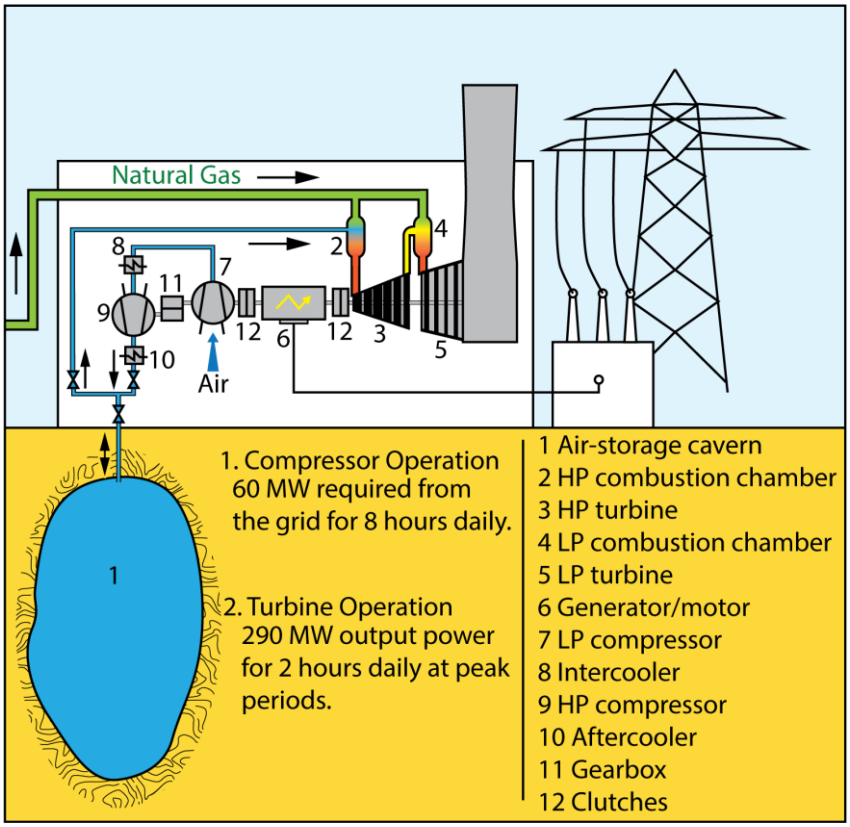

Figure 4-7: Huntorf plant schematic. Data from (Hoffeins, 1994)

The Huntorf plant parameters are given in the Table 4-4. A synthetic data set matching the charging and production pressures at the downhole was created manually in excel and passed on to the Python program.

Table 4-4: Input data used calibrate the Python Plant Model using the Huntorf plant input parameters. (Continues onto next page)

Parameter	Value	Units	Reference
Low-pressure compressor isentropic efficiency	0.82	dimensionless	(Liu, Li, *et al.*, 2014)
High-pressure compressor isentropic efficiency	0.81	dimensionless	
Turbine Isentropic Efficiency	0.85	dimensionless	

Dry Air Gas Constant	0.287	kJ/(kg.K)	(Lemmon *et al.*, 2000; Cohen and Taylor, 2016)
Compressor and Turbine Stages	2	n.a	(Crotogino, Mohmeyer and Scharf, 2001)
Polytropic Exponent	1.4	dimensionless	(Çengel, 2004)
Production Rate	417	Kg/s	(Crotogino, Mohmeyer and Scharf, 2001; Liu, Li, *et al.*, 2014)
Injection Rate	108	Kg/s	
Production Time	2	Hours	
Injection Time	8	Hours	
Well Internal Radius	0.26	m	(Oldenburg and Pan, 2013a; Pan and Oldenburg, 2014a)
Well Fanning friction coefficient	0.003	n.a	From calibration of (Cullender and Smith, 1956) method using (Oldenburg and Pan, 2013a) pressure profiles
Atmospheric Pressure	1.01325	bar	(Hoffeins, 1994; Liu, Li, *et al.*, 2014)
Atmospheric Temperature	10	°C	
Turbine 1st HP Stage Inlet Conditions	42 / 550 (823)	bar / °C (°K)	
Turbine 2nd LP Stage Inlet Conditions	11 / 825 (1,098)	bar / °C (°K)	
Compressor Outlet Temperature (post-cooling)	50	°C	(Liu, Liu, *et al.*, 2014)
Low-pressure compressor Outlet Pressure	6	bar	(Kaiser and Efzn, 2015)
High-pressure compressor Outlet Pressure	66	bar	(Hoffeins, 1994)
Pressure ratio of high-pressure compressor	2.15	dimensionless	(Liu, Li, *et al.*, 2014)
Pressure ratio of low-pressure compressor	6	dimensionless	(Liu, Li, *et al.*, 2014)
Low-pressure compressor Stages	1	n.a	(Liu, Liu, *et al.*, 2014)
High-Pressure Compressor Stages	3	n.a	(Liu, Liu, *et al.*, 2014)
Natural Gas LHV	50,030.04	kJ/kg	(Liu, Liu, *et al.*, 2014)
Combustor Efficiency (correction for partial combustion)	0.93	Frac.	Calibrated to meet Heat Rate target of 5870 kJ/kWh LHV
Well Length	650	m	(Hoffeins, 1994)

Heat capacities for gases (Cp)	From tables	J/K/mol	(Stephan *et al.*, 2013)

4.2.5.2 Huntorf Plant Model used for Code Calibration

The key changes from the original model can be found as code in the digital supplementary information and are presented and discussed here. The way the work calculation for the compressor and turbine have been completed in this model differs from the original code in that the optimum pressure ratio for the compression and expansion stages given by Eq. 4-7 is not used since data for each compression and expansion stage at Huntorf power plant was available. However, Eq. 4-2 is still used to calculate work input to each compressor stage and the work output from each turbine stage. Like in the plant model, the polytropic efficiency of the turbomachinery devices are also included in the calculation. The assumptions presented previously and implemented in the code to calculate work at each individual stage were retained. In the test model, both the total compression work and the total expansion work are calculated as sums of the individual stages. The heat addition calculations are realised in the same way as in the plant model, by using the pressures and temperatures resulting from the work calculations.

Now that both the plant and wellbore models have been tested against an existing CAES system, for which the results are presented in section 4.4, it was possible to perform a sensitivity analysis on it to identify parameters important in terms of power output and efficiency.

4.3 Sensitivity Analysis of Plant and Grid Parameters

Similarly to the design of the sensitivity analysis for the reservoir model (section 3.3.2), the turbine, compressor, and heat storage technologies used in CAES plants are varied and likely to evolve significantly in the next 10 years (Xing and Jihong, 2013). In order to compare PM-CAES with existing conventional CAES plants however, the conventional diabatic system, presented in section 2.1, was chosen in this study. This section will present the ranges for the plant parameters used in the sensitivity analysis.

A literature search was performed in order to estimate the value of the parameters used in the plant model. These parameters include:

1. Gas Turbine Isentropic Efficiency (%)
2. Compressor Isentropic Efficiency (%)
3. Motor / Generator Isentropic Efficiency (%)
4. Expansion Stages
5. Compression Stages

6. Natural Gas LHV
7. Well Fanning friction coefficient
8. Combustor Efficiency.
9. Fuel Conversion Efficiency: represents the amount of energy from the fuel converted to electricity in a conventional CAES plant.

Note: The literature search was performed on isentropic efficiencies as they are readily available in the literature, however due to their sensitivity to the pressure ratio they were converted to polytropic efficiencies. More details can be found in section 2.3.6.

Understanding what ranges might be expected is essential since it enables constraining the sensitivity analysis to likely parameter combinations. In addition, using likely plant parameter ranges enables a comparison between the importance of store geology on the plant power output and roundtrip efficiency compared to that of plant characteristics. Weighing the impact of a parameter on the system and comparing its effect to other tested parameters can only be achieved in a meaningful way if the value range is carefully selected to be representative of true components. Ranges for each plant and wellbore model parameter of interest was compiled in Table 4-5.

Table 4-5: Plant parameter values and/or ranges gathered from the CAES literature. (Continues onto next page)

Parameter	Value/Range	Source
Gas Turbine Isentropic Efficiency (%)	92.5	(Helsingen, 2015)
	0.80 +/-0.1	(Kaiser and Efzn, 2015)
	0.7 to 0.88	
	0.90	(Kreid, 1976)
		(Lund and Salgi, 2009)
	0.87	(Karellas and Tzouganatos, 2014)
	0.85	(Kim *et al.*, 2012)
	0.82	(Maton, Zhao and Brouwer, 2013)
Small turbines	0.70	(Çengel, 2004)
Large turbines	0.90	
Compressor Isentropic Efficiency (%)	87.5	(Helsingen, 2015)
	0.80 +/-0.1	(Kaiser and Efzn, 2015)
	0.7 to 0.88	
	0.90	(Kreid, 1976)
	0.85	(Karellas and Tzouganatos, 2014)
		(Kim *et al.*, 2012)
	0.75	(Maton, Zhao and Brouwer, 2013)
	0.80	(Lund and Salgi, 2009)

	0.80 to 0.90	(Çengel, 2004)
1. Axial Compressor	0.82	(Liu, Liu, *et al.*, 2014)
2. Centrifugal Compressor	0.80	
Motor / Generator	0.95	(Kreid, 1976)
		(Kim *et al.*, 2012)
Turbine Stages	2	(Crotogino, Mohmeyer and Scharf, 2001)
		(Safaei and Aziz, 2014)
		(Liu, Liu, *et al.*, 2014)
Compressor Stages	3	(Giramonti *et al.*, 1978)
		(Safaei and Aziz, 2014)
	1 to 6	(Grazzini and Milazzo, 2012)
	2	(Crotogino, Mohmeyer and Scharf, 2001)
	4	(Liu, Liu, *et al.*, 2014)
Natural Gas LHV	50030.04 kJ/kg	(Liu, Liu, *et al.*, 2014)
Well Fanning friction coefficient	0.003 – 0.004	(Smith, 1950)
Combustor Efficiency (including heat recuperator effect, if any)	80 to 100%	(Schlein, 1985)
Grid Efficiency (%)	33 to 47.6	(Succar and Williams, 2008)

Based on the literature review and the plant and wellbore model calibrations, the final parameter ranges and values selected for the sensitivity analysis are displayed in Table 4-6.

Table 4-6: Parameters used for the sensitivity analysis of the PM-CAES power plant.

Parameter	Range/Value
Gas Turbine Isentropic Efficiency (%)	70 - 92.5
Compressor Isentropic Efficiency (%)	70 - 90
Motor / Generator Isentropic Efficiency (%)	0.95
Expansion Stages	2
Compression Stages	Calculated to ensure a compression ratio as close as, and limited to, 3.
Natural Gas Low Heating Value	50 MJ/kg
Well Fanning friction coefficient	0.003
Combustor efficiency (%)	92.98
Fuel Conversion Efficiency (%)	47.6

4.4 Huntorf Test Model Results

The Huntorf test model described in section 4.2.5, made possible the verification that the equations presented in this chapter to model the compressor work input, the turbine work output and the combustion of natural gas, provided the expected results when combined. Table 4-7 shows the results of the simulation compared to the Huntorf published data discussed thereafter. The lack of calculation details on the widely reported value of 42% loosely related to either the roundtrip, cycle, or overall process efficiency made this value meaningless to perform any comparison (Xing and Jihong, 2013; Kaiser and Efzn, 2015). Indeed, as discussed in section 2.1.2.3 there are many ways to calculate a roundtrip efficiency for a Diabatic-CAES plant (Succar and Williams, 2008). Fortunately, work by (Liu, Li, *et al.*, 2014; Liu, Liu, *et al.*, 2014) provides the methodology used to calculate the efficiencies of a CAES system and applies it to the Huntorf plant.

Table 4-7: Efficiency of system simulation results compared to Huntorf's published data and the overall efficiency proposed by (Liu, Liu, *et al.*, 2014)**.**

Parameter	Huntorf Published Data	Simulation Results	Difference between published and modelled data (%)
Compressor Power (MW)	57.90	55.59	4.0
Turbine Power (MW)	295.55	295.01	-0.2
Heat Rate (kJ/kWh LHV)	5870	5869.7	0.0
Natural Gas Mass Flow Rate (kg/s)	11 (Boveri, 1986)/ 9.53 (Liu, Liu, *et al.*, 2014)	10.25	-7.0 / 7.0
Overall Efficiency η_{ee} (%)	41.73 (Liu, Liu, *et al.*, 2014)	40.4	-4.2
Roundtrip Efficiency η_{RT} (%)	60.04 (Liu, Liu, *et al.*, 2014)	58.9	-1.9
Electricity Ratio (Wc/Wt)	0.78	0.75	-3.8

The test model yielded a roundtrip efficiency of 58.9% using the Eq. 4-50 proposed by (Succar and Williams, 2008) and presented as the "efficiency of electricity storage" by W. Liu, Li, *et al.* (2014):

$$\eta_{RT} = \frac{W_{out} - Q_{in} \times \eta_{NG}}{W_{in}} \quad 4\text{-}50$$

Where, η_{RT} is the roundtrip efficiency, W_{out} the electrical work produced, Q_{in} the fuel energy added, η_{NG} the efficiency of the energy system used to convert thermal energy to electricity equivalent, W_{in} the electrical work from the compressor.

A value of 40.4% was calculated using the "overall efficiency" equation from W. Liu, Liu, *et al.* (2014):

$$\eta_{ee} = \frac{W_{out}}{W_{in} + Q_{in}} \quad 4\text{-}51$$

Liu, *et al.* (2014) noted that for Huntorf the "overall efficiency", η_{ee} , is 41% and the roundtrip efficiency is approximately 60.4%. These values closely match the 40.4 and 58.9% outputs from the test model respectively. This match gives confidence that the roundtrip efficiency of the Huntorf plant can be matched with a good accuracy of within 2%.

The Charging Electricity Ratio, introduced in section 2.1.2.2 as the ratio of generator electricity output to compressor electricity input, was of 1.3 from the test model simulation, which is at the lower end of the 1.2 to 1.8 values proposed by (Succar and Williams, 2008). It is also within 4% of the 1.28 value calculated by (Liu, Li, *et al.*, 2014).

The Heat Rate (HR) was estimated as 5869 kJ/kWh LHV, practically the same as the 5870 kJ/kWh LHV from plant data found in the literature for Huntorf (Succar and Williams, 2008; Xing and Jihong, 2013). This value was reached after calibrating the combustor efficiency to 92.98%, which is within the 80-100% range expected for combustors in the 1980s (Schlein, 1985). This is expected as the combustion and heat transfer from that combustion are not 100% efficient. In addition, in the combustion model the air is approximated to a mixture of 21% of oxygen and 79% of nitrogen, and the natural gas is assumed to be 100% methane.

The results reported in this section have shown that the plant model used to perform a sensitivity analysis of an inter-seasonal PM-CAES system suitably represents current adiabatic CAES plants for the purpose of performing a national scale storage resource assessment.

4.5 Plant Sensitivity Analysis Results

The results from the plant sensitivity analysis are extensive and provided in a spreadsheet in the digital supplementary information. These results have been summarised in graphical form in this section.

4.5.1 Power Outputs

A power law correlation exists between the reservoir depth and the well power output (Figure 4-8). Similarly a linear relationship exists between the turbine polytropic efficiency and the well power output (Figure 4-9). Plotting the data as a histogram in Figure 4-10, indicates that there is a 10% chance that a well will produce at least 9.5-10 MW, a 50% chance that it will produce at least 8-8.5 MW, and a 90% chance that it will produce at least 6.5-7 MW.

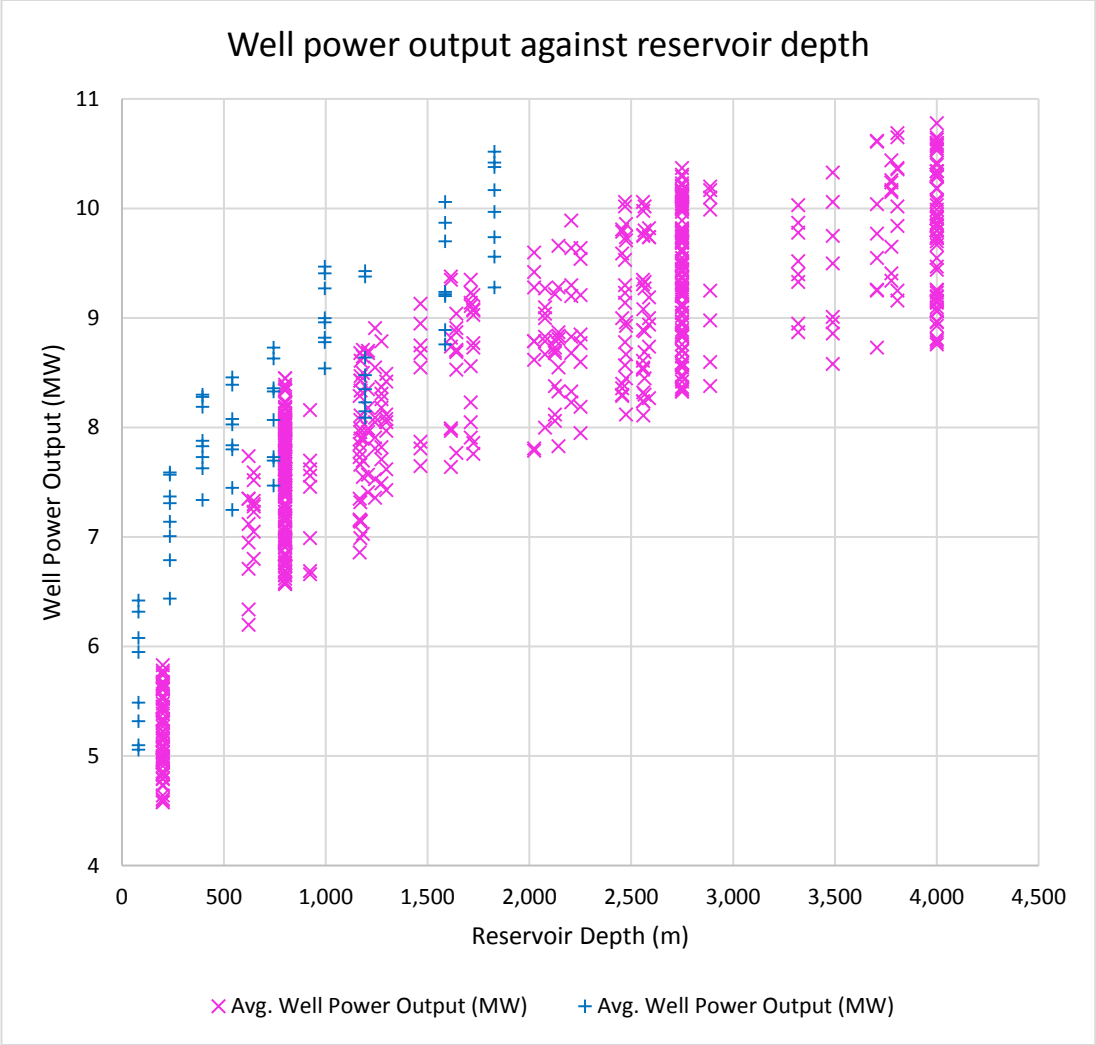

Figure 4-8: Two power law trends can be identified in the relationship between reservoir depth and well power output. The "+" (blue) trend is associated with reservoirs being operated close to fracture pressure. The "×" (magenta) trend is associated with reservoirs operated close to hydrostatic pressure. The blue trend power outputs are, on average, greater than those of the magenta trend at equivalent depth.

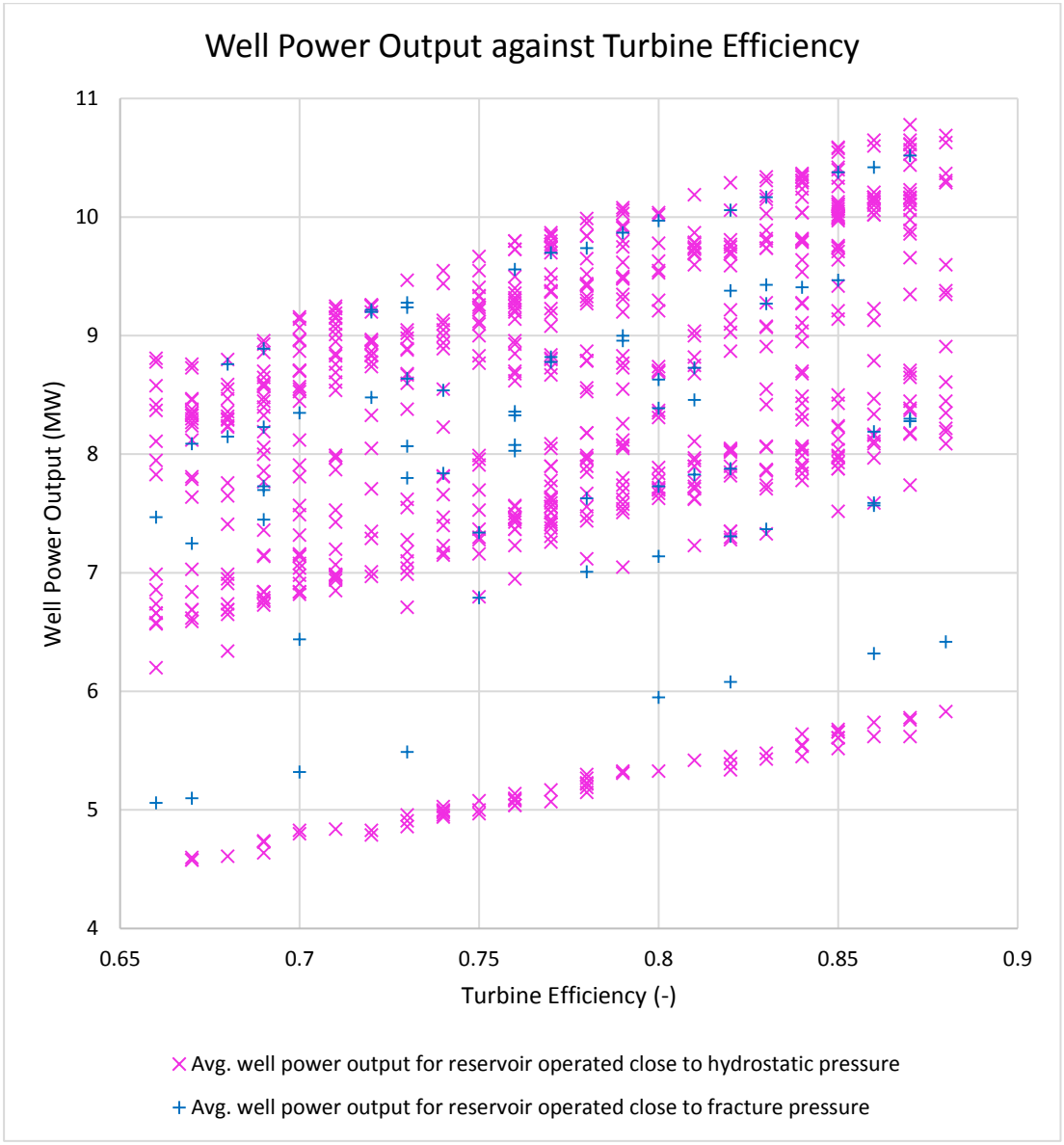

Figure 4-9: Power output per well vs turbine polytropic efficiency. A linear correlation exists between turbine efficiency and the well power output. This correlation exists both when reservoirs are operated close to fracture pressure and close to hydrostatic pressure.

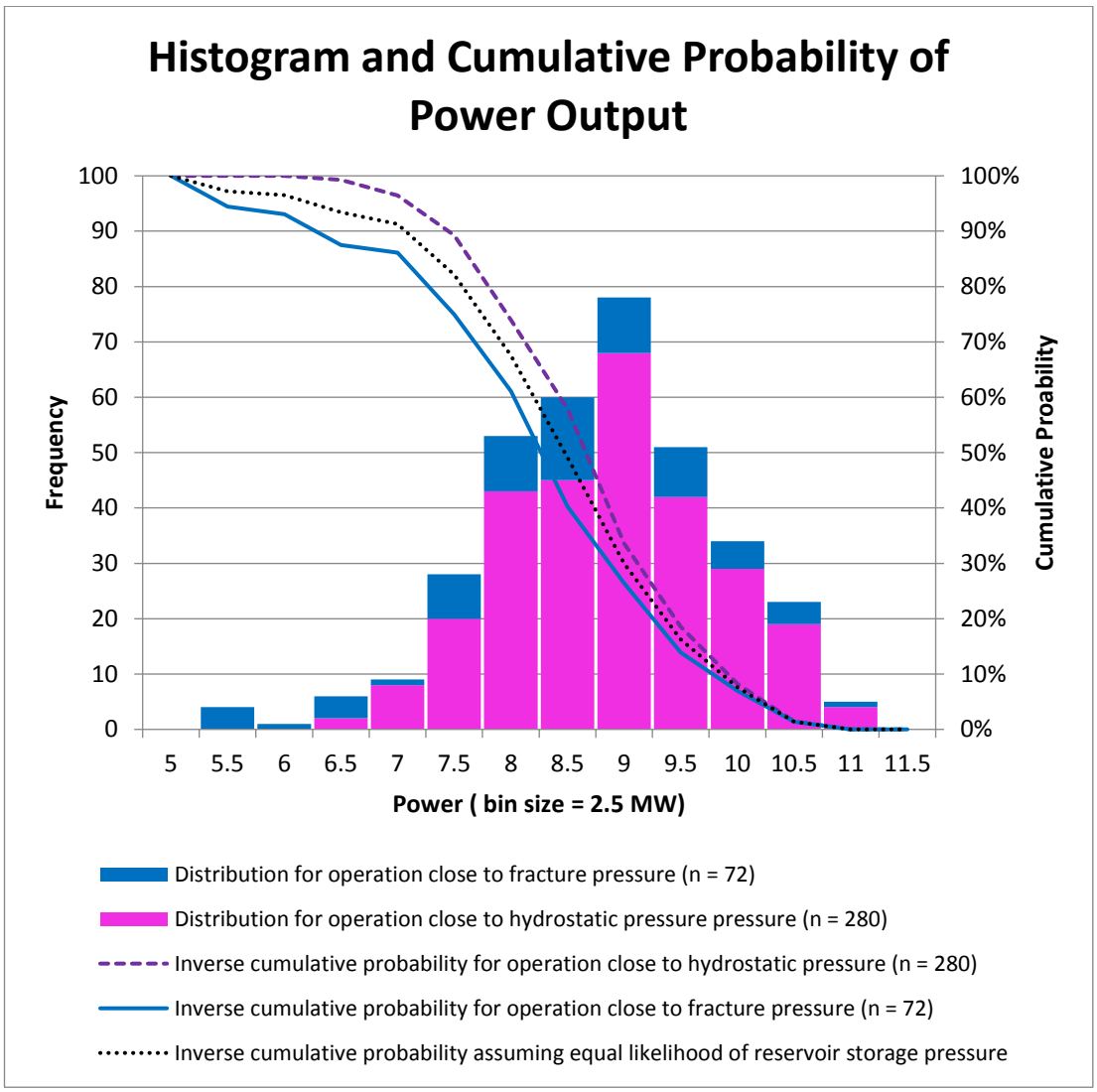

Figure 4-10: The power output data from the simulations based on stochastic parameter selection is reported. The magenta data corresponds to the simulations in which the reservoirs are operated close to hydrostatic pressure and the blue data to reservoirs operated close to fracture pressure. The black dotted line indicates the inverse cumulative probability of a well producing at least the corresponding amount of power on the x-axis. To remove the bias of having more data for hydrostatic storage pressures, the black dotted line assumes both a storage pressure close to fracture pressure and one close to hydrostatic are equally likely. There is a 50% chance that a well will produce at least 8-8.5 MW, and a 90% chance that it will produce at least 6.5-7 MW.

4.5.2 Roundtrip Efficiency

No apparent correlation can be established between the reservoir depth and the average roundtrip efficiency, due the variability in the data which suggests that other parameters of the models have a greater influence (Figure 4-11). The data obtained from hydrostatic simulations could possibly indicate a power law correlation since for depths of 200 m no roundtrip efficiency greater than 60% has been recorded and for depth greater than about 600 m none lower than 45% have been recorded. Subsequent investigation was carried out in Chapter 5 to evaluate this possibility.

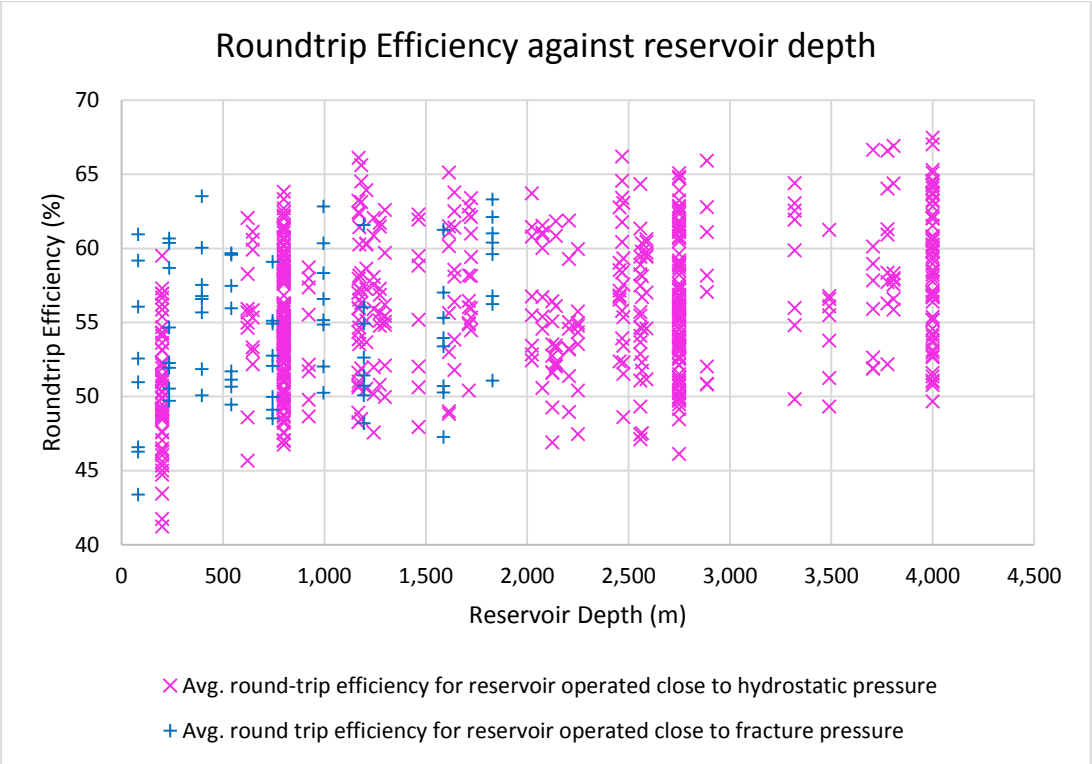

Figure 4-11: Average roundtrip efficiency against reservoir depth. For reservoir operated close to hydrostatic pressure a power law correlation can be inferred between the reservoir depth and the roundtrip efficiency of the system. The influence of depths greater than 1000 m on roundtrip efficiency is negligible.

A linear correlation between the average roundtrip efficiency and the turbine and compressor isentropic efficiencies can be observed (Figure 4-12).

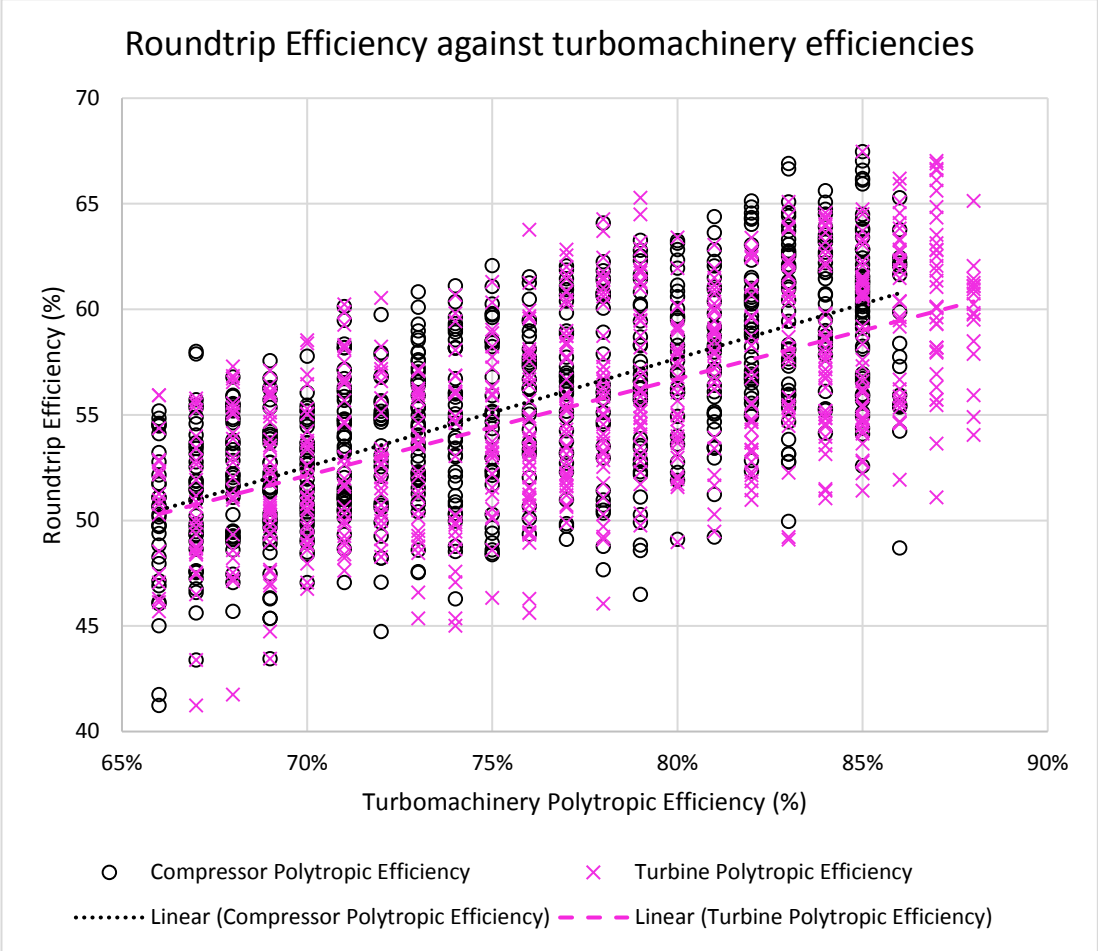

Figure 4-12: Average roundtrip efficiency against the polytropic efficiency of the compressor and the turbine. The data reveals a linear trend between the turbomachinery efficiency and the roundtrip efficiency of the PM-CAES system. Which of the compressor or turbine polytropic efficiency is more closely correlated to the roundtrip efficiency is difficult to determine from the data.

Plotting the roundtrip efficiency in a histogram as well as cumulative probability curves in Figure 4-13, reveals that there is a approximately 90% chance that the roundtrip efficiency will be greater than 50%. Similarly, there is a 10 and 50% chance that it will be greater than 65 and 55% respectively. Furthermore, PM-CAES storage sites operated with a storage pressure close to fracture pressure appear to be less efficient than sites operated close to hydrostatic pressure.

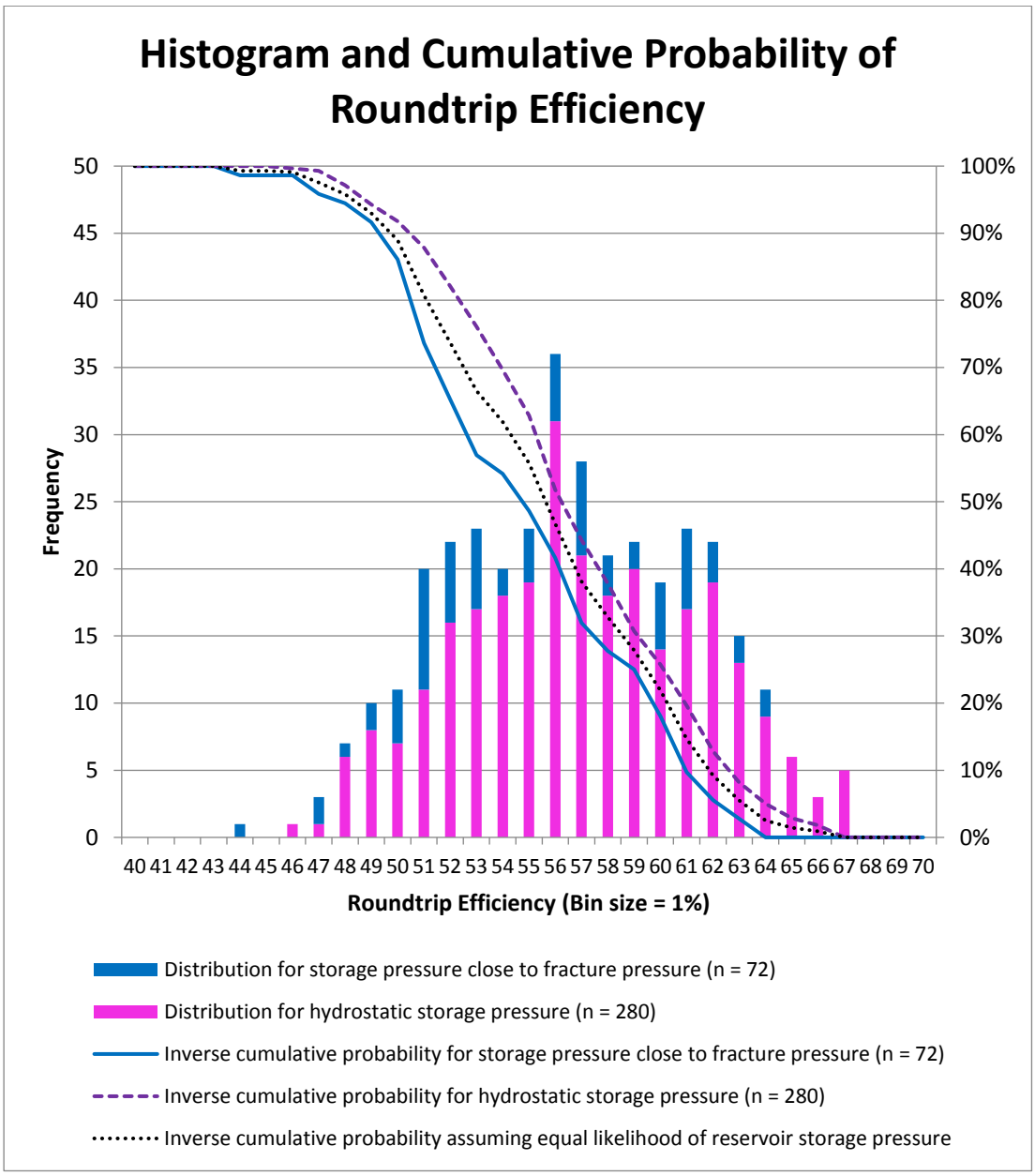

Figure 4-13: The roundtrip efficiency of simulations with reservoirs operated at a storage pressure close to fracture pressure and those operated close to hydrostatic pressure both show the same trend. The data from the stochastic scenarios ranges from 44 to 67%. The inverse cumulative probability curve of the data from simulations with reservoir storage pressures close to hydrostatic is to the right of the curve from the other dataset. This implies higher efficiencies are more likely when operating storage closer to hydrostatic conditions.

4.5.3 Charging Electricity Ratio

The charging electricity ratio has been introduced in section 2.1.2.2. In itself it is a biased measure as it does not account for the natural gas added to the system. It is however useful to be able to determine the amount of energy consumed by the compressor using the turbine power output. The results in Figure 4-14 show that more than half the scenarios yielded a charging electricity ratio inferior to one. Scenarios where the charging electricity ratio is in

excess of one indicate that the amount of added energy from the natural gas significantly contributes to the power outputs

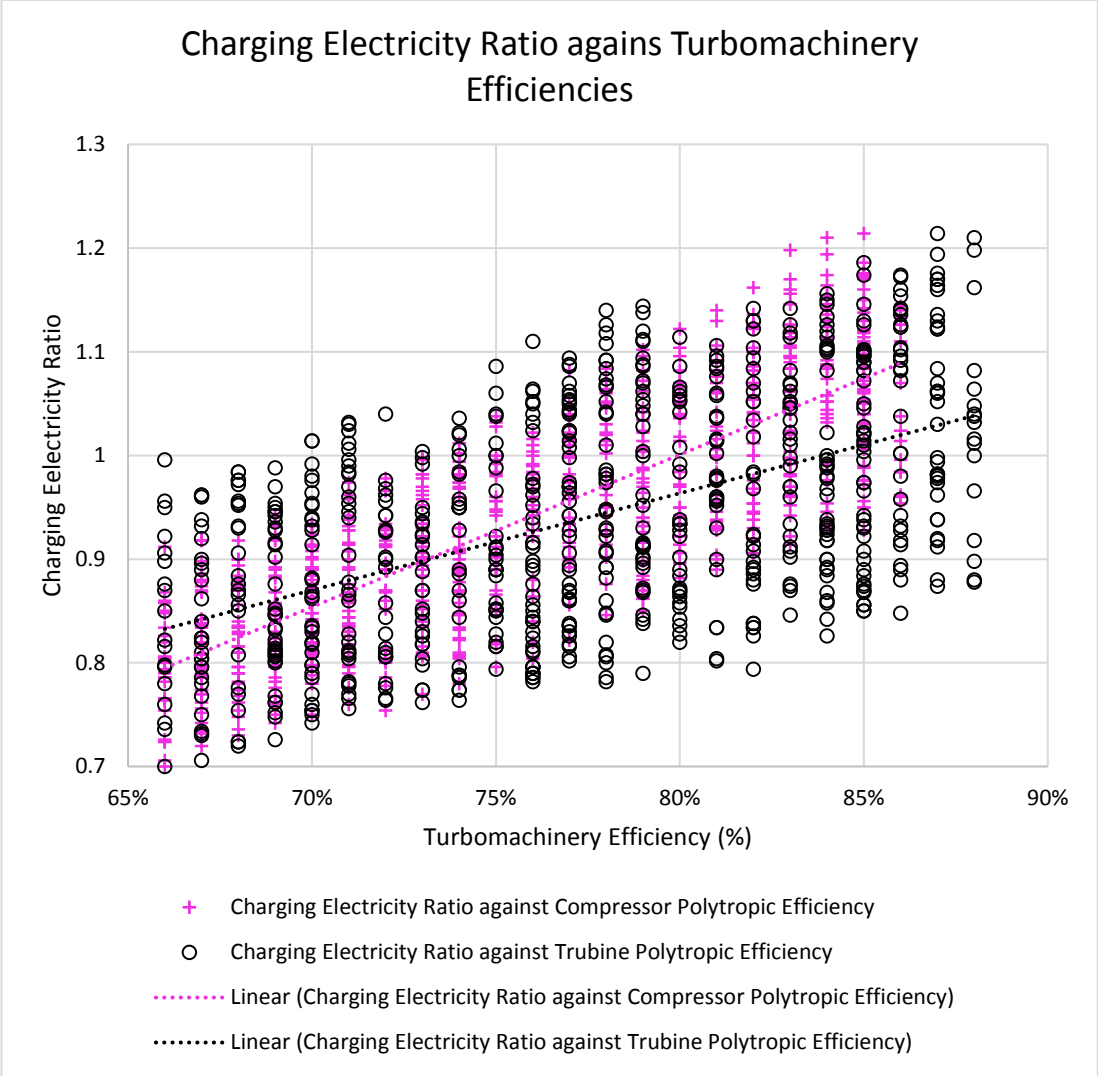

Figure 4-14: The data plotted encompasses results from simulations done with reservoir storage pressures close to hydrostatic and close to fracture pressure. The spread in the data show is lower for the compressor than for the turbine. This shows a stronger correlation between the compressor polytropic efficiency and the charging electricity ratio, than that between the turbine polytropic efficiency and the charging electricity ratio. Plotting a linear trend line through each dataset indicates that the dependence of the charging electricity ratio on the compressor efficiency is greater than its dependence on the turbine efficiency.

4.6 Discussion and Limitations

4.6.1 Limited Impact of Reservoir Depth on Cycle Roundtrip Efficiency

The results in Figure 4-11, have shown that for reservoir depths greater than 1,000 m the correlation between reservoir depth and roundtrip efficiency becomes almost linear, with a slope of zero. This can be explained by considering a few relationships of the PM-CAES system:

1) For PM-CAES the storage pressure is proportional to the store depth, when the storage pressure is assumed to be equal to either the hydrostatic pressure in the reservoir, or near its fracture pressure.
2) As presented in the turbomachinery modelling section 4.2.1, the work output of a turbine obeys a logarithmic relationship to the pressure ratio across the turbine. Because the outlet pressure is fixed to atmospheric pressure, the pressure ratio across the turbine is controlled by its inlet pressure (i.e. the depth of the store).

Therefore, the impact of having a much higher injection pressure than production pressure on the roundtrip efficiency will be stronger for changes in depth at shallow depth, compared to those at deeper depths.

4.6.2 Impact of Turbomachinery Polytropic Efficiencies on Power Output and Roundtrip Efficiency

A linear relationship, shown in Figure 4-9, exists between the turbine polytropic efficiency and the power output achievable from a PM-CAES well. The compressor has no impact on the produced power output of the turbine. However, the slopes of the linear best fit lines from Figure 4-12 indicate that, the influence of the compressor polytropic efficiency on the roundtrip efficiency is greater than that from the polytropic turbine efficiency. Using the current results it is difficult to draw any more conclusions with respect to the effects of the turbomachinery efficiencies on the roundtrip efficiency of the PM-CAES system and its power output.

4.6.3 PM-CAES Power Outputs Compared to Wind Turbine Power Outputs

It is expected that if PM-CAES is developed offshore it would be to benefit offshore windfarms. A comparison of the power outputs of both a PM-CAES well and a wind turbine is therefore interesting. This study finds that the expected power output from a PM-CAES well is between 4 and 12 MW. It is important to remind the reader that the well flow rate has been fixed to 15 kg/s which corresponds to a high production rate in the natural gas production and storage industry. It is unlikely that wells will be physically able to produce much faster than this value. Wells with smaller delivery rates would also be likely to be less economically viable to drill and operate for PM-CAES. Therefore the output of a PM-CAES well is equivalent to that of a generic offshore wind turbine which range from 4 to 8 MW (www.siemens.com), and slightly higher than the output from onshore wind turbines ranging from 2 to 4 MW. It is doubtful that a layout associating each well directly to a wind turbine would be viable as it would require many compressors and turbines. A layout were the compression and expansion is centralised (on an offshore platform for example) is much more likely. This aspect should however be investigated in further research as it is site specific.

4.6.4 PM-Roundtrip Efficiency vs CAES Systems in General

The match with published data is accurate. Literature values range from 41 to 75% and modelled ranges from 41 to 68% (including the deterministic simulations). If a useful probabilistic range from 90 to 10% is considered then roundtrip efficiencies range from at least 49 to 62% for PM-CAES. At this point it is important to remind the reader that the assumptions underlying this work are conservative and result in the maximum pressure difference between the storage pressure and the minimum production pressure at the end of the discharge period (i.e. highest amounts of energy expanded on compression and lowest amounts recovered on expansion). The efficiencies reported in this work reflect that. In Figure 4-15 the inverse cumulative probability curve from this research is to the left of that derived from literature data. This reflects that, in this study, higher efficiencies are less likely to be achieved, than for CAES technologies in general (mostly technologies with thermal storage, i.e. Adiabatic-CAES). An efficiency value in this study between 40 to 75% for PM-CAES is 15% less likely than the same efficiency value for a generic CAES technology. This value of 15% accounts for the greater efficiency difference occurring for the most likely efficiencies by multiplying each difference between the two curves in Figure 4-15 by their mean.

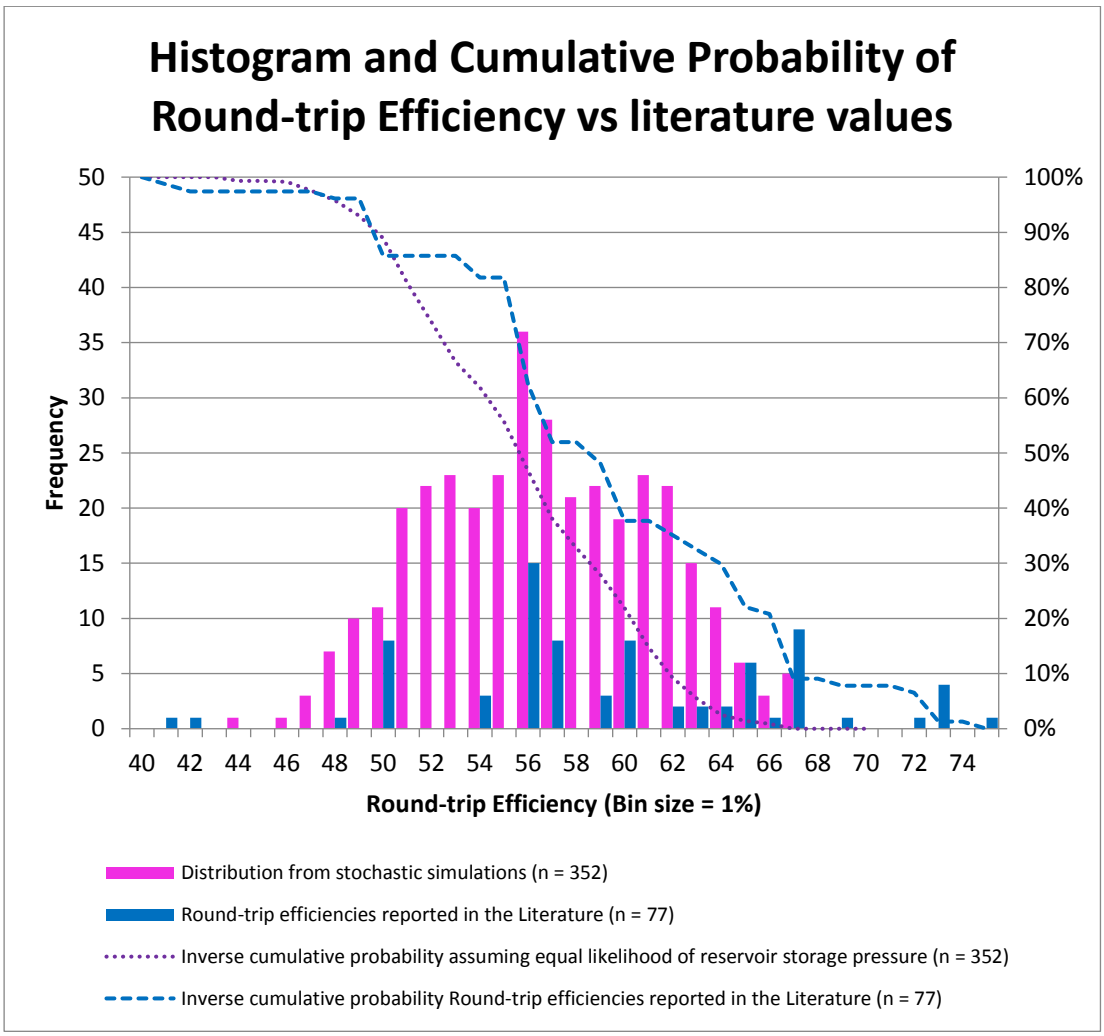

Figure 4-15: The magenta frequency data in this figure is the sum of the data presented in Figure 4-13. The blue frequency data is the distribution in CAES efficiencies gathered from the literature. It encompasses multiple CAES technologies. The blue and magenta curves represent the likelihood of reaching a given roundtrip efficiency value based on the literature values and those from this study, respectively. The difference between the two curves indicates that CAES efficiencies in general are greater than those for PM-CAES by about 15%.

The match between published roundtrip efficiencies and the modelled ones provides confidence that the parameter ranges selected are corresponding to a real system. As discussed in section 2.1.2, the complexity of calculating an efficiency for a CAES system is significant and can take many forms. As it is not always possible to find the procedure used to obtain the efficiencies reported in the literature it is important to realise that some of the spread in the data gathered in the literature is caused by different methods being used to calculate the efficiency.

4.6.5 Qualitative Understanding of PM-CAES System

The results of this study are of limited use to make predictive quantitative estimates of the power output and roundtrip efficiency. In order to achieve this the results need to be further

processed in order to establish quantifiable relationships between the parameters and the outputs. Then key parameters affecting the power output and roundtrip efficiency can be determined quantitatively. One of the aims of this work is to establish which of the geological or the plant parameters affect the power output the most. In addition for quantitative storage capacity estimates to be achieved for the UK it is necessary to be able to perform predictive modelling. This is why it was deemed necessary to find simple mathematical models capable of explaining those results as such models could then be statistically tested and analysed to determine how each parameter affects the variance of the results. This procedure is detailed in Chapter 5.

4.7 Conclusions

This chapter presented a well and CAES plant model which was validated using available data from the Huntorf CAES plant. It was demonstrated that the model predicted within a 2% accuracy the compressor consumption, turbine production, and round-trip efficiency of the Huntorf CAES plant. This provides confidence that the assumptions underlying the model design and the use of polytropic efficiencies for the compressor and turbine, predicted the performance of the system with enough accuracy to use the model for a nationwide scoping of inter-seasonal PM-CAES.

The conclusions which can be drawn from the sensitivity analysis conducted on the Plant model described in this chapter provide qualitative insight into the relationships between the model parameters and the outputs. As expected an increase in turbine efficiency leads to an increase in power output. The compressor efficiency has no impact on the output of the system, as the compressor is not part of the "producer part" of the diabatic CAES system (see section 2.1.1.1). An increase in compressor efficiency however has a greater positive impact on the round-trip efficiency of the system than an equivalent increase in turbine efficiency. This can be explained by the fact that the compression stages are varied in the analysis to maintain a compression pressure ratio close to 3:1, whereas the expansion stages are fixed to two (representative of most conventional CAES designs). Hence, the benefits from more efficient compressor are often felt over more than two stages, whereas those of turbine are not. Similarly the charging electricity ratio is more influenced by the compressor efficiency than by the turbine's one. This is most likely a combination of the effect caused by the difference in stages between compression and expansion (as mentioned above), and the fact that the efficiency of the turbine also affects the conversion of the fuel's thermal energy into electricity, a benefit which is not accounted for by the charging electricity ratio. The results shows that the power output of a PM-CAES well producing at 15 kg/s will be somewhat equivalent to that of a large

offshore wind turbine (i.e. 4-12 MW). Care should be taken when interpreting this result, as well flow rates will eventually be site-specific. The round-trip efficiency of a PM-CAES system, when used for inter-seasonal storage was found to be equivalent to that of a similar system used for daily storage. This observation has not been documented before.

In addition to the relationship between plant parameters and power output, round-trip efficiency, and charging electricity ratio, the results also show that the influence of the store's depth on the round-trip efficiency appears to be limited, whereas it has a more significant impact on the power output. This is to be expected as the depth of the store is correlated to the mean production pressure, which leads to greater production pressure ratios and hence higher power outputs.

These relationship will be used for two main purposes in the following Chapter; first to inform which plant parameters should be included in the power output, round-trip efficiency and charging electricity ratio predictive models; second, to allow conclusions to be drawn from a study of the variance in the relationships between input parameters to the predictive models and the output.

Chapter 5 Predictive Models Development

The purpose of this chapter is to develop predictive models for inter-seasonal PM-CAES using the results from the modelling of the reservoir, wellbore, and plant. This will be useful to estimate the PM-CAES potential of any geological formation of interest within the parameter space of the models (summary in Table 5-1). The predictive models developed allow the power output per well, the roundtrip efficiency of the system, and its charging electricity ratio (see 2.1.2.2), to be determined. This chapter will introduce the algebraic predictive models and how they were developed using multiple linear regressions. The next chapter will apply those mathematical models to the database of offshore UK saline aquifer formations.

Due to the mathematical and statistical concepts discussed in this chapter the following terminology will be used: Parameters, such as reservoir depth and thickness, will be called *predictors*, the parameter space (i.e. ranges over which the predictors vary) will be referred to as the *domain*. The output of the models (e.g. power, roundtrip efficiency, and charging electricity ratio) will be referred to as *dependent variables*.

Table 5-1: Domain over which the predictive models are valid.

Parameter	*Min*	*Max*
Reservoir Thickness (m)	*50*	*350*
Reservoir Shallowest Depth (m)	*260*	*4,000*
Reservoir Porosity (%)	*15*	*30*
Reservoir Permeability (mD)	*100*	*1,330*

The discussions in Chapters 3 and 4 provide a good understanding of the reservoir, well and plant model limitations and the processes modelled, this understanding can be used to determine which predictors should be used within the predictive models as well as the nature of the relationship between them. Once the predictive models have been developed, further statistical analysis is performed to quantify the effects of each individual predictor, as well as their interactions, on the dependent variable. This informs for which predictor constraining uncertainty is crucial.

5.1 Multiple Linear Regression

The tool used to determine the mathematical relationship between the predictors, and the power output, efficiency, and charging electricity ratio, is the multiple linear regression of the form:

$$y = c_1 x + c_2 z + \cdots + c_n \quad \text{5-1}$$

Where *y* is the dependent variable of interest (i.e. the power output, the roundtrip efficiency or the charging electricity ratio), *x* and *z* the predictors (i.e. input parameters, such as reservoir depth or turbine efficiency) and c the coefficients associated with these variables. This form of regression assumes a linear relationship between the predictors and the dependent variable. If this is not the case, the predictors (say *x*) from Eq. 5-1 need to be subjected to another function (*f*) so that the output from that function (*f(x)*) is linearly related to *y*. So doing allows *f(x)* to be used as the predictor since it is follows the assumption of linearity. For example, if the relationship between *x* and *y* seems to be logarithmic then Eq. 5-1 becomes:

$$y = c_1 \log_{10}(x) + c_2 z + \cdots + c_n \quad \text{5-2}$$

As with any approximation, the results of the predictive models will be associated with some error compared to the result that would have been obtained using the reservoir, plant and wellbore models described Chapters 3 and 4. This error will be assessed in order to quantify the uncertainty in the predictive model outputs. An analysis of variance (ANOVA) was used to ensure the regression was valid and to understand the importance and validity of predictors used.

5.2 Analysis of Variance & Evaluation Metrics

An analysis of variance is a data analysis method developed by Sir Ronald Fisher in the 1920s (Armstrong, Slade and Eperjesi, 2000). The method was developed to provide a single statistical test comparing the statement that the groups studied have 'no difference' or 'no association' against an alternative hypothesis proposing association (Armstrong, Slade and Eperjesi, 2000; Everitt and Skrondal, 2013). The statement of 'no difference' is usually referred to as the Null hypothesis. In ANOVA, disproving the Null hypothesis is achieved by testing the difference in variance between the groups and the variance within the groups (Armstrong, Slade and Eperjesi, 2000). This difference is expressed by a variance ratio, named 'F'. The procedure to calculate that ratio is hence known as the 'F-test' (Snedecor and Cochran, 1980). The variance ratio 'F' indicates how many times greater the variance between the groups is compared to the variance of the groups. This value is then compared to tables which indicate the probability of observing the value of 'F' by chance if the Null hypothesis is true. Although debatable, it is generally acknowledged that if this probability is less than 5% then the Null hypothesis which states that there is 'no associations' between the groups can be safely rejected. Once this has been established, other tests are applied to examine the difference between the groups and explore their relationship. A typical multiple regression summary from Excel®, which includes an ANOVA, is provided in Table 5-2.

.

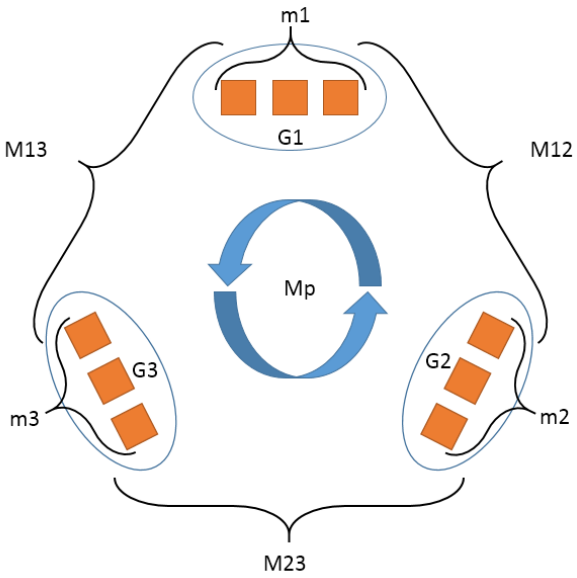

Figure 5-1: Illustration of the ANOVA principle. An experiment is performed on three groups denoted by the letter G. Each square is a result from the experiment. The means of the results from each group are denoted by m. The mean of the means, m, from each group are denoted by the letter M. "If the difference between the means of the three groups (m1,m2,m3) is insignificant, then the 9 results are distributed around a common population mean, Mp. If this is the case then the intra and inter group variance should be estimates of the same quantity" hence validating the Null hypothesis (Armstrong, Slade and Eperjesi, 2000)**.**

Table 5-2: Summary output example of a multiple linear regression provided by Excel®. The key terms of interest, namely the multiple correlation coefficient R, the squared multiple correlation coefficient R^2, adjusted R square, the residual and total sum of squares (SS), the significance of the regression, F-test, t-test and P-values, are described in the main text. The formulae of each of them is indicated in the table. n_i is the number of predictors in the regression. In Excel® the coefficients are determined using the Ordinary least squares estimator. The "Lower 95%" and "Upper 95%" indicate the range in which there is 95% chance that the true coefficient will lie, with 2.5% chance that it is below the lower value and 2.5% that it is above the upper value.

Regression Statistics	
Multiple R	coefficient of multiple correlation = Pearson Coefficient
R Square	Regression SS / Total SS
Adjusted R Square	1 - (Total df / Residual df)(Residual SS / Total SS)
Standard Error	$(\text{Residual MS})^{0.5}$
Observations	N

ANOVA

	df	*SS*	*MS*	*F*	*Significance F*
Regression	n_i	Total SS - Residual SS	Regression SS / Regression df	Regression MS / Residual MS	See text.
Residual	N – 1 - n_i	$\sum_i^N (y_i - y_{i,p})^2$	Residual SS / Residual df		
Total	n-1	(n-1)*(std. dev. of y)^2			

	Coefficients	*Standard Error*	*t Stat*	*P-value*	*Lower 95%*	*Upper 95%*
Intercept	-5.1	0.3	Coef. / Std. Err.	0	-5.6	-4.5
X_1	2.7	0.1	"	0	2.5	2.9
X_2	4.2	0.1	"	0	4.1	4.3
X_3	0.0	0.0	"	0.621	0.0	0.0

The multiple correlation coefficient, R, indicates how well the model fits the sample on which the analysis was performed (Jaccard and Turrisi, 2003). It is defined as the Pearson correlation coefficient, a metric which offers a measure of similarity between two sets of data, between the known and predicted dependent variable values (Pearson, 1895).

The squared multiple correlation, R^2, represents the proportion of variance in the dependent variable explained by the linear regression of the predictors (Jaccard and Turrisi, 2003).

The adjusted multiple correlation, adjusted R^2, is used to account for the likelihood that the R^2 value might be due to chance. Indeed, adding predicators or higher order polynomials might increase the R^2 because of overfitting, but the adjusted R^2 will then start to decrease (Allen and Patrick, 1997).

The regression's Sum of Squares, SS, is the variation in the input explained by the regression, whereas the **residual Sum of Squares** is the portion not explained by the regression. The regression's sum of squares, divided by the total sum of squares is equal to the squared multiple correlation coefficient, R^2.

As explained earlier, the significance of the regression is established by means of an F-test. The F value resulting from it can then be compared to probability tables and yields the **regression significance**.

The coefficients are used in the linear equation from the regression. Their significance can be established using a particular case of F-test known as a t-test. The t value is obtained by dividing a regression coefficient by its standard error. The P-value corresponding to the t value is representative of the coefficient's significance. A parameter is significant if its P-value is less than 0.05 (Jaccard and Turrisi, 2003).

5.3 Developing the Predictive Models

This following section describe the predictive models developed to estimate the downhole pressure during the storage cycle, the power output per well, the roundtrip efficiency, and charging electricity ratio of the PM-CAES system.

5.3.1 Reservoir Depth: Geological Predictor of Significance

This section quantifies the contribution of the geological predictors to the pressure output of the well. This first step is performed following the qualitative observations made in Chapter 3 that within the domain of this study, only the reservoir depth has a significant impact on the downhole pressure. To test this hypothesis the opposite assumption is being evaluated: that

reservoir depth, permeability, thickness and porosity all have an impact on the downhole pressure sufficiently pronounced to be explained by a multiple linear regression.

The results from the regression displayed in Table 5-3 shows that the P-values of all predictors but depth were insignificant. Hence, using the shallowest depth as the only predictor yields a reasonable prediction for the minimum reservoir storage pressure reached at the end of production.

Table 5-3: Regression output from Excel® for the downhole pressure at the end of the production period in Pascal for a store operated with a storage pressure which is hydrostatic (i.e. using grey data points from Figure 5-2 d.). It can be seen that the only parameter which has a coefficient with a meaningful P-value lower than 0.05 is the reservoir depth. This implies that over the domain considered in this study, the porosity, thickness and permeability of the reservoir do not have an influence on the downhole pressure which is significant enough to be approximated using a linear relationship.

Regression Statistics	
Multiple R	0.9874
R Square	0.9750
Adjusted R Square	0.9727
Standard Error	855,848.76
Observations	48

ANOVA

	df	*SS*	*MS*	*F*	*Significance F*
Regression	4	$1.23 \cdot 10^{15}$	$3.07 \cdot 10^{14}$	420	0
Residual	43	$3.15 \cdot 10^{13}$	$7.32 \cdot 10^{11}$		
Total	47	$1.26 \cdot 10^{15}$			

	Coefficients	*Standard Error*	*t Stat*	*P-value*	*Lower 95%*	*Upper 95%*
Intercept	571,290	926,876	0.62	0.54	-1,297,934	244,051
Store Depth	5,261	129	40.65	0.00	5,000	5,523
Reservoir Porosity	-10,279	29,721	-0.35	0.73	-70,217	49,658
Reservoir Thickness	-170	1,515	-0.11	0.91	-3,225	2,886
Reservoir Permeability	85	373	0.23	0.82	-668	838

Figure 5-2 shows the linear regression trends for both data obtained from simulations with reservoirs operated with a hydrostatic storage pressure, and those with one close to fracture pressure (i.e. 77% of the lithostatic pressure). For each of the storage pressure operating conditions a linear trend can be fitted to the storage pressure (i.e. when the store is fully charged) and the minimum production pressure (i.e. the downhole pressure after 60 days of production, when only the cushion gas remains in the store).

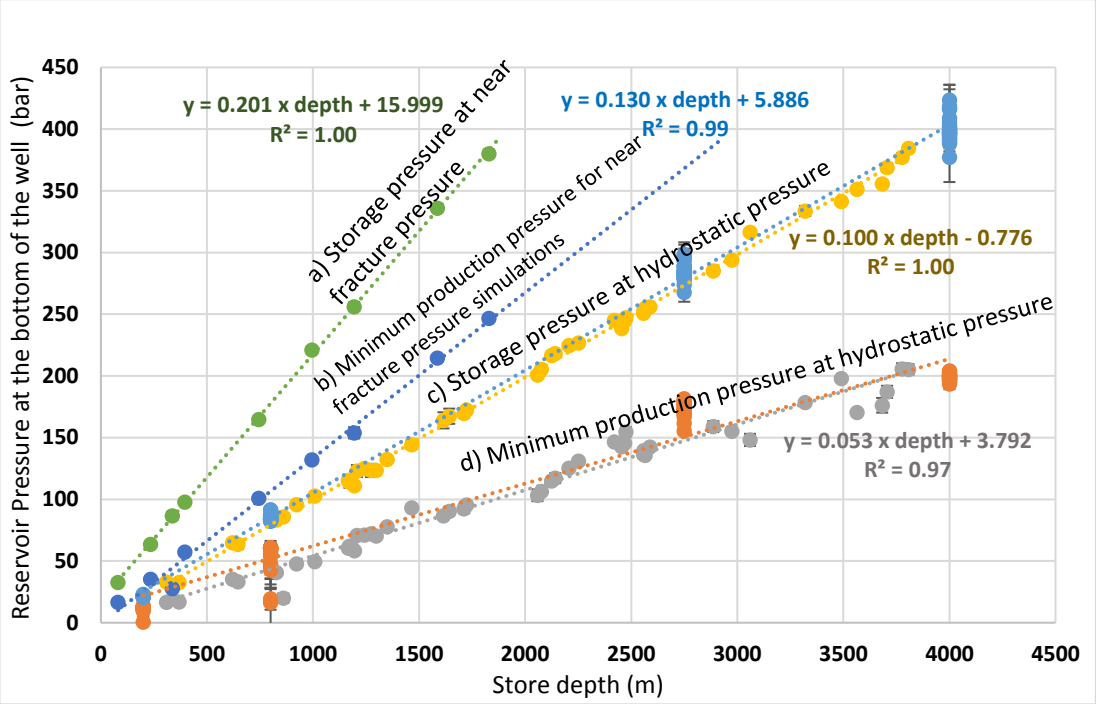

Figure 5-2: Linear regression lines fitted to data from the reservoir model. The green line (a) represents a store operation with a storage pressure close to the fracture pressure. When these stores are depleted after 60 days of air production the minimum pressure is given by the blue line (b). The yellow line (c) represents a store operation with a storage pressure at hydrostatic pressure. When these stores are depleted after 60 days of air production the minimum pressure is given by the grey line (d). To avoid bias caused by the deterministic models done for the hydrostatic case (blue and orange points in (c) and (d) respectively), only the data from the random sampling of the depth distribution was used to determine the best fit line.

Since some of the models represent an operation of the reservoir close to fracture pressure (77% of lithostatic pressure) and other at hydrostatic pressure, it is also possible to linearly interpolate what the pressure, P_α, corresponding to an operation between those two end members might be. This is achieved by using a parameter alpha, α, where $0 < \alpha \leq 1$ and equal to 1 for scenarios operating at hydrostatic pressure, P_h, and 0 for scenarios operating close to fracture pressure, P_{77},.

Consequently, it follows that:

$$P_\alpha = \alpha P_h + (1 - \alpha) P_{77} \qquad 5\text{-}3$$

The variance is well explained by the regressions (see Figure 5-2 all $R^2 \geq 0.97$). The F-test performed on all four of those linear regressions indicates that the regressions are significant and hence that the Null hypothesis that "no relationship exists between depth and downhole pressure" can be rejected. The significance of depth is also high as the P-value of that predicator is much smaller 0.05. The intercept on the other hand is not significant (P-value of > 0.05), yet its impact on the pressure estimate is only significant, relative to the depth term,

when the storage reservoir is outcropping at the surface, an implausible scenario since reservoirs of at least 260 m depth are being considered, hence this term was retained for convenience.

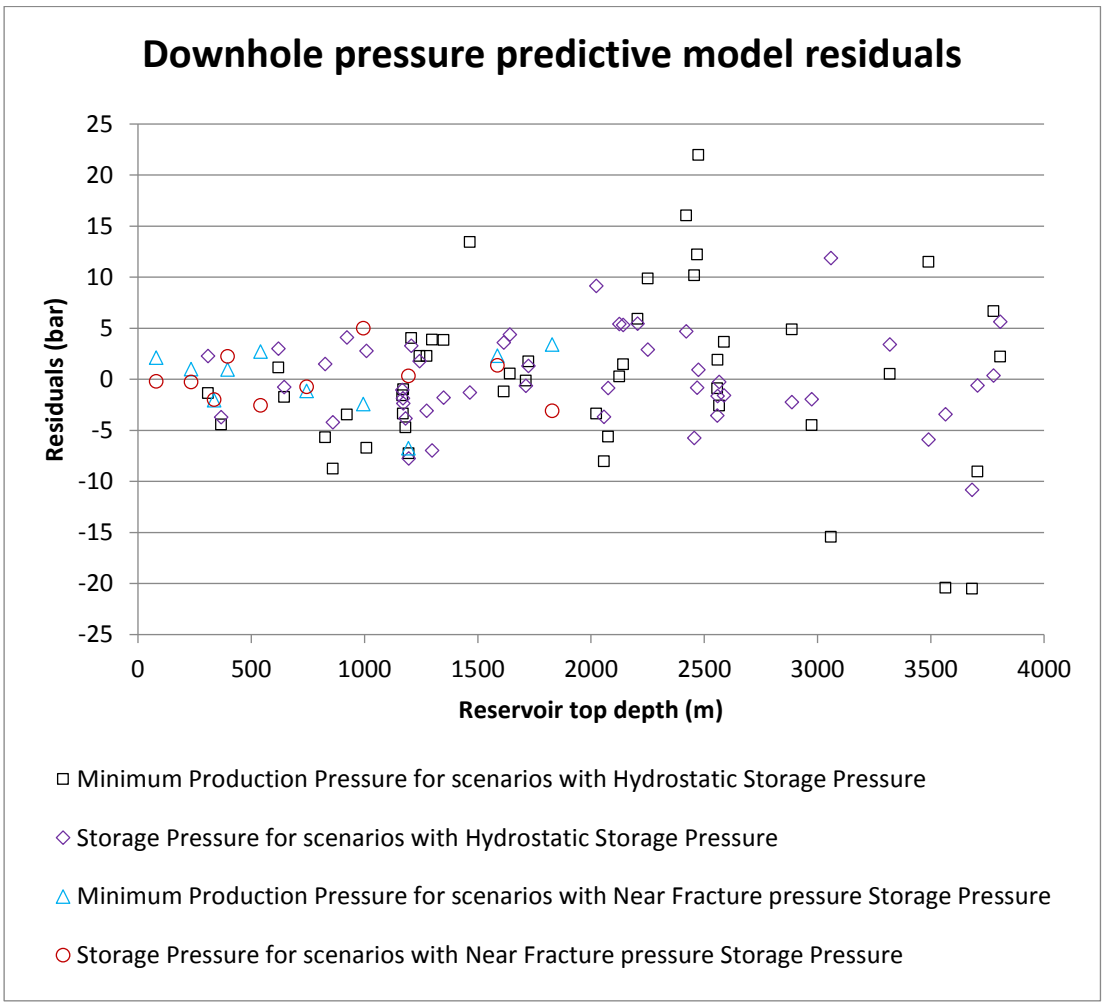

Figure 5-3: Residuals between the downhole pressure modelled using the OpenGeoSys reservoir model described in Chapter 3 and the linear regressions presented in Figure 5-2.

Figure 5-3 shows the residuals between the OpenGeoSys reservoir model and the linear regressions dependent variable values. The residuals are evenly distributed about the x-axis, however residuals greater than ±10 bars are more common at depth greater than 2 km than they are for shallower depths, for the minimum production pressures. This indicates that the model provides less accurate minimum production pressures for scenarios with a store deeper than approximately 2.2 km. This is of limited influence since the storage pressures, rather than the minimum production ones, will be used to determine the mass of stored air within a given store pore volume. In addition, the regressions are developed for the purpose of assessing the numerous offshore sandstone saline aquifers of the UK, which spread over the depth range studied relatively evenly. This even spread causes over and under-estimates from the

regression to cancel out on a study level, resulting in no systematic error. Finally, the logarithmic relationship between the pressure inlet at the turbine and the power output (explored in Chapter 4), implies that the inaccuracies in high production pressures' predictions will have a limited impact on the power output predictions.

Using those relationships it is now possible to estimate the density of the air at storage conditions for a certain depth. The reader is reminded that a geothermal gradient of 34 °C/km is assumed in this study, as well as isothermal conditions in the store throughout the cycle.

5.3.2 Well Power Output Predictive Model

The next step was to develop a predictive model for the well power output, which can then be used to estimate the energy storage capacity of a PM-CAES project. Results in Figure 4-8 from section 4.5.1, have shown that a trend exists between the minimum reservoir depth and the well power output. The trend which best explained the data of this relationship was found to be logarithmic in nature, rather than linear. Therefore, in order to perform a linear regression the logarithm of the reservoir depth must be used. In addition to this relationship between depth and power, a relationship between the turbine efficiency and the well power output also exists and this trend is linear (Figure 4-9 in section 4.5.1). The alpha parameter, which represents where between the hydrostatic and fracture pressure the storage pressure of the reservoir is, was added to the regression. It was expected from the two trends between reservoir depth and power output observed in Figure 4-8, that alpha (i.e. the chosen storage pressure) would have an impact on the power output.

$$P_{out} = -7.3160 - 1.2914\,\alpha + 3.4392\,log_{10}(\text{depth}) + 7.7904\,\eta_{T,pol} \qquad 5\text{-}4$$

Table 5-4: Multiple Linear Regression outputs for the well power output using alpha, reservoir depth and turbine polytropic efficiency as predictors. (see text below and section 5.2 for interpretation).

Regression Statistics	
Multiple R	0.9947
R Square	0.9893
Adjusted R Square	0.9893
Standard Error	0.1527
Observations	544

ANOVA

	df	*SS*	*MS*	*F*	*Significance F*
Regression	3	1,169	390	16,715	0.000
Residual	540	13	0		
Total	543	1,182			

	Coefficients	*Standard Error*	*t Stat*	*P-value*	*Lower 95%*	*Upper 95%*	*VIF*	*Std. Dev.*
Intercept	-7.3160	0.0949	-77.13	0.000	-7.502	-7.130	NA	NA
Alpha	-1.2914	0.0236	-54.61	0.000	-1.338	-1.245	1.05	0.28
Log10(depth)	3.4392	0.0165	207.88	0.000	3.407	3.472	1.04	0.40
Turbine Polytropic Efficiency	7.7904	0.1027	75.842	0.000	7.589	7.992	1.01	0.06

The relationship between the power output of the PM-CAES system and the storage pressure, reservoir top depth, and turbine polytropic efficiency is given as Eq. 5-4. Table 5-4 shows how the multiple linear regression developed offers a very good fit to the sample (multiple R = 0.995) and a good explanation for its variance (R^2 = 0.989). The relationship was also found to be significant and hence the Null hypothesis that "no relationship exists between turbine efficiency, alpha, store depth, and power output" can be rejected with confidence. The three predicators of the model (i.e. the logarithm of depth, the turbine efficiency and alpha), all show a good significance with P-value approximately 0 in their coefficients. Although no multicollinearity (i.e. dependence of one predicators on one another) was expected, since the pressure of the reservoir is controlled by geological parameters independent form the turbine polytropic efficiency, this was confirmed using the Variance Inflation Factor (VIF). The Variance Inflation Factor is a useful tool in determining multicollinearity between the predicators of a model (Table 5-5) (Everitt and Skrondal, 2013; Kittner, Lill and Kammen, 2017).

Table 5-5: This table shows how the collinearity between predicators is associated to the Variance Inflation Factor.

Variance Inflation Factor	Status of predictors
VIF = 1	Not correlated
1 < VIF < 5	Moderately correlated
VIF > 5	Strongly correlated

The ease with which simple calculations can be performed using computers also allows the regression to be tested on a different sample (test set) to the one used to determine the regression coefficients. This ensures that the model behaves as expected and that no overfitting occurs. The predictive model is validated against a test set of data which comprises of approximately 25% of the PM-CAES system sensitivity analysis results reported in Chapter 4. The Pearson coefficient between the test set outputs and the predicted outputs is of 0.985, indicating that the predictive model offers predictive capabilities equivalent to the ones from the more complex modelling undertaken in the Chapters 3 and 4.

It is important to stress that the predictive model is only applicable to aquifers which are likely to contain storage site with a depth, permeability, porosity and thickness which fall within the domain considered for this study which can be found at the start of this chapter in Table 5-1.

5.3.3 Roundtrip Efficiency Predictive Model

Now that the predictive model for the power output has been developed it is important to understand how much energy input into the PM-CAES system is required to achieve the predicted output. In order to determine the energy required for a PM-CAES cycle, the roundtrip storage efficiency needs to be known. The regression developed to predict this efficiency is presented next.

Note, that the roundtrip efficiency incorporates the total energy input into the system, which includes the electrical energy used to compress the air and the energy from the fuel (converted to electrical energy equivalent). This makes roundtrip efficiency a good measure of the energy cost of PM-CAES with respect to the entire energy system in which it operates, but not a good one in terms of the electrical load the compressor provides during the charging period. This will be estimated later using the Charging Electricity Ratio, introduced in Chapter 2.

The predictors for the roundtrip efficiency model, include the square root of the reservoir depth, the turbine polytropic efficiency, and the compressor polytropic efficiency. The number of expansion stages is not included since it was fixed to two, to represent the set-up of existing and planned CAES plants (Crotogino, Mohmeyer and Scharf, 2001; Kaiser and Efzn, 2015; Gaelectric, 2017). To avoid multicollinearity, the number of compression stages is not included either, as it is also correlated to the reservoir depth via the storage pressure. Indeed, it is calculated on the basis that the compression pressure ratio at each stage is as close as possible to 1:3 (Liu, Li, *et al.*, 2014). The turbine inlet temperature was assumed to be 400 K greater than the inlet temperature to the combustion chamber, which is within the inlet temperature range for the Huntorf and McIntosh CAES plants (Kaiser and Efzn, 2015).

$$\eta_{RT=} -23.23 - 1.078\,\alpha + 0.1413\,\sqrt{depth} + 46.464\,\eta_{T,pol} + 50.521\,\eta_{C,pol} \quad \text{5-5}$$

Table 5-6: Multiple Linear Regression outputs for the roundtrip efficiency using alpha, reservoir depth, compressor polytropic efficiency and turbine polytropic efficiency as predictors. (see text below and section 5.2 for interpretation).

Regression Statistics	
Multiple R	0.976
R Square	0.953
Adjusted R Square	0.9529
Standard Error	1.044
Observations	544

ANOVA

	df	*SS*	*MS*	*F*	*Significance F*
Regression	4	11987	2997	2750	0.000
Residual	539	587.37	1.090		
Total	543	12575			

	Coefficients	*Standard Error*	*t Stat*	*P-value*	*Lower 95%*	*Uppe r 95%*	*VIF*	*Std. Dev.*
Intercept	-23.23	0.82245	-28.25	0.00	-24.8	-21.6	NA	NA
Alpha	-1.078	0.161156	-6.69	0.00	-1.39	-0.76	1.04	0.28
Depth^0.5	0.1413	0.002988	47.30	0.00	0.135	0.147	1.03	15.25
Turbine Polytropic Efficiency	46.464	0.702408	66.15	0.00	45.08	47.84	1.01	0.06
Compressor Polytropic Efficiency	50.521	0.773145	65.35	0.00	49.00	52.04	1.00	0.06

The relationship between the PM-CAES system roundtrip efficiency and the storage pressure, reservoir top depth, turbine and compressor polytropic efficiency is given as Eq. 5-5. Table 5 6 shows how the multiple linear regression developed offers a very good fit to the sample (multiple R = 0.976) and a good explanation for its variance (R^2 = 0.953). The four predicators of the model (i.e. the logarithm of depth, the turbine and compressor efficiency, and alpha), all show a good significance with P-value approximately 0 in their coefficients. The Variance Inflation Factors are close to 1, which indicates that the collinearity between the parameters is negligible.

The predictive model is validated against a test set of data. The Pearson correlation coefficient between the test set outputs and the predicted outputs is of 0.980, indicating that the predictive model offers reliable predictive capabilities.

5.3.4 Charging Electricity Ratio Predictive Model

As mentioned earlier it is now important to be able to estimate the energy required for the compression and storage of the air. This can be achieved by relating the power output from

the turbine to the compressor power consumption, using the Charging Electricity Ratio introduced in section 2.1.2.2.

The predictors for the Charging Electricity Ratio model, include the turbine polytropic efficiency, and the compressor polytropic efficiency. The discussion on why the number of expansion and compression stages of the turbomachinery are not included are discussed in the roundtrip efficiency predictive model description above. Since the fuel energy is not accounted for in the charging electricity ratio, the energy inputs and outputs of the PM-CAES system are essentially controlled by the depth of the store. Therefore the effects of depth on the energy inputs is proportional to the effects of depth on the output of the system. Hence, the only variables which will show a variation in the charging electricity ratio are the efficiencies of the compressor and turbine which are independent of one another, as well as independent of store depth.

$$CER = -0.8941 + 0.9434\,\eta_{T,pol} + 1.457\,\eta_{C,pol} \qquad 5\text{-}6$$

Table 5-7: Multiple Linear Regression outputs for the Charging Electricity Ratio using alpha, reservoir depth, compressor polytropic efficiency and turbine polytropic efficiency as predictors. (see text below and section 5.2 for interpretation).

Regression Statistics	
Multiple R	0.9816
R Square	0.9636
Adjusted R Square	0.9634
Standard Error	0.0205
Observations	544

ANOVA

	df	*SS*	*MS*	*F*	*Significance F*
Regression	2	6.0	3.0	7153	0.00
Residual	541	0.2	0.0		
Total	543	6.2			

	Coefficients	*Standard Error*	*t Stat*	*P-value*	*Lower 95%*	*Upper 95%*	*VIF*	*Std. Dev.*
Intercept	-0.8941	0.01548	-57.8	0.00	-0.9246	-0.8638	NA	NA
Turbine Polytropic Efficiency	0.9434	0.01373	68.7	0.00	0.9165	0.9704	1.00	0.06
Compressor Polytropic Efficiency	1.457	0.01517	96.1	0.00	1.4274	1.4870	1.00	0.06

The relationship between the charging electricity ratio of the PM-CAES cycle and the turbomachinery efficiency is given by Eq. 5-6. Like for the previous models, Table 5-7, shows how the multiple linear regression developed offers a very good fit to the sample (multiple R

= 0.983) and a good explanation for its variance (R^2 = 0.967). The two predicators of the model (i.e. the turbine and compressor efficiency), all show a good significance with P-value approximately 0 in their coefficients. The Variance Inflation Factors are equal to 1, which indicates that there is no collinearity between the parameters.

The predictive model is validated against a test set of data. The Pearson correlation coefficient between the test set outputs and the predicted outputs is of 0.986, indicating that the predictive model offers reliable predictive capabilities. This provides a way of approximating the outputs of the complex numerical PM-CAES models developed in Chapters 3 and 4 with good accuracy.

5.4 Predictor Significance and Uncertainty

As well as providing a useful approximation of the finite element and analytical models which can be used to perform a computationally efficient nation scale storage assessment using a Monte Carlo method, as will be demonstrated in Chapter 6, the predictive models can also be used to understand the sensitivity of the results and provide an understanding of the key predictors affecting the various dependent variables modelled.

5.4.1 Global Variance-Based Sensitivity Analysis

To perform such sensitivity analysis on the predictive models a variance-based global method can be used. The term 'global' refers to sensitivity methods in which all predictors are varied simultaneously. Variance-based global methods are based on decomposing the variance of the output of the regression into portions which can be attributed to inputs or interactions between inputs (Sobol, 1993; Zhang *et al.*, 2015). Such methods offers a measure of sensitivity as a fraction of how each predictor affects the variance in the output. Using a variance-based method allows the sensitivity-analysis to be performed specifically over the entire input domain, making it a more representative approach than using a One-Factor-at-a-Time conventional approach. The drawback of this method is that for models with many inputs the computation time is extensive. This is why using regression approximation makes this type of analysis possible. Such type of analysis has the advantage of quantifying both the individual effect of a predictor as well as any interaction effect between the predictors (Saltelli and Annoni, 2010; Zhang *et al.*, 2015)

The sensitivity of the variance to predictors is characterised by two sensitivity indices, the *first order sensitivity index*, S_i, which accounts for the effects of a predictor X_i alone, and the *total order sensitivity index*, S_{Ti}, which accounts for the effects of predictor X_i and its interactions. (Saltelli and Annoni, 2010)

$$S_i = \frac{Expected\ reduction\ in\ variance\ achievable\ if\ X_i was\ fixed}{Total\ variance} \quad 5\text{-}7$$

$$S_{Ti} = \frac{Expected\ variance\ that\ would\ remain\ if\ all\ parameters\ \ but\ X_i were\ fixed}{Total\ variance} \quad 5\text{-}8$$

Two common variance-based methods are the Fourier amplitude sensitivity analysis (FAST) and the Sobol method (Sobol, 1993), the detailed study of the two methods is beyond the scope of this work, and according to (Zhang *et al.*, 2015) the two methods are comparable. The Sobol method was use, as it has been implemented in a statistical Python library (SALib).

The Sobol method operates by generating quasi-random input sets based on provided ranges for each predictor. Using a quasi-random sampling algorithm over a random one, ensures that the predictor ranges are more uniformly sampled, and enhances the convergence of the method (Zhang *et al.*, 2015). The generated input sets are then used to estimate the output using the predictive models developed earlier, and the sensitivity indices are calculated based on the variance of the outputs according to Eqs. 5-7 and 5-8. The indices can them be studied to understand the sensitivity of the model and the potential interactions between predictors. A summary diagram of the Sobol method is provided in Figure 5-4.

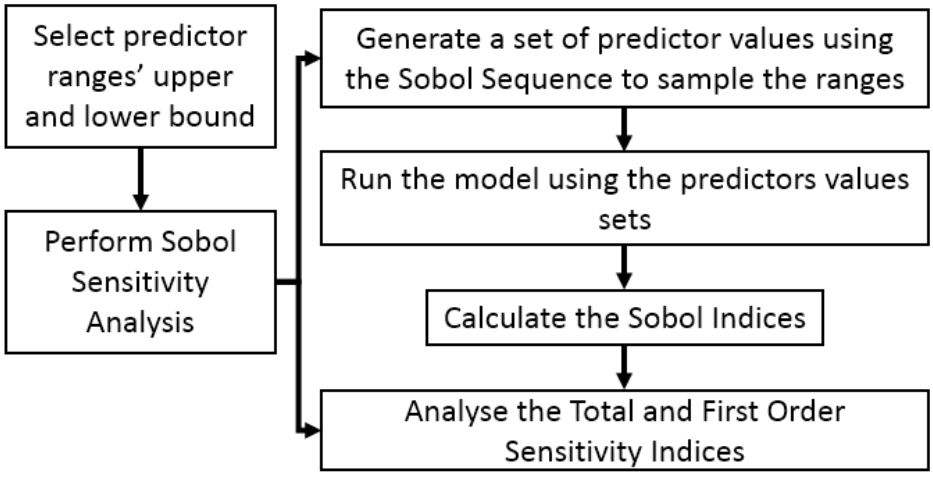

Figure 5-4: Flow chart summarizing the implementation of a sensitivity analysis performed using the Sobol method. The Sobol method requires predictor ranges to be specified prior to undertaking the sensitivity analysis. The method itself is formed of 4 setps: (i) generate quasi-random inputs, (ii) run model using the input sets, (iii) calculate the first and total order sensitivity indices, (iv) analyse them. The first three steps are performed using the SALib Python library (http://salib.readthedocs.io/en/latest/).

5.4.2 Sobol Sensitivity Analysis Results and Discussion

The results provided novel quantitative insight on how to maximize the efficiency and the power output of a PM-CAES site within the geological and operating parameters of this study. Firstly, the turbine and compressor efficiencies contributed to over 84% of the total variance in roundtrip efficiency, whereas the store depth contributed only 15%. Therefore, roundtrip efficiency should be maximized by optimizing the plant turbomachinery, rather than by targeting deeper stores. Secondly, the depth of the store accounted for 75% of the variance in power output, as compared with only 16% for the turbine efficiency, making depth an important control of power output. Finally, the variation in storage pressure when the store is fully charged (represented by α) had limited control on both roundtrip efficiency and power output, accounted for only 0.4% of the roundtrip efficiency variance, and 9% of the variance in power output.

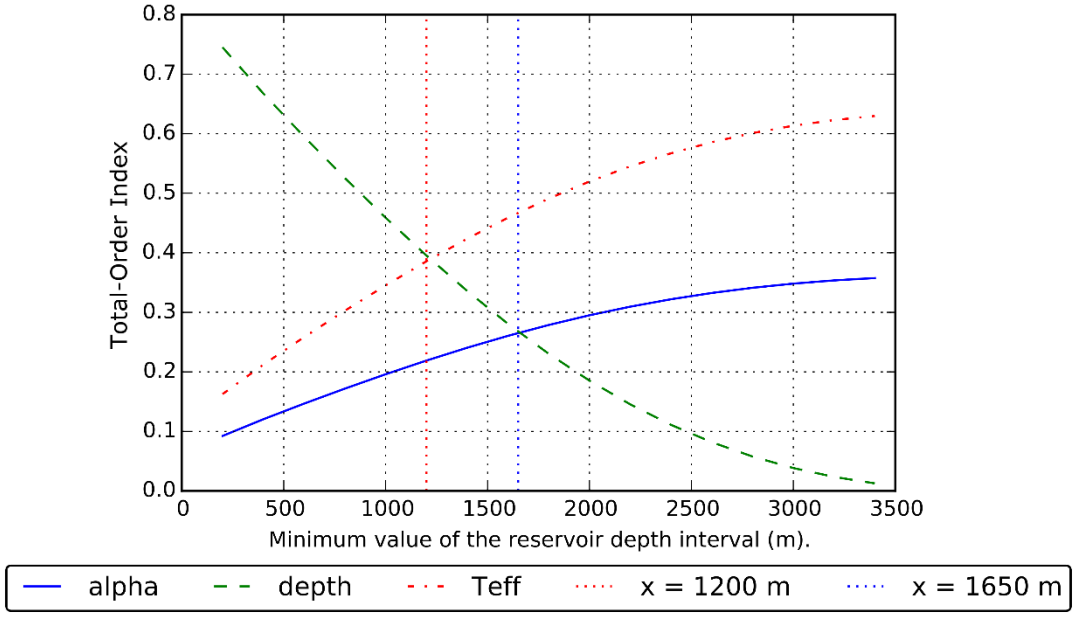

Figure 5-5: The figure shows the change in total-order indices for each of the predictors affecting the power output of a PM-CAES, as depth range is reduced by setting the minimum depth closer to the maximum depth (4 km). Teff is the polytropic turbine efficiency. When the whole range of depths is considered the impact of depth on the power output variance is greater than that of the turbine efficiency and alpha. However, as the minimum depth increases the influence of depth on the output variance is reduced. This can be explained by the logarithmic relationship between reservoir depth and power output. At about 1.2 km depth the main control on the power output variance becomes the turbine efficiency. This implies that from 1.2 km depth down, the benefits of increasing turbine efficiency, will outweigh the benefits from targeting higher pressure reservoirs, located at greater depths.

Although the results from the Sobol sensitivity analysis over the entire domain are useful to understand the impact of each predictor over the entire domain it is important to consider the impact of the non-linear relationship between reservoir depth and power output. Indeed, the logarithmic nature of that relationship implies that the highest increase in power output per

meter of reservoir depth are achieved at shallow depths. Using the Sobol method, this effect can be quantified. It is possible to determine a threshold depth of 1.2 km, at which the turbine efficiency's contribution to the variance in power output becomes greater than that of the reservoir depth. An interesting observation is that up to a minimum reservoir depth of 1,650 m the increase in storage pressure caused by the increase in store depth has a greater contribution to the power output variance than the variations in alpha. In other words, if the operator is uncertain about the depth of the reservoir, but knows that it is at least 1,650 m deep, then focus should be placed on increasing the storage pressure toward the fracture pressure (i.e. reducing alpha) as much as possible as the gains from it will likely be greater than the gains from targeting a deeper store.

Caution is of the essence when discussing the relationship of alpha to the power output variance. As it has been mentioned in section 3.3.5, the maximum inlet pressure of state-of-the-art CAES gas turbines is in the order of 250 bars (dashed magenta horizontal line on Figure 5-6). The blue solid line on Figure 5-6 indicates that when the reservoir is operated with a storage pressure which is hydrostatic (alpha = 1), then the minimum production pressure (blue dashed line) never reaches 250 bars. Although some throttling will be needed at the start of the cycle for reservoir depths greater than 2.5 km, the full turbine output can still be used during a portion of the cycle. When the reservoirs with a depth of more than ~ 1,950 m are operated at a storage pressure close to fracture pressure however, the minimum production pressure will always be greater than the turbine maximum inlet pressure. Therefore throttling losses occur during the entire production period. If this is considered a limitation, then the alpha range has to be reduced for reservoir depths greater than ~ 1,950 m. For example a reservoir with a depth of ~ 2,200 m will only be able to have alpha values between 0.1 and 1 (Figure 5-6).

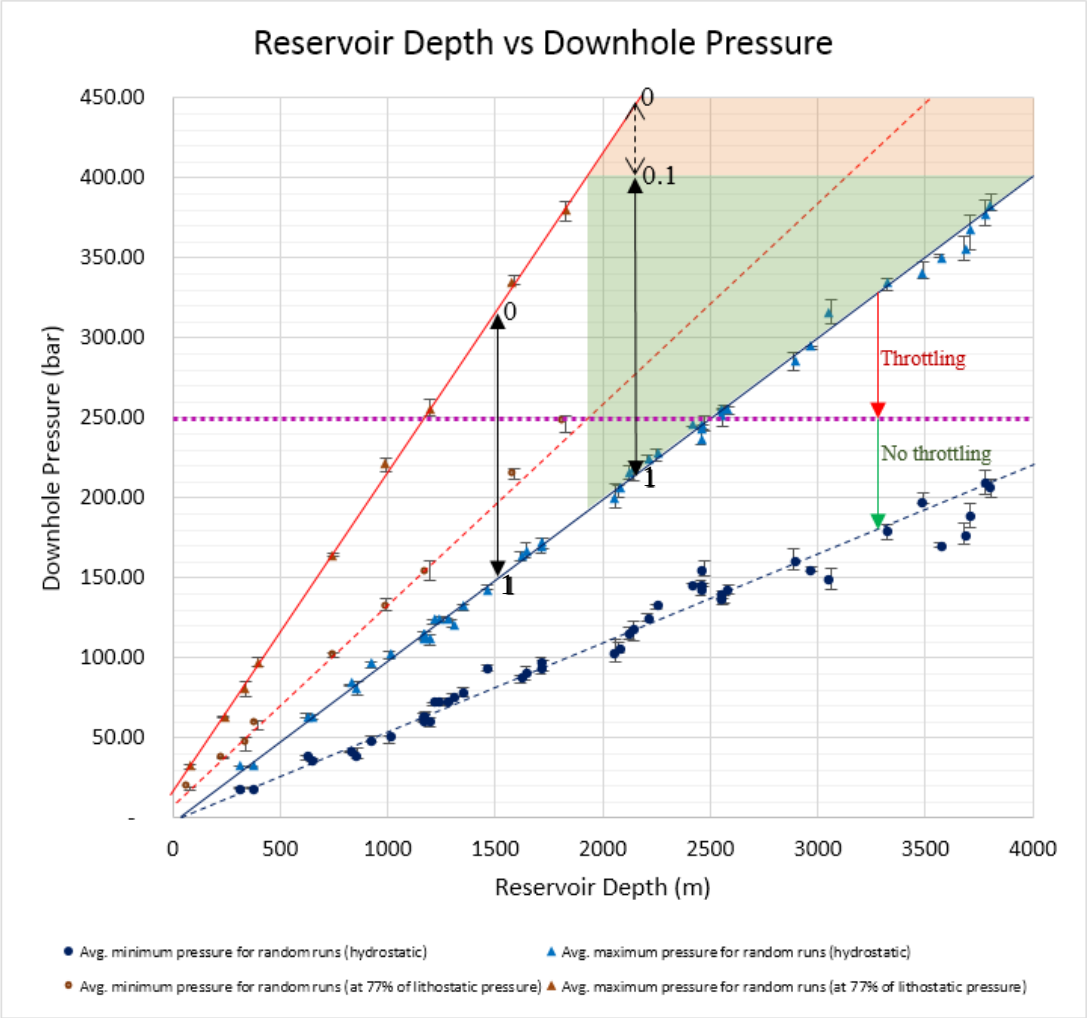

Figure 5-6: Illustration of the capping of the maximum storage pressure to avoid pressures in excess of 250 bars reaching the turbine inlet.

Factoring in this effect into the Sobol sensitivity analysis, shows that when the full range of reservoir depths is considered, the effects of the predictors on the variance in power output remain similar to the base case. Indeed, the dominant contribution to the variance in power output is still the reservoir depth (72%), followed by the turbine efficiency (22%) and by alpha (7%). However, as can be observed in Figure 5-7, the influence of alpha on the power output variance never exceeds that of reservoir depth. This is explained by alpha now being influenced by the reservoir depth, and not completely independent. In fact, the contributions given calculated from the total-order indices sum up to 1.04. The sum of the total-order indices being greater than 1 indicates that interactions occurs between the parameters, namely between store depth and alpha. Note that the reduction of the alpha range was not included in the multiple linear regression used to determine the predictive models, as all the data was used regardless of the reservoir depth, hence why the multicollinearity in the predictive models is low. The reduction of alpha will be included when estimating the UK's storage potential, as it

was deemed that the throttling at the inlet of the turbine during the entire production period would likely not be included in PM-CAES project designs, since throttling results in increased pressure losses, and hence efficiency losses.

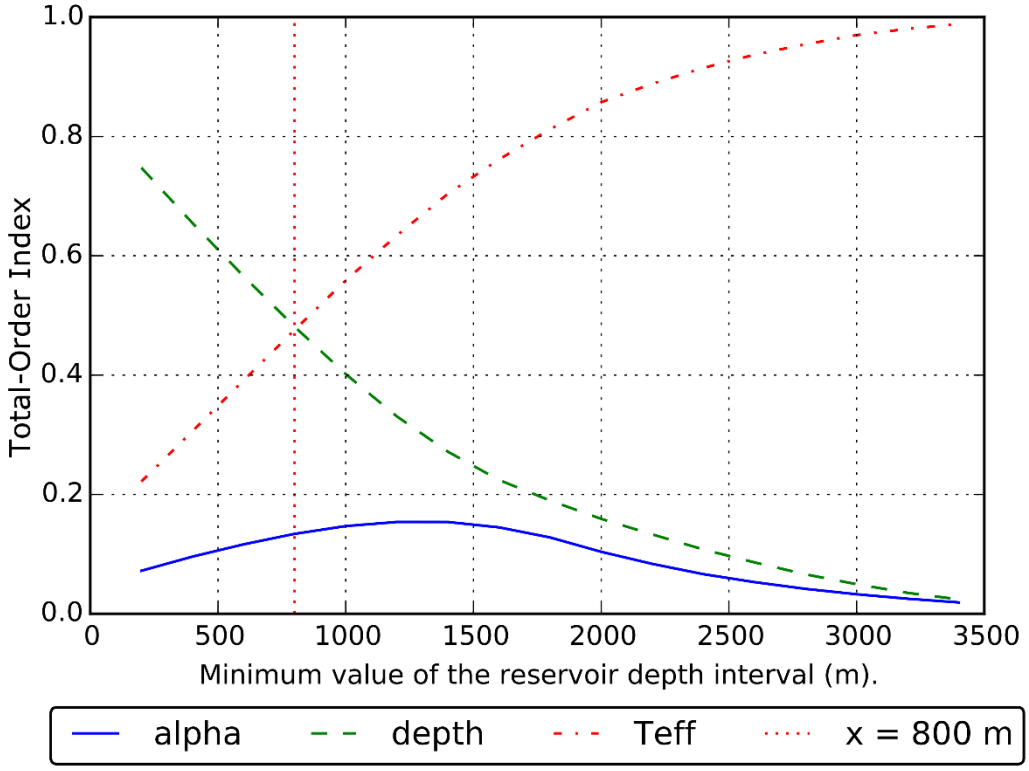

Figure 5-7: The figure shows the change in total-order indices for each of the predictors affecting the power output of a PM-CAES, as depth range is reduced by setting the minimum depth closer to the maximum depth (4 km). Teff is the polytropic turbine efficiency. When the whole range of depths is considered the impact of depth on the power output variance is greater than that of the turbine efficiency and alpha. However, as the minimum depth increases the influence of depth on the output variance is reduced. This can be explained by the logarithmic relationship between reservoir depth and power output. At about 800 m depth the main control on the power output variance becomes the turbine efficiency. This implies that from 800 m depth down, the benefits of increasing turbine efficiency, will outweigh the benefits from targeting higher pressure reservoirs, located at greater depths. As this figure reflects the reduction of the alpha range for depths greater than 1,950 m, it appears that the depth threshold for the benefits of deeper store (vertical red dotted line) is reduced from 1,200 m to 800 m.

5.5 Conclusions

This chapter has shown that the results of the PM-CAES model system can be approximated using algebraic predictive model as long as the values of the predictors are within the domain reminded at the start of this chapter. The predictive models have been shown to not only describe the training set from which they were derived well, but most importantly to provide good predictive ability on data from a test set (the full sets are provided as supplementary digital information).

A sensitivity analysis of the predictive models has shown that the roundtrip efficiency was primarily controlled by the compressor and turbine efficiencies. On the other hand, the power output was controlled mostly by the depth of the chosen store, when the full depth range (260 m to 4 km) was considered. This is the key finding of this chapter.

The insight from the sensitivity analysis can also be used to propose a depth threshold beyond which the turbine efficiency has a greater relative impact on the power output than the store's depth has. This relative impact should be seen as a potential to maximise the power output with all other parameters fixed and the possibility to increase either the depth of the store or the turbine's efficiency. When the alpha parameter is coupled to the store's depth to represent the minimisation of throttling losses, then a threshold depth of about 800 m can be proposed. For example, if it is identified that most of the stores are located shallower than 800 m, then the benefits of targeting the stores as close to that depth, would yield a greater relative benefit than trying to increase the efficiency of the turbine. At depths greater than 800 m though, it would be more advantageous to expend resources improving turbine technology. Some limitations to this analysis should be mentioned. Firstly, the analysis was performed using the predictive models and their underlying assumptions, such as a fixed well diameter with a vertical orientation and a flow rate of 15 kg/s; secondly, the analysis did not include any economic parameters. In reality, for such an analysis to be truly applicable to a specific site it would have to take into account the site specific uncertainty in the target store's depth, the cost of increasing well depth or using a horizontal well, or increased diameter, against the cost of developing and deploying a more efficient turbine. The conclusions from this work however, might still be of interest at a larger scale, to assess the benefits of funding further research in turbine efficiency or trying to constrain and identify depths of specific sites.

Chapter 6 Assessing PM-CAES Potential in the UK

6.1 Introduction

The aim of this chapter is to provide an estimate of the PM-CAES potential in offshore UK saline aquifers. When the term "storage potential" is used in this chapter it includes the amount of energy that can be delivered using PM-CAES over 60 days, its power capacity and its roundtrip efficiency. The bulk of this potential is estimated by applying the predictive models developed in Chapter 5 to a dataset of offshore UK saline aquifer formations. These models relate store depth, storage pressure (represented by alpha, introduced in section 5.3.1) and turbomachinery efficiencies, to PM-CAES power output. The UK CO_2 Store dataset contains characteristics of porous rock aquifers covering large areas of the Southern, Central and Northern UK North Sea, and the East Irish Sea. This data set was developed from 2009, by a consortium of 10 public and private sector institutions, using seismic, well data and literature. It contains information on the location, lithology, porosity, permeability, thickness and depth of offshore UK saline aquifers. It was initially developed in order to assess the potential for CO_2 to be stored offshore of the UK (Bentham *et al.*, 2014).

Table 6-1: Siting criteria used to filter the entries of the CO_2 Stored database. Maximum depth was extended to account for compressor and turbine technology being able to operate efficiently up to pressures of 250 bar. The minimum thickness of the store was defined as 50 m because the modelling performed showed that well collapse was common for scenarios with a store thickness less than 50 m.

Parameter	Range/Value
Depth to the top of the formation	260 m to 4,000 m
Permeability	100 mD to 1,330 mD
Thickness	50 m to 350 m
Porosity	15 to 30%
Presence of trapping mechanism capable of retaining the stored air in the vicinity of the well	Only aquifers for which the containment of air in geological traps was likely were considered.
Lithology	Sandstone
Heterogeneity	'complex' geology was rejected

The steps taken to estimate the storage potential offshore UK were: 1) filtering the CO_2 Stored database using the criteria in Table 6-1, 2) Perform a Monte Carlo analysis using the pore volumes from the selected formations, combined with the predictive models developed in Chapter 5, to infer the *Initial Bulk Storage* potential of each formation (1st Pass in Figure 6-1). 3) Refine the *Initial Bulk Storage* potential to account for the limitations of this study (2nd Pass in Figure 6-1). This is achieved by investigating the geology of the formations which present the most storage potential, in order to ensure that they are suited to air cycling, rather than

permanent gas storage. 4) Once the location of the *Refined Bulk Storage* potential has been established, it is necessary to identify the key logistical challenges, such as compressed air transportation, and examine how they might affect the likelihood of the identified storage resource being used. 5) This analysis of the key logistical challenges reveals that the scenario of offshore power generation and air compression is most likely to be developed. The colocation of PM-CAES with offshore windfarms would maximise the benefits of the storage potential. The final step is to refine the initial estimates by identifying the storage resource colocated with offshore windfarms and estimate the costs of such projects (3rd Pass in Figure 6-1). These final estimates are referred to as *Colocated Storage potential.*

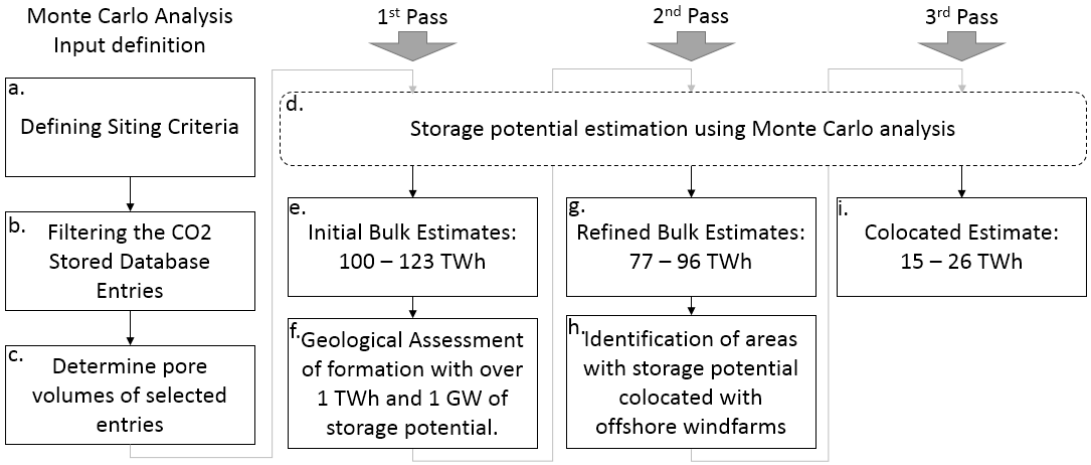

Figure 6-1: Schematic of the procedure followed to estimate the energy storage potential achievable using offshore PM-CAES technology. The Monte Carlo procedure which computes the power output, energy delivered over 60 days, and roundtrip efficiency estimates using the predictive model from Chapter 5 is repeated three time, each time, some of the entries are removed based on some further analysis (i.e. geological assessment, GIS identification of colocation between areas with storage potential and offshore windfarms).

6.2 UK Bulk Storage Potential Estimation Method

Note: This section has been almost integrally reused as part of a publication: *Inter-seasonal compressed air energy storage using saline aquifers*, currently under revision for resubmission at *Nature Energy*. The full article, co-authored with M. Wilkinson, D. Mignard, C. McDermott, R.S. Haszeldine and Z.K. Shipton. As such the co-authors have been actively involved in this section, including re-writes, which requires special acknowledgments.

The predictive models were applied to entries from the CO_2 Stored database (Bentham *et al.*, 2014). The key steps used to estimate the *Initial Bulk Storage* potential (Figure 6-1 e.) are : 1) Defining siting criteria for PM-CAES stores based on published criteria ranges modified for state of the art CAES turbine technology (Table 6-1 and Figure 6-1 a.); 2) Performing the filtering of the CO_2 Stored database using the criteria (Figure 6-1 b.); 3) Determining the volume of pore space within each of the aquifers in the database in which air can be stored

(Figure 6-1 c.). 4) Using the depth and pore volumes from the selected dataset entries as input, perform a Monte Carlo analysis by randomly sampling turbomachinery parameters to determine power output and roundtrip efficiency (Figure 6-1 d.).

6.2.1 Filtering of UK Dataset

The aquifers from the CO_2 Stored dataset, whose characteristics indicate they are likely to contain rocks suitable for PM-CAES, were identified based on their shallowest depth, porosity, permeability, thickness, lithology, and the presence of a geological trap to contain stored air and absence of features impeding the flow of air (mineral cement, heterogeneity of the rock mass). A geological trap is defined by a porous reservoir with an impermeable caprock plus lateral seals to flow. Such lateral seals could be provided by doming of the top seal, lateral changes in rock type to lower porosity units, or the presence of impermeable faults. In the following text this sealing mechanism is referred to as a trap geometry.

The filtering procedure (Figure 6-1 b. and e.), can be broken down into five steps. Firstly we remove all the entries for which no data is available for one or more of the siting criteria. Secondly, data outwith the allowable ranges of the siting criteria are rejected (Table 6-1). Thirdly, as is described in section 6.3, aquifers are rejected if geological problems (e.g. heterogeneity, mineral cement, fractured seals, and overpressure) are identified from the literature. This step is performed after the 1st Pass only for formation with storage potential over 1 TWh and 1 GW (Figure 6-1 e.). Performing the geological assessment after the 1st Pass enabled it to be focused on key formations. Fourthly, the entries are divided into 3 categories: type 1 are entire single aquifer units; type 2 are subsets of single aquifers which are subdivided in the database into pressure compartments. These pressure cells are usually much larger than traps; type 3, are individual storage sites, i.e. locations within an aquifer defined usually as single geological traps. When an aquifer is characterized by entries of both type 1 and type 3, the type 3 were used.

Finally, entries in the CO_2 Stored database for entire aquifers (type 1) were subdivided using criteria identified in the literature (Knox and Holloway, 1992; Mudge and Bujak, 1996; Armour, Evans and Hickey, 2003; Kilhams, 2011; Kilhams *et al.*, 2012), to subdivide them into type 2 entries. Parameters used for sub-division included burial depth; thickness; where available, permeability and the ratio of sandstone to shale (i.e. the net-to-gross ratio). The superposition of the parameters in ArcMap® GIS software enabled the calculation of the pore volume of the sub-divided portions of the aquifers. A detailed description of the subdivision is done in section 8.4.5.2.1.

6.2.2 Calculation of Pore Volume Fraction of Selected Aquifers Usable for Storage

Only a fraction of the pore volume of an aquifer, referred to as the usable pore volume (V_{usable}, Eq. 6-1), can actually be used for air storage. The usable pore volume is the pore volume within geological traps potentially capable of retaining fluids (e.g. a dome of porous rock overlain by impermeable caprock). It excludes geological traps containing hydrocarbons or defects such as a fractured caprock.

$$V_{usable} = V_{traps} \times \eta_{usable} \quad 6\text{-}1$$

where V_{traps} is the pore volume contained in all the areas of the aquifer contained within a geological trap capable of retaining fluids (e.g. air, CO_2 or hydrocarbons), η_{usable} is the fraction of geological traps usable for air storage.

For Type 2 aquifers, this volume was estimated using Eq. 6-2.

$$V_{traps} = {}^{V_h}/_{\eta_h} \quad 6\text{-}2$$

where V_h is the total pore volume of all the geological traps that contain hydrocarbons within an aquifer (a known value), and η_h the ratio of V_h to the total pore volume within geological traps.

The average success rate of hydrocarbon exploration wells in the UK continental shelf, from 1963 to 2002, is ~30% (Munns *et al.*, 2002). Assuming exploration wells are targeted at traps within an aquifer which can be identified by seismic imaging technics, this value can be used as η_h. The pore volume of geological traps exploited for hydrocarbons (V_h) was calculated from the hydrocarbon volumes originally in place in all the hydrocarbon fields within the aquifers offering potential for PM-CAES (sample size = 44, Table 6-2).

Table 6-2: Hydrocarbon volumes (V_h) from (Maher, 1981; Harker, Green and Romani, 1984; Bifani, 1986; Tonkin and Fraser, 1991; Schmitt, 1991; Jolley, 1993; Ritchie and Pratsides, 1993; Swale and Vass, 1994; Jewell and Ward, 1997; Taylor *et al.*, 2003; Gluyas and Hichens, 2003; Doré and Robbins, 2005) **used to estimate the usable storage volumes within aquifer entries of type 2 from the CO_2 Stored dataset. OIIP indicates the oil initially in place within the hydrocarbon field, and GIIP the gas initially in place. 1 MMBBL (million barrels) is equal to 158,987.3 m^3, and 1 BCF (billion cubic feet) is equal to 28,316,800 m^3. The formation volume factor and gas expansion factor were used to convert volumes of hydrocarbon at surface pressure and temperature conditions to corresponding volumes at store conditions. The formation volume factor is defined as the in-situ hydrocarbon volume to that at surface conditions, whereas the gas expansion factor is the inverse. The hydrocarbon initial saturation was used to account for pore space occupied by other fluids, usually brine, it is defined as 1 minus the water remaining in the pore space after hydrocarbon migration (i.e. connate water saturation)Highlighted values were taken as averages from all other existing values. For example, 1.4 was the average of all the FVF and 168 that of all the gas expansion factors. For the fields marked with an asterisk the hydrocarbon volume could be found and the GIIP was back-calculated for the sake of completeness. (Continues onto next page)**

Aquifer	Field Name	Hydrocarbon Type	OIIP (MMBBL)	GIIP (BCF)	FVF / Gas Expansion Factor	Hydrocarbon Initial Saturation	V_h (m^3)
Balder	Harding	Oil	322		1.1	0.91	$6.35 \cdot 10^7$
Balder	West Brae	Oil	116		1.2	0.92	$2.33 \cdot 10^7$
Balder	Brimmond	Oil	15		1.4	0.7	$4.56 \cdot 10^6$
Bunter	Main Hewett Lower Bunter	Gas		2,100	140	0.80	$5.31 \cdot 10^8$
Bunter	Main Hewett Upper Bunter	Gas		1,356	97	0.78	$5.08 \cdot 10^8$
Bunter	Gordon	Gas		1,843	165	0.78	$4.06 \cdot 10^8$
Bunter	Esmond*	Gas		1,671	158	0.83	$3.60 \cdot 10^8$
Bunter	Caister B*	Gas		1,235	225	0.67	$2.32 \cdot 10^8$
Bunter	Forbes*	Gas		1,116	179	0.84	$2.10 \cdot 10^8$
Bunter	Orwell	Gas		283	168	0.78	$6.11 \cdot 10^7$
Bunter	Caister C	Gas		230	285	0.68	$3.36 \cdot 10^7$
Bunter	Little Dotty	Gas		100	185	0.76	$2.01 \cdot 10^7$
Burns	Buzzard	Oil	990		1.4	0.78	$2.74 \cdot 10^8$
Claymore	Claymore	Oil	1,453		1.2	0.78	$3.49 \cdot 10^8$
Forties	Forties	Oil	4,196		1.2	0.85	$9.57 \cdot 10^8$
Forties	Nelson	Oil	790		1.4	0.78	$2.19 \cdot 10^8$
Forties	Arbroath	Oil	334		1.3	0.55	$1.28 \cdot 10^8$
Forties	Montrose	Oil	236		1.5	0.55	$1.03 \cdot 10^8$
Forties	Arkwright	Oil	73		1.5	0.51	$3.31 \cdot 10^7$
Maureen	Maureen	Oil	398		1.3	0.67	$1.22 \cdot 10^8$
Maureen	Moira	Oil	12		1.3	0.78	$3.17 \cdot 10^6$
Maureen	Fleming	Gas		1,064	200	0.78	$1.93 \cdot 10^8$
Mey	Andrew	Oil	4,196		1.2	0.85	$9.57 \cdot 10^8$
Mey	MacCulloch	Oil	200		1.2	0.90	$4.24 \cdot 10^7$
Mey	Balmoral	Oil	151		1.4	0.78	$4.18 \cdot 10^7$
Mey	Cyrus	Oil	82		1.4	0.78	$2.27 \cdot 10^7$
Ormskirk	South Morecambe	Oil	946		1.5	0.75	$3.10 \cdot 10^8$
Ormskirk	Lennox	Oil	184		1.3	0.78	$4.88 \cdot 10^7$
Ormskirk	Douglas	Oil	202		1.1	0.78	$4.43 \cdot 10^7$
Ormskirk	North Morecambe	Gas		5,500	143	0.65	$1.68 \cdot 10^9$
Ormskirk	Hamilton	Gas		627	120	0.78	$1.90 \cdot 10^8$
Ormskirk	Hamilton North	Gas		230	108	0.78	$7.73 \cdot 10^7$
Piper	Piper	Oil	1,368		1.3	0.95	$2.86 \cdot 10^8$
Piper	Rob Roy Main	Oil	790		1.4	0.96	$1.78 \cdot 10^8$
Piper	Rob Roy Supra	Oil	101		1.3	0.94	$2.30 \cdot 10^7$
Piper	Ivanhoe	Oil	100		1.2	0.91	$2.09 \cdot 10^7$
Piper	Scott	Oil	42		1.7	0.91	$1.23 \cdot 10^7$
Piper	Hamish	Oil	7		1.4	0.95	$1.70 \cdot 10^6$
Piper	Chanter	Gas		95.4	263	0.82	$1.25 \cdot 10^7$
Piper	Telford	Oil	126		2.2	0.78	$5.65 \cdot 10^7$

Aquifer	Field Name	Hydrocarbon Type	OIIP (MMBBL)	GIIP (BCF)	FVF / Gas Expansion Factor	Hydrocarbon Initial Saturation	V_h (m³)
Statfjord	Brent	Oil	3,800		1.8	0.78	$1.39 \cdot 10^9$
Statfjord	Statfjord	Oil	1,319		1.5	0.52	$5.98 \cdot 10^8$
Tor	Banff	Oil	304		1.3	0.78	$8.06 \cdot 10^7$
Valhall/Wick	Captain	Oil	1,000		1.0	0.84	$1.98 \cdot 10^8$

The next step was to estimate how many of those traps would be suitable for PM-CAES. The study of 382 hydrocarbon wells from Xia and Wilkinson (2017) proposes that 49%±8 of the traps in an aquifer can be successfully exploited for CO_2 storage. Because the prerequisites for CO_2 storage sites and compressed air storage sites are comparable, it was assumed that for CAES in aquifers, the only suitable traps would be the ones which could be successfully exploited as CO_2 stores but did not contain hydrocarbons. In that case, η_{usable} is equal to 19% of the overall geological traps, see Figure 6-2.

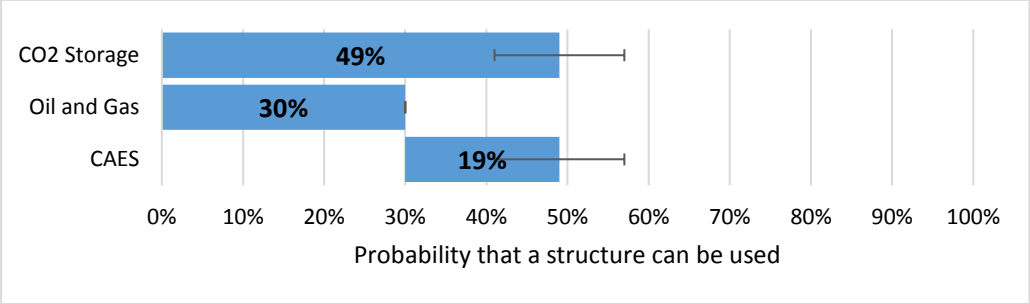

Figure 6-2: Successful exploitation probability for CO_2 storage, oil and gas and CAES. The error bars indicate the variation in likelihood of success reported by Xia and Wilkinson for different aquifers (Xia and Wilkinson, 2017)**.**

The storage efficiency of type 2 aquifers is given by Eq. 6-3.

$$\eta_{storage} = \frac{V_{usable}}{V_{dataset,Type2}} \qquad 6\text{-}3$$

For Type 3 aquifers, for which the geological trap pore volume, V_{traps}, is provided in the database, the efficiency is given by Eq. 6-4.

$$\eta_{storage} = \eta_{usable} \qquad 6\text{-}4$$

6.2.3 Monte Carlo Simulation

A Monte Carlo simulation of the population of selected aquifers was performed to estimate the storage potential of PM-CAES offshore UK. This part of the procedure was repeated in each of the three passes (Figure 6-1 d.); each time using more refined inputs. This repetition was used to identify which formations would have to be studied further. It was more time efficient to repeat the Monte Carlo simulation rather than doing a geological assessment of

every single formation. In the 1st Pass to estimate the *Initial Bulk Storage* potential of all offshore formations. In the 2nd Pass to estimate the *Refined Bulk Storage* potential after removing geological formation deemed unsuitable (see section 6.3). In the 3rd Pass to estimate the *Colocated Storage* potential to offshore windfarms.

The steps of the algorithm used to perform each realization of the simulation were; 1) Selecting a storage pressure using the α parameter and the hydrostatic pressure at the depth of the geological store. α was varied between 0 which represents a storage pressure closer to fracture pressure, and 1 or less for one close to hydrostatic pressure (the reader is referred back to section 5.4.2 for a discussion on alpha); 2) Selecting turbomachinery efficiencies from normal distributions; 3) The power output per well and the roundtrip efficiency were calculated using the predictive models described in section 5.3.2 and 5.3.3 respectively; 4) The power output was varied randomly by up to ±3% from the calculated value to account for the uncertainty caused by using a constant specific heat for air in the turbine mathematical model (as explained in section 4.2.1); 5) The air mass which could be stored is the product of the usable pore volume (calculated using the storage efficiency $\eta_{storage}$ corresponding to the aquifer type), the gas density (determined using the storage pressure and temperature) and the fraction of the pore space occupied by air within a PM-CAES store (i.e. the gas saturation). An arithmetic average of 47% for the gas saturation was calculated from ten OpenGeoSys numerical store models representative of the parameter space in Table 6-1; 6) The number of wells needed is calculated as the mass of air which can be contained in the pore volume divided by twice the amount of air which would be extracted over 60 days (1,440 hours) at a rate of 15 kg/s, equating to 158 million kg of air. The amount of air was doubled to account for the cushion gas requirement, which is the amount of air which remains in the store throughout the cycle (i.e. for each well the mass of air cycled and the mass of cushion gas required for that well were both taken into consideration); 7) The power output per aquifer is computed as the number of wells multiplied by the power output per well; 8) The energy storage potential is determined as the power output per well multiplied by the duration of the production period; 9) The total power and energy storage potential per aquifer were achieved by a sum of all the entries' values for each aquifer.

For each pass, 3 simulations of 10,000 realisations were performed resulting in a maximum difference between simulations of ± 0.1 GW for power capacity estimates and ± 0.1 TWh for energy capacity estimates.

6.2.4 Initial Bulk Storage Potential

The method described in the previous section finds that combining commercially mature conventional-CAES technology with storage in the offshore UK sandstone saline aquifer resource offers an *Initial Bulk Storage* potential of 100 to 123 TWh (69 to 85 GW during 60 days) with 10 to 90% probability, respectively, that the storage potential will be less than the stated value (Figure 6-3). The storage potential suggested by the results is encouraging as it is, on average, over twice the UK's electricity consumption during the months of January and February 2017.

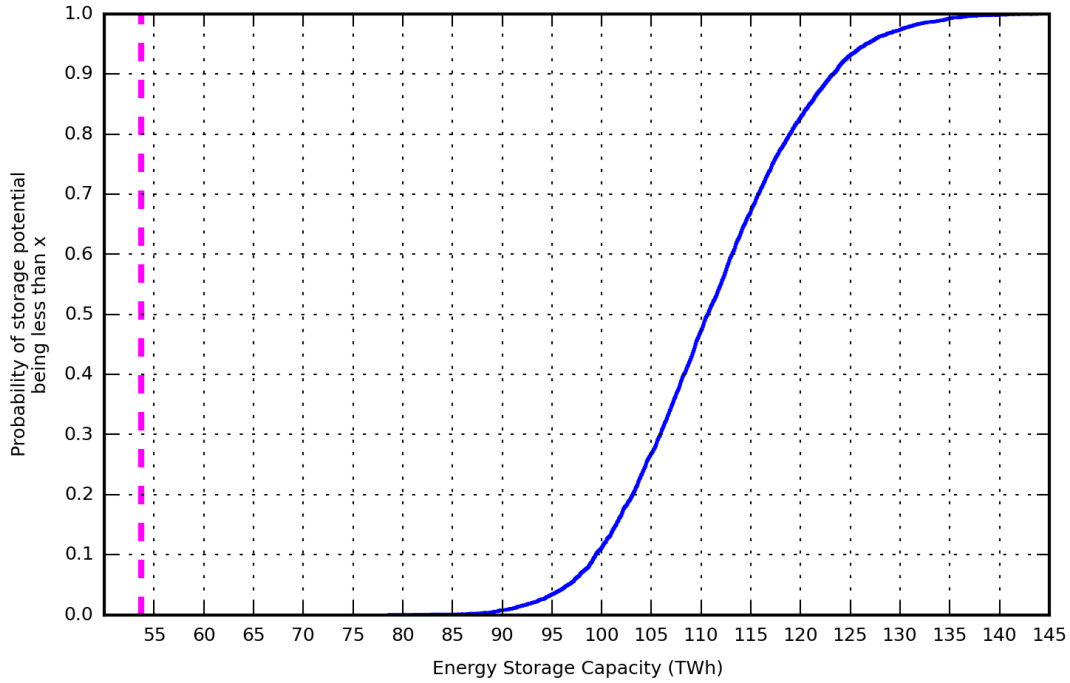

Figure 6-3: The Initial Bulk Storage potential's energy storage capacity using offshore UK aquifers combined to a conventional CAES plant. The energy values on the graph indicate the amount of energy recovered from discharging the stored air. The blue curve represents the Initial Bulk Storage potential's energy storage capacity for the UK. The dashed line represents the UK's electricity consumption from the 1st January 2017 to the 28th of February 2017.

It is now important to consider in which geological formations the identified storage is found and analyse the geology of formations which contain significant potential to ensure that no shortcomings are found. The spread of the storage potential shows a negative exponential distribution (i.e. most of the storage is found in a few formations in Figure 6-4), with about half the storage potential (56 TWh) identified within the structures of the Bunter Sandstone. Formations offering more than 1 TWh of energy storage, deliverable at 1 GW or more (using median values) will be studied in further details, using sources from the literature to determine if they are likely to be suitable for cyclic air storage.

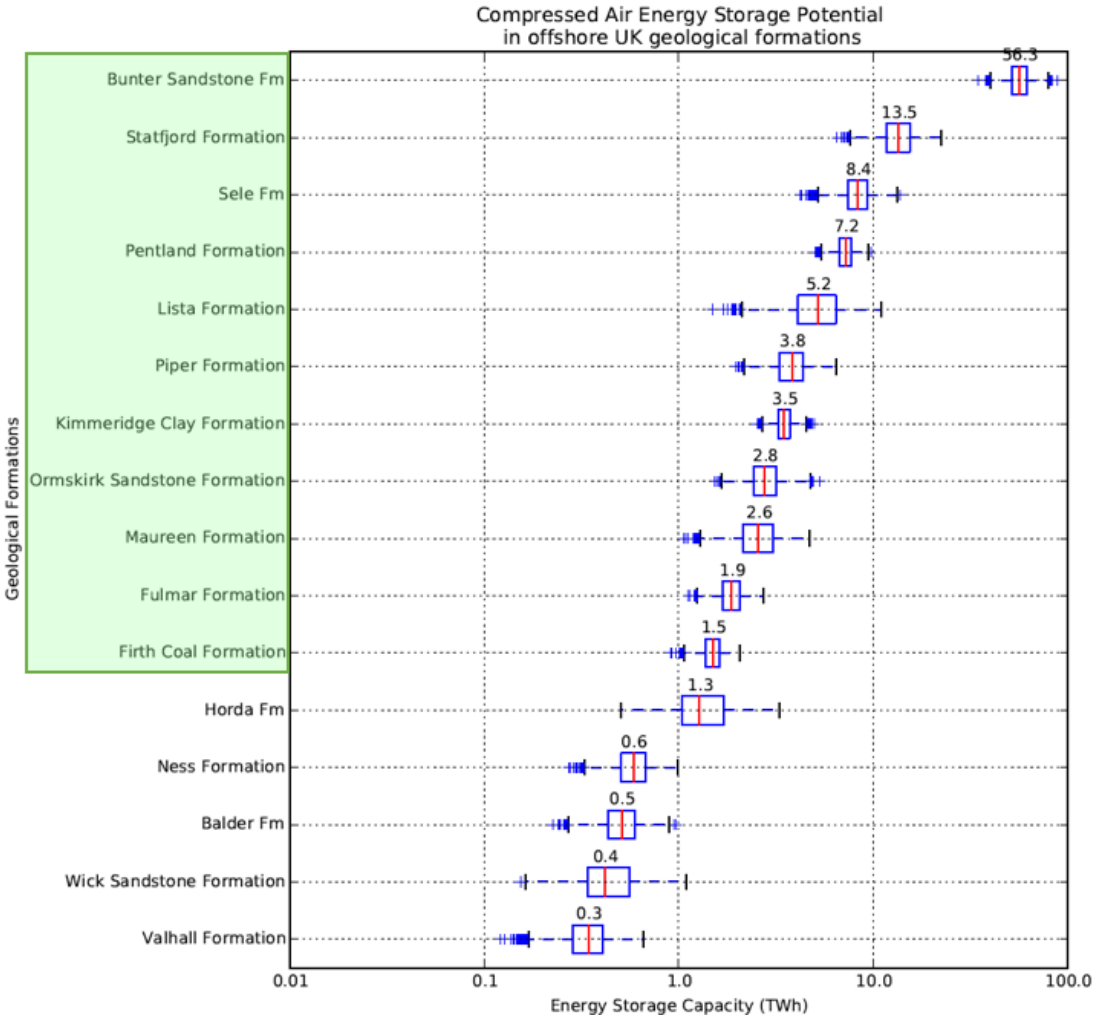

Figure 6-4: The box plots in the figure plot the logarithm of the storage potential contained in each formation which passed the initial filtering described in section 6.2.1. The length of the whiskers of the box plot are ±1.5×IQR. The Horda Formation is not included in the geological estimates despite having an energy storage potential of 1.3 TWh, because its power output potential is lower than 1 GW. A geological assessment was performed on the formation inside the green box.

6.3 Geological Assessment of the Key Formations

After the 1st Pass, the key formations presenting more than 1TWh and 1GW of storage potential were assessed to identify if there were any geological limitations, not addressed in the modelling, which could limit that potential or increase the uncertainty of the results.

The CO_2 Stored database was chosen as being representative of the UK's offshore saline aquifer resource relevant for PM-CAES operations. Since the initial database contains formation suitable for CO_2 gas storage, a further geological study to assess the cyclic air storage potential of the formations presented in the database had to be done for the most promising formations. The formations assessed in this section, which offered more than 1TWh and 1GW of storage potential, are: the Bunter Sandstone Formation, the Statfjord Formation, the Sele Formation, the Pentland Formation, the Lista Formation, the Piper Formation, the

Kimmeridge Clay Formation, the Ormskirk Formation, the Maureen Formation, the Fulmar Formation, and the Firth Coal Formation. The summary of the geological assessment of each of those formations using available literature can be found in Appendix 8.4.

6.3.1 Conclusions on Geological Model Limitations

The two main sources of uncertainty which the modelling does not address are the aquifer pressure connectivity, as well as the impact of heterogeneities on the reservoir pressure response. Due to the approach chosen of modelling a single well from an array it is difficult to implement aquifer recharge to address the lack of connectivity in the models. Nonetheless, this limitation, although significant on an individual site assessment, is mitigated on a nation scale assessment since the greatest pressure fluctuations are being modelled. Should a store be well connected to the wider aquifer, the storage pressure could be lower, reducing the costs and engineering challenges of compression, whilst the aquifer would keep the pressure up when the store is being discharges (a mechanism known as the water drive in the hydrocarbon industry).

The second main source of uncertainty: heterogeneity of the reservoir, is likely to be a severe hindrance to the cycling of air. Therefore it was deemed appropriate to remove the Statfjord, Pentland and Firth Coal Formation from the bulk estimates (and the Fulmar due to its overpressure). Removing those formation leads to the storage potential to be of 77 to 96 TWh (53 to 67 GW over 60 days), with 10 to 90% probability, respectively, that storage will be less than the stated value. This potential is still sufficient to be of interest as it represents approximately 160% of the UK's electricity consumption for January and February of 2017. Figure 6-5 provides a graphical summary of the likelihood of achieving at least a given storage energy capacity value for each of the selected formation who passed the geological screening. Table 6-3 provides a summary of the contribution of each formation to the total storage potential, as well as the corresponding P50 for the expected power capacity, and Figure 6-6 the total offshore UK cumulative storage potential distribution remaining after the Statfjord, Fulmar, Pentland and Firth Coal Formation have been removed from the bulk estimates.

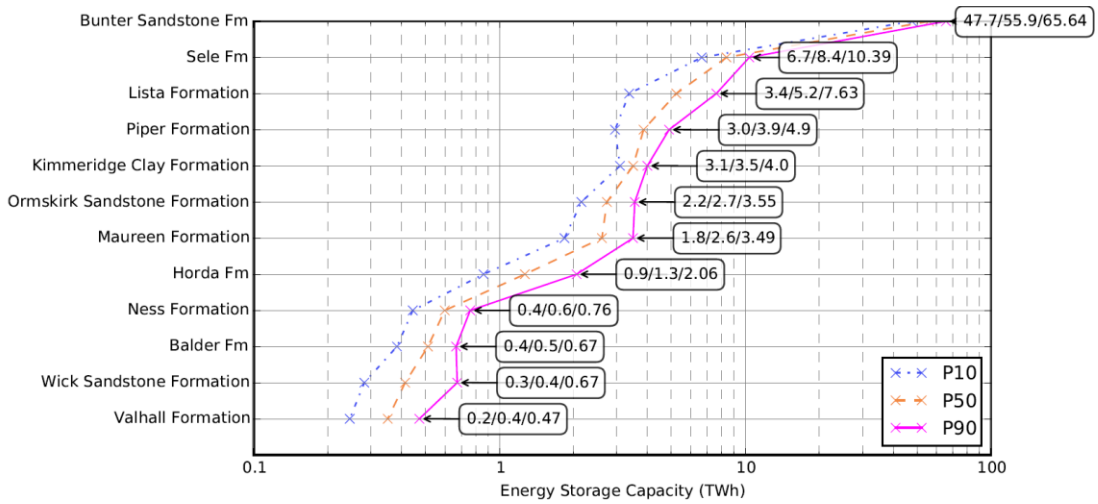

Figure 6-5: Graphical summary of the *Refined Storage Potential* where the P10/P50/P90 values correspond to the 10, 50 and 90% likelihood of achieving the stated potential value or less. The logarithmic scale on the x-axis clearly indicates that approximately 66% of the storage potential is found in the Bunter Sandstone Formation. Another observation is that the range in storage potential (between P10 and P90) is positively correlated to the amount of storage potential.

Table 6-3: Summary of the formations included in the assessment of the PM-CAES storage potential in offshore UK saline aquifers. Stating the 50th percentile value for energy capacity, power capacity and the estimated share of the total storage.

Formation Name	Subjected to a Geological Assessment?	Included in *Refined Storage Potential*?	Energy Storage Potential (50th%ile) TWh	Power Capacity (50th%ile) GW	Share of Storage Potential (%)
Bunter Sandstone Fm.	Yes	Yes	55.9	38.2	66%
Statfjord Fm.	Yes	No	13.5	9.2	NA
Sele Fm	Yes	Yes	8.4	5.7	10%
Pentland Fm.	Yes	No	7.2	4.9	NA
Lista Fm.	Yes	Yes	5.2	3.6	6%
Piper Fm.	Yes	Yes	3.9	2.6	5%
Kimmeridge Clay Fm.	Yes	Yes	3.5	2.4	4%
Ormskirk Sandstone Fm.	Yes	Yes	2.7	1.9	3%
Maureen Fm.	Yes	Yes	2.6	1.8	3%
Fulmar Fm.	Yes	No	1.9	1.3	NA
Firth Coal Fm.	Yes	No	1.5	1.0	NA
Horda Fm.	No	Yes	1.3	0.9	1%
Ness Fm.	No	Yes	0.6	0.4	1%
Balder Fm.	No	Yes	0.5	0.3	1%
Wick Sandstone Fm.	No	Yes	0.4	0.3	0%
Valhall Fm.	No	Yes	0.4	0.2	0%

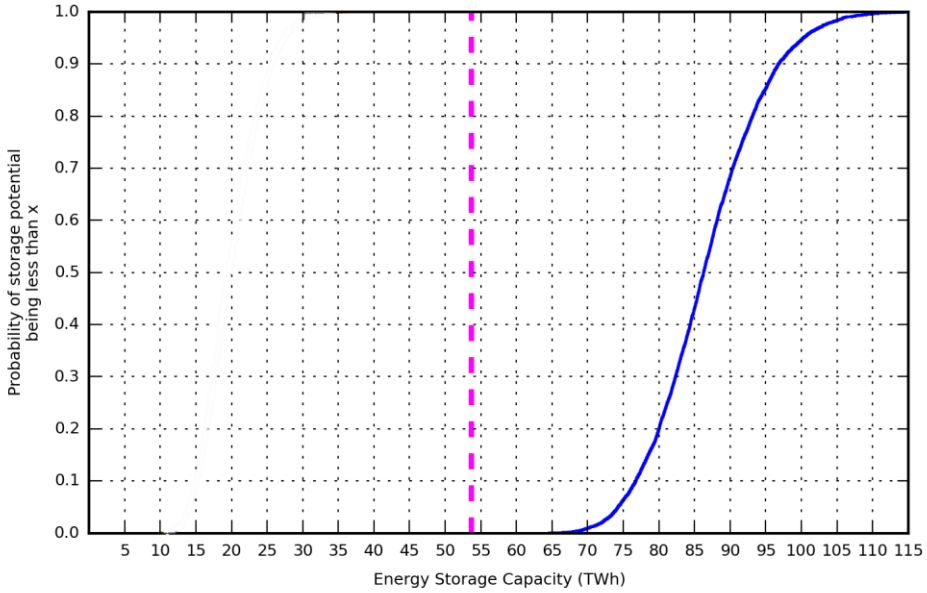

Figure 6-6: In blue, the PM-CAES storage potential found in offshore UK saline aquifers with no significant heterogeneity likely to hinder the cycling of air. The vertical dashed line represents the UK's electricity consumption over the months of January and February 2017.

6.4 Logistical Challenges

So far the assessment of the PM-CAES potential offshore UK has been focused on the geology. The use of offshore resources has proven to lead to several logistical challenges. It is therefore important to understand what those challenges are and what the best solutions to address them are. It is important to note that this scoping study focuses on the national scale for storage potential rather than attempting to identify specific storage sites. Although this section will discuss challenges relevant to individual sites, used to put the storage potential identified into perspective, it will not attempt to identify specific sites.

The key logistical challenges associated with developing an offshore PM-CAES project would be:

1. Air Transportation: How far does the pressurised air needs to be transported in pipelines after being compressed, or before being expanded in the turbine.
2. Electricity Transportation: How far does the electricity generated or consumed needs to be transported.
3. Proximity to shore: The distance from shore is likely to inform on whether the generation and compression will take place offshore or onshore.
4. Proximity to power source: How far from the power source used to compress the air can the storage be placed for it to remain viable?

5. Electricity Generation: what is the maximum generation capacity which could be installed offshore? How reliable and efficient would it be?

6.4.1 Air Transportation

Two options exist to transport air to and from the storage site: 1) use existing infrastructure, 2) build new infrastructure.

Using existing infrastructure would reduce the capital costs and legal procedure compared to building new infrastructure (DECC, 2012). In the case of air transportation, from the compression/expansion site to the storage site, there is an extensive network of oil and gas pipelines in the offshore UK waters which are due to be decommissioned. If those pipeline are able to operate safely under PM-CAES operation, using them could significantly reduce the cost of developing the technology offshore.

According to a report commissioned by the former UK Department of Energy and Climate Change available on the Global Carbon Capture and Storage Institute website, the main limitation to reusability of existing infrastructure is the design pressure of existing pipelines, generally 60 to 80 bars (DECC, 2012). Such operating pressure would limit the pressure of the storage. Indeed, if a storage site is located at depth greater than about 700 m it is likely that the storage pressure will lead to wellhead pressures greater than 60 bars which exceeds the pipeline maximum design pressure making existing pipelines unsuitable. This pipeline design pressure limitation would lead to the formations deeper than 700 m, with storage potential, to be unusable. Therefore, to make the most of the scoped storage potential new pipelines with higher operating pressure would have to be built.

Assuming then, that new pipeline will need to be built, calculation of the pressure drop occurring during the air transportation in the pipeline is needed in order to estimate a realistic distance between wellhead and plant. Unlike for natural gas and oil, adding boosting stations to maintain the pressure in the pipeline is not an option as it would defeat the purpose of having a single compression and expansion per CAES cycle and would make the system inefficient. Calculations of the pressure drop along a horizontal pipe, using Eq. 6-5 (Uhl, 1965; Mokhatab and Poe, 2012; PetroWiki, 2015b) and inputs from Table 6-4, were performed for different pipeline lengths and diameters. These calculations indicate (Figure 6-7) that the wider the pipeline the lower the pressure drop. However, the gas velocity also needs to be taken into account. A flow rate which is too high represents safety risks and increases the corrosion due to particles, whilst too low flow rates lead to fluid and particles deposition in the pipeline. The industry ballpark figures for maximum and minimum gas velocity in a pipeline are 24 m/s and

5 m/s respectively (Mokhatab and Poe, 2012) . The associated air flow velocity within the pipeline (Figure 6-8) can be calculated using Eq. 6-6 (Crane Co., 1988; PetroWiki, 2015a).

$$P_1^2 - P_2^2 = 1.2495 \cdot 10^{-3} \left[\frac{Q_a^2 Z T f_D L}{d^5}\right] \quad 6\text{-}5$$

Where, P_1 is the upstream pressure (bar), P_2 is the downstream pressure (bar), Q_a is the air flow rate ($stdm^3/s$), Z is the dimensionless compressibility factor of air, T is the flowing temperature (°K), f_D is the Darcy-Weisbach friction factor (dimensionless), d is the pipe internal diameter (m), L is the length of the pipe (m). This equation assumes that no work is performed, steady-flow, and f_D is a function of the pipe length. (Uhl, 1965; Mokhatab and Poe, 2012; PetroWiki, 2015b)

$$\mathrm{v} = 0.5985 \frac{Q_a T Z}{d^2 P} \quad 6\text{-}6$$

Where v the air velocity inside the pipe, m/s, Q_a the air flow rate in $stdm^3/s$, T the flowing gas temperature °K (taken as the sea floor temperature of 8°C), P the flowing gas pressure in bar (approximated as the difference between upstream and downstream pressures), Z the compressibility factor of the gas, d the pipe diameter in meters. (Crane Co., 1988; PetroWiki, 2015a)

These calculation suggest that a pipe diameter of 48 inches would lead to air velocities which are too low for pipelines ranging from 500 m to 100 km in length for pressure above 60 bars (red line in Figure 6-8). A Pipe diameter of 24 inches on the other hand, seems to offer velocities within the optimal velocity range of 24 m/s to 5 m/s for flowing pressure in the 80 to 250 bar range. As this range of pressure are likely to be encountered during PM-CAES operation, this suggests that pipelines around 24 inches in diameter are the most suitable. However flowing pressure should be at least above 110 bars in order to loose less than 10% of the upstream pressure through pipelines up to 10 km long. Pressure drops associated with the transfer of air through a 24 inch pipeline longer than about 10 km is unlikely to be economically viable to justify transporting the air to and from the shore.

Overall, an economic study should be performed in order to determine what pressure drop can be tolerated for the air transportation to and from the offshore storage site to the onshore plant in order for air transportation to be considered instead of offshore generation.

Table 6-4: Input parameters for the calculations of the pressure drop along pipelines as well as the transported air velocity. The air viscosity is assumed constant due to the flowing temperature being fixed to surface temperature. Note that the 417 kg/s flow rate is given as mass flow rate to make it comparable to Huntorf. Since the volumetric flow rates are given at standard the conversion is achieved by dividing by the air density at standard conditions.

Parameter	Imperial Units	Metric Units	SI Units	Imperial (Metric/SI)
$P_{upstream}$	x-axis			psia (bar/Pa)
$P_{downstream}$	y-axis (as% of $P_{upstream}$)			psia (bar/Pa)
Air flow rate, Q_a	1,060.29	417.00	2.59	MMscf/D (kg/s, $stdm^3/s$)
Compressibility Factor, Z	0.92			dimensionless
Flowing Temperature, T	506.07	8.00	281.15	°R (°C/°K)
Darcy-Weisbach friction factor, f_D	0.01			dimensionless
Pipe internal diameter, d	35.83	0.91		inches (m/m)
Pipe length, L	1,640 to 328,084	0.5 to 100,000		ft (m/m)
Pipe Roughness absolute	0.01	$2.54 \cdot 10^4$		inches for galvanized iron (m/m)
Pipe Roughness relative	0.0002			dimensionless
Air Dynamic Viscosity	0.0217		$2.17 \cdot 10^{-5}$	centipoise (NA/Pa.s)
Reynolds number, Re	$2.74 \cdot 10^7$			dimensionless

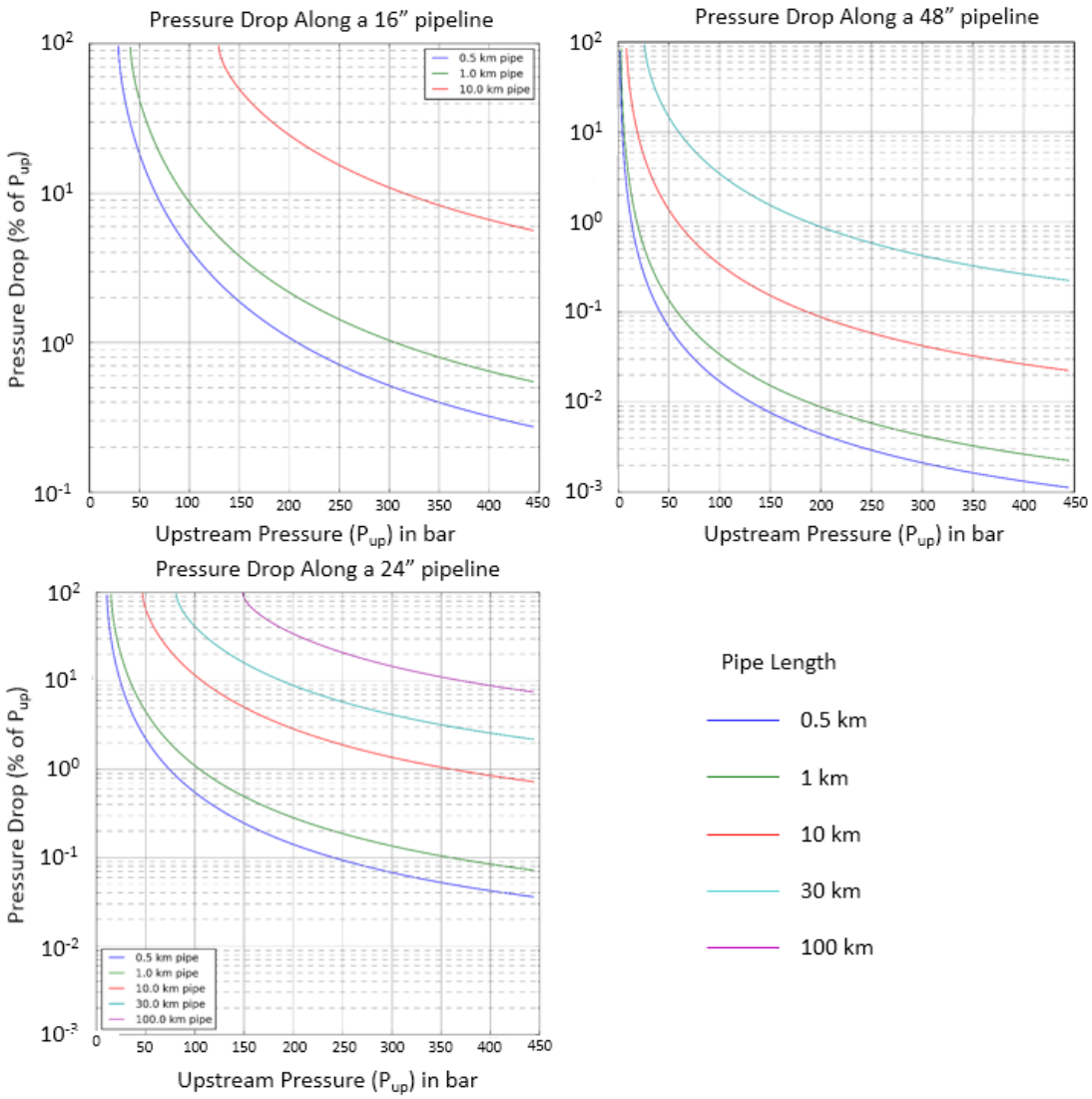

Figure 6-7: Pressure drop along a 16, 24 and 48 inches diameter pipelines as a function of upstream pressure. These result indicate that the greater the length of the pipeline the greater the pressure drop at the outlet of the pipeline. This observation is independent from the pipe's diameter.

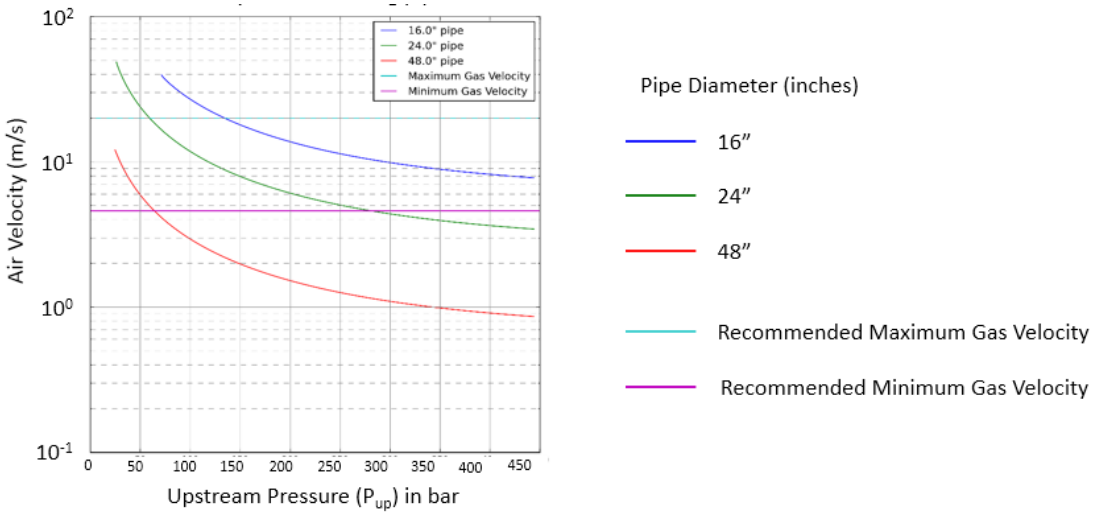

Figure 6-8: Air velocity in pipeline as a function of upstream pressure. The optimal pipe would be a 24" pipe up to 10 km long, for this pipe both the pressure drop and the air velocity would be acceptable.

6.4.2 Electricity Transportation

The 10 km pipeline length threshold recommended above as the upper limit which allows transportation of the compressed air between an offshore store and an onshore plant indicates that, in order to benefit from most of the storage potential identified, generation and compression would occur offshore. Hence, electricity would need to be transported both from the windfarms to the compression site, and then from the generation site to the mainland grid. This alternative seems to present limited issues since international interconnectors and cables from windfarms to shore have already proven to be a viable option. The detailed costing would need to be studied further, but using existing cables should prove feasible since the storage will likely be in operation when the windfarms are not producing. This could also make existing subsea cable more profitable as they could be used more often. In the costings presented in section 6.5.2, it was assumed that the electricity transportation costs would be similar to those of a windfarm (OWPB, 2016).

6.4.3 Offshore Electricity Generation and Air compression

Compressing air and generating electricity from it offshore is hindered by low turbomachinery efficiencies, and limited compressor load capacity and turbine generation capacity (Wall, Lee and Frost, 2006). Load capacity is the ability of a device to consume electrical power. The term "gas turbine package" includes all the equipment needed to operate a conventional gas turbine, including a compressor. Operating gas turbine packages offshore has been common practice for decades in the hydrocarbon industry (Wall, Lee and Frost, 2006). There is extensive experience which could be transferred to developing PM-CAES.

To understand what may incentivise a PM-CAES operator to decide to generate electricity offshore, it is important to understand the drivers for the hydrocarbon industry, and to compare them to the drivers for conventional industrial power generation. The main drivers for using turbines in the hydrocarbon industry are: availability and reliability, to cope with sudden changes in operation; ruggedness, to deal with harsh offshore operating conditions; high power output to device weight ratio, to maximize the use of available space and preserve the structural integrity of the offshore platform (Wall, Lee and Frost, 2006). On the other hand the main drivers for using turbines in industrial power generation are the cost of electricity and the efficiency to maximize profits, and low cost of operations and maintenance (Wall, Lee and Frost, 2006).

It is interesting to consider which of those drivers a PM-CAES operator would share. For a PM-CAES project using Conventional-CAES turbomachinery, the cost of fuel burned in the turbine would be important, hence making efficiency a prevalent driver. Considering that PM-CAES would be designed for inter-seasonal storage and used as baseload, one could expect availability and start up time to be less significant drivers.

The typical gas turbine power capacity for offshore generation is typically 1 MW to 30 MW and two turbines per platform is a norm (Wall, Lee and Frost, 2006). Considering that transporting the compressed air to and from the platform will lead to efficiency losses (see section 6.4.2) and considering the Southern North Sea, where over 50% of the storage potential is found, has over 100 platforms (Figure 6-9), spreading the generation over platforms could be beneficial as it would prevent decommissioning of platforms and reduce the pressure losses of air transportation between the storage and the turbomachinery. The main limitation to offshore production using existing infrastructure would be to ensure that a suitable store is located within 10 km of the compressor and turbine installations. It is likely if the target store is a depleted gas field which used to be exploited from a nearby platform, it is much less likely if the target store is a saline aquifer.

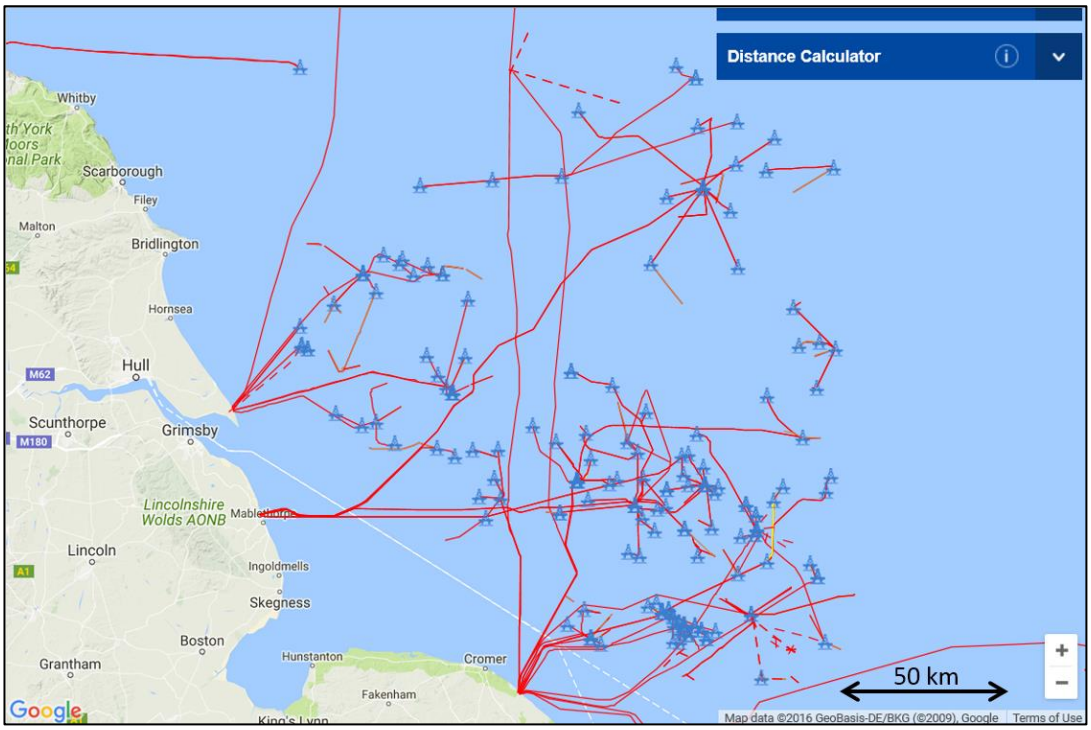

Figure 6-9: Map showing offshore platforms and pipelines in the SNS (with authorisation from www.fishsafe.eu)

Offshore compression in the hydrocarbon industry is achieved using a gas turbine to drive the compressor. This is because gas is readily available at a relatively low cost for the platform operators. In the case of a PM-CAES project it is likely that the compressor will be driven by an electrical motor (most likely also able to act as a generator during production phase in order to maximise the use of space on the platform).

In conclusion offshore power generation can be expected to reach up to 60 MW per platform using existing technology and expertise from the hydrocarbon industry. It appears that assessment would be required for sites identified within the areas with a storage potential identified in this work.

6.4.4 An Alternative to Decommissioning

Although the costs of developing large scale offshore inter-seasonal PM-CAES are high, an order of magnitude greater than Pumped Hydro Storage (PHS) (see section 6.5.2), its development could postpone or reduce the cost of decommissioning in the North Sea. The cost of decommissioning an estimated 8,563 pieces of hydrocarbon industry infrastructure (including: platforms, pipelines, wells and production systems) in the UK North Sea are projected to range from £30 to £50 billion over the next 30 years (Royal Academy of Engineering, 2013; KPMG, 2015). Furthermore, the UK government's position on decommissioning intend to "recognise the need to maximise energy production as a

contribution to the UK energy security and take impacts on climate change into account" (BEIS, 2017). Developing storage technologies such as offshore PM-CAES would contribute to both of those policy aims by doubling the capacity factor of renewable wind generation (Cavallo, 1995; Succar and Williams, 2008; Denholm and Sioshansi, 2009), as well as reduce the UK's reliance on power imports (Pfenninger and Keirstead, 2015). It is also important to note that the financial incentive of postponing, where possible, the cost of decommissioning, does not only apply to the hydrocarbon sector but also to the UK Government in the form of tax relief which are estimated at up to £20 billion (Royal Academy of Engineering, 2013; KPMG, 2015), although the hydrocarbon sector has significantly contributed through the Petroleum Revenue Tax.

Arguing that all decommissioning could be postponed is unrealistic, however experts agree that building decommissioning experience will greatly reduce the costs of further decommissioning projects (Royal Academy of Engineering, 2013; KPMG, 2015; Oil & Gas Authority, 2016). Hence, providing an alternative such as PM-CAES would extend the period of time over which experience and innovation in the sector of offshore decommission could be acquired.

6.5 Refining Estimates Accounting for Winfarms

It has been reported that PM-CAES developed alongside windfarms could raise their capacity factor from 30-40% to 80-90% (Cavallo, 1995; Succar and Williams, 2008; Denholm and Sioshansi, 2009). Such an increase in capacity factor would allow windfarms to deliver, as a baseload, the minimum annual electricity demand throughout the year (Mason and Archer, 2012). For this reason, it was assumed that economically attractive PM-CAES storage sites would be positioned near windfarms. A geographic information system (GIS) (Figure 6-1 h.) was used to identify this fraction of the 77 to 96 TWh storage potential (Figure 6-1 i.). This section presents the offshore windfarm resource and developments plans for the UK, followed by the storage potential contained in stores co-located with the windfarms which minimise the costs of transportation.

6.5.1 GIS Study

As of February 2018, the UK has a total of 1,660 operational offshore wind turbines, spread around 31 projects, equivalent to 6.4 GW of nameplate capacity (that is the theoretical maximum amount the windfarms can produce in simultaneous optimal operation) (RenewableUK, 2018). The windfarm capacities range from 630 MW for the "London Array 1" to 4 MW for Blyth. The consented projects Creyke Beck A and B, at Dogger Bank in the Southern North Sea, will each have a capacity of 1.2 GW making them the largest offshore

windfarms in the UK. A storage site should be able to operate at about 10% of the capacity of the windfarm it will be designed for (personal conversation with SENVION electrical engineers). This implies that, according to this work, much more storage is available than is currently required.

The GIS analysis was performed by using the outlines of the CO_2 Stored entries and displaying them alongside windfarms areal data. It was found that about 40% of the offshore windfarms of the UK are located on geological saline aquifer formations with storage potential. This is equivalent to approximately 7.4 GW of installed generation capacity (i.e. 3 GW assuming a capacity factor of 40%) of windfarms that are either in operation, under-construction or have consent for development. When refining the outlines using only aquifer subsets (type 2 and 3) it was found that seven entries where colocated to windfarm developments (see Figure 6-10). The entries are spread amongst the East Irish Sea, Moray Firth and Southern North Sea. According to this study, the most promising area is the Southern North Sea where over 93% of the colocated storage potential is found.

Geographical data available on the windfarm sites shows that transporting the air back to shore is not a viable option since most windfarms are more than 10 km from the shore. Furthermore, only a small portion of the areas with storage potential are within 10 km of the shore.

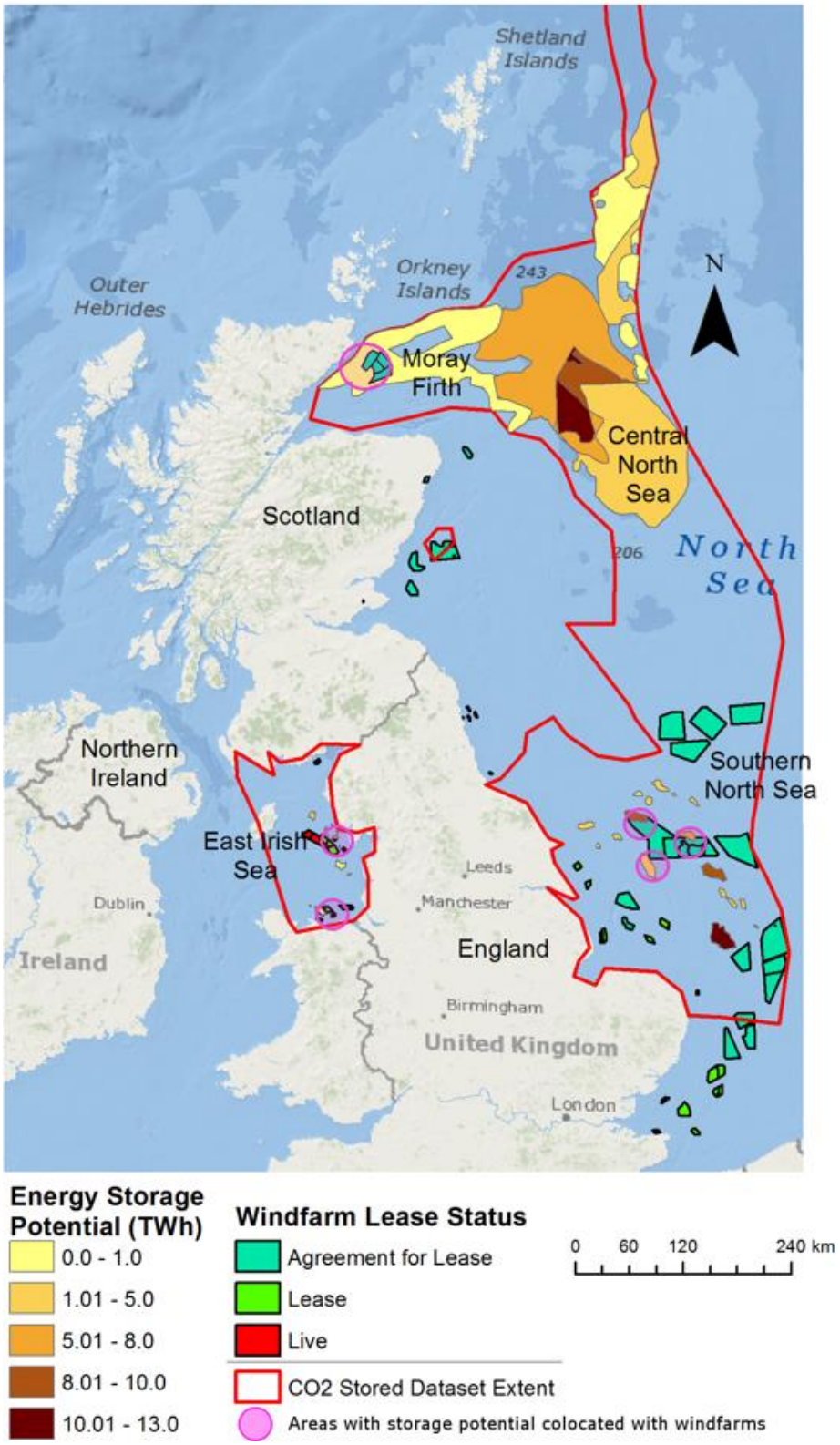

Figure 6-10: Map of the UK's offshore windfarms and potential storage formations from the CO2 Stored database. The Windfarms include all the existing offshore windfarms as well as projects of interest to be developed in the next 5-10 years (including dudgeon, Race Bank, Dogger Bank, Moray Firth, East Anglia ONE, Hywind pilot projects). Windfarm data under © Crown Copyright 2017. Additional maps showing

the power capacity of the storage during discharge and the roundtrip efficiency of the system can be found in Appendix 8.5.

6.5.2 Refined Storage Estimates and Costings

Seven areas offshore UK with good storage potential, that are colocated with windfarms, have been identified, namely: the Burns member of the Kimmeridge Clay formation, three geological traps in the Bunter Sandstone Formation (numbered 1, 2 and 35 in the CO_2 Stored database), and three in the Ormskirk Formation (numbered 4, 6, 12). The Monte Carlo analysis described in section 6.2.3 was run once more using only those seven entries to estimate their likely potential. A storage potential of 20 TWh was found to be colocated with windfarms, for which construction permission has been approved. It could be delivered at 13.6 GW for a period of 60 days. There is a 50% chance that higher energy and power capacity values are possible (orange line in Figure 6-11). The results show that the expected capacity within those seven areas is greater than 10% of the outputs from the windfarms with which it is colocated, hence sufficient to accept the excess capacity that the windfarms would produce. Yet, the storage capacity is not sufficient to meet the entire electricity demand for 2 winter months in the UK, as is shown by the orange line being to the left of the dotted vertical line in Figure 6-11.

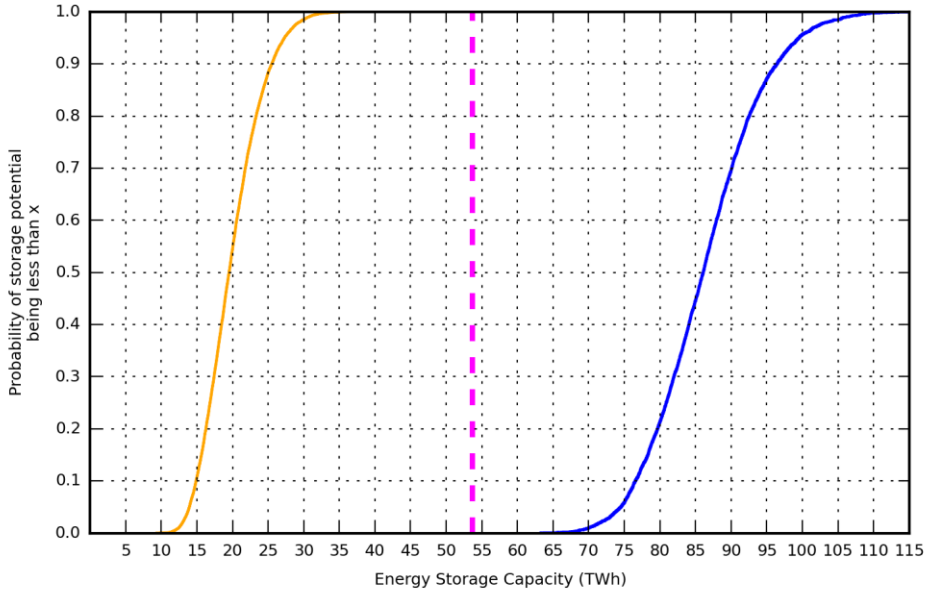

Figure 6-11: In orange, the storage potential contained in the seven areas colocated with offshore UK windfarms. In blue, the PM-CAES storage potential found in offshore UK saline aquifers with no significant heterogeneity likely to hinder the cycling of air. The vertical dashed line represents the UK's electricity consumption over the months of January and February 2017.

Cost estimates were then performed to compare inter-seasonal PM-CAES to other storage technologies. The analysis is based on the net present value (NPV), for 2015; of the cost of

offshore wells (Pale Blue Dot Energy, 2016); electricity transmission costs to shore (OWPB, 2016); turbine and compressor capital expenditure (CAPEX) (Mignard, 2014) and operation and maintenance costs (O&M); natural gas fuel costs; and electricity cost to power the compressor (Steward *et al.*, 2009). A 10% discount rate was assumed in the calculations. The same value is used in costing assessments for offshore Carbon Capture and Storage projects (Pale Blue Dot Energy, 2016). The costs associated with decommissioning have also been included in the estimate, assuming they would be similar to those of a storage site for Carbon Capture and Storage (Pale Blue Dot Energy, 2016). The results from research on CAES sites on islands by Mignard (2014) were used to calculate the CAPEX for the turbine and compressor. The heat rate of the CAES plant was estimated at 4,000 Btu/kWh, which is similar to the heat rate of the McIntosh plant (Steward *et al.*, 2009).

The levelised cost of electricity (LCOE) for the CAES system was calculated as the sum of the discounted costs per year over the discounted annual energy production from the storage facility as described in Eq. 6-7.

$$LCOE = \frac{\sum_{t=1}^{n} \frac{W_t + T_t + C_t + M_t + F_t + S_t + D_t}{(1+r)^t}}{\sum_{t=1}^{n} \frac{E_t}{(1+r)^t}} \qquad 6\text{-}7$$

where W_t is the well investment expenditure; T_t and C_t the turbine and compressor investment, respectively; M_t, the fixed operation and maintenance expenditures; F_t and S_t the fuel and compressor electricity supply expenditure, respectively. The subscript t denotes the year in which the expenditure occurs. E_t is the electrical energy generated by the CAES plant. r is the discount rate and n the lifetime of the CAES project. The tabulated detailed costings are provided as digital supplementary information.

This study finds that the levelised cost of electricity for offshore PM-CAES, would range from 0.87 $/kWh to 1.88 $/kWh. These estimates assume a net present value cost per well of approximately 9 million US 2015 dollars. They suggest that the cost of offshore PM-CAES would be about one order of magnitude greater than that of onshore PM-CAES and PHS reported in the literature (Table 6-5). Even the 20 TWh storage potential colocated with offshore windfarms would necessitate approximately 1,700 air cycling wells. The average levelised cost of developing an offshore PM-CAES site colocated with a windfarm would be of 0.99 $/kWh, for projects starting in 2020. It is therefore recommended that PM-CAES projects should be originally undertaken onshore, in order to allow the technology to mature and the costs to go down.

Table 6-5: Cost of storage technologies. Batteries have been included for comparison, despite not being suited to bulk grid-connected inter-seasonal storage. The levelised costs of electricity presented for PHS, generic underground CAES (which includes the use of salt caverns, mines and porous rocks as stores), and Onshore CAES in porous rock, are all applicable to projects with capacities of hundreds of megawatts. However, no data was found for projects capable of providing inter-seasonal storage with a production of 60 days equivalent to the one in this study.

Technology	Costs $/kWh		
	Min	Max	Most Likely
Batteries (NiCd) (Zakeri and Syri, 2015)	0.35	0.49	0.42
PHS (Succar and Williams, 2008; Obi *et al.*, 2017)	0.095	0.269	0.182
Generic underground CAES (Succar and Williams, 2008; Zakeri and Syri, 2015; Obi *et al.*, 2017)	0.058	0.250	0.154
Onshore CAES in porous rocks (Zakeri and Syri, 2015)(McGrail *et al.*, 2013)	0.060	0.12	0.110
Offshore CAES in saline aquifers (this study)	0.870	1.879	1.453

6.6 Conclusion

This chapter presented the workflow to estimate a national PM-CAES potential. It highlighted that the offshore UK sandstone saline aquifers alone have the potential to hold 77 to 96 TWh. This storage potential is large enough to meet a demand equivalent to the UK's electricity consumption during January and February 2017. This chapter also highlighted the importance of logistical and economical challenges likely to hinder the development of offshore PM-CAES. This study finds that those challenges are likely to limit the development of the technology to seven areas were the benefits of PM-CAES could be maximised by increasing the capacity factor, that is the useable output, of windfarms. In addition, even in those areas the cost of the development is found to be around an order of magnitude greater than onshore PM-CAES. This chapter results in the paradox that the UK possesses a significant storage resource in the form of offshore saline aquifers, but that most of this potential is currently logistically challenging to achieve and economically unattractive. This conclusion highlights the crucial difference between the concept of known resource and usable reserves. This study succeeded in providing a workflow to estimate storage resource on a large scale using simple predictive models, yet it shows that more specific investigations are needed to identify actual storage sites within the areas identified as having storage potential.

Chapter 7 Conclusions

The aim of this study was to provide an estimate of how much energy could be delivered, at what power and with what roundtrip efficiency in the UK, with inter-seasonal PM-CAES in offshore saline aquifers. This was achieved by developing numerical and analytical models of the key components of the PM-CAES system applicable to inter-seasonal storage. These models included: a numerical finite element model of the saline aquifer store developed in the open source code OpenGeoSys; an analytical model of the wellbore; a computer model of the compressor and turbine used for air compression and electricity generation respectively, in conventional-CAES. The outputs from the sensitivity analysis of those models enabled algebraic predictive models to be developed. These simple models could be used to efficiently perform Monte Carlo simulations of storage potential, using inputs from a dataset of offshore UK saline aquifers called the CO_2 Stored database.

7.1 Models' Development

The storage model was developed to allow an understanding of changes occurring in the store during an inter-seasonal PM-CAES cycle. The model design was focused on flexibility and computational efficiency in order to achieve an understanding of those changes, over the ranges of geological criteria suitable for PM-CAES compiled from the literature. This was achieved by developing a streamlined, multiphase flow, finite element, idealised reservoir model. This model represents the area of a store affected by the pressure changes, caused by a single well forming part of a wider array of wells. The idealised model could them be approximated using a computationally efficient 2D solution, which enabled multiple simulations to be ran using different input combinations for the rock's permeability, depth, porosity, and thickness covering the range of these criteria.

The development of the computer plant model incorporated models of the energy consumption of the compressor and energy generation from the turbine, as well as a combustor model to estimate the natural gas consumption needed to reheat the air entering the turbine. The three models were integrated together in a Python 2.7 code. The code also integrated a wellbore model which determined the pressure and temperature changes occurring as the compressed air travelled between the store and the surface.

Finally, algebraic predictive models for the power output, roundtrip efficiency and charging electricity ratio of the inter-seasonal PM-CAES system studied were developed using multiple linear regressions, on the outputs of the sensitivity analyses of the numerical store and plant models. The predictive models showed an accuracy comparable to those of the numerical

models, enabling them to be used with confidence to predict the storage potential of the inter-seasonal PM-CAES system, based on the store's depth and the turbomachinery efficiencies.

7.2 Findings

The power output which can be attributed to an individual well used to perform inter-seasonal PM-CAES was found to be in the order of that obtain for single offshore wind turbine, which is 4 to 12 MW during the production phase. These well power outputs lead to an average cost for offshore inter-seasonal PM-CAES of ~1.9 $\$_{2017}$/kWh, which is over an order of magnitude higher than the cost of developing the PM-CAES onshore for daily to weekly storage. It is therefore suggested that the cost difference might be due to two factors: first, the limited power output per well, which would lead to a cost per MW greater than that of wind turbines; second, inter-seasonal storage requires a single annual cycle with only two months of production per year. One must however consider that these estimates do not consider the potential gains from the electricity price difference between the compression and production phase. Neither do they consider the income which might result from the service of providing a load to the electricity network when needed (i.e. ability to consume electricity). Such gains might be greater for inter-seasonal storage than daily storage.

Another key finding of this work, is that for aquifers with characteristics within the siting criteria, it is reasonable to estimate the downhole pressure of the well using a linear correlation to the depth of the store, at any given time during the cycle. This work finds that the inaccuracies in that linear relationship do not significantly impact the overall assessment estimate.

This work is able to identify offshore areas with the highest storage potential based on a GIS analysis of the results and the overlapping of the various aquifer units containing storage potential. The greatest storage potential is found in the Bunter Sandstone closures, in the Southern North Sea. Most of the remaining potential is found in the Northern North Sea and Central North Sea within the Statfjord and Sele Formations. Some potential has also been identified within areas of the Ormskirk Sandstone under the East Irish Sea. This storage potential is the only one identified offshore of the West coast of the UK.

A key achievement of this work was to develop predictive models which can be applied to other saline aquifer datasets worldwide, as long as the aquifers fall within the parameter ranges defined by the siting criteria of this work. As the main assumptions of this work are conservative, the prediction made using these models should provide a reasonable estimate of the storage resource. This is an important output of this work as it enables other assessments of storage potential to be made, without the need to perform the computationally expensive

numerical simulations of the PM-CAES system. These predictive models are only valid to estimate storage potential on a national scale, using a dataset covering the range of store depths recommended in this work. The predictive models are not suited to estimate potential contained in individual sites, since such estimates would only be meaningful alongside a techno-economic assessment.

7.3 Recommendations

This research provides a basis on which to identify storage sites suitable for inter-seasonal PM-CAES offshore UK. Areas highlighted in this work as offering significant storage potential should be investigated to identify how much of this storage is likely to be converted into useful reserves. The lack of accurate energy storage and power capacity estimates at specific storage sites, within the areas with storage potential, is a major limitation of this work, further research is needed to identify specific storage sites. These estimates could be used to quantify the inaccuracies of the scoping storage potential estimates proposed by this work.

Due to the sheer scale of the required storage volumes it is important that further work should be done to investigate the potential interferences of developing inter-seasonal PM-CAES sites in saline aquifers in which hydrocarbon production is currently taking place. Investigations should consider potential positive interactions, like the pressure support that a PM-CAES site might be able to provide for oil extraction during the injection phase, as well as the potential negative interactions such as seasonal drops in pressure and loss of productivity of hydrocarbon wells, as well as over pressure issues caused by the rapid injection of air in the vicinity of hydrocarbon fields.

The numerical model of the store could be improved to allow the modelling of geochemical reactions throughout the lifetime of the store. Such modelling might be able to confirm or inform previous conclusions from a field test that the geochemical reactions occurring within the store only occur in the initial development of the store. This would be an important study as geochemical reactions can modify the flow capabilities of the reservoir. Another improvement would be the accurate modelling of temperature within the store. This would enable other storage options to be studied, such as the injection of hot air, or cool air resulting from an isothermal compression. Such developments could lead to a roundtrip efficiency increase in the overall system, due to reduced heat losses, reducing the costs. Although this study showed no major issues from water ingress into the well, it could prove to be a problematic issue for inter-seasonal PM-CAES in open aquifers. The importance of this issue has been debated for daily PM-CAES, but further work is needed to address it at inter-seasonal scales. Finally, a comparative study between the results obtained using OpenGeoSys and a

standard industry simulator could be performed to increase the confidence and impact of this work.

In conclusion, this research has been useful in demonstrating that the UK has potential to develop inter-seasonal PM-CAES within its offshore saline aquifers. It shows that this storage potential is in excess of what will likely actually needed, despite the large uncertainty in future inter-seasonal storage needs (Blanco and Faaij, 2018). It lays the foundations for further storage site specific investigations, by identifying in which geological formations the storage potential might be found. Any further site specific work should consider the implications of using horizontal against vertical wells. This study however finds, that the cost of offshore development of the technology is likely to be too high to be economically attractive in the short term, and recommends onshore investigations in order to provide a "proof of concept" initial project. The parameter ranges developed in this research should serve as a sound basis to identify onshore potential.

References

Aadnoy, B. (1991) ‘Effects of reservoir depletion on borehole stability’, *Journal of Petroleum Science and Engineering*, 6, pp. 57–61.

Aadnoy, B. S. and Kaarstad, E. (2010) ‘History Model for Sand Production During Depletion’, in *SPE EUROPEC/EAGE Annual Conference and Exhibition*, pp. 14–17.

Allen, R. D., Doherty, T. J., Erikson, R. L. and Wiles, L. E. (1983) *Factors affecting storage of compressed air in porous-rock reservoirs*. Available at: http://www.osti.gov/scitech/biblio/6270908 (Accessed: 23 September 2014).

Allen, R. D., Doherty, T. J., Schainker, R. B., Istvan, J. A. and Pereira, J. C. (1984) ‘Preliminary results from the pittsfield aquifer field test applicable to commercialization of CAES technology.’, in *Intersociety Energy Conversion Engineering Conference*. San Francisco, USA, p. pp.1081–1090.

Allen, R. D., Doherty, T. J. and Thoms, R. L. (1982) *Geotechnical Factors and Guidelines for Storage of Compressed Air in Solution Mined Salt Cavities. Technical Report PNL-4242*.

Allen, R. D. and Gutknecht, P. J. (1980) *Porous Media Experience Applicable to Field Evaluation for Compressed Air Energy Storage, Pacific Northwest Laboratory*. Available at: http://scholar.google.com/scholar?hl=en&btnG=Search&q=intitle:No+Title#0 (Accessed: 26 September 2014).

Allen and Patrick, M. (1997) ‘The coefficient of determination in multiple regression’, in *Understanding Regression Analysis*. Boston, MA: Springer, pp. 91–95. doi: 10.1007/978-0-585-25657-3_19.

Amid, A. (2013) ‘MSc Dissertation Thesis MSc in Sustainable Energy Systems Practicalities of using disused gas reservoirs for the storage of renewable hydrogen’, *Unpublished*, (August).

Antoine, C. (1888) ‘Tensions des vapeurs: nouvelle relation entre les tensions et les températures.’, *Comptes Rendus des Séances de L’Aacadémie des Sciences,* 106, pp. 57–60. Available at: http://visualiseur.bnf.fr/CadresFenetre?O=NUMM-3063&I=681&M=tdm.

Argaud, M. J. (1992) ‘Predicting the Interfacial Tension of Brine/Gas (or Condensates) Systems, in *International Symposium of the Society of Core Analysts*. Paris, pp. 147–174. Available at: http://www.ux.uis.no/~s-skj/ipt/Proceedings/SCA.1987-2004/1-SCA1992-08EURO.pdf.

Armour, A., Evans, D. and Hickey, C. (2003) *The Millennium Atlas : petroleum geology of*

the central and northern North Sea, Petroleum Geology. London: The Geological Society of London.

Armstrong, R. a, Slade, S. V and Eperjesi, F. (2000) 'An introduction to analysis of variance (ANOVA) with special reference to data from clinical experiments in optometry.', *Ophthalmic & physiological optics : the journal of the British College of Ophthalmic Opticians (Optometrists)*, 20(3), pp. 235–241. doi: 10.1046/j.1475-1313.2000.00502.x.

Austin, S. P. (1995) 'Rock Mechanics', in Jaak J.K. Daemen, R. A. S. (ed.) *35th US Symposium on Rock Mechanics*, p. 956.

Azin, R., Nasiri, a. and Entezari, J. (2008) 'Underground Gas Storage in a Partially Depleted Gas Reservoir', *Oil & Gas Science and Technology - Revue de l'IFP*, 63(6), pp. 691–703. doi: 10.2516/ogst:2008028.

Bachu, S. (2015) 'Review of CO2 storage efficiency in deep saline aquifers', *International Journal of Greenhouse Gas Control*, 40, pp. 188–202. doi: 10.1016/j.ijggc.2015.01.007.

Barbour, E. (2013) *An Investigation into the potential of Energy Storage to tackle Intermittency in Renewable Energy Generation*. The University of Edinburgh. Available at: https://www.era.lib.ed.ac.uk/bitstream/handle/1842/8189/Barbour2013.pdf?sequence=1&isAllowed=y.

Barbour, E., Mignard, D., Ding, Y. and Li, Y. (2015) 'Adiabatic Compressed Air Energy Storage with packed bed thermal energy storage', *Applied Energy*, 155, pp. 804–815.

Bastin, J. C., Boycott-Brown, T., Sims, A. and Woodhouse, R. (2003) 'The South Morecambe Gas Field, Blocks l10/2a, l10/3a, l10/7a and l10/8a, East Irish Sea', *United Kingdom Oil and Gas Fields, Commemorative Millennium Volume*, (14), pp. 107–118.

Bauer, S., Beyer, C., Dethlefsen, F., Dietrich, P., Duttmann, R., Ebert, M., Feeser, V., Görke, U., Köber, R., Kolditz, O., Rabbel, W., Schanz, T., Schäfer, D., Würdemann, H. and Dahmke, A. (2013) 'Impacts of the use of the geological subsurface for energy storage: an investigation concept', *Environmental Earth Sciences*, 70(8), pp. 3935–3943. doi: 10.1007/s12665-013-2883-0.

Bear, J. (1972) *Dynamics of Fluids in Porous Media*. New York: Elsevier.

BEIS (2017) 'Guidance Notes (draft): Decommissioning of Offshore Oil and Gas Installations and Pipelines', (December), p. 126. Available at: https://www.ogauthority.co.uk/decommissioning/programmes-guidance/.

References

Benson, S., Pini, R., Reynolds, C. and Krevor, S. (2013) *Global CCS institute targeted report no. 2 relative permeability analyses to describe multi-phase flow in co 2 storage reservoirs*.

Bentham, M., Mallows, T., Lowndes, J. and Green, A. (2014) 'CO2 STORage Evaluation Database (CO2 Stored). The UK's online storage atlas', *Energy Procedia*. Elsevier B.V., 63(0), pp. 5103–5113. doi: 10.1016/j.egypro.2014.11.540.

BERR (2007) *BERR Well Production*. Available at: https://itportal.decc.gov.uk/information/wells/pprs/Well_production_offshore_gas_fields/offshore_gas_fields_by_well/offshore_gas_fields_by_well.htm (Accessed: 25 August 2017).

Bifani, R. (1986) 'Esmond gas complex', in Brooks, J., Goff, J. C., and van Hoorn, B. (eds) *Habitat of Palaeozoic Gas in N.W. Europe. Geological Society Special Publication No. 23*, pp. 209–221.

Blanco, H. and Faaij, A. (2018) 'A review at the role of storage in energy systems with a focus on Power to Gas and long-term storage', *Renewable and Sustainable Energy Reviews*. Elsevier Ltd, 81(August 2017), pp. 1049–1086. doi: 10.1016/j.rser.2017.07.062.

Bloomfield, J. P., Gooddy, D. C., Bright, M. I. and Williams, P. J. (2001) 'Pore-throat size distributions in Permo-Triassic sandstones from the United Kingdom and some implications for contaminant hydrogeology', *Hydrogeology Journal*, 9(3), pp. 219–230. doi: 10.1007/s100400100135.

Boote, D. R. D. and Gustav, S. H. (1987) 'Evolving depositional systems within an active rift, Witch Ground Graben, North Sea', in Brooks, J. and Glennie, K. W. (eds) *Petroleum geology of North West Europe*. London: Graham & Trotman, pp. 819–833.

Boveri, B. B. (1986) 'Operating Experience With the Huntorf Air-Storage Gas Turbine Power Station', *Brown Boveri Review*, 73(6), pp. 297–305.

Bradford, S. A. and Leij, F. J. (1995) 'Wettability effects on scaling two- and three-fluid capillary pressure-saturation relations', *Environ. Sci. Technol.*, 29(6), pp. 1446–1455.

Braester, C. and Bear, J. (1984) 'Some Hydrodynamic Aspects of Compressed Air Energy Storage in Aquifers', *Journal of Hydrology*, 73, pp. 201–225. Available at: http://scholar.google.com/scholar?hl=en&btnG=Search&q=intitle:No+Title#0 (Accessed: 29 September 2014).

Bridgeman, O. C. and Aldrich, E. W. (1964) 'Vapor Pressure Tables for Water', *Journal of Heat Transfer*, 86(2), pp. 279–286. doi: 10.1115/1.3687121.

References

Brill, J. P. and Mukherjee, H. (1999) 'Multiphase Flow in Wells', *SPE Monograph Series*, 17.

Brooks, R. H. and Corey, A. T. (1966) 'Properties of porous media affecting fluid flow', *Proceedings of the American Society of Civil Engineers*, 92(IR2), pp. 61–87. Available at: http://cedb.asce.org/cgi/WWWdisplay.cgi?14175.

Bushell, T. P. (1986) 'Reservoir Geology of the Morecambe Field', *Geological Society, London, Special Publications*, 23(1), pp. 189–208. doi: 10.1144/GSL.SP.1986.023.01.12.

Cameron, T. D. J. (1993) '4. Triassic, Permian and Pre-Permian of the Central and Northern North Sea', in Knox, R. W. O. and Cordey, W. G. (eds) *Lithostratigraphic nomenclature of the UK North Sea*. British Geological Survey on behalf of the UK Offshore Operators Association. Available at: http://www.bgs.ac.uk/downloads/browse.cfm?sec=1&cat=195.

Carstens, H. and Jepsen, B. (1981) 'Geotemperatures of North Sea Basins: Implications to Exploration: ABSTRACT', *AAPG Bulletin*, 65(7), pp. 1359–1360.

Castelletto, N., Ferronato, M., Gambolati, G., Janna, C., Teatini, P., Marzorati, D., Cairo, E., Colombo, D., Ferretti, A., Bagliani, A. and Mantica, S. (2010) '3D geomechanics in UGS projects: a comprehensive study in northern Italy', in *44th American Rock Mechanics Association Symposium*. Available at: http://treuropa.com/uploads/2010_3D_geomechanics_in_UGS_projects_comprehensive_study_in_northern_Italy.pdf (Accessed: 19 September 2014).

Cavallo, A. J. (1995) 'High-Capacity Factor Wind Energy Systems', *Journal of Solar Energy Engineering*, 117(May 1995).

Çengel, Y. a. (2004) 'Thermodynamics: An Engineering Approach', *McGraw-Hill*.

Centrica (2015) 'Rough Gas Storage Facility, An operational Overview'.

Chang, C., Zoback, M. D. and Khaksar, A. (2006) 'Empirical relations between rock strength and physical properties in sedimentary rocks', *Journal of Petroleum Science and Engineering*, 51(3–4), pp. 223–237. doi: 10.1016/j.petrol.2006.01.003.

Chen, H., Ngoc, T., Yang, W., Tan, C. and Li, Y. (2009) 'Progress in electrical energy storage system : A critical review', *Progress in Natural Science*. National Natural Science Foundation of China and Chinese Academy of Sciences, 19(3), pp. 291–312. doi: 10.1016/j.pnsc.2008.07.014.

Clark, D. N., Riley, L. A. and Ainsworth, N. R. (1993) 'Stratigraphic, structural and depositional history of the Jurassic in the Fisher Bank Basin, UK North Sea', *Geological*

Society, London, Petroleum Geology Conference series, 4(1), p. 415 LP-424. Available at: http://pgc.lyellcollection.org/content/4/1/415.abstract.

Clausius, R. (1854) 'Über eine veränderte Form des zweiten Hauptsatzes der mechanischen Wärmetheorie', *Annalen der Physik.*, Poggendoff(xciii), pp. 481–506.

Cohen, E. R. and Taylor, B. N. (2016) 'CODATA recommended values of the fundamental physical constants: 2014', *Reviews of modern physics*, 88(3), p. 35009. doi: 10.1063/1.555817.

Commission, E. (2016) *Appraisal well, detailed design & commercial structure 1.12-0006-UK-S-M-16 Part of Project of Common Interest 1.12*. Available at: https://ec.europa.eu/inea/sites/inea/files/1.12-0006-uk-s-m-16.pdf (Accessed: 30 August 2017).

Converse, A. O. (2012) 'Seasonal energy storage in a renewable energy system', *Proceedings of the IEEE*, 100(2), pp. 401–409. doi: 10.1109/JPROC.2011.2105231.

Cooke-Yarborough, P. and Smith, E. (2003) 'The Hewett fields: Blocks 48/28a, 48/29, 48/30, 52/4a, 52/5a, UK North Sea: Hewitt, Big Dotty, Little Dotty, Della, Dawn and Delilah fields', in Gluyas, J. . and Hichens, H. M. (eds) *United Kingdom Oil and Gas Fields, Commemorative Millenium Volume. Memoir 20*. London: Geological Society, pp. 731–740.

Coward, R. N. (2003) 'The Erskine Field, Block 23/26, UK North Sea', *Geological Society, London, Memoirs*, 20, pp. 523–535. doi: 10.1144/GSL.MEM.2003.020.01.42.

Crane Co. (1988) *Flow of Fluids Through Valves, Fittings and Pipe*. Joliet.

Crotogino, F., Mohmeyer, K.-U. and Scharf, R. (2001) 'Huntorf CAES : More than 20 Years of Successful Operation', in *Solution Mining Research Institute (SMRI) Conference*, pp. 1–7.

Cullender, M. H. and Smith, R. V (1956) 'Practical Solution of Gas-Flow Equations for Wells and Pipelines with Large Temperature Gradients', *SPE*, 207.

Darcy, H. (1856) *Les fontaines publiques de la ville de Dijon : exposition et application des principes à suivre et des formules à employer dans les questions de distribution d'eau*. Victor Dal. Paris. Available at: http://scholar.google.com/scholar?hl=en&btnG=Search&q=intitle:Les+fontaines+publiques+de+la+ville+de+dijon#0.

Davis, E. L. (1994) 'Effect of temperature and pore size on the hydraulic properties and flow of a hydrocarbon oil in the subsurface', *Journal of Contaminant Hydrology*, 16, pp. 55–86.

References

DECC (2012) *Potential cost reductions in CCS in the power sector*. London. Available at: https://hub.globalccsinstitute.com/sites/default/files/publications/47086/deccpotentialcostreductionsinccs.pdf.

Deegan, C. E. and Scull, B. (1977) *A standard lithostratigraphic nomenclature for the Central and Northern North Sea., Institute of Geological Siences Report 77/25; NPD-Bulletin No.1.*

Denholm, P. and Sioshansi, R. (2009) 'The value of compressed air energy storage with wind in transmission-constrained electric power systems', *Energy Policy*. Elsevier, 37(8), pp. 3149–3158. doi: 10.1016/j.enpol.2009.04.002.

Doré, C. and Robbins, J. (2005) 'The Buzzard Field', in Doré, A. G.&VINING, B. A. (ed.) *Petroleum Geology: North-West Europe and Global Perspectives — Proceedings of the 6th Petroleum Geology Conference*, pp. 241–252.

Dornhof, D., Kristiansen, T. G., Nogel, N. B., Pattillo, P. D. and Sayers, C. (2006) 'Compaction and Subsidence', *Oilfield Review*, Autumn, pp. 50–68.

Dresser-Rand (2017) *SMARTCAES®*. Available at: http://www.dresser-rand.co.uk/products-solutions/systems-solutions/compressed-air-energy-storage-solutions/.

Duchateau, C. and Broseta, D. (2012) 'A simple method for determining brine–gas interfacial tensions', *Advances in Water Resources*. Elsevier Ltd, 42, pp. 30–36. doi: 10.1016/j.advwatres.2012.03.008.

Dvorkin, J. P. (2008) 'Can gas sand have a large Poisson's ratio?', *Geophysics*, 73(2), pp. E51–E57. doi: 10.1190/1.2821820.

Ecf (2011) 'Power Perspectives 2030: On the road to a Decarbonised Power Sector', *Power*, pp. 1–85. Available at: www.roadmap2050.eu/pp2030.

Elliott, D. (2016) 'A balancing act for renewables', *Nature Energy*. Macmillan Publishers Limited, 1(1), p. 15003. doi: 10.1038/nenergy.2015.3.

Elmegaard, B. and Brix, W. (2011) 'Efficiency of Compressed Air Energy Storage', in *The 24th International Conference on Efficiency, Cost, Optimization, Simulation and Environmental Impact of Energy Systems: The 2011 conference motto: International Smart Energy Networks of Cooperation for Sustainable Development.*

EPRI (1990) *Compressed-air energy storage: Pittsfield aquifer field test - Test data: engineering analysis and evaluation, Report GS-6688*. Palo alto, California.

References

Everitt, B. S. and Skrondal, A. (2013) *The Cambridge Dictionary of Statistics*. 4th Editio, *Journal of Chemical Information and Modeling*. 4th Editio. Cambridge: Cambridge University Press. doi: 10.1017/CBO9781107415324.004.

Fernando, A. and Raman, A. (2009) 'Gas storage: An onshore operator's perspective', *Geological Society, London, Special Publications*, 313(1), pp. 17–24. doi: 10.1144/SP313.3.

Flanigan, O. (1995) 'Characteristics of underground storage', *Underground Gas Storage Facilities*, pp. 54–67. doi: http://dx.doi.org/10.1016/B978-088415204-0/50006-6.

Freeze, R. A. and Cherry, J. A. (1979) *Groundwater*. Prentice Hall, New Jerse.

Furati, K. M. (1997) 'Effects of Relative Permeability History Dependence on Two-Phase Flow in Porous Media', *Transport in Porous Media*, 28(2), pp. 181–203.

Gaarenstroom, L., Tromp, R. a. J., de Jong, M. C. and Brandenburg, a. M. (1993) 'Overpressures in the Central North Sea: implications for trap integrity and drilling safety', *Petroleum Geology of Northwest Europe: Proceedings of the 4th Conference*, 2(1990), pp. 1305–1313. doi: 10.1144/0041305.

Gaelectric (2017) *Gaelectric(R)*. Available at: http://www.project-caeslarne.co.uk/ (Accessed: 30 August 2017).

Garvey, S. D. and Pimm, A. (2016) 'Chapter 5 - Compressed Air Energy Storage', in *Storing Energy*. Elsevier Inc., pp. 87–111. doi: 10.1016/B978-0-12-803440-8/00005-1.

van Genuchten, M. T. (1980) 'A Closed-form Equation for Predicting the Hydraulic Conductivity of Unsaturated Soils', *Soil Science Society of America Journal*, 44(5), p. 892. doi: 10.2136/sssaj1980.03615995004400050002x.

Gilbert, W. (1600) *De Magnete*. 1893 Trans. New York London.

Giordano, R. M., Salter, S. J. and Mohanty, K. K. (1985) 'The Effects of Permeability Variations on Flow in Porous Media', *SPE Annual Technical Conference and Exhibition*. doi: 10.2118/14365-MS.

Giramonti, A. J., Lessard, R. D., Blecher, W. A. and Smith, E. B. (1978) 'Conceptual Design of Compressed Air Energy Storage Electric Power Systems', *Applied Energy*, (4).

Gluyas, J. and Hichens, H. M. (eds) (2003) *United Kingdom Oil and Gas Fields Commemorative Millenium Volume*. Memoirs, 2. London: The Geological Society.

Grappe, J. (2008) 'UGS technology improvements : Some answers of the UGS industry to the

evolution of gas markets', in *International Gas Union Research Conference*.

Grazzini, G. and Milazzo, A. (2012) 'A thermodynamic analysis of multistage adiabatic CAES', *Proceedings of the IEEE*, 100(2), pp. 461–472. doi: 10.1109/JPROC.2011.2163049.

Hall, S. A. (1992) 'The Angus Field, a subtle trap', in Hardman, R. F. P. (ed.) *Exploration Britain: Geological insights for the next decade*. Geological Society Special Publication No.67, pp. 151–185.

Harker, S. D., Green, S. C. H. and Romani, R. S. (1984) 'The Claymore Field, Block 14/19, UK North Sea', *United Kingdom Oil and Gas Fields, 25 Years Commemorative Volume, Geological Society Memoir*, 62(14), pp. 149–157.

Harker, S. D., Mantel, K. A., Morton, D. J. and Riley, L. A. (1993) 'Oxfordian-Kimmeridgian (Late Jurassic) reservoir sandstones in the Witch Ground Graben, UK North Sea.', *AAPG Bulletin*, 77(10), pp. 1693–1709.

Hassanizadeh, S. M. and Gray, W. G. (1987) 'High velocity flow in porous media', *Transport Porous Media*, 2, pp. 521–531.

Haszeldine, R. S. (2009) 'Carbon Capture and Storage: How Green Can Black Be ?', *Science*, 325, pp. 1647–1651. Available at: http://dx.doi.org/10.1007/978-1-4471-4385-7_17.

Heijden, van der (1996) *Scenarios: the art of strategic conversation.* Wiley. New York.

Helmig, R. (1997) *Multiphase Flow and Transport Processes in the Subsurface: A Contribution to the Modeling of Hydrosystems*. 1st edn. Germany: Springer-Verlag Berlin Heidelberg.

Helsingen, E. M. (2015) *Adiabatic compressed air energy storage*. Norwegian University of Science and Technology.

Hempton, M., Marshall, J., Sadler, S., Hogg, N., Charles, R. and Harvey, C. (2005) 'Turbidite reservoirs of the Sele Formation, Central North Sea: geological challenges for improving production', in Parker, J. R. (ed.) *Petroleum Geology of Northwest Europe and Global Perspectives: Proceedings of the 6th Petroleum Geology Conference*. London: Geological Society, pp. 449–459.

Hoffeins, H. (1994) 'Huntorf Air Storage Gas Turbine Power Plant', *Energy Supply - Brown Boveri Mittelungen*. Available at: http://www.kraftwerk-wilhelmshaven.com/pages/ekw_de/Kraftwerk_Wilhelmshaven/Mediencenter/_documents/BBC_Huntorf_engl.pdf.

References

Holm, G. (1998) 'Distribution and origin of overpressure in the Central Graben of the North Sea', *AAPG MEMOIRS*, 70, pp. 123–144.

Horne, R. N. and Shinohara, K. (1979) 'Wellbore Heat Loss in Production and Injection Wells', *Journal of Petroleum Technology*, 31(1), pp. 116–118. doi: 10.2118/7153-PA.

Hubbert, M. K. (1956) 'Darcy's Law and the Field Equations of the Flow of Underground Fluids', *International Association of Scientific Hydrology. Bulletin*, 2(1), pp. 23–59. doi: 10.1080/02626665709493062.

Ishii, M. (1977) *One-dimesnional drift-flux model and constitutive equations for relative motion between phases in various two-phase flow regimes*. Available at: http://www.osti.gov/scitech/servlets/purl/6871478/.

Istok, J. (1989) *Groundwater Modeling by the Finite Element Method*. American Geophysical Union. doi: 10.1029/WM013.

Jaccard, J. and Turrisi, R. (2003) *Quantitative Applications in the Social Sciences: Interaction effects in multiple regression : SAGE*. doi: 10.4135/9781412984522.

Jackson, D. I., Jackson, A. A., Wingfield, R. T. R., Evans, D., Barnes, R. P., Arthur, M. J., Howells, M. F., Hughes, R. A., Petterson, M. G., Department of Trade and Industry, G. and DECC, G. (1995) *The geology of the Irish Sea, United Kingdom Offshore Regional Report*. London.

Jarvis, A. (2015) 'Feasibility Study of Porous Media Compressed Air Energy Storage In South Carolina , United States of America'.

Jewell, S. and Ward, C. (1997) 'SPE 00039047 The Telford Field Development'.

Johnson, H., Warrington, G. and Stoker, S. J. (1994) 'Permian and Triassic of the southern North Sea. 6. Lithostratigraphic nomenclature of the UK North Sea.', *Lithostratigraphic nomenclature of the UK North Sea*, pp. 1–141.

Jolley, J. E. (1993) 'The Andrew and Cyrus Fields, Blocks 16/27a, 16/28, UK North Sea', *United Kingdom Oil and Gas Fields, Commemorative Millenium Volume. Memoir 20*, pp. 698–710.

Joule, J. P. (1843) 'On the Calorific Effects of Magneto-Electricity, and on the Mechanical Value of Heat.', *Philosophical Magazine*, 23, p. 263–347, and 435.

Kaiser, F. and Efzn, E. N. (2015) 'Steady State Analyse of existing Compressed Air Energy

Storage Plants Thermodynamic Cycle modeled with Engineering Equation Solver', in *Power and Energy Student Summit (PESS)*.

Karellas, S. and Tzouganatos, N. (2014) 'Comparison of the performance of compressed-air and hydrogen energy storage systems: Karpathos island case study', *Renewable and Sustainable Energy Reviews*, 29, pp. 865–882.

Katz, D. L. and Lady, E. R. (1976) *Compressed air storage for electric power generation*. 1st edn. Edited by Ann Arbor. Ulrich's Books.

Kiameh, P. (2002) 'Chapter 12 - Gas turbine combustors', in *Power Generation Handbook: Selection, Applications, Operation, Maintenance*. McGraw-Hil.

Kilhams, B. A. (2011) *An Integrated Characterisation of the Paleocene Submarine Fan Systems (Lista and Maureen Formations) in the Central Graben of the North Sea*. University of Aberdeen.

Kilhams, B., Hartley, A., Huuse, M. and Davis, C. (2012) 'Characterizing the Paleocene turbidites of the North Sea: the Mey Sandstone Member, Lista Formation, UK Central Graben', *Petroleum Geoscience*, 18, pp. 337–354. doi: 10.1144/SP403.1.

Kim, Y. M., Lee, J. H., Kim, S. J. and Favrat, D. (2012) 'Potential and evolution of compressed air energy storage: Energy and exergy analyses', *Entropy*, 14(8), pp. 1501–1521. doi: 10.3390/e14081501.

Kittner, N., Lill, F. and Kammen, D. M. (2017) 'Energy storage deployment and innovation for the clean energy transition', *Nature Energy*, 2(July), p. 17125. doi: 10.1038/nenergy.2017.125.

Kleiber, M. (2016) *Process Engineering: Addressing the Gap Between Studies and Chemical Industry*. Berlin/Boston: De Gruyter.

Knox, R. W. and Holloway, S. (1992) 'Paleogene of the central and northern North Sea.', in Knox, R. W. and Cordey, W. G. (eds) *Lithostratigraphic Nomenclature of the UK North Sea*.

Kolditz, O. (1997) *Strömung, Stoff- und Wärmetransport im Kluftgestein*. Stuttgart: Bortraeger Verlag.

Kolditz, O. (2002) *Computational Methods in Environmental Fluid Mechanics*. Springer-Verlag Berlin Heidelberg. doi: 10.1007/978-3-662-04761-3.

Kolditz, O., Bauer, S., Bilke, L., Böttcher, N., Delfs, J. O., Fischer, T., Görke, U. J., Kalbacher,

References

T., Kosakowski, G., McDermott, C. I., Park, C. H., Radu, F., Rink, K., Shao, H., Shao, H. B., Sun, F., Sun, Y. Y., Singh, A. K., Taron, J., Walther, M., Wang, W., Watanabe, N., Wu, Y., Xie, M., Xu, W. and Zehner, B. (2012) 'OpenGeoSys: An open-source initiative for numerical simulation of thermo-hydro-mechanical/chemical (THM/C) processes in porous media', *Environmental Earth Sciences*, 67(2), pp. 589–599. doi: 10.1007/s12665-012-1546-x.

Kolditz, O., Görke, U. J., Shao, H. and Wang, W. (2012) *Lecture Notes in Computational Science and Engineering 86, Kolditz, O., Görke, U.J., Shao, H., Wang, W., (eds.) Thermo-hydro-mechanical-chemical processes in porous media : benchmarks and examples*. Springer, Berlin, Heidelberg.

Kolodzie, J. S. (1980) 'Analysis of Pore Throat Size And Use of the Waxman-Smits Equation To Determine OOIP in Spindle Field, Colorado', in *SPE Annual Technical Conference and Exhibition*. Dallas, pp. 191–198.

Koša, E. (2007) 'Differential subsidence driving the formation of mounded stratigraphy in deep-water sediments; Palaeocene, central North Sea', *Marine and Petroleum Geology*, 24(10), pp. 632–652. doi: 10.1016/j.marpetgeo.2007.04.001.

KPMG (2015) *Decommissioning strategy A New Imperative for E&P Firms*.

Kreid, D. K. (1976) *Technical and Economic Feasibility Analysis of the No-Fuel Compressed Air Energy Storage Concept*.

Kreid, D. K. and McKinnon, M. A. (1978) *FY-1977 Progress Report Compressed Air Energy Storage Advanced Systems Analysis*. Richland, Washington.

Kushnir, R., Ullmann, A. and Dayan, A. (2010) 'Compressed Air Flow within Aquifer Reservoirs of CAES Plants', *Transport in Porous Media*, 81(2), pp. 219–240. doi: 10.1007/s11242-009-9397-y.

Kushnir, R., Ullmann, A. and Dayan, A. (2012) 'Thermodynamic and hydrodynamic response of compressed air energy storage reservoirs: a review', *Reviews in Chemical Engineering*, 28(2–3), pp. 123–148. doi: 10.1515/revce-2012-0006.

Kutun, K., Tureyen, O. and Satman, A. (2015) 'Analysis of wellhead production temperature derivatives', in *40th Workshop on Geothermal Reservoir Engineering, Stanford University*. Stanford, California, pp. 1–12. Available at: https://pangea.stanford.edu/ERE/db/GeoConf/papers/SGW/2015/Kutun.pdf.

Lee, W. J. and Wattenbarger, R. A. (1996) 'Gas Reservoir Engineering', *SPE Textbook Series*.

Edited by SPE. Richardson, Texas: SPE, 5.

Leeder, M. R., Boldy, S. R., Raiswell, R. and Cameron, R. (1990) 'The Carboniferous of the Outer Moray Firth Basin, quadrants 14 and 15, Central North Sea', *Marine and Petroleum Geology*, 7(1). doi: 10.1016/0264-8172(90)90053-J.

Lemmon, E. W. and Jacobsen, R. T. (2004) 'Viscosity and Thermal Conductivity Equations for Nitrogen, Oxygen, Argon, and Air', *International Journal of Thermophysics*, 25(1), pp. 21–69. doi: 10.1023/B:IJOT.0000022327.04529.f3.

Lemmon, E. W., Jacobsen, R. T., Penoncello, S. G. and Friend, D. G. (2000) 'Thermodynamic Properties of Air and Mixtures of Nitrogen, Argon, Oxygen from 60 K to 2000 K at Pressures to 2000 MPa', *Journal of Physics and Chemistry*, 29(3), p. 331.

Lenhard, R. J. and Parker, J. C. (1987) 'A model for hysteretic constitutive relations governing multiphase flow: 1. Saturation-Pressure relations', *Water Resources Research*, 23(12), p. 2197. doi: 10.1029/WR023i012p02197.

Liu, C. T. and Lindsay, W. T. J. (1970) 'Vapor Pressure of D2O from 106 to 300 ºC', *Journal of Chemical Engineering Data*, 15(4), pp. 510–513. doi: 10.1021/je60047a015.

Liu, W., Li, Q., Liang, F., Liu, L., Xu, G. and Yang, Y. (2014) 'Performance Analysis of a Coal-Fired External Combustion Compressed Air Energy Storage System', *Entropy*, 16(11), pp. 5935–5953. doi: 10.3390/e16115935.

Liu, W., Liu, L., Zhou, L., Huang, J., Zhang, Y., Xu, G. and Yang, Y. (2014) 'Analysis and Optimization of a Compressed Air Energy Storage—Combined Cycle System', *Entropy*, 16(6), pp. 3103–3120. doi: 10.3390/e16063103.

Liu, X. and Galloway, W. E. (1997) 'Quantitative Determination of Tertiary Sediment Supply to the North Sea Basin 1', 9(9), pp. 1482–1509.

Lu, J., Cook, P. J., Hosseini, S. A., Yang, C., Romanak, K. D., Zhang, T., Freifeld, B. M., Smyth, R. C., Zeng, H. and Hovorka, S. D. (2012) 'Complex fluid flow revealed by monitoring CO2 injection in a fluvial formation', *Journal of Geophysical Research: Solid Earth*, 117(3), pp. 1–13. doi: 10.1029/2011JB008939.

Lund, H. and Salgi, G. (2009) 'The role of compressed air energy storage (CAES) in future sustainable energy systems', *Energy Conversion and Management*. Elsevier Ltd, 50(5), pp. 1172–1179. doi: 10.1016/j.enconman.2009.01.032.

Maher, C. E. (1981) 'The Piper Oilfield', in Illing, L. V. and Hobson, G. D. (eds) *Petroleum*

geology of the continental shelf of North-West Europe. London: Heyden & Son, pp. 358–370.

Maher, C. E. and Harker, S. D. (1987) 'Claymore oil field', in Brooks, J. and Glennie, K. W. (eds) *Petroleum Geology of North West Europe*. London: Graham & Trotman, pp. 835–845.

Marchand, A. M. E., Smalley, P. C., Haszeldine, R. S. and Fallick, A. E. (2002) 'Note on the importance of hydrocarbon fill for reservoir quality prediction in sandstones', *AAPG Bulletin*, 86(9), pp. 1561–1571. doi: 10.1306/61EEDD00-173E-11D7-8645000102C1865D.

Martin, A. J., Solomon, S. T. and Hartmann, D. J. (1997) 'Characterization of Petrophysical Flow Units in Five Carbonate Reservoirs', *American Association of Petroleum Geologists Bulletin*, 81(5), p. 734.

Mason, J. E. and Archer, C. L. (2012) 'Baseload electricity from wind via compressed air energy storage (CAES)', *Renewable and Sustainable Energy Reviews*. Elsevier Ltd, 16(2), pp. 1099–1109. doi: 10.1016/j.rser.2011.11.009.

Maton, J.-P., Zhao, L. and Brouwer, J. (2013) 'Dynamic modeling of compressed gas energy storage to complement renewable wind power intermittency', *International Journal of Hydrogen Energy*. Elsevier Ltd, 38(19), pp. 7867–7880. doi: 10.1016/j.ijhydene.2013.04.030.

Matthews, C. S. and Russell, D. G. (1967) *Pressure Buildup and Flow Tests in Wells*. New York, Dallas: Society of Petroleum Engineers of AIME.

McCafferty, T. W. (1980) *Compressed Air Energy Storage: Preliminary Desgin and Site Development Program in an Aquifer, Prepared for Department of Energy*. Argonne, Illinois. Available at: http://www.eolss.net/Sample-Chapters/C08/E3-14-03-01.pdf.

McCain, W. D. J. (1991) 'Reservoir Fluid Property Correlations-State of the Art', *SPE - Reservoir Engineering*, 6(2), pp. 266–272.

McCraw, C., Edlmann, K., Miocic, J., Gilfillan, S., Haszeldine, R. S. and McDermott, C. I. (2015) 'Experimental investigation and hybrid numerical analytical hydraulic mechanical simulation of supercritical CO2 flowing through a natural fracture in caprock', *International Journal of Greenhouse Gas Control*. Elsevier Ltd, 48, pp. 120–133. doi: 10.1016/j.ijggc.2016.01.002.

McGrail, B. P., Davidson, C. L., Bacon, D. ., Chamness, M. ., Reidel, S. ., Spane, F. ., Cabe, J. ., Knudsen, F. S., Bearden, M. D., Horner, J. A., Schaef, H. T. and Thorne, P. D. (2013) *Techno-economic Performance Evaluation of Compressed Air Energy Storage in the Pacific Northwest*.

References

Mehenni, M. and Roodenburg, W. Y. (1990) 'Fulmar Field-U. K. South Central Graben, North Sea', *Structural Traps IV: Tectonic and Nontectonic Fold Traps*, V, pp. 113–139. Available at: http://search.datapages.com/data/specpubs/fieldst3/data/a018/a018/0001/0100/0113.htm.

Meyer, W. H. (1971) *A history of electricity and magnetism*. Cambridge, Mass.: MIT Press.

Mignard, D. (2014) 'Estimating the capital costs of energy storage technologies for levelling the output of renewable energy sources', *International Journal of Environmental Studies*, 71(6), pp. 796–803. doi: 10.1080/00207233.2014.967103.

Mokhatab, S. and Poe, W. A. (2012) 'Sales Gas Transmission', in *Handbook of Natural Gas Transmission and Processing*, pp. 425–450. doi: 10.1016/B978-0-12-386914-2.00012-1.

Moss, B., Barson, D., Rakhit, K., Dennis, H. and Swarbrick, R. (2003) 'Formation pore pressures and formation waters.', *The millennium atlas: Petroleum geology of the central and northern North Sea: Geological Society (London)*, pp. 317–329.

Mudge, D. C. (2014) 'Regional controls on Lower Tertiary sandstone distribution in the North Sea and NE Atlantic margin basins', *Tertiary Deep-Marine Reservoirs of the North Sea Reservoirs of the North Sea*, p. 403. doi: 10.1144/SP403.5.

Mudge, D. C. and Bujak, J. P. (1996) 'An integrated stratigraphy for the Paleocene and Eocene of the North Sea', *Geological Society, London, Special Publications*, 101(101), pp. 91–113. doi: 10.1144/GSL.SP.1996.101.01.06.

Munns, J. W., Gray, J. C., Stoker, S. J., Andrews, I. J. and Cameron, T. D. J. (2002) 'The remaining hydrocarbon potential of the UK Continental Shelf', in Doré, A. G. & Vining, B. A. (ed.) *Petroleum Geology: North-West Europe and Global Perspectives — Proceedings of the 6th Petroleum Geology Conference, 41–54. Petroleum Geology Conferences Ltd.* London: Geological Society.

Nabawy, B. S., Géraud, Y., Rochette, P. and Bur, N. (2009) 'Pore-throat characterization in highly porous and permeable sandstones', *AAPG Bulletin*, 93(6), pp. 719–739. doi: 10.1306/03160908131.

NationalGrid (2011) 'UK Future Energy Scenarios', p. 73.

Noy, D. ., Holloway, S., Chadwick, R. A., Williams, J. D. O., Hannis, S. A. and Lahann, R. W. (2012) 'Modelling large-scale carbon dioxide injection into the Bunter Sandstone in the UK Southern North Sea', *International Journal of Greenhouse Gas Control*, 9, pp. 220–233.

O'Driscoll, D., Hindle, A. D. and Long, D. C. (1990) 'The structural controls on Upper

References

Jurassic and Lower Cretaceous reservoir sandstones in the Witch Ground Graben, UK North Sea', in Hardman, R. F. . and Brooks, J. (eds) *Tectonic events responsible for Britain's oil and gas reserves*. London: Geological Society, Special Publication No. 55, pp. 191–205.

Obi, M., Jensen, S. M., Ferris, J. B. and Bass, R. B. (2017) 'Calculation of levelized costs of electricity for various electrical energy storage systems', *Renewable and Sustainable Energy Reviews*. Elsevier, 67, pp. 908–920. doi: 10.1016/j.rser.2016.09.043.

Oil & Gas Authority (2016) *Decommissioning strategy*.

Oldenburg, C. M. and Pan, L. (2013a) 'Porous Media Compressed-Air Energy Storage (PM-CAES): Theory and Simulation of the Coupled Wellbore–Reservoir System', *Transport in Porous Media*, 97(2), pp. 201–221. doi: 10.1007/s11242-012-0118-6.

Oldenburg, C. M. and Pan, L. (2013b) 'Utilization of CO2 as cushion gas for porous media compressed air energy storage.', *Greenhouse Gases: Science and Technology*, 3(2), pp. 124–135. doi: 10.1002/ghg.1332.

OWPB (2016) *Transmission Costs for Offshore Wind Final Report April 2016*.

Pale Blue Dot Energy (2016) *Progressing development of the UK's Strategic Carbon Dioxide Storage Resource: A Summary of Results from the Strategic UK CO2 Storage Appraisal Project*. Available at: http://www.eti.co.uk/project/strategic-uk-ccs-storage-appraisal/?utm_medium=email&utm_campaign=Strategic UK CCS Storage Appraisal announcement&utm_content=Strategic UK CCS Storage Appraisal announcement+CID_3258184913365b7308725bbdb1076a42&utm_source=Emai.

Pan, L. and Oldenburg, C. M. (2014a) 'Rigorous process simulation of compressed air energy storage (CAES) in porous media systems', in Al-Khoury, R. and Bundschuh, J. (eds) *Computational Models for CO2 Geo-sequestration & Compressed Air Energy Storage*, pp. 479–498.

Pan, L. and Oldenburg, C. M. (2014b) 'T2Well—An integrated wellbore–reservoir simulator', *Computers & Geosciences*. Elsevier, 65, pp. 46–55. doi: 10.1016/j.cageo.2013.06.005.

Partnership Energy Research (2011) *The future role for energy storage in the UK*. Available at: http://www.energyresearchpartnership.org.uk/dl291.

Pearson, K. (1895) 'VII. Note on regression and inheritance in the case of two parents', *Proceedings of the Royal Society of London*, 58, pp. 240–242. Available at: http://rspl.royalsocietypublishing.org/content/58/347-352/240.full.pdf+html.

References

PetroWiki (2015a) *Pipeline design consideration and standards*. Available at: http://petrowiki.org/Pipeline_design_consideration_and_standards#Velocity_considerations (Accessed: 5 February 2018).

PetroWiki (2015b) *Pressure drop evaluation along pipelines*. Available at: http://petrowiki.org/Pressure_drop_evaluation_along_pipelines (Accessed: 5 February 2018).

Pfenninger, S. and Keirstead, J. (2015) 'Renewables, nuclear, or fossil fuels? Scenarios for Great Britain's power system considering costs, emissions and energy security', *Applied Energy*. Elsevier Ltd, 152, pp. 83–93. doi: 10.1016/j.apenergy.2015.04.102.

Pittman, E. D. (1992) 'Relationship of Porosity and Permeability to Various Parameters Derived from Mercury Injection-Capillary Pressure Curves for Sandstone.', *The AAPG Bulletin*, 76(2), pp. 191–198.

PowerSouth Energy Cooperative (2014) 'The McIntosh Power Plant'. Available at: www.powersouth.com.

Ramey Jr., H. (1962) 'Wellbore Heat Transmission', *Journal of Petroleum Technology*, (April), pp. 427–435. doi: 10.2118/96-PA.

RenewableUK (2018) *Wind Energy Statistics*. Available at: http://www.renewableuk.com/page/UKWEDhome (Accessed: 5 February 2018).

Reynolds, C. A. and Krevor, S. (2015) 'Characterizing flow behavior for gas injection: Relative permeability of CO2-brine and N2-water in heterogeneous rocks', *Water Resources Research*, 51(12), pp. 9464–9489. doi: 10.1002/2015WR018046.

Richards, P. C., Lott, G. K., Johnson, H., Knox, R. W. O. and Riding, J. B. (1993) 'Jurassic of the Central and Northern North Sea', *Lithostratigraphic Nomenclature of the UK North Sea*, p. 252.

Ringrose, P. and Bentley, M. (2015) *Reservoir Model Design*. Edited by Springer. New York London. doi: 10.1007/978-94-007-5497-3.

Ritchie, J. S. and Pratsides, P. (1993) 'The Caister Fields, Block 44/23a, UK North Sea', *Petroleum Geology of Northwest Europe: Proceedings of the 4th Conference*, pp. 759–769. doi: 10.1144/0040759.

Robertson, J. (2013) 'Overpressure and Lateral Drainage in the Palaeogene Strata of the Central North Sea'.

References

Rosenberg, D. M., Bodaly, R. a. and Usher, P. J. (1995) 'Environmental and social impacts of large scale hydro-electric development: Who is listening?', *Global Environmental Change*, 5(2), pp. 127–148. doi: 10.1016/0959-3780(95)00018-J.

Royal Academy of Engineering (2013) 'Decommissioning in the North Sea Decommissioning in the North Sea: A report of a workshop held to discuss the decommissioning of oil and gas platforms in the North Sea', p. 15.

Rushing, J. A., Newsham, K. E., Fraassen, K. C. Van, Mehta, S. A. and Moore, G. R. (2008) 'Laboratory Measurements of Gas-Water Interfacial Tension at HP/HT Reservoir Conditions', *CIPC/SPE Gas Technology Symposium 2008 Joint Conference*. doi: 10.2118/114516-ms.

Safaei, H. and Aziz, M. J. (2014) 'Thermodynamic Analysis of a Compressed Air Energy Storage Facility Exporting Compression Heat to an External Heat Load', in *Proceedings of ASME 2014 12th Biennial Conference on Engineering Systems Design and Analysis*. Copenhagen: ESDA, pp. 1–10.

Saltelli, A. (2002) 'Sensitivity Analysis for Importance Assessment', *Risk Analysis*, 22(3), pp. 579–590.

Saltelli, A. and Annoni, P. (2010) 'How to avoid a perfunctory sensitivity analysis', *Environmental Modelling and Software*. Elsevier Ltd, 25(12), pp. 1508–1517. doi: 10.1016/j.envsoft.2010.04.012.

Sarathi, P. (1998) 'In-situ combustion handbook--principles and practices', (Junio), p. 423. doi: 10.2172/3175.

Scheidegger, A. E. (1974) *The Physics of Flow Through Porous Media.* 3rd edn. Toronto and Buffalo: University Toronto Press.

Schenectady (1976) *Economic and Technical Feasibility Study of Compressed Air Storage*.

Schlein, B. (1985) 'Gas Turbine Combustion Efficiency', in *Beijing International Gas Turbine Symposium and Exposition*. The American Society of Mechanical Engineers, pp. 1–6.

Schmitt, H. R. H. (1991) 'The Chanter Field, Block 15/17, UK North Sea', *Geological Society London Memoirs*, 14(1), pp. 261–268. doi: 10.1144/GSL.MEM.1991.014.01.32.

Schmitt, H. R. H. and Gordon, A. F. (1991) 'The Piper Field, Block 15/17, UK. North Sea', *United Kingdom Oil and Gas Fields 25 years Commemorative Volume*, 14(1), pp. 361–368. doi: 10.1144/GSL.MEM.1991.014.01.32.

References

Schoenung, S. M. and Hassenzahl, W. V. (2003) 'Long- vs. Short-Term Energy Storage Technologies Analysis A Life-Cycle Cost Study A Study for the DOE Energy Storage Systems Program', *Power Quality*, SAND2011-2(April), p. 84. Available at: http://infoserve.sandia.gov/sand_doc/2003/032783.pdf.

Smith, G. C., Stottlemyre, J. A., Wiles, L. E., Loscutoff, W. V. and Pincus, H. J. (1978) *Stability and Design Criteria Studies for Compressed Air Energy Storage reservoirs*.

Smith, R. V. (1950) 'Determining friction factors for measuring productivity of gas wells', *Petroleum Transactions*, 189, pp. 73–82.

Snedecor, G. W. and Cochran, W. G. (1980) *Statistical Methods*. Ames, Iowa: Iowa State Univeristy Press.

Sobol, I. M. (1993) 'Sensitivity analysis for nonlinear mathematical models', *Mathematical Modeling and Computational Experiment*, 1, pp. 407–414.

Sommerfeld, A. (1908) 'Ein Beitrag zur hydrodynamischen Erkläerung der turbulenten Flüssigkeitsbewegüngen (A Contribution to Hydrodynamic Explanation of Turbulent Fluid Motions)', *International Congress of Mathematicians*, 3, pp. 116–124.

Spivey, J. P. and Mccain, W. D. (2004) 'Estimating Density , Formation Volume Factor , Compressibility , Methane Solubility , and Viscosity for Oilfield Brines at Temperatures From 0 to 275 ° C , Pressures to 200 MPa , and Salinities to 5 . 7 mole / kg', *Journal of Canadian Petroleum Technology*, 43(7), pp. 52–61.

Stephan, P., Kabelac, S., Kind, M., Martin, H., Mewes, D. and Schaber, K. (2013) *VDI Heat Atlas*. 2nd edn. Edited by VDI-GVC. Dusseldorf: Springer. doi: 10.1007/978-3-540-77877-6.

Steward, D., Saur, G., Penev, M. and Ramsden, T. (2009) *Lifecycle Cost Analysis of Hydrogen Versus Other Technologies for Electrical Energy Storage*. Available at: http://www.nrel.gov/docs/fy10osti/46719.pdf (Accessed: 4 December 2014).

Stockbridge, C. P. and Gray, D. I. (1991) 'The Fulmar Field, Blocks 30116 & 30/llb, UK North Sea', *United Kingdom Oil and Gas Fields, 25 Years Commemorative Volume, Geological Society Memoir*, 14, pp. 309–316.

Storengy (2017) *Storengy Sites In Operation*. Available at: https://www.storengy.com/countries/france/en/our-sites.html (Accessed: 8 September 2017).

Stottlemyre, J. A. (1978) *Preliminary Stability Criteria for Compressed Air Energy Storage in Porous Media Reservoir*. Richland, Washington.

References

Strbac, G., Aunedi, M., Pudjianto, D., Djapic, P., Gammons, S. and Druce, R. (2012) *Understanding the Balancing Challenge*. London.

Succar, S. and Williams, R. (2008) *Compressed Air Energy Storage : Theory, Resources, And Applications For Wind Power*. Available at: https://acee.princeton.edu/wp-content/uploads/2016/10/SuccarWilliams_PEI_CAES_2008April8.pdf.

Swale, A. M. and Vass, M. (1994) 'IADC / SPE 27523 Orwell Field : Case History of a Low-Cost Subsea Development in the Southern North Sea', in *1994 1ADC/SPE Drilling Conference*. Dallas, Texas, USA, pp. 851–864.

Swarbrick, R. E., Seldon, B. and Mallon, A. J. (2005) 'Modelling the Central North Sea pressure history', in Doré, A. G. and Vining, B. A. (eds) *Petroleum Geology:North-West EuropeandGlobal Perspectives—Proceedingsof the 6thPetroleum Geology Conference*. London: Geological Society, pp. 1237–1245.

Szymkiewicz, A. (2013) *Modelling Water Flow in Unsaturated Porous Media*, *GeoPlanet: Earth and Planetary Sciences*. doi: 10.1007/978-3-642-23559-7.

Taylor, S. R., Almond, J., Arnott, S., Kemshell, D. and Taylor, D. (2003) 'The Brent Field, Block 211/29, UK North Sea', in Gluyas, J. G. and Hichens, H. M. (eds) *United Kingdom Oil and Gas Fields, Commemorative Millennium Volum*. London: Geological Society, pp. 233–250. doi: 10.1144/gsl.mem.2003.020.01.20.

The Electricity Storage Network Ltd (2014) *The Electricity Storage Network Consultation Document*. Available at: www.electricitystorage.co.uk.

Tonkin, P. C. and Fraser, a. R. (1991) 'The Balmoral Field, Block 16/21, UK North Sea', *Geological Society, London, Memoirs*, 14(1), pp. 237–244. doi: 10.1144/GSL.MEM.1991.014.01.29.

Tronvoll, J., Larsen, I. and Li, L. (2004) 'SPE 86468 Rock Mechanics Aspects of Well Productivity in Marginal Sandstone Reservoirs : Problems, Analysis Methods , and Remedial Actions'.

Uhl, A. E. (1965) *Steady Flow in Gas Pipelines. IGT Report No. 10.* Chicago.

UK Department of Energy and Climate Change (2013) 'Updated energy and emissions projections 2013', (September), pp. 1–51. Available at: https://www.gov.uk/government/uploads/system/uploads/attachment_data/file/239937/uep_2013.pdf.

References

UN (2015) ‘FCCC/CP/2015/L.9/Rev.1’, in *UNFCCC. Conference of the Parties (COP)*, p. 32. doi: FCCC/CP/2015/L.9/Rev.1.

USDOE (2017) *Global Energy Storage Database*, *US Department of Energy*. Available at: http://www.energystorageexchange.org/.

Vavra, C. L., Kaldi, J. G. and Sneider, R. M. (1992) ‘Geological applications of capillary pressure: a review’, *American Association of Petroleum Geologists Bulletin*, 76(6), pp. 840–850. doi: 10.1306/BDFF88F8-1718-11D7-8645000102C1865D.

Wall, M., Lee, R. and Frost, S. (2006) *Offshore gas turbines (and major driven equipment) integrity and inspection guidance notes, Prepared by ESR Technology Ltd for the Health and Safety Executive*.

Watson, K. and Jones, C. (2010) ‘Cyclic Loading of a Rock Mass for Underground Gas Storage Applications’, in *SIMULIA Customer Conference*, pp. 1–9.

Weingarten, J. S. and Perkins, K. (1995) ‘Prediction of Sand Production in Gas Wells : Methods and Gulf of Mexico Case Studies’, *Society of Petroleum Engineers*, (July), pp. 596–600.

Winland, H. D. (1976) *Evaluation of gas slippage and pore aperture size in carbonate and sandstone reservoirs: Amoco Production Company Report F76-G-5*.

Xia, C. and Wilkinson, M. (2017) ‘Quantifying the geological risk of drilling a borehole for CO2 storage’, *International Journal of Greenhouse Gas Control*, 63, pp. 272–280.

Xing, L. and Jihong, W. (2013) *Overview of Current Development on Compressed Air Energy Storage. EERA Technical Report.* Coventry.

Zakeri, B. and Syri, S. (2015) ‘Electrical energy storage systems: A comparative life cycle cost analysis’, *Renewable and Sustainable Energy Reviews*. Elsevier, 42, pp. 569–596. doi: 10.1016/j.rser.2014.10.011.

Zhang, X. Y., Trame, M. N., Lesko, L. J. and Schmidt, S. (2015) ‘Sobol Sensitivity Analysis : A Tool to Guide the Development and Evaluation of Systems Pharmacology Models’, *CPT: pharmacometrics & systems pharmacology*, 4(October 2014), pp. 1–4. doi: 10.1002/psp4.6.

Zoback, M. D., Moos, D., Mastin, L. and Anderson, R. N. (1985) ‘Well bore breakouts and in situ stress’, *Journal of Geophysical Research*, 90(B7), p. 5523. doi: 10.1029/JB090iB07p05523.

Appendices

8.1 OpenGeoSys Store Models

This appendix presents, in tabulated form, all the parameter combinations modelled for the reservoir top depth, its porosity, thickness and permeability. It also contains the preliminary maximum mass flow rate assessment assuming there would be a 10 bar difference between the well edge and the model edge. The Reynold Number was capped to a value of 10 which ensures that the flow will be laminar and suitable for the equation used. The instability column indicates how many cycles could be completed after 12 hours of simulations. If no value is provided the simulation completed the full 10 cycles normally. If an "i" is present then the solution failed to converge before the end of the first cycle. As can be seen, all of the 40 m thick reservoir scenarios at 200 m depth failed according to the analytical predictions. This is why the minimum thickness threshold was raised to 50 m in the UK assessment. Similarly, although not all scenarios at 200 m failed, some proved to be unable to sustain the flow rate imposed during 60 days of production. Therefore, the filtering of the database was done using the next best recommended threshold of 260 m as the minimum top depth for "good" PM-CAES reservoirs (Succar and Williams, 2008).

Top Depth (m)	Porosity (%)	Thickness (m)	Permeability (mD)	Max Mass Flow Rate (kg/s)	Reynold Number	Instability
1009	19	228	1168	407	8.48	
1167	28	121	314	63	2.66	
1170	17	218	665	244	5.68	
1172	26	85	587	81	4.82	
1182	23	275	945	460	8.46	
1196	25	127	1077	232	9.21	
1207	20	285	1195	566	10.00	
1243	21	242	1255	484	10.00	
1274	30	141	898	230	8.11	
1298	18	59	360	35	2.96	
1350	18	344	381	257	3.66	4
1465	29	162	462	152	4.50	
1615	24	160	831	245	10.00	
1642	24	232	1284	358	10.00	
1712	29	164	394	143	5.60	
1724	17	288	421	270	6.00	

2023	28	42	457	44	6.39	
2058	28	199	697	265	10.00	
2076	25	294	359	265	6.76	
2125	26	275	387	271	7.34	
2142	29	243	503	313	9.54	
2206	28	265	735	361	10.00	
2251	25	118	849	162	10.00	
2420	18	334	626	469	10.00	1
2456	19	180	1085	254	10.00	
2469	24	286	1301	405	10.00	
2475	26	81	801	115	10.00	
2558	18	95	930	117	10.00	
2559	26	118	977	145	10.00	
2566	28	221	1274	272	10.00	
2588	15	61	1260	75	10.00	
2887	18	70	767	90	10.00	
2974	16	229	838	298	10.00	2
3060	29	42	1013	49	10.00	
310	19	263	684	83	0.21	2
3320	22	262	750	317	10.00	
3380	15	344	1189	419	10.00	3
3490	27	90	1091	102	10.00	
3565	20	216	1123	246	10.00	3
3582	20	102	1029	116	10.00	
3683	28	200	604	230	10.00	
368	19	156	1241	104	0.86	
3706	20	232	123	84	3.12	
3777	26	84	270	63	6.44	
3807	28	269	368	305	9.73	
621	18	75	1237	84	3.35	
621	18	75	1237	84	3.35	
646	20	169	426	72	1.27	
827	26	231	870	266	4.52	2
860	28	81	107	11	0.53	
923	25	209	565	170	3.54	
1194	29	243	503	230	4.78	
1587	15	344	1189	525	10.00	
1829	28	269	368	249	5.82	
235	18	75	1237	29	0.26	
337	28	81	107	4	0.07	
395	25	209	565	78	0.48	
541	20	285	1195	311	2.68	
744	24	160	831	162	3.51	

81	19	263	684	1	0.00	
995	15	61	1260	109	8.48	
200	15	174	100	4	0.01	i
200	15	174	1330	49	0.19	
200	15	174	650	24	0.09	
200	15	350	100	8	0.01	i
200	15	350	1330	102	0.20	i
200	15	350	650	50	0.10	
200	15	40	100	1	0.01	i
200	15	40	1330	11	0.18	i
200	15	40	650	5	0.09	i
200	23	174	100	4	0.01	i
200	23	174	1330	50	0.19	
200	23	174	650	24	0.09	
200	23	350	100	8	0.02	i
200	23	350	1330	106	0.20	
200	23	350	650	52	0.10	
200	23	40	100	1	0.01	i
200	23	40	1330	11	0.18	i
200	23	40	650	5	0.09	i
200	30	174	100	4	0.01	i
200	30	174	1330	51	0.20	
200	30	174	650	25	0.10	
200	30	350	100	8	0.02	i
200	30	350	1330	108	0.21	
200	30	350	650	53	0.10	
200	30	40	100	1	0.01	i
200	30	40	1330	11	0.19	i
200	30	40	650	5	0.09	i
2750	15	174	100	45	2.05	
2750	15	174	1330	220	10.00	
2750	15	174	650	220	10.00	
2750	15	350	100	96	2.17	
2750	15	350	1330	442	10.00	1
2750	15	350	650	442	10.00	3
2750	15	40	100	10	1.93	
2750	15	40	1330	51	10.00	
2750	15	40	650	51	10.00	
2750	23	174	100	47	2.12	
2750	23	174	1330	220	10.00	1
2750	23	174	650	220	10.00	
2750	23	350	100	99	2.25	
2750	23	350	1330	442	10.00	4

2750	23	350	650	442	10.00	
2750	23	40	100	10	2.00	
2750	23	40	1330	51	10.00	
2750	23	40	650	51	10.00	
2750	30	174	100	48	2.17	
2750	30	174	1330	220	10.00	
2750	30	174	650	220	10.00	
2750	30	350	100	102	2.30	
2750	30	350	1330	442	10.00	4
2750	30	350	650	442	10.00	
2750	30	40	100	10	2.04	
2750	30	40	1330	51	10.00	
2750	30	40	650	51	10.00	
4000	15	174	100	49	2.52	
4000	15	174	1330	192	10.00	4
4000	15	174	650	192	10.00	
4000	15	350	100	103	2.67	
4000	15	350	1330	387	10.00	2
4000	15	350	650	387	10.00	3
4000	15	40	100	11	2.37	
4000	15	40	1330	44	10.00	
4000	15	40	650	44	10.00	
4000	23	174	100	50	2.61	3
4000	23	174	1330	192	10.00	4
4000	23	174	650	192	10.00	<1
4000	23	350	100	107	2.78	
4000	23	350	1330	387	10.00	1
4000	23	350	650	387	10.00	
4000	23	40	100	11	2.45	
4000	23	40	1330	44	10.00	
4000	23	40	650	44	10.00	
4000	30	174	100	51	2.67	
4000	30	174	1330	192	10.00	
4000	30	174	650	192	10.00	<1
4000	30	350	100	110	2.84	
4000	30	350	1330	387	10.00	4
4000	30	350	650	387	10.00	
4000	30	40	100	11	2.51	
4000	30	40	1330	44	10.00	
4000	30	40	650	44	10.00	
800	15	174	100	20	0.40	
800	15	174	1330	271	5.34	4
800	15	174	650	133	2.61	

800	15	350	100	43	0.42	
800	15	350	1330	575	5.62	
800	15	350	650	281	2.75	4
800	15	40	100	4	0.38	i
800	15	40	1330	59	5.06	
800	15	40	650	29	2.47	
800	23	174	100	21	0.41	
800	23	174	1330	280	5.51	
800	23	174	650	137	2.69	
800	23	350	100	45	0.44	
800	23	350	1330	594	5.81	4
800	23	350	650	290	2.84	<1
800	23	40	100	5	0.39	i
800	23	40	1330	61	5.21	
800	23	40	650	30	2.55	
800	30	174	100	22	0.42	
800	30	174	1330	286	5.62	
800	30	174	650	140	2.75	
800	30	350	100	46	0.45	
800	30	350	1330	606	5.93	3
800	30	350	650	296	2.90	
800	30	40	100	5	0.40	
800	30	40	1330	62	5.31	
800	30	40	650	30	2.59	
2750	30	40	1330	51	10.00	

8.2 Python Code for PM-CAES Plant Model

```
def Run(list,alpha,pexp,effC,comp_ratio,effT,stageT,effB,effG,Wellf,
ProdRate, filepath):

    to_print_to_file =['']
    def print_temp(str):
        to_print_to_file[0] += str

    to_print_to_plot_data = ['']
    def print_plt_dat(str):
        to_print_to_plot_data[0] += str

    depth = list[2]
    thick = list[3]
    poro = list[0]
    kmd = list[1]

    filepath = filepath.format(depth,poro,thick,kmd)
    os.chdir(os.path.dirname(filepath))

    print_temp
('_____START_OF_RUN_____
_____\nDate and
Time:%s\nFileFolder:%s\n\n'%(str(datetime.datetime.now()),os.getcwd(
)))
    print_plt_dat
('START_OF_RUN,%s,%s,\n'%(str(datetime.datetime.now()),os.getcwd()))
    print "...Testing:
Depth_{}_Poro_{}_Thick_{}_Perm_{}".format(depth,poro,thick,kmd)

    ##### Input Parameters ####
    Tres = depth * 0.0338 + 282.0636 # reservoir temperature and air
temperature exiting the reservoir in K
    WellH = depth #maximum well depth
    InjRate = ProdRate/2. #since injection last 4 months and
production 2, the mass flow rate of injection is half that of
production

#    #working out pressure correction from well using Smith, 1950
analytical solution verified against O&P data
    def P_well_core(flowrate,pressure, Tin, Tout):
            Tflow = (Tin + Tout)/2.#Tflow in K
            Z = calc_Z_factor(pressure,Tflow) #compressibility factor
takes a T in K, P in Pa
            pressure *= 0.000145038 # converts Pa to Psi
            s = 0.0375*1*(WellH/0.3048)/(Z*Tflow*1.8) # here, T is
converted to Rankine, Well height taken as a positive value here
since the equation used uses Pw as the unknown pressure
            Q = ((flowrate/1.22)*3600*24)*35.3147 # from kg/s to
stdcf/d. old calc : flowrate/1.22/0.0283168*3600*24
            fac_a =
(Q*Z*atmP*0.000145038*Tflow*1.8)/(548.58*(atmT*1.8))
            fac_b = Wellf*(np.exp(s)-1.0)/(WellRad*2)**5.0
            P2cor = np.sqrt((pressure**2. -
fac_a**2*fac_b)/np.exp(s))
            return P2cor/0.000145038 #converts back to Pa
```

```
    #####Setting up cycle schedule information
    injtimes = [InjStart]
    SI1times = [injtimes[0]+InjTime]
    prodtimes = [SI1times[0]+ShutInTime+1]
    SI2times = [prodtimes[0]+ProdTime-1]

    prevtime = [injtimes[0]] #will be reset at the begining of each
cycle anyway
    for cycle in range(cyclenum-1):
        cycle = cycle+1
        Inj = InjStart+cycle*(InjTime+ProdTime+2*ShutInTime)+cycle*1
        injtimes.append(Inj)

        SI1 = injtimes[cycle]+InjTime
        SI1times.append(SI1)

        Prod = SI1times[cycle]+ShutInTime+1
        prodtimes.append(Prod)

        SI2 = prodtimes[cycle]+ProdTime-1
        SI2times.append(SI2)

    ##Data storage for summary
    CERlist = []
    RTlist = []
    GBlist = []
    MWhwell = []

    ##Extracting P2 and timestep times to lists
    raw_t = []
    raw_p = []
    with open (filepath, "r") as myfile: #opens .txt file created at
line 27 #txt_name
            data=csv.reader(myfile, delimiter=' ')  #extracts data
from .txt as lines
            for val in data: #iterates through lines of data file
                try:# skips headers
                    raw_t.append(float(val[0])) #populates times
                    raw_p.append(float(val[2])) #populates pressures
                except ValueError:
                        pass
            myfile.close()

    ''' Extracts inital maximum charging pressure to determine the
number of compression stages the plant will have'''
    storage_pressure = raw_p[0]   #calc_cp(P2cor, atmT, Tin,
cp_O2_dict, temps_O2)
    ##calculate cp of air approximatively
    ## convert it to J/kg by dividing the value in J/K/mol by the
molar mass of 0.02897 kg/mol
    ## use it with the equation from the heat loss script
    Twelltop = heat_loss.calculate_dT_well(depth, 3600.*24*30.,
massflow= ProdRate,
air_cp=calc_cp(storage_pressure,max(Tres*0.89,273.16),
min(Tres*1.11,1173.14), cp_Air_dict, temps)/AirMolarMass)[1]
    Twelltop += 273.15 # degC to Kelvin
    Tin = Twelltop + 400.
```

```
    compressor_maximum_storage_pressure = P_well_core(InjRate,
storage_pressure,  Tres, Twelltop)
    stageC, comp_ratio = get_stage(atmP,
compressor_maximum_storage_pressure, comp_ratio)


    print_temp( 'Mode:%s\n\nCycle Schedule:\nNumber of
Cycles:%s\nStart of Injection:%shrs\nInjection Time:%shrs\nShut-In
Time:%shrs\nProduction Time:%shrs\n\nCycle Rates:\nInjection
Rate:%skg/s\nProduction Rate:%skg/s\n\nTurbomachinery & Well
Parameters:\nCompressor inlet pressure:%sbar\nCompressor inlet
temperature:%sK\nCompressor Stage:%s\nCompressor
Ratio:%s\nCompressor Ideal/Actual Efficiency:%s\n\nTurbine inlet
pressure: See in log below\nTurbine inlet temperature:%sK\nTubine
Stages:%s\nTubine Ideal/Actual Efficiency:%s\nWell depth:%sm\n\nHeat
Addition Parameters:\nMethane Heating
Value:%sMWh/kg\nBoiler/Combustion Efficiency:%s\n\nThermodynamic
Parameters:\nPolytropic Exponent:%s\nAir R
constant:%skJ/(kg.K)\n\nOther efficiencies:\nGrid
Efficiency:%s\nNational Storage Power Target:%sMW\nNational Storage
Energy Target:%sMWh\nTotal Period of Storage:%sWeeks at%sh
production per day\n
\n'%(modetxt,cyclenum,InjStart/3600,InjTime/3600,ShutInTime/3600,Pro
dTime/3600,InjRate,ProdRate,atmP/100000,atmT,stageC,comp_ratio,effC,
Tin,stageT,effT, WellH,
LHV,effB,pexp,Rcst,effG,MWs,MWhs,StoreTime,ProdTime/3600))
    print_plt_dat('Mode,Number of Cycles,Injection Time(hrs),Shut-In
Time(hrs),Production Time(hrs),Injection Rate(kg/s),Production
Rate(kg/s),Compressor inlet pressure(bar),Compressor inlet
temperature(K),Compressor Stage,Compressor ratio,Compressor
Ideal/Actual Efficiency,Turbine inlet temperature(K),Turbine
Stages,Turbine Ideal/Actual Efficiency,Well depth(m),Methane Heating
Value(MWh/kg),Boiler/Combustion Efficiency,Polytropic Exponent,Air R
constant(kJ/(kg.K)),Grid Efficiency,National Storage Power
Target(MW),National Storage Energy Target(MWh)\n')

print_plt_dat(str([modetxt,cyclenum,InjStart/3600,InjTime/3600,ShutI
nTime/3600,ProdTime/3600,InjRate,ProdRate,atmP/100000,atmT,stageC,co
mp_ratio,effC,Tin,stageT,effT, WellH,
LHV,effB,pexp,Rcst,effG,MWs,MWhs]).replace('[','').replace(']','\n')
)
    print_plt_dat( 'Time(hrs),Pressure(bar),Power(MWe)\n')


    '''Checks that the model has ran at least x cycles before
attempting
    the calculations...'''

    requiered_sim_tim =
InjStart+(InjTime+ShutInTime*2+ProdTime)*cyclenum
    if raw_t[-1] < requiered_sim_tim:
        print "Minimum Sim Time not reached for
Depth_{}_Poro_{}_Thick_{}_Perm_{}\n".format(depth,poro,thick,kmd)
        if output_to_file == True:
            summary_str =
"{},{},{},{},{},{},{},{},{},{},,,,Numerical
Unstability\n".format(depth,poro,thick,kmd,alpha,effC,stageC,comp_ra
tio,effT,effG)
            printf(summary_file_path, "a" ,summary_str)
```

```
        return "failed"
    else:
        print " time check passed"

    '''Checking if collapse pressure is reached or not.
    the ratios are based on Aadnoy and Kaarstad 2010'''

    cohesive_rock_strength = 3846.15 * depth
    horizontal_stress = 14519.2306*depth
    initial_pore_pressure = 10000*depth
    depleted_pore_pressure = max((atmP,min(raw_p)))
    poisson_ratio = 0.25
    rock_friction_angle = 27.

    init_collapse_p = 0.5*(3.*horizontal_stress-horizontal_stress)-
np.cos(np.radians(rock_friction_angle))/(1-
np.sin(np.radians(rock_friction_angle)))*cohesive_rock_strength
    depleted_collapse_p = init_collapse_p-(1.-2.*poisson_ratio)/(1.-
poisson_ratio)*(initial_pore_pressure-depleted_pore_pressure)
    if depleted_pore_pressure < depleted_collapse_p:
        print "Minimum collapse pressure for open hole reached,
reservoir is at risk of damage\n"
        if output_to_file == True:
            summary_str =
"{},{},{},{},{},{},{},{},{},,,,Numerical
Unstability\n".format(depth,poro,thick,kmd,alpha,effC,stageC,comp_ra
tio,effT,effG)
            printf(summary_file_path, "a" ,summary_str)
        return "failed"
    else:
        print " geomech test passed\n Currently Executing
Depth_{}_Poro_{}_Thick_{}_Perm_{}".format(depth,poro,thick,kmd)

    '''Checking if the depletion pressure is at least 10 bars for
minimum prod pressure'''

    if P_well_core(ProdRate,max((atmP,min(raw_p))), Tres, Twelltop)
< 1e6:
        print "Production Pressure is less than 10 bar\n",
P_well_core(ProdRate,min(raw_p),  Tres, Twelltop)
        if output_to_file == True:
            summary_str =
"{},{},{},{},{},{},{},{},{},{},,,,Numerical
Unstability\n".format(depth,poro,thick,kmd,alpha,effC,stageC,comp_ra
tio,effT,effG)
            printf(summary_file_path, "a" ,summary_str)
        return "failed"

    ##### Start of Cycle Calculations
    ##Setting up logic switches and counter
    End_of_cycle_switch = [0]
    First_Inj_switch = [1]
    First_Prod_switch = [1]
    Cy_count = 0#counter

    for t in range(0,len(raw_t)): #iterate through timesteps

       if First_Inj_switch[0] == 1: #so that the lists are cleared
at the beginning of each cycle
```

```
            ##Setting up datalists to store timestep data during the
cycle
            TotalWc = []
            TotalWt = []
            heatlist = []
            Timestep = 0 #counter

        ###Working out Injection Work
        if raw_t[t] >= float(injtimes[Cy_count]) and raw_t[t] <
float(SI1times[Cy_count]):#makes sure the raw_t[t] is located within
an injection period
            if First_Inj_switch[0] == 1:
                print_temp( 'XXXXXXXXXXXXX    %s CYCLE
XXXXXXXXXXXXXXXXX\n'%(Cy_count+1))
                First_Inj_switch[0] = 0
                prevtime[0] = injtimes[Cy_count]
            P2= raw_p[t] #stores the pressure value at the well for
that timestep
            delta_t = float(raw_t[t])-float(prevtime[0]) # calculates
the time elapsed since the previous time step
            print_temp( 'Injection Time is {}, delta_t =
{}\n'.format(raw_t[t],delta_t))

          ##working out pressure correction from well
            P2ogs = P2
            P2cor = P_well_core(InjRate,P2,  Tres, Twelltop)#
get_Pout_Tout(InjRate, P2, Tres)[0]

          ##Work Calculations
            print_temp( 'The maximum charging pressure is%s bar.
After wellbore correction%s
bar\n'%(round(P2ogs/100000,1),round(P2cor/100000,1)))

            Wcomp = (stageC*pexp*Rcst*atmT)/(pexp-
1)*(((P2cor)/atmP)**((pexp-1)/(effC*pexp*stageC))-1)# working out
compressor work in kj/kg
            print_temp( 'The isentropic compressor work input to
compress the gas from%s bar to%s bar is of%s
kj/kg.\n'%(atmP/100000,round((P2cor)/100000,1),round(Wcomp,2)))
            TotalWc.append(Wcomp*delta_t*InjRate*0.000000278)
#*0.000000278 is to convert from kJ to MWh
            Toutc = atmT * (((atmP**(stageC-
1.)*P2cor)**(1./stageC))/atmP)**((pexp-1.)/(effC*pexp))#Barbour et
al. 2015

            compMW  = Wcomp*0.000000278*InjRate*3600 #Converts the
Compressor work per unit mass to compressor power in MW
            print_temp( 'The compressor outlet temperature before
after-cooling is%sK.\n'%(round(Toutc,2)))
            print_temp( 'The compressor cumulated work is of%s
MWh(el) during the%s h of injection.
\n\n'%(round(TotalWc[Timestep],2),delta_t/3600))
            print_plt_dat( '{},{},{}\n'.format(raw_t[t]/3600,
P2cor/100000, compMW) )
            prevtime[0] = raw_t[t] #resetting prevtime
            Timestep += 1 #adds 1 to counter

        #### Turbine Work & Heat Addition from Natural Gas
```

```
        if raw_t[t] >= float(prodtimes[Cy_count]) and raw_t[t] <
float(SI2times[Cy_count]):#makes sure the raw_t[t] is located within
an production period
            if First_Prod_switch[0] == 1: # logic check to correct
the fact that the last of the post injection shut-in steps have been
skiped (see break below l.361)
                First_Prod_switch[0] = 0 #turns switch off
                print_temp('Total Work for Injection: {}MWh\n\nXXX
End of Injection XXX\n\nXXX Start of Production
XXX\n\n'.format(float(sum(TotalWc))))
                prevtime[0] = prodtimes[Cy_count] #sets the time to
the start of the production so that if the last shut-in timestep is
before the start of injection the delta t between this step and the
injection start doesn't include the remainder of the shut-in phase
                Timestep = 0 #counter

            delta_t = raw_t[t]-float(prevtime[0])
            print_temp( 'Production Time is {}, delta_t =
{}\n'.format(raw_t[t],delta_t))
            P2 = raw_p[t] #stores the production well pressure from
data file

          ##Working out Pressure corrections:
            P2ogs = P2
            P2cor = P_well_core(ProdRate,P2,  Tres, Twelltop) #The
pressure drop in the combustor is assumes part of the efficiency of
the turbine factor is used to represent the pressure drop due to the
combustor

          ##Working out Work from Turbine
            print_temp( 'The minimum production pressure is%s bar.
After wellbore losses%s
bar\n'%(round(P2/100000,1),round(P2cor/100000,1)))

            Wt = (stageT*pexp*Rcst*Tin)/(pexp-
1)*((atmP/P2cor)**(effT*(pexp-1)/(pexp*stageT))-1)# working out
turbine work using polytropic eff in kj/kg
            print_temp( 'The isentropic turbine work output when
expanding gas from%s bar to%s bar, is of%s
kj/kg.\n'%(round(P2cor/100000,1),atmP/100000,round(Wt,2)))
            TotalWt.append(Wt*delta_t*ProdRate*0.000000278)
#*0.000000278 is to convert from kJ to MWh
            Toutt = Tin * (((P2cor**(stageT-
1.)*atmP)**(1./stageT))/P2cor)**(effT*(pexp-1.)/pexp)#Barbour et al.
2015

            if Toutt<288: #checks for unrealistically low exhaust
temperatures
                print_temp( '/!\%s outlet temperature is too low,
results are insignificant, \n increase inlet temperature and try
again\n'%(round(Toutt,2)))
            else:
                print_temp( 'The turbine outlet temperature before
flue gas processing & heat-recuperator is%sK.\n'%(round(Toutt,2)))

            print_temp('The turbine cumulated work is of%s MWh(el)
during the%s h of production.
\n\n'%(round(TotalWt[Timestep],2),delta_t/3600))
```

```
            turbMW  = Wt*0.000000278*ProdRate*3600 #Converts the
turbine work per unit mass to compressor power in MW
            print_plt_dat( '{},{},{}\n'.format(raw_t[t]/3600,
P2cor/100000, turbMW) )
            Timestep += 1 #adds 1 to counter

            ## Heat Adition from Natural Gas combustion
            'First stage heating from Tres to Tinlet'
            DT= Tin-Twelltop #realistic approach, the welltop
temperature is estimated
            # ALL IN J/K/Mol taken from VDI-Warmeatlas and Kallman
            # change Tres to Tatm for other extreme
            cpO2 = calc_cp(P2cor, Twelltop, Tin, cp_O2_dict,
temps_O2)
            cpN2 = calc_cp(P2cor, Twelltop, Tin, cp_N2_dict,
temps_N2)
            cpH2O = calc_cp(P2cor, Twelltop, Tin, cp_H2O_dict,
temps_H2O)
            cpCO2 = calc_cp(P2cor, Twelltop, Tin, cp_CO2_dict,
temps_CO2)

            #####Working out heat addition rate based on flow rate
only for the first stage
            MT = ProdRate
            x =
(0.016*4*DT*(cpO2*31.25+134.3537415*cpN2))/(LHV*57914084.59-
DT*(2*cpH2O+cpCO2-2*cpO2)) # 57914084.59 is to convert LHV from MWh
to J/mol, all molar mass are divided by 1000 to express them in
kg/mol
            mO2 = MT/(x*0.25+4.761904762)
            mCH4 = x*0.25*mO2
            mN2 = 3.761904762*mO2
            heatadded = mCH4*LHV # heat added to heat up gas in
stage one to Tin

            #listing product mols
            pO2=mO2/0.032-2*mCH4/0.016
            pN2=mN2/0.028
            pCO2=mCH4/0.016
            pH2O= mCH4/0.016*2 #nH2O in mols
            ptot = pO2+pN2+pCO2+pH2O

            ''' Vapour Condensation Calc (if any) '''
            # Antoine's Equation to work out the saturation pressure
            Psat = antoine.Psat(Toutt)


            # Setting Poutt depending on the number of stages, Poutt
is in bars
            if stageT > 1: #if more than on stage is present them
Pout of the first stage != Poutt, and needs correction using Px
                Px=((P2cor/100000)**(float(stageT)-
1)*(float(atmP)/100000))**(1/float(stageT))
                Pratio = float(Px)/float((P2cor/100000)) # Pout/Pin
                Poutt = Px # here Px is the pressure at the end of
the first stage
            else:
                Poutt = float(atmP/100000) # Pressure at end of
turbine/stage in bar for 1 stage
```

```
            # Working out how much of the pH2O falls to liquid phase
            pH2Omax = (Psat*ptot)*(1/Poutt) # both Psat and Poutt in
bar. Here RH = 1 i.e 100%. this is the maximum number of moles which
can be held by the gas at the T & P cdt of exhaust
            deltapH2O = pH2O-pH2Omax #difference of maximum water
saturation in vapour and actual water saturation in vapour
            print_temp('----Stage 1----\nPoutt at stage 1 is {}
bar.\n'.format(round(Poutt,1)))
            if deltapH2O <= 0 or Toutt >= 373.15 +273.15:
                print_temp('No Condensation occurs in the 1st
stage.\n')
            else:
                print_temp('Out of the%s kg of water vapour in 1st
stage exhaust gas,%s kg condensate.\n'%(pH2O*0.018,deltapH2O*0.018))

            #Multiple Stage Calculations#
            if stageT > 1: #checking if multiple stages

                for n in range(1,stageT):
                    print_temp('----Stage {}----\n'.format(n+1))
                    if deltapH2O <= 0 or Toutt >= 373.15 +273.15:
#checking if water vapour condensates
                        deltapH2O = 0 #set to 0 so that no water is
"magically" added in pH2O-deltapH2O


                    Dt= Tin-Toutt #delta T
                    'Resetting cp to match the new combustion mean
temperature'
                    Dt= Tin-Toutt #delta T between stage
                    #here, Poutt is the pressure after each stage
                    cpO2 = calc_cp(Poutt*1e5, Toutt, Tin,
cp_O2_dict, temps_O2)
                    cpN2 = calc_cp(Poutt*1e5, Toutt, Tin,
cp_N2_dict, temps_N2)
                    cpH2O = calc_cp(Poutt*1e5, Toutt, Tin,
cp_H2O_dict, temps_H2O)
                    cpCO2 = calc_cp(Poutt*1e5, Toutt, Tin,
cp_CO2_dict, temps_CO2)

                    heatIn = cpO2*Dt*pO2+cpN2*Dt*pN2+cpH2O*Dt*(pH2O-
deltapH2O)+cpCO2*Dt*pCO2 #pH2O-deltapH2O = removing the condensation
from previous stage
                    heatIn= heatIn*2.77778e-10 #from kJ/s to MWh/s

                    ## defining new exhaust products for the given
stage
                    fCH4 = heatIn/(LHV*0.016)# heatIn/(LHV*CH4 molar
mass)
                    pCO2 = pCO2+fCH4 # new pCO2 = oldpCO2 +
heatIn/(LHV*CH4 molar mass)
                    pH2O = pH2O+2*fCH4 # new pH2O = oldpH2O +
2*heatIn/(LHV*CH4 molar mass)
                    pO2 = pO2-2*fCH4
                    # pN2 remains unchanged
                    ptot = pO2+pN2+pCO2+pH2O # new product total
```

```
                    ## Working out heat addition energy over the
delta_t
                    heatIn =heatIn*(raw_t[t]-float(prevtime[0]))
#heatIn is now an enrgy quantity not a rate
                    heatlist.append(heatIn)
                    print_temp('and total heat added is {}
MWh\n'.format(round(heatIn,1)))

                    ##Working out how much of the pH2O falls to
liquid phase
                    Poutt=Poutt*Pratio # Poutt recalculation for the
stage/Pressure at end of turbine/stage
                    pH2Omax = (Psat*ptot)*(1/Poutt) # here RH = 1
i.e 100%. this is the maximum number of moles which can be hold by
the gas at the T & P cdt of exhaust
                    deltapH2O = pH2O-pH2Omax
                    if deltapH2O <= 0 or Toutt >= 373.15 +273.15:
                        print_temp('No Condensation occurs at
stage%s.\n'%(n+1))
                    else:
                        print_temp('Out of the%s kg of water vapour
in stage%s exhaust gas,%s kg
condensate.\n'%(pH2O*0.018,n+1,deltapH2O*0.018))
                    print_temp('Poutt at stage {} is {}
bar.\n'.format(n+1,round(Poutt,1)))
                print_temp('\n')

            prevtime[0] = raw_t[t] #resetting prevtime

       elif raw_t[t] >= float(SI2times[Cy_count]) and
End_of_cycle_switch[0] == 0:
            End_of_cycle_switch[0] = 1 #flips switches to avoid
repeating calculations below for all SI2 times
           #calcutations of total cycle stuff and store it for
overall cycles efficiencies
            final_workt = TotalWt[-1]
            TotalWc= float(sum(TotalWc))
            TotalWt= float(sum(TotalWt))
            print_temp( 'The turbine cumulated work is of%s MWh(el)
during the%s h of production.\n'%(round(TotalWt,2),ProdTime/3600.))
            print_temp( 'The losses incured by using a valve to
reduce the turbine outlet pressures and maintain constant power
output are%s of cumulated
work\n'%(get_error(final_workt,delta_t/3600.,TotalWt,ProdTime/3600.)
))
            MWhwell.append(TotalWt/(ProdTime/3600))

            HeatPtotal =
(heatadded*ProdTime+sum(heatlist))*(1.0/effB)
            true_mCH4 = HeatPtotal/ ProdTime / LHV

            if Tin <= atmT:
                HeatPtotal = 0 # just for safety in case HeatPtotal
values are stored in console
                print_temp( 'No heat is added.\n\n')
            else:
                print_temp( 'Heat added is%s MWh. \nThe CH4 massflow
rate is of%s kg/s (true:%s kg/s) and that of air%s kg/s
\n\n'%(round(HeatPtotal,2), mCH4, true_mCH4, mN2+mO2))
```

```
                print_temp('The heat rate is {} kJ/KWh
LHV\n'.format(round((HeatPtotal*3.6e6)/(abs(TotalWt)*1000)),0))
                gCO2 = (true_mCH4 * 3600) / (abs(TotalWt) /
(ProdTime / 3600.)) / 0.01604 * 0.04401 # gCO2/KWh = kgCO2/MWh
                print_temp('The emissions are {}
gCO2/KWh\n'.format(round(gCO2),0))


            '''Working out efficiencies'''
            RTe = abs(TotalWt)/(abs(TotalWc)+abs(HeatPtotal)*effG)
            RTe = round((RTe*100),1)#need to replace 1 by heat

            CER = round(abs(TotalWt)/abs(TotalWc),2)

            print_temp('The CAES Electricity Ratio of the%s cycle
is%s. CER = Wturbine/Wcomp.\n'%(Cy_count+1,CER))
            print_temp( 'The CAES Roundtrip Efficiency of the%s
cycle is%s%%.
Ert=(Wturbine(el)/[Wcomp(el)+Heat(el)]).\n'%(Cy_count+1,RTe)) #need
to replace 1 by cycle

            CERlist.append(CER)
            RTlist.append(RTe)

            print_temp( 'XXXXXXXXXXXXX  %s CYCLE END
XXXXXXXXXXXXXXXXX\n\n'%(Cy_count+1))
            Cy_count += 1 #Marks the end of the cycle
            #reset switches
            First_Inj_switch[0] = 1
            First_Prod_switch[0] = 1
            End_of_cycle_switch[0] = 0
            try:
                '''sets prevtime to the beginning time of the next
cycle
                using only Cy-count and not Cycount+1 since +1 added
in line 411'''
                prevtime[0] = injtimes[Cy_count]
            except:
                break

    print_temp(
'XXXXXXXXXXXXXXXXXXXXXXXXXXXXXXXXXXXXXXXXXXXXXXXX\nXXXXXXXXXXXXX
SUMMARY
XXXXXXXXXXXXXXXX\nXXXXXXXXXXXXXXXXXXXXXXXXXXXXXXXXXXXXXXXXXXXXXXXX\
n')
    avgGB = sum(GBlist) / int(len(GBlist))

    print_temp( 'Average RT efficiency is%s%%\n'%(sum(RTlist) /
int(len(RTlist))))
    print( 'Average RT efficiency is%s%%\n'%(sum(RTlist) /
int(len(RTlist))))

    if mode == 0 and round(Toutc,2) == round(Tin,2): #makes sure we
are in polytropic mode and checks that no extra heat is added during
expansion
        adRT = str(int(round(abs(TotalWt)/abs(TotalWc)*100,0)))
        print_temp('The Adiabatic RT efficiency of the last cycle
is%s%%.\n'%(adRT))
```

```
    if sum(GBlist) == 0  or mode != 0:
        print_temp( 'The Green to Black energy ratio is 1 for 0.\n')

    else:
        print_temp( 'Average GB output ratio is%s green unit out for
1 black unit out\n'%(round(avgGB,1)))

    if int(len(MWhwell)) == 0:
        print_temp( '/!\ ERROR in RUN\n')

    else:
        WellTotal= MWs/abs(round(sum(MWhwell) /
int(len(MWhwell)),2))
        TotalWellPower = round(sum(MWhwell) / int(len(MWhwell)),2)
        print_temp( 'Average well output%s MW.\nTotal Number of
Wells to meet%sMW
demand:%s\n_____________________________________END_OF_RUN_____________
_____________________\n\n \n'%(TotalWellPower, MWs,
round(WellTotal,0)))

    if output_to_file == True:
        printf(
'Power_Pressure_Data_{}_{}.csv'.format(version,date.today()), "a"
,to_print_to_plot_data[0])

printf("ThermoEfficiency_{}_SA_MultiGrid_{}.txt".format(version,date
.today()), "a" ,to_print_to_file[0])
        summary_str =
"{},{},{},{},{},{},{},{},{},{},{},{},{}\n".format(depth,poro,thick,k
md,alpha,round(effC,2),stageC,round(comp_ratio,2),
round(efft,2),effG,abs(TotalWellPower),sum(CERlist) /
int(len(CERlist)),sum(RTlist) / int(len(RTlist)))
        printf(summary_file_path, "a" ,summary_str)
```

8.3 Python Function for Monte Carlo Simulation

```
def MonteCarlo(filename, output_name, threshold, write = False,
max_iter = 1e6, max_plotable = 50000.):
    #makes sure to reset global variables
    global well_temp
    global refinement_well_count_list
    global well_counter
    global total_wells

    well_temp = [0,0,0,0,0,0,0]
    refinement_well_count_list = []
    well_counter = 1
    total_wells = []

    #extract the input data from the file
    filedata, fm = data_extraction(filename)

    #prepare an array to receive all the data from the calculations
    # 19 is the number of columns needed in the array to contain all
the information
    # requiered for the calculations. The array will be populated
through
    # each function called.
    data = np.full((len(fm),19),0)
    #assign the inital filedata to the first columns of the data
array
    data[:,0:filedata.shape[1]] = filedata



    #create the variables which will contain the outputs
    output = None #the overall average for power and energy are
stored here

    sample_num = max_iter/max_plotable
    sample_array = np.full((len(fm),max_plotable),0)
    large_output = np.full((len(fm),sample_num),0) # the result of
every single iteration for energy is stored here

    #counters and checks
    error = threshold + 1
    iteration_count = 0
    sample_count = 0

    while error > threshold and iteration_count < max_iter:
        iteration_count += 1

        #perform the calculation for the reservoir variables (only
needed once)
        res_var = reservoir_variables_assignment(data)

        #perform iteration calculations
        plant_var = plant_variables_assignment(res_var)
        power_energy_effRT_var =
calculations_power_energy_efficiency(plant_var,
(0.579,1.421))#(0.579,1.421)

        #assign outputs and update error
```

```
        if output == None:
            output = power_energy_effRT_var
            variance = np.var(output[:,0])

            sample_array[:,iteration_count-1] =
power_energy_effRT_var[:,1] #stores the energy array
        else:
            output += power_energy_effRT_var
            new_variance = np.var(output[:,0]/iteration_count)
            error = abs(variance - new_variance)
            variance = new_variance

            if iteration_count / max_plotable > sample_count + 1:
                large_output[:,sample_count] = np.mean(sample_array,
axis=1)
                sample_count += 1

            sample_array[:,(iteration_count - max_plotable *
sample_count)-1 ] = power_energy_effRT_var[:,1] #stores the energy
array

    #calculate the average of the power and energy outputs
    output = output/iteration_count

    print "iteration_count : ", iteration_count
    print"error: ", error
    print "st dv: ", np.std(output[:,0])
    print "Total Power (GW): {}, Total Energy (TWh):
{}".format(round(output[:,0].sum(),1), round(output[:,1].sum(),1))

    if write:
        to_write = np.c_[ fm, output ]
        headers = "Formation,Power(GW),Energy(TWh),Round-Trip
Efficiency (%)"
        np.savetxt(output_name, to_write, header = headers,
delimiter=",", fmt="%s")


np.savetxt("C:\Workspace\Fm_Estimates_Total_Well_Num_{}_reg_{}.csv".
format(version,date.today()), np.array(total_wells), delimiter=",")

        #save refinement GIS well count

np.savetxt("C:\Workspace\Fm_Estimates_Refinement_Well_Num_{}_reg_{}.
csv".format(version,date.today()),
np.array(refinement_well_count_list), delimiter=",")

        #save energy output of all iterations
        np.savetxt(output_name.replace('{}_'.format(version),
"{}_bulk_".format(version)), np.c_[ fm, large_output ],
delimiter=",", fmt="%s")

    return int(sample_num)

def data_extraction(filename):
    with open(filename, 'rb') as f:
        reader = csv.DictReader(f)
        filters = ['irth Coal','entland', 'ulmar']
```

```
        rows = [[float(v)  if k != 'Formations' and k !=
'Storage_Type' else v for k,v in row.iteritems()] for row in reader
if len([1 for filt in filters if filt in row['Formations']]) == 0
and  40 <= float(row['grossthicknessml']) <= 350 and 200 <=
float(row['shallowestdepthml']) <= 4000 and 100 <=
float(row['storagepermeabilityml']) <= 1330 and 15 <=
float(row['porosityml']) <= 30]
        fm = np.array(rows)[:,[6]]
        data = np.array(rows)[:,[0,3,4,11]].astype(np.float)
        return data, fm

def add_col(array):
    row, col = array.shape
    return np.c_[ array, np.ones(row) ]

def plant_param_gen(iters,mode = 'uniform'):
    if mode == 'normal':
        effC = np.random.normal(0.77, 0.03, iters)
        effT = np.random.normal(0.77, 0.03, iters)
        effG = np.random.normal(0.403, 0.025, iters)
    else:
        effC = np.random.uniform(0.66, 0.88, iters)
        effT = np.random.uniform(0.66, 0.88, iters)
        effG = np.random.uniform(0.33, 0.467, iters)

    return effC, effT, effG

def reservoir_variables_assignment(data):

    #hashs used to reference columns in the "data" array and
increase legibility
    porevol, temp, storage_eff, mindepth, pprod, pinj, rho_a, alphaD
=  0, 1, 2, 3, 4, 5, 6,7

    # accounts for the uncertainty resulting from the linear
approximations
    # of the reservoir pressure. +- 20% is assumed here.
    pressure_error = np.random.uniform(low = 0.8, high = 1./0.8,
size=data[:,mindepth].shape)

    #minimum production pressure hydrostatic
    data[:,pprod] = (0.05325 * data[:,mindepth] +
0.9689)*pressure_error

    #maximum injection pressure hydrostatic
    data[:,pinj] = (0.0995 * data[:,mindepth] +
5.7236)*pressure_error

    #maximum injection pressure 77
    pinj_frac = (0.19951 * data[:,mindepth] +
18.808963)*pressure_error

    #minimum production pressure 77
    pprod_frac = (0.13417 * data[:,mindepth] +
8.2118)*pressure_error

    #alpha random
    alpha = np.random.random_sample((1,data[:,[pinj]].shape[0]))
```

```
    alpha[0][pprod_frac>250.] = random.uniform(1.-(250.-
data[:,pprod][pprod_frac>250.])/(pprod_frac[pprod_frac>250.]-
data[:,pprod][pprod_frac>250.]),1.)

    data[:,alphaD] = alpha[0]

    data[:,pinj]= alpha[0]*data[:,pinj] + (1. - alpha[0])*pinj_frac

    data[:,pprod] = alpha[0]*data[:,pprod] + (1. -
alpha[0])*pprod_frac

    # air density
    data[:,rho_a] = np.array([eos.rho_air(t,p) for t,p in
zip(data[:,temp], data[:,pinj])])

    return data

def get_fracture_injP(array):
    return 2.006*array + 6.6084

def get_fracture_prodP(array):
    return 2.5196*array - 3.2626

def plant_variables_assignment(data): #where alpha is how close to
Hydrostatic the operation is taking place
    #hashs
    porevol, temp, storage_eff, mindepth, pprod, pinj, rho_a, alphaD
=  0, 1, 2, 3, 4, 5, 6, 7

    effC, effT, effG, cs, es, wellpow = 8,9,10,11,12,13


    #adding effC, effT, effG
    data[:,[effC,effT,effG]] = data[:,[effC,effT,effG]]*0 + 1
    data[:,[effC,effT,effG]] *= np.array(plant_param_gen(1,
'normal')).transpose()

    #adding Compression Stages
    Patm = 101325.0
    data[:,cs] =
get_comp_stage(np.full(data[:,pprod].shape,Patm),data[:,pinj]/1e-
5,3.0)

    #adding Expansion Stages
    data[:,es] = np.full(data[:,cs].shape,2.0)

    #adding true operation wellpower
    n = 1.4
    R = 0.287
    Tatm = 283.15 # K
    #get wellpow in joules/kg
    #the average pressure between injection and production is used
and weighted for the operation mode using alpha
    # alpha = 1 for full hydrostatic operation and alpha = 0 for
full fracture pressure operation
    #published reg
    data[:,wellpow] = -7.52334084664091 -1.22396032866836 *
data[:,alphaD] + 3.42270764277401 * np.log10(data[:,mindepth]) +
8.06600755861608 * data[:,effT]
```

```
    cp_err = np.random.uniform(0.97, 1.03,
data[:,storage_eff].shape) #uncertainty caused by constant specific
heat assumption +2% to -3%
    data[:,wellpow] *= cp_err # has less than 1 GW and 1 TWh on the
final storage potential

    return data

def get_comp_stage(pin, pout,ratio): #pin at compressor inlet, pout
at compressor outlet, target ratio
    stage_float = np.log(pin/pout)/(np.log(pin)-np.log(pin*ratio))
    stage_round = np.ceil(stage_float)

    return stage_round

def calculations_power_energy_efficiency(data, effS_range):
    #hashs
    porevol, temp, storage_eff, mindepth, pprod, pinj, rho_a, alphaD
=  0, 1, 2, 3, 4, 5, 6,7
    effC, effT, effG, cs, es, wellpow = 8,9,10,11,12,13
    airmass, num_well, fm_power, fm_energy, fm_effRT = 14, 15, 16,
17,18

    #set up an efficiency modifier
    effS_min, effS_max = effS_range
    effS_mod = np.random.triangular(effS_min, 1., effS_max,
data[:,storage_eff].shape)
    sg = 0.47 #gas saturation in reservoir
    #calculates the airmass in each formation
    data[:,airmass] = data[:,porevol] * 1e6 * 1 * data[:,rho_a] *
data[:,storage_eff] * effS_mod * sg

    wellrates = 15. #kg.s

    #calculates the number of wells per formation for a given
airmass
    data[:,num_well] =
data[:,airmass]/(wellrates*60.*24.*3600.*2.)#158112000.0 #air mass
in reservoir for 2 months at 15kg/s

    #determines number of well just for entries colocated with
windfarms
    for n,w in enumerate([0,5,8,21,34,35,40]):
        well_temp[n] += data[:,num_well][w]
    global well_counter
    global refinement_well_count_list

refinement_well_count_list.append(np.array(well_temp)/float(well_cou
nter))
    well_counter += 1

    #stores total well necessary data
    global total_wells
    total_wells.append( np.sum(data[:,num_well]))

    #calculates the total power that the wells in the formation can
generate
    data[:,fm_power] = data[:,num_well]*data[:,wellpow]/1000. #GW
```

```
    #and the corresponding energy delivered over two months
    data[:,fm_energy] = data[:,fm_power] * 24.*61.*0.001 #TWh

    #and the roundtrip efficiency
    data[:,fm_effRT] = -23.981296219648700 -0.884842746228878 *
data[:,alphaD] + 0.128603538374262 * data[:,mindepth]**0.5 +
51.516313610315300 * data[:,effC] + 46.710688484866000 *
data[:,effT]

    return data[:,[fm_power, fm_energy, fm_effRT]]
```

8.4 Geological Assessment of the Key Geological Formations

A map of the Central and Northern North Sea, where most the formations are found, is given in Figure 8-1 to serve as reference to the reader.

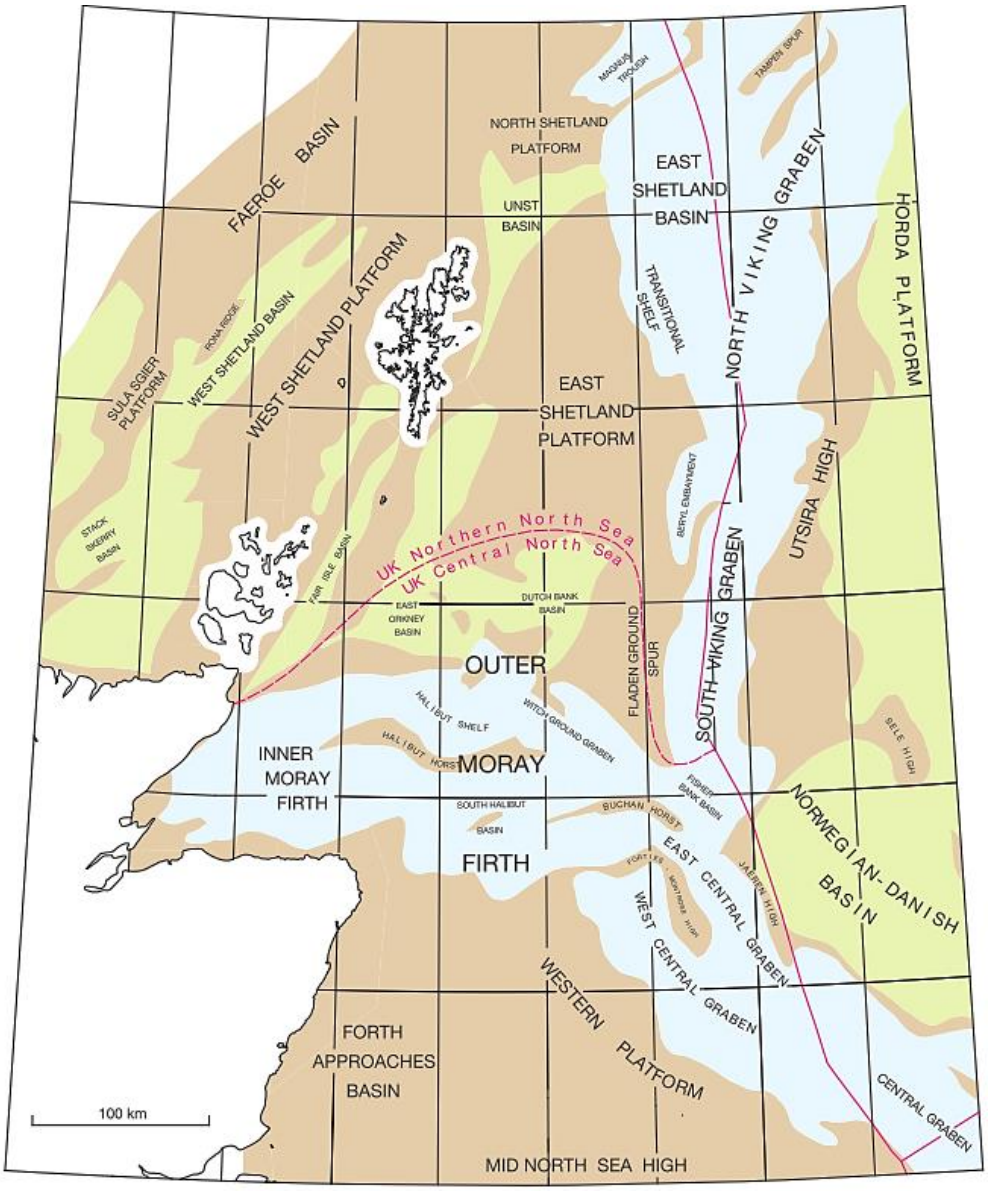

Figure 8-1: Structural framework of the Northern and Central North Sea, serves as reference for the following descriptions (Richards *et al.*, 1993)**. Reproduced with the permission of the British Geological Survey ©NERC. All rights Reserved.**

8.4.1 Bunter Sandstone Formation

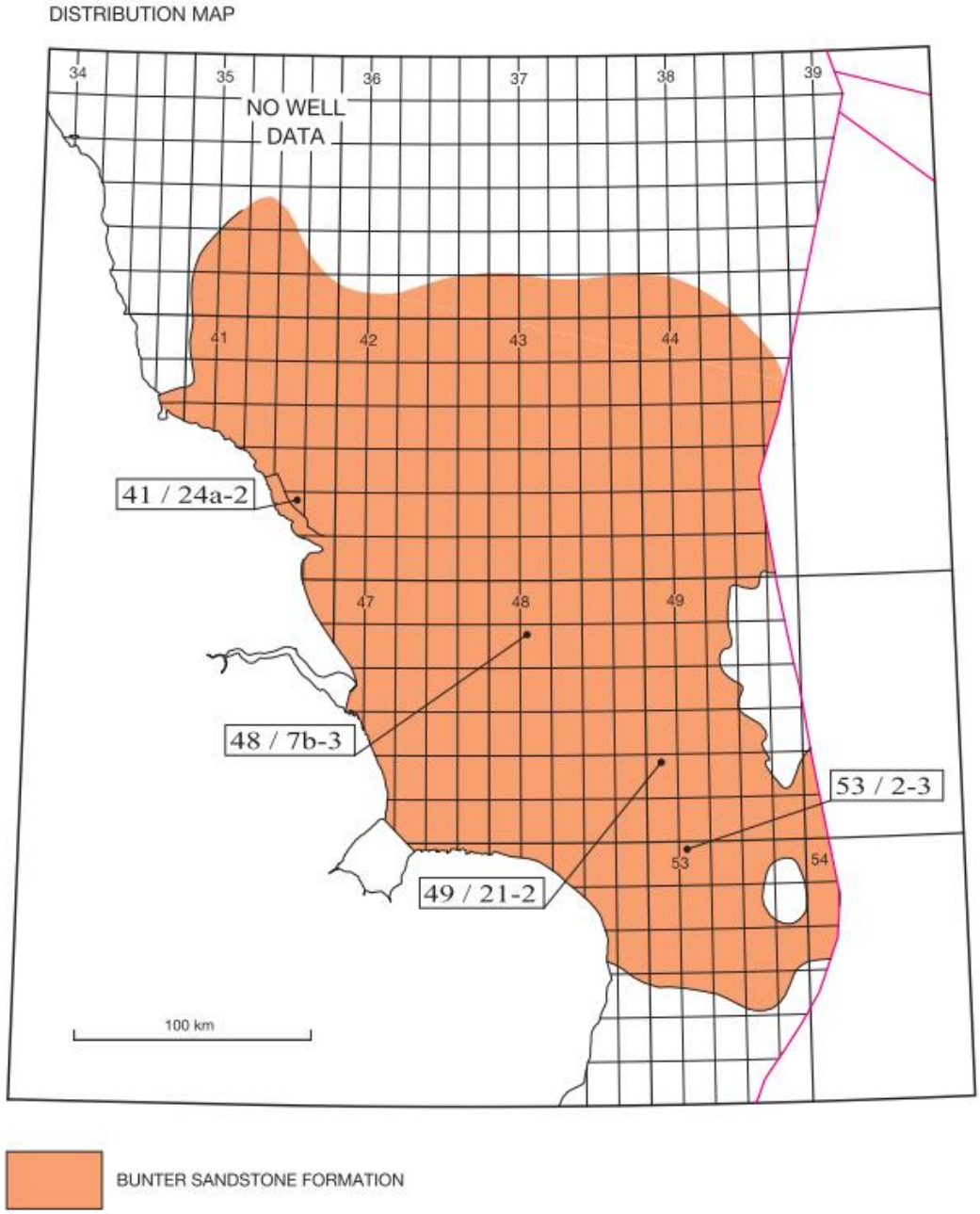

Figure 8-2: Location of the Bunter Sandstone Formation, located in the Southern North Sea. (Johnson, Warrington and Stoker, 1994) **Reproduced with the permission of the British Geological Survey ©NERC. All rights Reserved**

8.4.1.1 Description

The Bunter Sandstone Formation is composed of sandstones interbedded with mudstones, deposited in a fluvial environment during the Early Triassic (*circa*. 250 Ma). Some dolomitic or anhydritic cementation of the sandstones occurs (Bifani, 1986). In places it appears that the cement completely obstructs the porosity which might in turn reduce the permeability and reduce pressure communication across the aquifer (Noy *et al.*, 2012). Sandstones at the top of

the formation tend to be cleaner, i.e. less argillaceous than the lower ones. (Johnson, Warrington and Stoker, 1994).

Pressure communication between the Hewett gas field and the Little Dotty gas field (Cooke-Yarborough and Smith, 2003) implies that fault bounded compartments within the Bunter Sandstone are connected to some extent. Hence, brine movement through the pore space is likely to occur on a reservoir scale. Porosity varies significantly from less than 1% to 35% with an arithmetic mean of porosity is 19% (Noy *et al.*, 2012). Similarly permeability varies from ~ 0.01 to 10,000 mD, with a ratio of vertical to horizontal air permeability close to 0.7 (Noy *et al.*, 2012). Reported typical permeability for the Hewett, Little Dotty, Esmond and Caister B gas fields within the Bunter Sandstone range from 87 mD to 500 mD (Noy *et al.*, 2012).

8.4.1.2 Uncertainty

The degree of interconnectivity of the various pressure compartments within the Bunter Formation is not well known (Noy *et al.*, 2012). It appears that there is some pressure connectivity which would most likely mean that the actual reservoir pressure swing, observed during a PM-CAES cycle, would be lower than the one modelled. However, the model accounts for the worst case scenario, where the lack of connectivity leads to the maximum and fastest pressure variations within the reservoir. Should the reservoir display a greater connectivity it is likely that the production from the reservoir at the pressures imposed by the surface turbomachinery could be maintained for periods of times in excess of the ones modelled (i.e. more than two months for production and four for injection).

The greater unknown is the heterogeneity of the permeability across the reservoir caused by faults and cementation, as well as the channelised nature of the sandstone. These heterogeneities could lead to non-uniform spread of air within the porous rock of the reservoir, known as fingering. This causes unpredictable downhole pressure changes due to pockets of stored air remaining blocked within the porous matrix until a certain pressure is reached, leading to a sudden pressure change as the pocket empties. The unpredictable changes would have adverse effect on PM-CAES operation. Such effects are difficult to account for with the data available and the scope of this study. However the method used, which aims at estimating "usable pore space" using existing hydrocarbon data and success rates, accounts for errors in reservoir assessment.

Since this formation has proven to be able to contain stored gas in the form of natural gas for millions of years, it provides confidence that the seal is effective in many places. Furthermore, the database contains many Type 3 entries which indicate that extensive research on the

feasibility of this formation to contain stored gas has been done. Even though the data used to establish those Type 3 entries, it can be assumed that they are highly likely to be viable options for PM-CAES and should be included in the storage potential estimates.

8.4.2 The Statfjord Formation

8.4.2.1 Description

First described by Deegan & Scull (1977), the Statfjord Formation described a heterolithic unit comprising sandstones, siltstones and mudstones deposited in a channel rich depositional environment, located in the Northern North Sea in the Late Triassic to Early Jurassic (i.e. approximately 203 to 196 Ma) (Figure 8-3 a.). The unit was located between the Triassic beds and the Dunlin Group. Initially it included three members: the 'Raude Member', the 'Eiriksson member', and the 'Nansen Member'. In the CO_2 Stored database and therefore in this study, the 'Nansen Member' was not considered part of the Statfjord formation, following the subdivision from (Richards *et al.*, 1993).

The Statfjord Formation is heterogeneous (Figure 8-3 b.). It is composed of interbedded mudstones, siltstones and sandstones, with some minor coals in some areas (Richards *et al.*, 1993). In the East Shetland basin, the sandstones themselves are heterogeneous and are fine to very coarse grained, occasionally pebbly, micaceous, with occasional kaolinite clay as well as sporadic cross-bedding. The sandstone, mudstone and siltstone section have a thickness in the order of 5 m (Richards *et al.*, 1993). In the Beryl Embayment however, sandstones fine upwards from coarse or medium grained to fine or very fine grained. The sandstones are typically 3 m thick, with some occasional stacking up to 10 m (Richards *et al.*, 1993). The database accounts for the total formation thickness which can attain up to 300 m in thickness in the East Shetland Basin and 80 m in the Beryl Embayment (Figure 8-3).

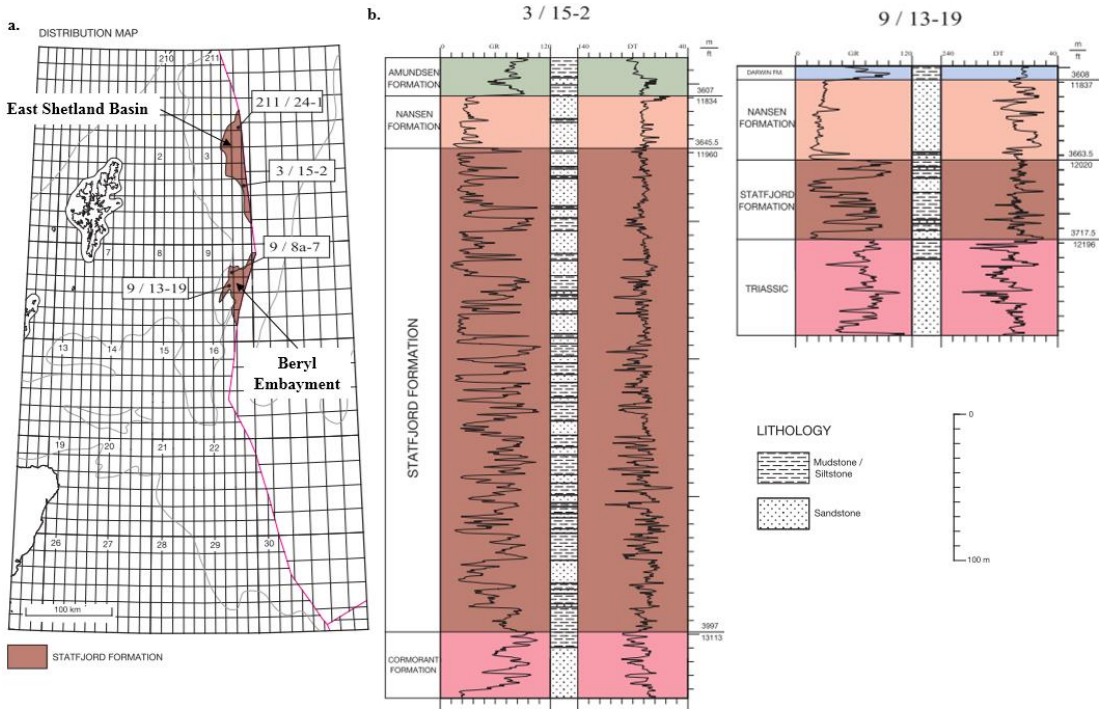

Figure 8-3: Location of the Statfjord Formation (a.), alongside two representative interpreted well logs which show the formation scale heterogeneity of the formation (b.). Based upon Richards *et al.* (1993), with the permission of the British Geological Survey.

8.4.2.2 Uncertainty

The scale of heterogeneity of this formation is likely to be problematic for PM-CAES operations. It will render any reservoir within the formation prone to fingering, and would make the retrieval of the stored air difficult. It is also likely to lead to variable and unpredictable downhole pressures. The sandstone bed-sets' thicknesses are also under the 50 m threshold deemed suitable for PM-CAES. Due to the strong heterogeneity of the formation even the extensive thicknesses found in the East Shetland Basin are likely to be unsuable. The Statfjord Formation was removed from the assessment to achieve more realistic storage potential estimates.

8.4.3 The Sele Formation

8.4.3.1 Description

The Sele Formation as described by Knox & Holloway (1992) refers to a unit of mudstone, deposited in the Late Paleocene to Early Eocene (approximately 59 to 48 Ma), which lays between the Forties Formation and the Balder Formation. This mudstone unit contains prominent sandstone members. It is those members which correspond to the entries in the CO_2 Stored database.

The first of those members is the 'Cromarty Sandstone Member', it is found in the Outer Moray Firth (Figure 8-4 a.). The sandstone is clean, very fine to fine grained and

unconsolidated. It is interbedded with grey, carbonaceous mudstone. Interpreted well log 21/ 2-1 shows continuous sand packages of approximately 60 m (Figure 8-4 b.). The member is reported to have a maximum thickness of about 120 m.

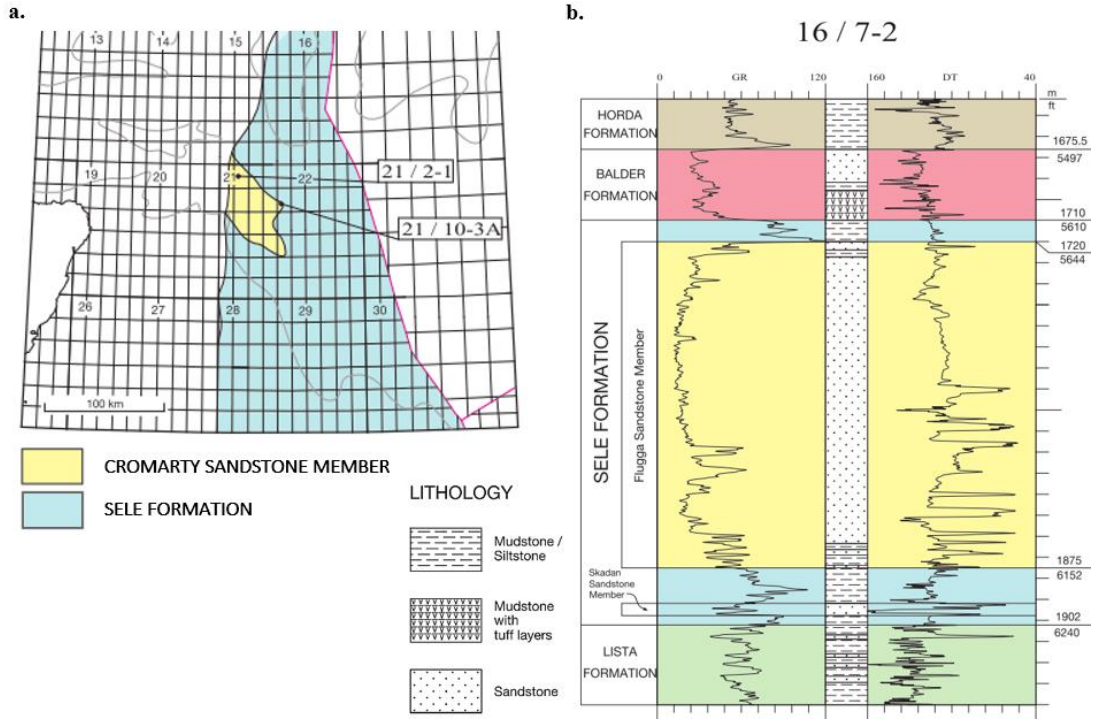

Figure 8-4: Location of the Cromarty Sandstone Member within the Sele Formation, including a representative interpreted well log which shows clean, 60 m thick, continuous sand packages. Based upon Knox & Holloway (1992), with the permission of the British Geological Survey.

The next member is located to the south of the Viking Graben and is called the Flugga Sandstone Member (Figure 8-5 a.). It is mostly composed of clean, fine to medium grained sandstone, displaying ‘blocky’ well-log profiles as observed in well 21/2-1 (Figure 8-5 b.). In areas it is more than 270 m thick. (Knox and Holloway, 1992)

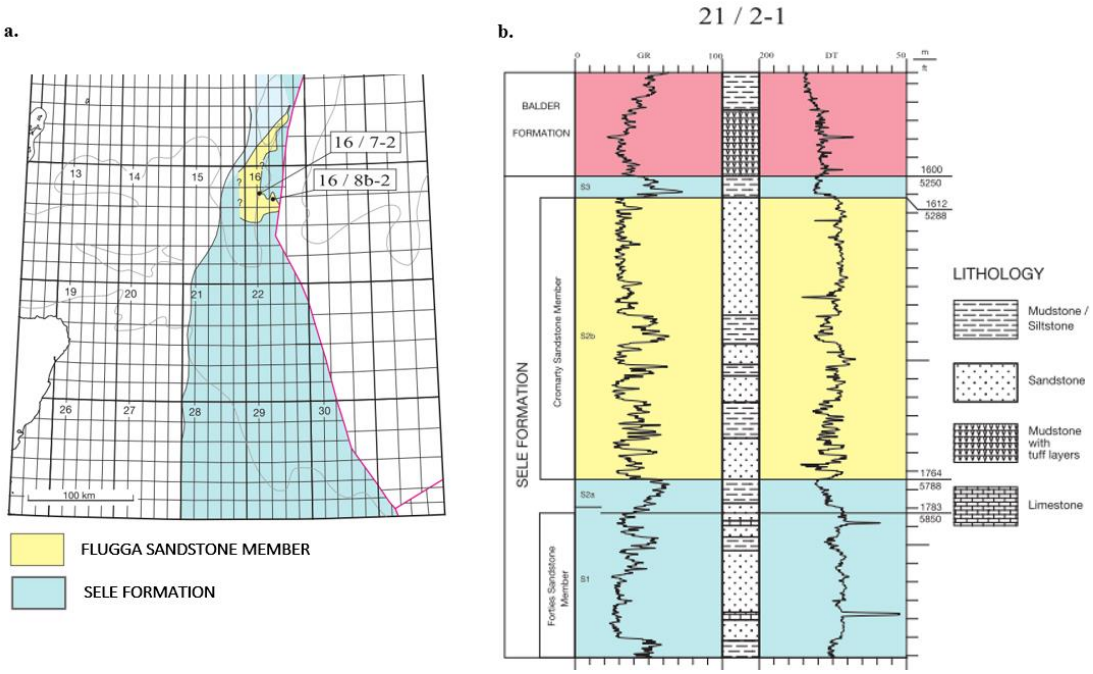

Figure 8-5: Location of the Flugga Sandstone Member within the Sele Formation, including a representative interpreted well log which shows clean, 200 m thick, blocky sandstone. Based upon Knox & Holloway (1992), with the permission of the British Geological Survey.

The next member screened from the database is the Hermod Sandstone Member (Figure 8-6 a.). It is a unit composed mostly of clean, very fine to medium grained 'blocky' sandstone (Figure 8-6 b.). It is very similar to the Flugga Sandstone Member in composition, but is slightly thinner, with thicknesses of less than 100 m. (Knox and Holloway, 1992)

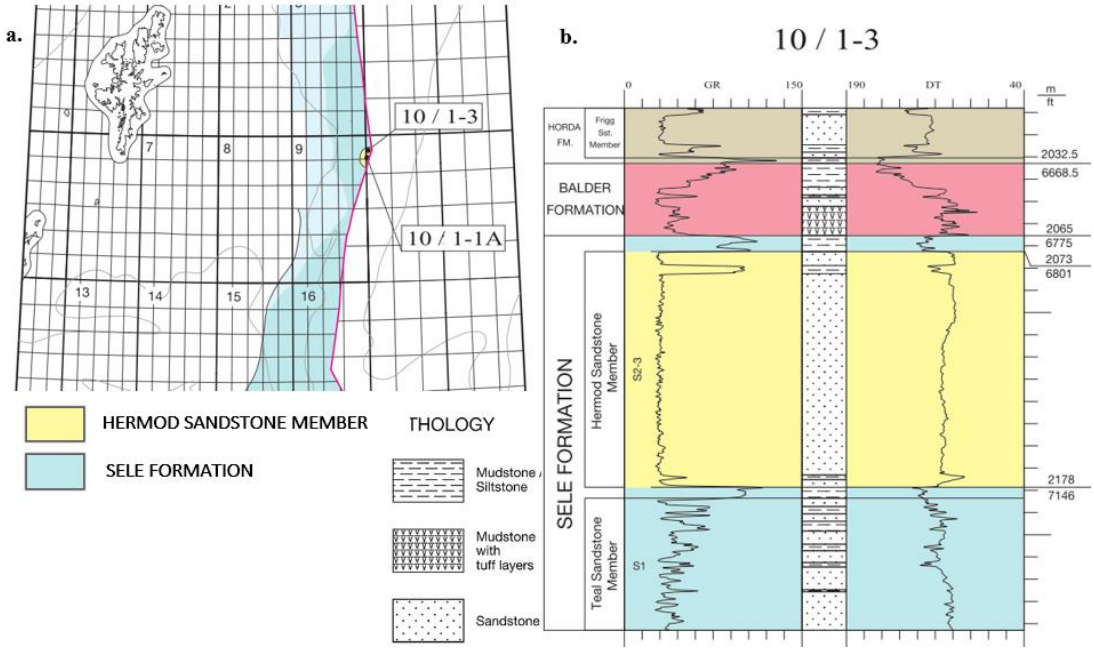

Figure 8-6: Location of the Hermod Sandstone Member within the Sele Formation (a.), including a representative interpreted well log which shows clean, approximately **100 m thick, blocky sandstone (b.). Based upon Knox & Holloway (1992), with the permission of the British Geological Survey.**

The final member to pass the screening was the Teal Sandstone Member (Figure 8-7 a.). It consists of fine to coarse grained sandstone which contains some sporadic intercalations of mudstone (Figure 8-7 b.). The sandstone is poorly to moderately sorted and in the order of 100 m thick. (Knox and Holloway, 1992)

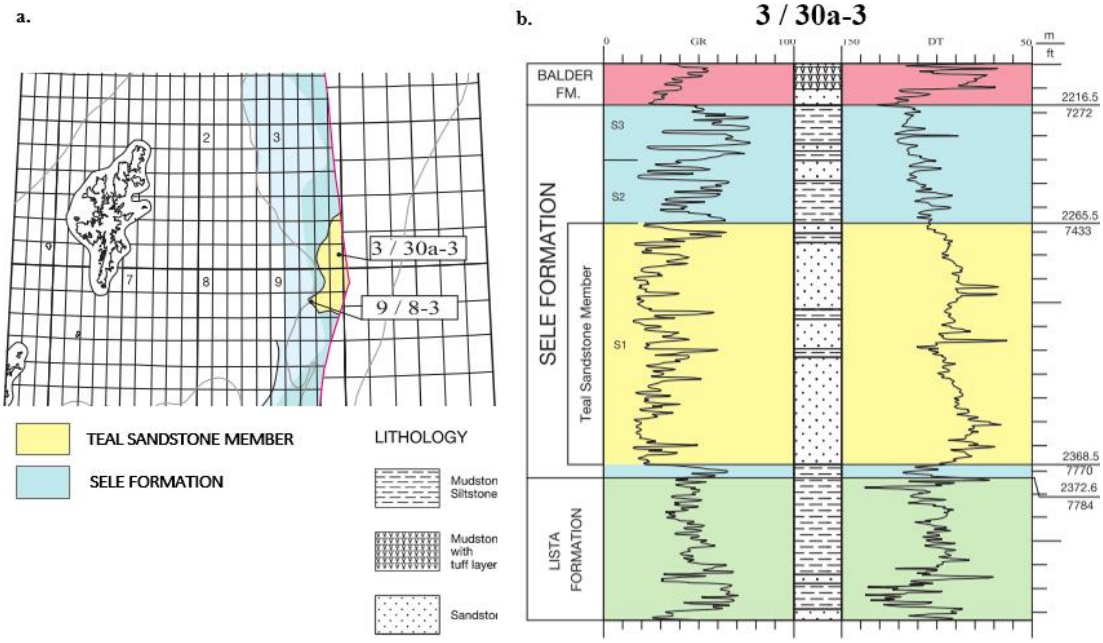

Figure 8-7: Location of the Teal Sandstone Member within the Sele Formation (a.), alongside a representative interpreted well log which shows clean, approximately **100 m thick, blocky sandstone (b.). Based upon Knox & Holloway (1992), with the permission of the British Geological Survey.**

8.4.3.2 Uncertainty

Although the Cromarty Sandstone Member contains unconsolidated sands, a well screen can be used to reduce the likelihood of sand production in the well, and mitigate against it should it happen. Continuous sandstone packages of 60 m could be used for compressed air storage. The interpreted well log 16/7-2 highlight the extensive blocky sandstone (Figure 8-4 b.). The Flugga, Hermod and Teal Sandstone Members all seem to offer reasonably blocky and thick sandstones in excess of 50 m which could be used for PM-CAES. In addition the Teal and Hermod members overlap geographically which mean that they could both be used on a single storage project.

8.4.4 The Pentland Formation

8.4.4.1 Description

The Pentland Formation covers a large areal extent, it appears in the Outer Moray Firth, the Central Graben, the Unst Basin, and in the basins to the east of the East Shetland Platform (Figure 8-8 a.). It was deposited in marsh/deltaic environments during the Jurassic, between the Toarcian and the Oxfordian (approximately 183 to 155 Ma). It is faulted into numerous compartments. The formation is very heterogeneous and composed of variably interbedded sandstones, siltstones, shales and coal beds (Figure 8-8 b.). In the Central Graben and the Outer Moray Firth areas volcanics from the Rattray Volcanics Member are present. In places they compose most of the formation thickness. Lavas are 1 to 9 m thick and are associated with agglomerates, tuffs, and tuffaceous claystones. In places the volcanics are interbedded with the sandstone (Richards *et al.*, 1993).

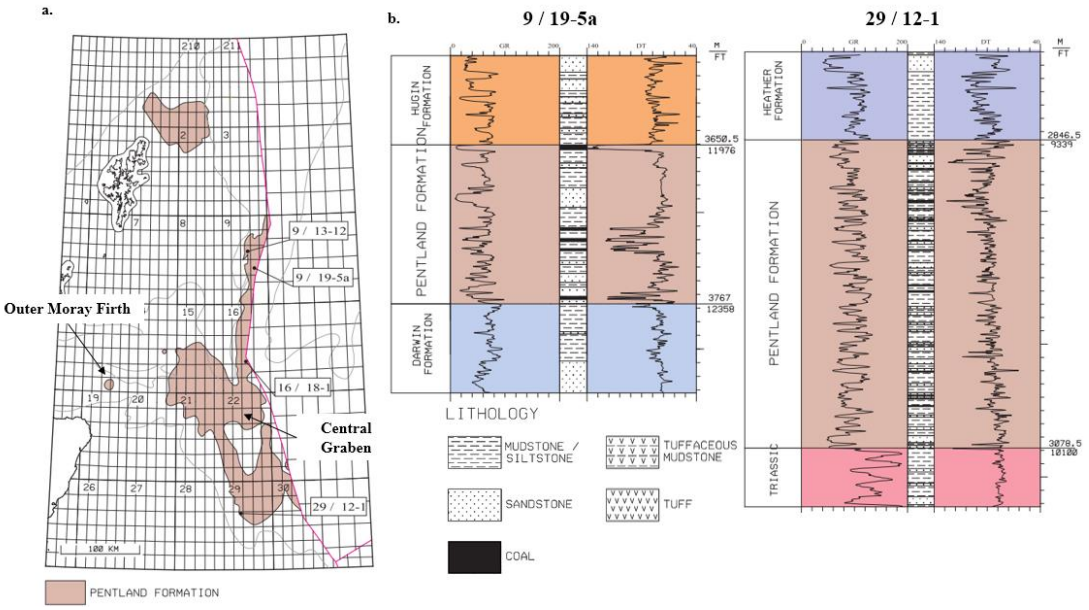

Figure 8-8: Location of the Pentland Formation (a.), alongside two representative interpreted well logs which shows the very heterogeneous nature of the formation (b.). Based upon Richards *et al.* (1993), with the permission of the British Geological Survey.

8.4.4.2 Uncertainty and Model Limitations

Using the data published from the Erskine Field, in the Central Graben, it appears that the heterogeneity of the reservoir is significant and should be taken into account when modelling this formation (Coward, 2003) (Figure 8-9). The high degree of heterogeneity is also observed at other locations as indicated by the well logs in Figure 8-8 b; it is likely to lead to significant fingering during the initial cushion gas injection, limiting the potential of the formation to be used for PM-CAES in which the cyclic recovery of the gas can be greatly hindered by uneven air saturation in the reservoir (Smith *et al.*, 1978; Allen *et al.*, 1983; Grappe, 2008). For this reason the formation was removed from the storage estimates as it is likely that, due to its high heterogeneity, it would be costly to identify a potential CAES suitable site.

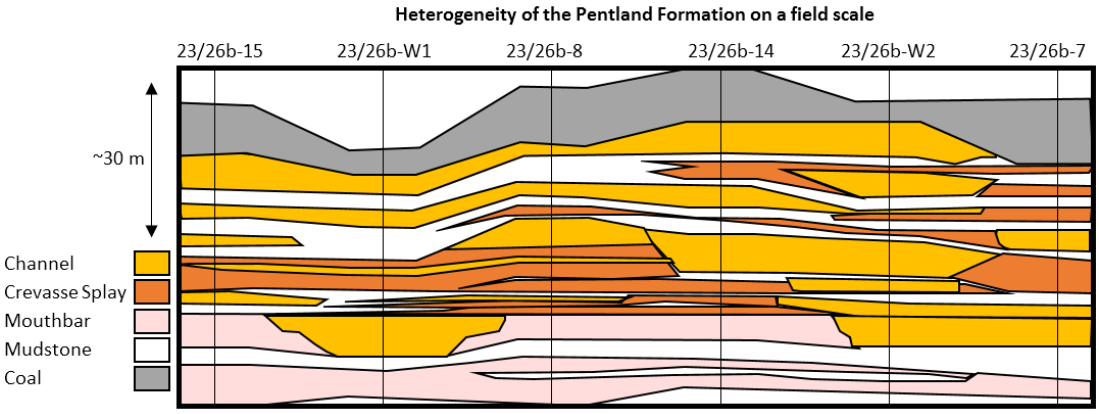

Figure 8-9: Pentland reservoir facies over a portion of the Erskine Field. Amended from Coward (2003).

8.4.5 The Lista Formation's Mey Sandstone Member

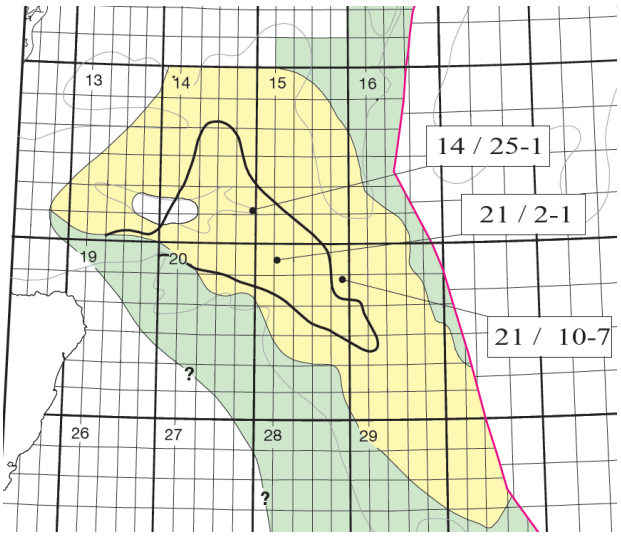

Figure 8-10: Extent of the Lista formation (green) and of the Mey Sandstone member (yellow), the black line outlines the area in which the Balmoral Tuffite is present. (Knox and Holloway, 1992) **Reproduced with the permission of the British Geological Survey ©NERC. All rights Reserved.**

8.4.5.1 Description

The Mey member is part of the Lista Formation, deposited in the Late Paleocene (approximately 59 Ma). The Lista Formation is dominated by pale green-grey shales, yet the Mey member is usually composed of massive, stacked units of fine-to medium-grained, and sometimes coarse-grained sandstones with common mudstone and chalk clasts (Knox and Holloway, 1992; Mudge, 2014). The Mey Member is the target reservoir, whilst the overlying shales are the proposed seal.

The Mey Member, deep marine fan system containing channel deposits, reaches thicknesses of 100s of meter (350 m according to Mudge (2014) and over 500 m according to Knox & Holloway (1992)) in the Outer Moray Firth area to the north of the Halibut Horst primarily,

and to a lesser extent to the south. It thins gradually towards the east. Continuous sand packages can be found in excess of 75 m in the Northern part of the Central Graben (Kilhams *et al.*, 2012); thicknesses do not usually exceed some 10s of meters in the Central Graben (Kilhams *et al.*, 2012). In the Outer Moray Firth section, the Mey Sandstone member is divided into two sandstone units by the Balmoral Tuffite, above it the formation is referred to as the Balmoral Sandstone, and beneath it as the Andrew Sandstone (Figure 8-10).

A net-to-gross ratio, defined as the ratio of rock suitable for gas storage to the total, of ~ 0.7 can be encountered in the northern part of the Central Graben and in the Outer Moray Firth (Knox and Holloway, 1992). In those areas large continuous volumes of sandstone can be targeted for air storage.

Hempton *et al.* (2005) have proposed four key facies to describe the Mey Member which can be used to determine areas suitable for air storage. From highest to lowest sand content they are: amalgamated sandstone facies, sand-prone heterolithics facies, mud-prone heterolithic facies and hemipelagic mudstone facies. The amalgamated sandstone facies, has average horizontal permeabilities of 360 mD and vertical ones of ~ 370 mD, whilst the other three facies have permeabilities of less than 100 mD (Hempton *et al.*, 2005). This would make the amalgamated sandstones facies the only viable target for PM-CAES according to existing siting criteria which recommend a minimum reservoir permeability of 100 mD (Stottlemyre, 1978; Allen *et al.*, 1983). The overall porosity of the Mey Member is within the range allowing PM-CAES, from ~ 10 to 35% (Kilhams *et al.*, 2012).

8.4.5.2 Uncertainty

One source of uncertainty lies in the total pore volume available for storage. This is reflected by the divergence in proposed net-to-gross ratios in the database and the ones proposed in the literature. On the one hand, the net-to-gross ratio used to calculate the pore volume in the CO_2 Stored database is 0.7. On the other, according to Kilhams *et al.* (2012) both the amalgamated sandstone facies and the sand-prone heterolithics are considered as reservoir sands whilst the mud-prone heterolithics and the hemipelagic mudstone facies are considered as non-reservoir for the net-to-gross ratio calculations. They calculated a maximum net-to-gross ratio for the Northern Central Graben Mey Member to be of 0.35, which is lower than the 0.7 value presented in the database. This can be due to the Mey formation being more sand dominated in the Northern Central Graben and Outer Moray Firth as suggested by Knox & Holloway (1992) and Mudge (2014). Mudge (2014) states that the Andrew Sandstone unit, a subset of the Mey Member, thins out significantly in the Central Graben. Another hypothesis explaining this difference in net-to-gross ratio is that Knox & Holloway (1992) chose a different

classification of sand and muds when calculating the net-to-gross ratio. Their classification might include some of the facies with permeabilities unsuitable for air storage. The lower net-to-gross ratio calculated by Kilhams *et al.* (2012) using a wide range of methods suggests that a 0.35 net-to-gross ratio might, in fact, be more representative of the Mey Formation. This could lead to pore volume of the Mey Member being overestimated by a factor of 2 in the database.

8.4.5.2.1 Refined Pore Volume Assessment

To address this uncertainty in net-to-gross ratio, and therefore in areas with pore volume suitable for inter-seasonal PM-CAES, an assessment of the Mey Member was done to refine the pore volume estimates from the CO_2 Stored database. This assessment results in making the Type 1 entry for the Mey Member into a Type 2 entry, according to the classification used in this study.

For the area of the Central Graben covered by the work of Kilhams *et al.* (2012) their porosity, thickness and permeability maps were used in combination to the siting criteria used in this work. The assessment of the Central Graben found that most of the area actually had a permeability which was less than a 100 mD, the minimum allowing PM-CAES to be feasible, with the exception of the zone to the North West of the central graben where a significant sand input from the Outer Moray Firth and Forties Platform occurred.

Approximately 40 interpreted well logs from Armour *et al.* (2003) and Knox & Holloway (1992) were used for the assessment of the formation in the Outer Moray Firth. Bulk thickness maps were calculated using a deterministic inverse distance weighted interpolation method in ArcMap®. This method was chosen to prevent statistical uncertainty which would have resulted from using other interpolation methods due to the limited number of well data. By means of an interpreted map (Figure 8-11) showing the location of thick sand packages, sand and mud facies of the Mey Member, resulting from sediment input from the shelf into the basin (Mudge and Bujak, 1996), it was possible to assign the high net-to-gross ratio of 0.7 to areas with massive sand packages facies, and the lower ratio of 0.35 to sand facies. Zones with mud rich facies were removed. By multiplying the bulk thickness raster map (formed of 500 x 500 m cells) to the net-to-gross ratio raster map it was possible to estimate net sand thickness for the Mey Member in the Outer Moray Firth (Figure 8-12). This yielded a corrected pore volume for the Mey Member only 43% of the one presented in the CO_2 Stored database.

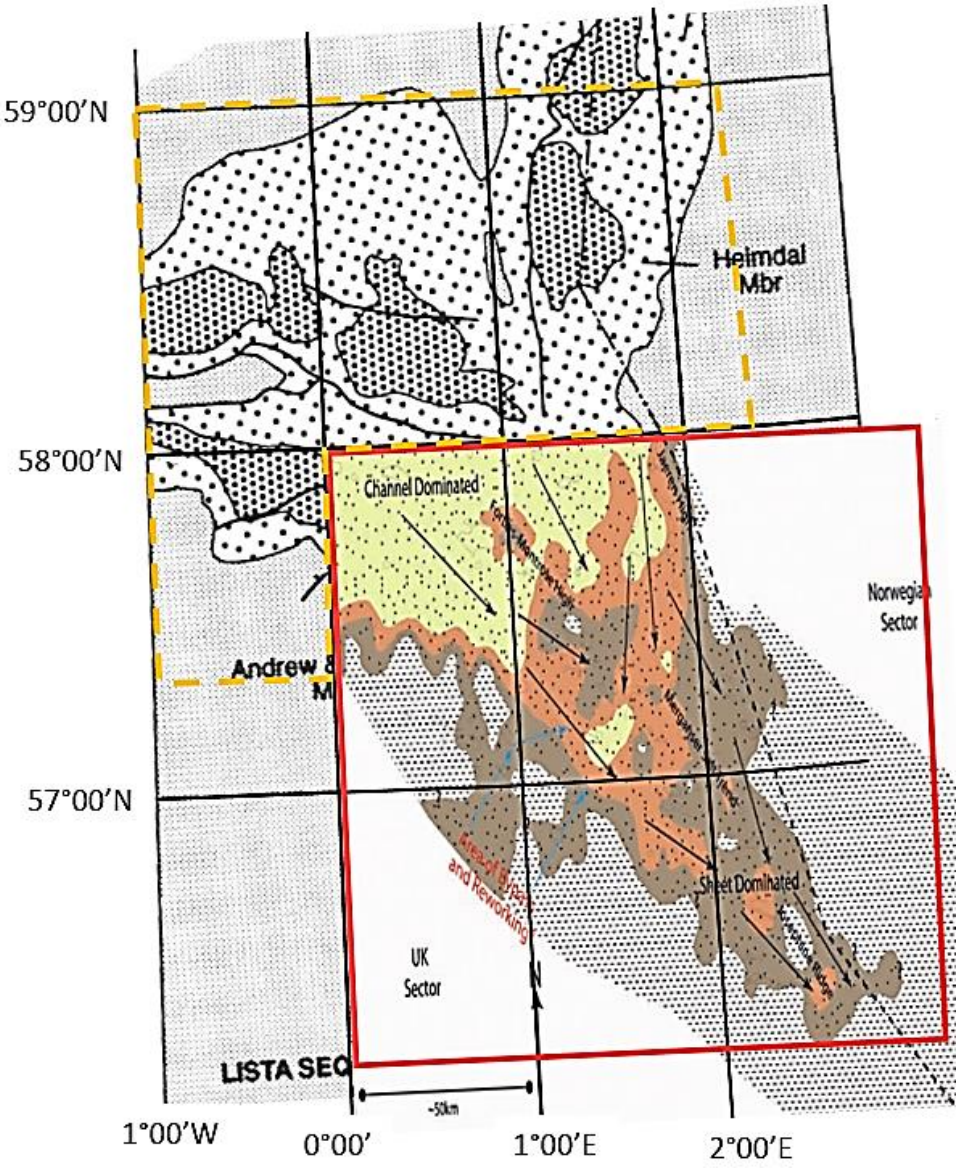

Figure 8-11: Combined maps from Mudge & Bujak (1996) and Kilhams *et al.* (2012) showing the sand thicks, sand and mudstone facies of the Mey Sandstone. The area in delimited by the red line was assessed using Kilhams et al.'s (2012) work whilst the area delimited by the dotted line used the work from Knox & Holloway (1992) and Mudge & Bujak (1996). In the North, heavy stipple indicates massive sand thicknesses, and light stipple sand, grey shading indicates mudstone. In the South yellow stipple indicates massive sand thicknesses, whilst orange and brown stipple indicates thinner sand sheets. The uncoloured steeple indicates mudstone.

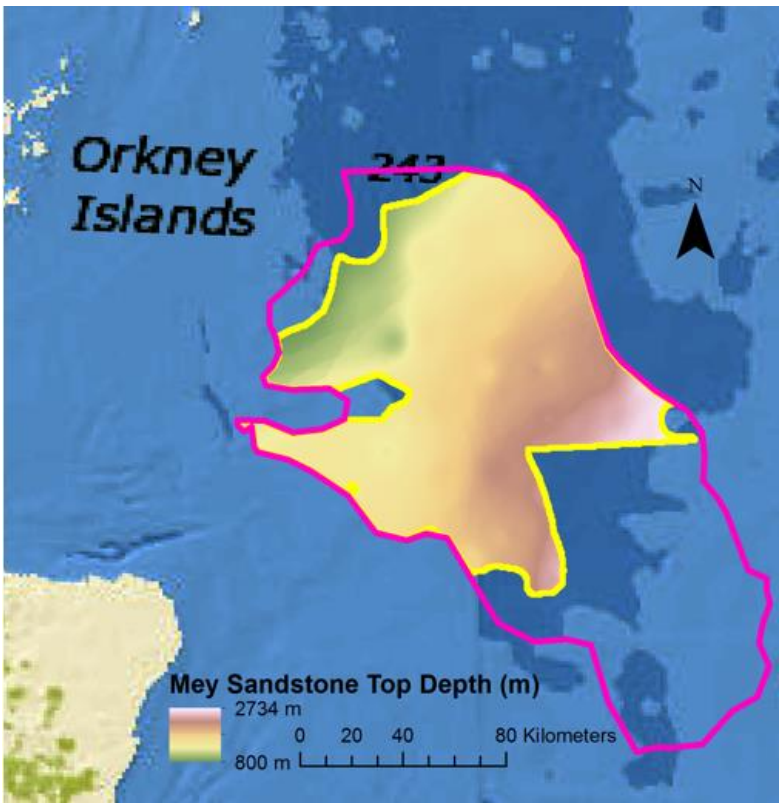

Figure 8-12: Map showing the remaining portion of the Mey Sandstone Member after the refinement of the pore volume performed in ArcMap®. The magenta line outlines the initial extent of the formation reported in the CO_2 Stored database, whilst the yellow one represents the remaining areas used to determine the pore volume.

Despite the choices made on the input parameters of the model, and the difference in values in the database, compared to the variability in parameters reported in the natural system, it is clear that the Mey Member present very good reservoir characteristics with high porosity and permeability in extensive sandstone bodies with limited cementation. A key aspect of the natural system which is represented in the model is the near 1:1 ratio of horizontal to vertical permeability of the amalgamated sand facies.

A key aspect of the late Palaeocene Mey Member fluid flow behaviour that the model fails to address due to the "well array" approach taken is the pressure connectivity of the mainly unfaulted, post-Cretaceous sandstone. However, the literature on CO_2 storage efficiency suggests that on the time scales considered for CAES, the storage efficiency of an open system containing a well array would have storage efficiencies closer to that encountered in pressure limited closed system due to pressure interference between wells (Bachu, 2015).

Further modelling should account for pressure effects within well arrays in open aquifer systems in order to understand how fast the pressure equilibration occurs after air injection or production and if it is likely to have a significant impact on inter-seasonal storage. Work by

Oldenburg & Pan (2013a) suggests that such an aquifer connectivity (modelled as a hydrostatic water leg in a single well scenario) would lead to a rebound in pressure in the well vicinity on a daily cycle, yet this effect would lead to both lower injection pressures and higher production pressures. This means that the efficiencies calculated from the model results will likely be lower than the real case and that the absolute power predictions will be lower as it will take less energy to inject the air and more energy will be produced from its recovery.

8.4.6 The Piper Formation

8.4.6.1 Description

The Piper Formation, was deposited during the Upper Jurassic (approximately 155 Ma) in a coastal environment of which the exact nature is debated (Richards *et al.*, 1993). It is composed for the most part of fine to coarse grained, poorly cemented sandstone units, with infrequent interbedded mudstones (Richards *et al.*, 1993). The CO_2 Stored database distinguishes two members within the formation: The Chanter Member and the Pibroch Member.

The Chanter Member encompasses the sandstone within the upper section of the Piper Formation in the Outer Moray Firth area (Figure 8-13). It is situated between the Kimmeridge Clay Formation and the lower Pibroch Member of the Piper Formation. The Chanter Member can be broken up into five main lithological facies, as reported by Richards *et al.* (1993) : (1) mudstone and siltstones; (2) fossiliferous, silty sandstones; (3) well-sorted and massive to cross-bedded medium grained sandstones; (4) well sorted planar to cross-bedded coarse-grained sandstones; (5) upward-fining very coarse to coarse grained sandstones. In the Halibut Horst area the member reaches a thickness of about 300 m.

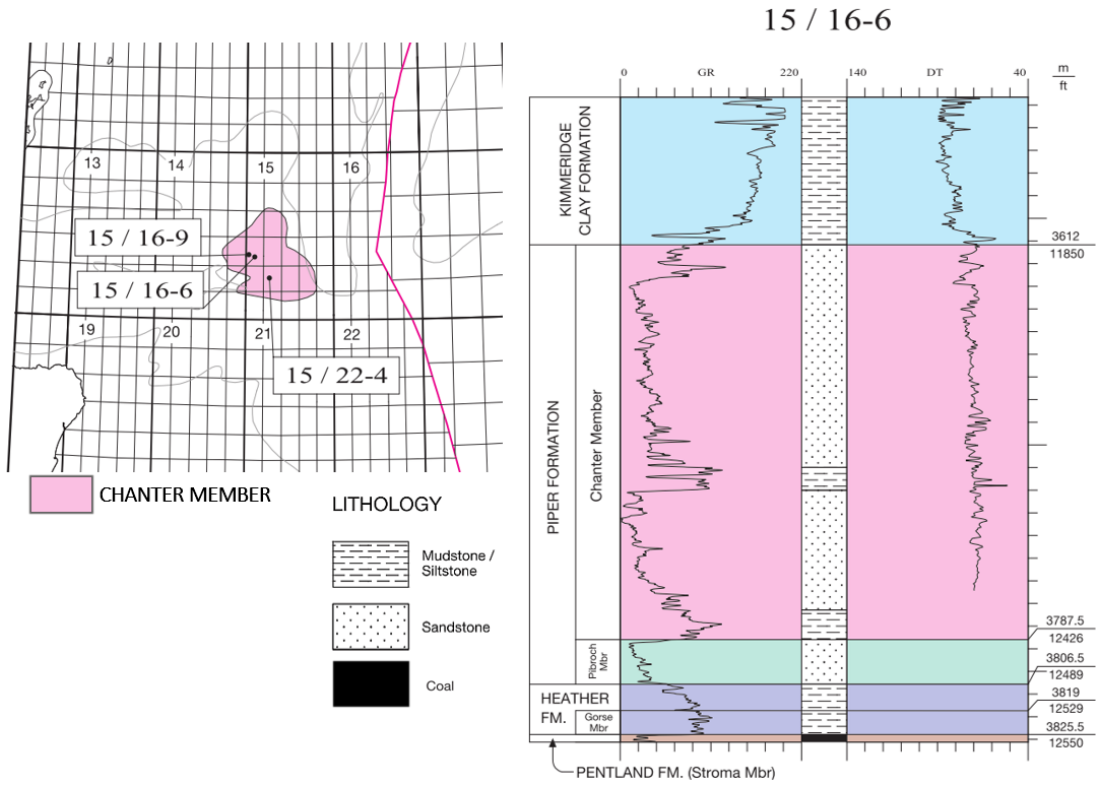

Figure 8-13: Chanter Member of the Piper Formation located in the Outer Moray Firth area of the Central North Sea. The interpreted well log from Richards *et al.* (1993) shows that the member contains areas with sandstone in excess of 50 m. Based upon Richards *et al.* (1993), with the permission of the British Geological Survey.

The Pibroch member of the Piper Formation is located in the Outer Moray Firth area in the centre of the Witch Ground Graben (O'Driscoll, Hindle and Long, 1990; Harker *et al.*, 1993). It is separated from the Chanter Member by a layer of mudstone referred to as the "I Shale" (Maher, 1981). Harker *et al.* (1993) recognised five lithological facies within the member. Three of them are described as follow: "well sorted, massive to cross-bedded, bioturbated medium-grained sandstones with sporadic shelly debris; well sorted, massive to planar bedded coarse-grained sandstones; and upward-fining, cross-bedded very coarse to coarse grained sandstones". Thicknesses over 150 m have been reported (O'Driscoll, Hindle and Long, 1990).

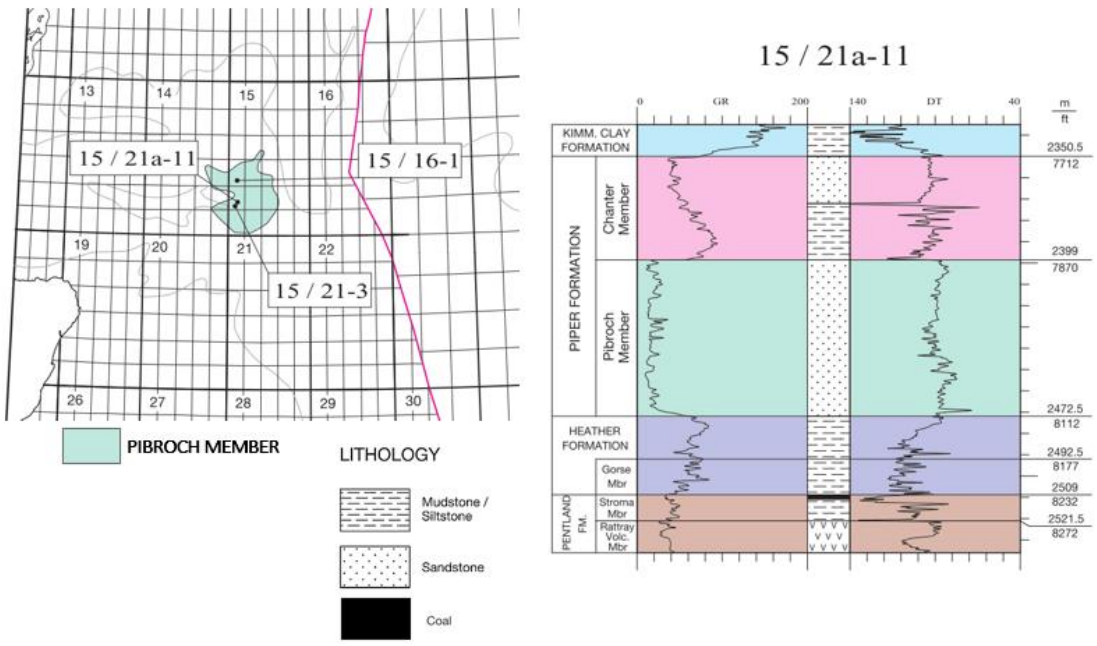

Figure 8-14: Pibroch Member of the Piper Formation located in the Outer Moray Firth area of the Central North Sea. The interpreted well log from Richards *et al.* (1993) shows that the member contains areas with sandstone in excess of 50 m, suitable for PM-CAES. Based upon Richards *et al.* (1993), with the permission of the British Geological Survey.

In the Piper Field, the formation is described as being "*a well organised reservoir with good lateral and vertical continuity*", with porosities ranging from 18 to 30% (avg. 24%) and permeabilities from 500 to 10,000 mD (avg. 4,000 mD), as well as a high net-to-gross ratio of between 0.7 and 0.9 (Schmitt and Gordon, 1991). These values are in reasonable agreements with the more conservative ones presented in the CO_2 Stored database: porosity ranging from 15 to 23% and permeability from 150 to 1,284 mD (Bentham *et al.*, 2014).

8.4.6.2 Uncertainty

Out of the 10 lithological facies identified in the two members of the Piper Formation. 3 facies in each of the members present some characteristics likely to lead to good reservoir properties, as indicated in the database. Indeed, those facies include well sorted, massive and coarse-grained sandstones ideal for gas storage. Investigation into the effects of the "I-Shale", which separates the two members, on the flow characteristics and patterns within a potential store is recommended as further work, in order to potentially operate a storage site using both the Pibroch and the Chanter member.

8.4.7 The Kimmeridge Clay Formation Burns Sandstone Member and Claymore Sandstone Member

8.4.7.1 Description

The Kimmeridge Clay Formation is composed primarily of dark organic-rich mudstones with local occurrences of siltstone and sandstone. More prominent sandstone units have been identified, two of which, according to this study, show potential for PM-CAES. These are the Burns Sandstone Member (Figure 8-15) and the Claymore Sandstone Member (Figure 8-16). The formation was deposited during a rifting event in the Upper Jurassic (approximately 150 Ma). Due to the deposition and rifting happening simultaneously, the formation thickened markedly on the footwall of fault bounded basins. (Richards *et al.*, 1993)

The Burns Sandstone Member encompasses sandstones interbedded with siltstones and mudstones. The sandstone occurs in beds a few meters thick or in composite units up to 80 m thick. They display a variable degree of carbonate cementation and are poorly to moderately sorted, mainly very-fine to medium grained. This member is highly variable in thickness but can reach thicknesses of over 1300 m close to faults (Richards *et al.*, 1993). The CO_2 Stored database has a net-to-gross ratio for the formation of 0.7 and an average porosity of 15%, with a permeability range from 0 to 1 D and a most likely value of 250 mD. Those values are lower, yet comparable, to those published for the Buzzard Oil Field of which the reservoir is formed of a similar rock. The reservoir sands of the Buzzard Oil Field are also gravity-flow deposited sandstones within the Kimmeridge Clay formation (Doré and Robbins, 2005). They are of good reservoir quality, characterised by a high net-to-gross ratio, 15 to 34% porosity, and 200 mD to 18,000 mD permeabilities. However the high reservoir quality of the Buzzard Oil Field could be due to the oil charge which has been shown to preserve reservoir quality in oil saturated parts of a reservoir (Marchand *et al.*, 2002). Based on this analysis the reservoir quality of this unit is compatible with PM-CAES.

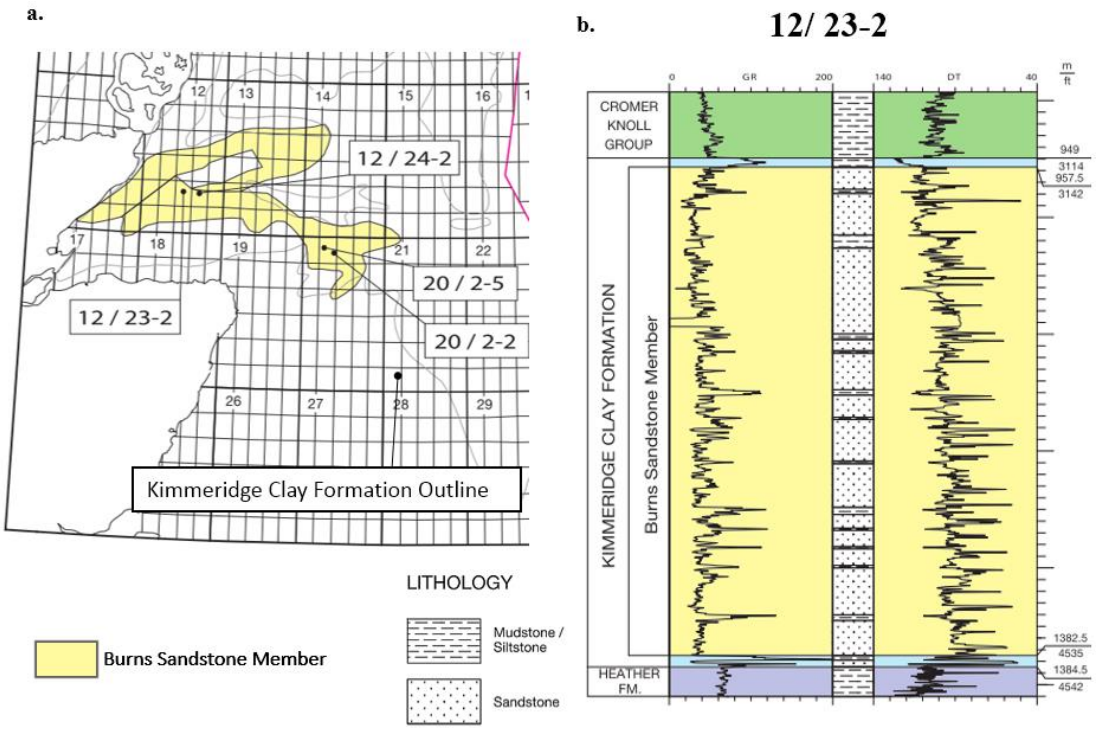

Figure 8-15: a. Burns Sandstone Member of the Kimmeridge Clay Formation located in the Outer Moray Firth area. b. The interpreted well log from Richards *et al.* (1993) shows that the member contains areas with sandstone in excess of 50 m, suitable for PM-CAES. Based upon Richards *et al.* (1993), with the permission of the British Geological Survey.

The Claymore Sandstone Member encompasses all mass-flow deposited sandstones within the Kimmeridge Clay Formation of the Witch Ground Graben which occurred during the Kimmeridgian up to Tithonian (approximately 155 to 145 Ma). Three main facies have been identified within the member, all dominated by sandstone (Boote and Gustav, 1987). The first is almost solely composed of medium-grained, amalgamated sets of sandstone with rare thin mudstone beds, the second encompasses medium to thin bedded, fine to medium grained sandstones with common interbedded mudstones. The third contains medium to thick bedded, medium-grained sandstones in amalgamated sets, with finely laminated and occasionally bioturbated mudstones (Richards *et al.*, 1993). The member is commonly between 50 and 250 m thick. Published data from the Claymore Oil Field indicates net-to-gross ratio of 0.90 for turbidite sands of the Claymore Member. An average porosity of 20% and a permeability range of 10 to 1,300 mD are also provided. These values match the data in the database which indicate a most likely porosity of 21%, a most likely permeability of 650 mD, a net-to-gross ratio of 0.90 and an average gross thickness of 173 m (CO_2 Stored).

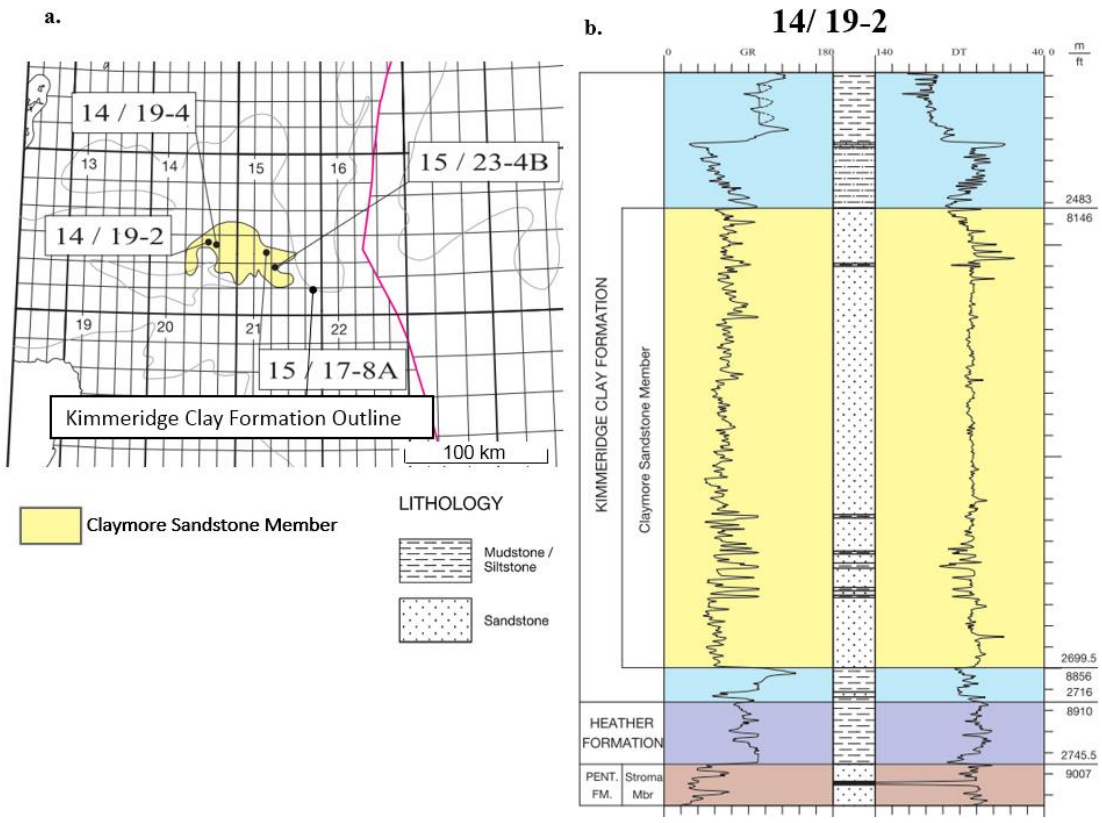

Figure 8-16: a. Claymore Sandstone Member of the Kimmeridge Clay Formation located in the Outer Moray Firth area. b. The interpreted well log from Richards *et al.* (1993) shows that the member contains areas with sandstone in excess of 50 m, suitable for PM-CAES. Based upon Richards *et al.* (1993), with the permission of the British Geological Survey.

8.4.7.2 Uncertainty

The Burns and Claymore Sandstone Members of the Kimmeridge Clay Formation both have reservoir properties making them suitable for PM-CAES. These units are heavily faulted and compartmentalised according to the database, and the relatively clean and homogeneous amalgamated sands that form the main part of the reservoir would indicate that the modelling undertaken is, although simplified, representative of the reservoir pressure variation patterns which could be expected if PM-CAES was to be developed in either of those members. The main difference with the scenarios modelled in this study is that the thickness of those formation seems to vary significantly over a field scale which could lead to uneven pressure responses at the different wells. This could be managed with appropriate planning and operation.

8.4.8 Ormskirk Sandstone Formation

8.4.8.1 Description

The Ormskirk Sandstone Formation is found in the East Irish Sea basin. It was deposited during the early Triassic (approximately 250 Ma). It is composed of clean and thickly bedded

sandstones (Jackson *et al.*, 1995). Those sandstones are usually fine to medium grained, poorly to moderately sorted, with subangular to subrounded quartz grains. It is overlain, in most of the East Irish Sea basin by the Mercia Mudstone Group shales and halites which for the seal (Jackson *et al.*, 1995). In this region the Ormskirk Sandstone Formation has an average thickness of 250 m. The occurrence of areas of Ormskirk Sandstone with a reservoir quality allowing gas production has been proven at the Morecambe Gasfield (Bastin *et al.*, 2003). A detailed geological investigation of the gasfield revealed that most of the high reservoir quality sandstones are channel sandstones, with porosities in the range of 15 to 25 % (Bushell, 1986). Other facies display porosities ranging from 10 to 28 % (Bushell, 1986). The presence of illite has been shown to have detrimental effect on the reservoir permeability (Bushell, 1986). However, approximately 65 % of the gas found at Morecambe is located in illite free sandstones (Bushell, 1986). Overall, the presence of areas like that of the Morecambe Gasfield, along with the Douglas, Hamilton and Lennox fields (all of which display average permeabilities in excess of 300 mD), within the Ormskirk Sandstone Formation, suggest that sites with characteristics suitable for PM-CAES would be likely.

8.4.8.2 Uncertainty

The CO2 Stored database contains type 3 entries for the Ormskirk Sandstone Formation (i.e. identified areas with a structure suitable for gas storage). Although this is helpful in estimating the available storage volumes (as described in section 6.2.2), it does not provide sufficient information to allow a detailed modelling of any of those areas. Hence, care should be taken when interpreting the storage estimates from those entries. As a whole, they provide a useful insight into where potential might lie, but should not be used as a definite value for any specific site. They could however, be used for comparison with future site specific modelling.

However, the correlation between the high quality reservoirs from existing hydrocarbon fields in the East Irish Sea, and the permeability and porosity values from the CO2 Stored database, gives confidence in that the Ormskirk Sandstone Formation has some unexploited potential PM-CAES sites.

8.4.9 Maureen Formation

8.4.9.1 Description

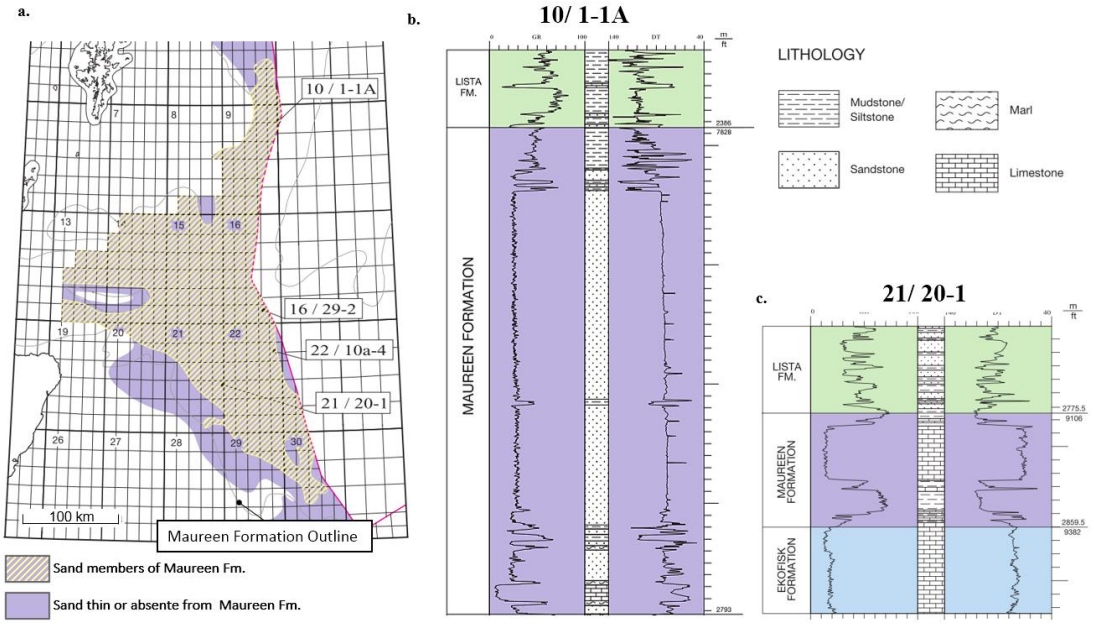

Figure 8-17: a. Areal extend of the Maureen Formation showing the areas dominated by sand (Knox and Holloway, 1992)**. b. interpreted well log from the Northern North Sea, east of the Beryl embayment, showing a sand dominated section likely to be suitable for PM-CAES. c. interpreted well log from the Central North Sea, south-eastern Central Graben, showing an area with limited sand, poorly suited for PM-CAES. Based upon Richards *et al.* (1993), with the permission of the British Geological Survey.**

The Maureen formation was deposited in the Early Paleocene, Daninan (*circa*. 63 Ma), by gravity flows originating from the eastern shelves of the Scottish Highlands and Shetland platforms, much like the previously discussed and posterior Mey Sandstone Member of the Lista formation. The sediment influx responsible for the Maureen Formation was channelled in basins in the Central Graben and the South Viking Graben (Figure 8-17 a.). The eastern limit of the deposition occurs in a gradual thinning and eventual pinch-out onto intra-basinal highs (e.g. the Jaeren High). (Armour, Evans and Hickey, 2003; Koša, 2007).

A large portion of the Maureen formation in the Central North Sea is composed of sandstone (Liu and Galloway, 1997). This formation is presented as the most sand rich of the Palaeocene submarine fans by Armour *et al.* (2003) who state that the formation has a net-to-gross ratio of 0.4. For simplicity the sandstone within the Maureen Formation will thereafter be referred to as the Maureen Sandstone Member. The thickness of the sandstone exceeds 100s of meters in the Outer Moray Firth, the South Viking Graben and North Central Graben where it can exceed 200 to 400 m (Knox and Holloway, 1992; Robertson, 2013) and decreases towards the south-east of the Central Graben due to the increasing distance from the sediment source (Robertson, 2013) (Figure 8-17 b. and c.). The thickest units of sandstone are usually poorly consolidated stacked units interpreted as channelized submarine fan deposits (Robertson,

2013). Most of the other sand rich section of the Maureen formation are thin beds of muddy, matrix-supported sandstone containing occasional mudstone and limestone fragments in the upper sections of the formation (Knox and Holloway, 1992).

8.4.9.2 Uncertainty

Like for the Lista's Mey Member, the Maureen Sandstone Member's net-to-gross ratio varies significantly between the CO_2 Stored database which reports a most likely value of 0.63 whereas Kilhams (2011) suggests a maximum value of 0.35 in the thickest sandstone accumulations of the Central Graben. This study also reports a maximum net sand thickness for the Maureen Sandstone Member south of 58.0° N of no more than approximately 10 m which is much lower than the 50 m threshold chosen in this study. A significant amount of carbonate within the Maureen formation is also reported which might lead to cementation and a reduction in reservoir quality of the Maureen Sandstone Members. Most of the formation is also reported to have a horizontal permeability lower than 100 mD in most of the Central Graben, except in areas in the vicinity of 0.5° E – 57.5° N where a region of approximately 100 km^2 displays permeabilities suitable for PM-CAES. In conclusion, it is likely that the estimates from the CO_2 Stored database are overly optimistic and that a refinement of pore volume should also be made for the Maureen formation, more so since no structure specific estimates are present for this formation in the database.

The same procedure as the one used for the Mey Member of the Lista Formation was applied to the Maureen Formation in ArcMap®. The Maureen formation was subdivided using, net thickness (Fig. 4.90), porosity (Fig. 4.106), net-to-gross ratio (Fig. 4.94), and permeability (Fig. 4.110) maps which can be found in Kilhams (2011), thickness map from Mudge (2014), as well as 46 well bore correlations from Armour, Evans, & Hickey (2004) and Knox & Holloway (1992) used to generate depth maps using the built-in "inverse distance weighting" tool in ArcMap® , and facies maps (Fig. 10) from Mudge & Bujak (1996) from which net-to-gross ratio could be estimated (0.7 in areas of sand thickness of 100s m, 0.35 in sand reach areas of less than ~ 100 m). The sand thickness is correlated to the net-to-gross ratio due to the depositional processes which consists in the addition of sand into a submerged basin, the sand accumulates in thick clean package, whilst the lighter muds remain in suspension for longer and form thinner deposits on the fringes of the massive sand units.

It was found that the sections of the Maureen formation which are suitable for PM-CAES are located to the east of the Outer Moray Firth and in the Beryl Embayment area, whilst the unsuitable ones are found in the Central Graben.

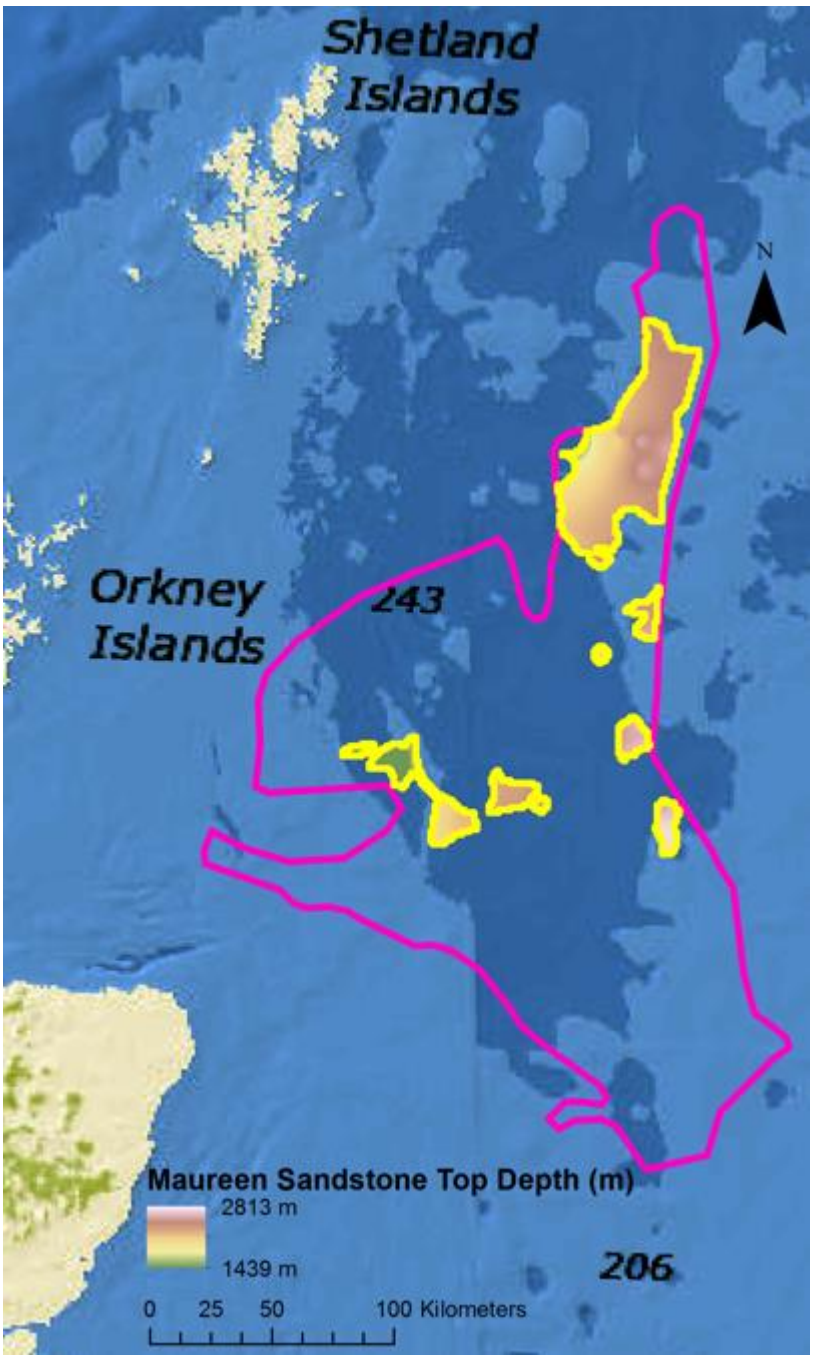

Figure 8-18: Map showing the remaining portion of the Maureen Sandstone member after the refinement of the pore volume performed in ArcMap®. The magenta line outlines the initial extent of the formation reported in the CO_2 Stored database, whilst the yellow one represents the remaining areas used to determine the pore volume.

8.4.10 The Fulmar Formation

8.4.10.1Description

The Fulmar Formation occurs in most of the UK Central Graben (Figure 8-19 a.). It was deposited in the Jurassic, between the Callovian and the Tithonian (approximately 161 to 150 Ma). It is composed mostly of fine to medium grained sandstones which are generally

argillaceous or cemented by carbonate, sometimes glauconitic (Figure 8-19 b.). The thickness of the formation varies, and is most thickly developed close to the fault-bounded graben margins where it reaches 366 m in the Fulmar Field. In most other places the formation tends to be thinner, 110 m in the Angus Field (Hall, 1992) and as low as 60 m in the Fisher Bank Basin (Clark, Riley and Ainsworth, 1993). At the Fulmar field some of the targeted sandstones display exceptional reservoir quality, with average porosities of 27% and permeability ranging from 1 to 10 D (Stockbridge and Gray, 1991). Most of the Fulmar formation is also overpressured, this would limit the amount of air that could be injected before the rock fails, and would most certainly require the withdrawal of water prior to air injection (Swarbrick, Seldon and Mallon, 2005; Robertson, 2013).

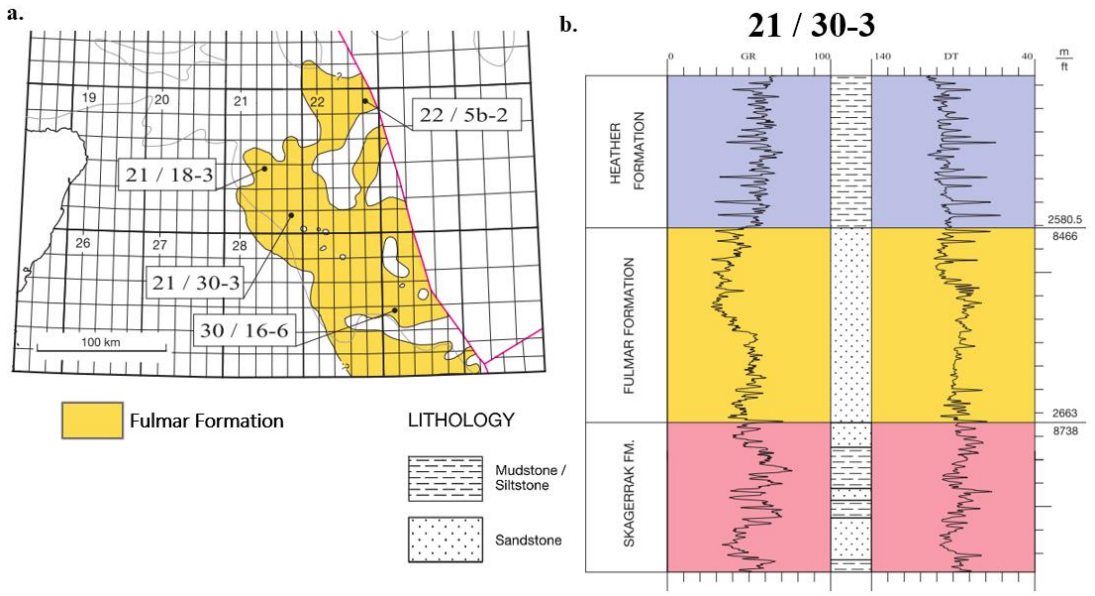

Figure 8-19: Location of the Fulmar Formation, in the Central North Sea offshore UK. Based upon Richards *et al.* (1993), with the permission of the British Geological Survey.

8.4.10.2Uncertainty

The Fulmar formation is one of the most homogenous sandstone formations resulting from multiple sea level change events. This makes the homogenous reservoir rock assumption used in the store models relatively well representative of the Fulmar Formation. However, the overpressure of the Fulmar Formation has already been highlighted as a limitation to gas storage in the Carbon Capture and Storage literature (Xia and Wilkinson, 2017). In addition the overpressured part of the formation also appears to be the part with the thickest most suitable sandstones (e.g. the good quality sandstones in the Fulmar field are overpressured by 75 bar above the hydrostatic pressure (Mehenni and Roodenburg, 1990)). The excessive overpressure in most of the area where the formation is present in the Western and Eastern

Central Graben was therefore considered a significant limitation to potential PM-CAES sites, as such the Fulmar formation was removed from the storage potential estimates.

8.4.11 Firth Coal Formation

8.4.11.1Description

The Firth Coal Formation, from the early Carboniferous (approximately 345 Ma), is located to the East of the Outer Moray Firth, in basins located to the North and South of the Buchanan horst (Figure 8-20 a.). It is dominated by alternations of sandstones and mudstones with occasional coal seems, limestone beds and volcanic horizons (Cameron, 1993). Up to 40% of the sandstones of the formation are cemented with ferroan calcite (Harker, Green and Romani, 1984; Maher and Harker, 1987). The sandstones constitute between 10 and 50% of the formation to the east of the Outer Moray Firth, the rest being siltstones, mudstones, or coal seams unusable for gas storage (Leeder *et al.*, 1990) (Figure 8-20 b.).

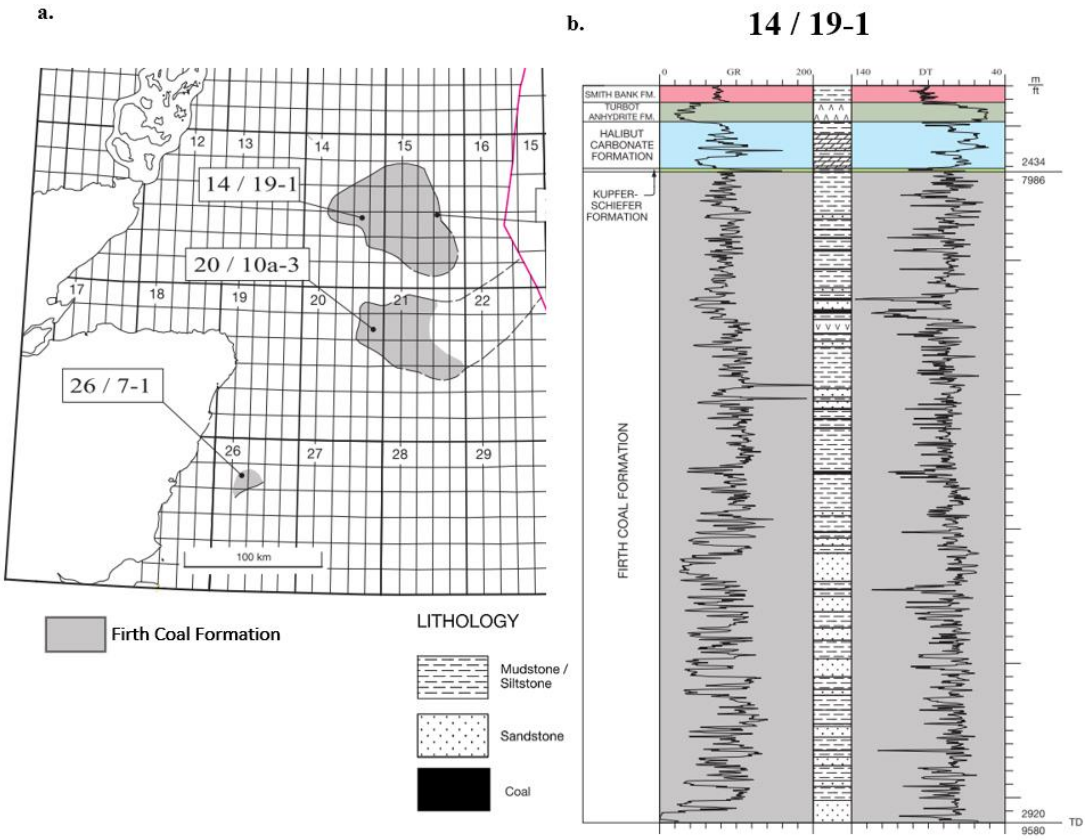

Figure 8-20: a. Firth Coal Formation location in the North Sea. b. Typical sequence of the Firth Coal Formation displaying significant heterogeneity. Based upon Cameron (1993), with the permission of the British Geological Survey.

8.4.11.2Uncertainty

The high degree of heterogeneity and cementation of the formation would likely lead to extensive fingering of air within the reservoir. This is very limiting in terms of PM-CAES

operations as it is likely to result in non-uniform, hard to predict, pressure variations within the reservoir and impede cycling (Smith *et al.*, 1978; Allen *et al.*, 1983). The maximum thickness of the sandstone packages being of 30 m it is also unlikely that this formation would be able to contain enough air to provide a decent amount of storage, nor be able to sustain the production flow rate for 60 days, so it was eliminated from the storage calculations.

8.5 Storage Power Potential and Storage Roundtrip Efficiency Maps

The two maps provided below are complementary to the one provided in Figure 6-10. The first represents the expected power output likely to be achieved in certain areas, whilst the second indicates the likely roundtrip efficiency of the PM-CAES system in those areas. Windfarm data under © Crown Copyright 2017.

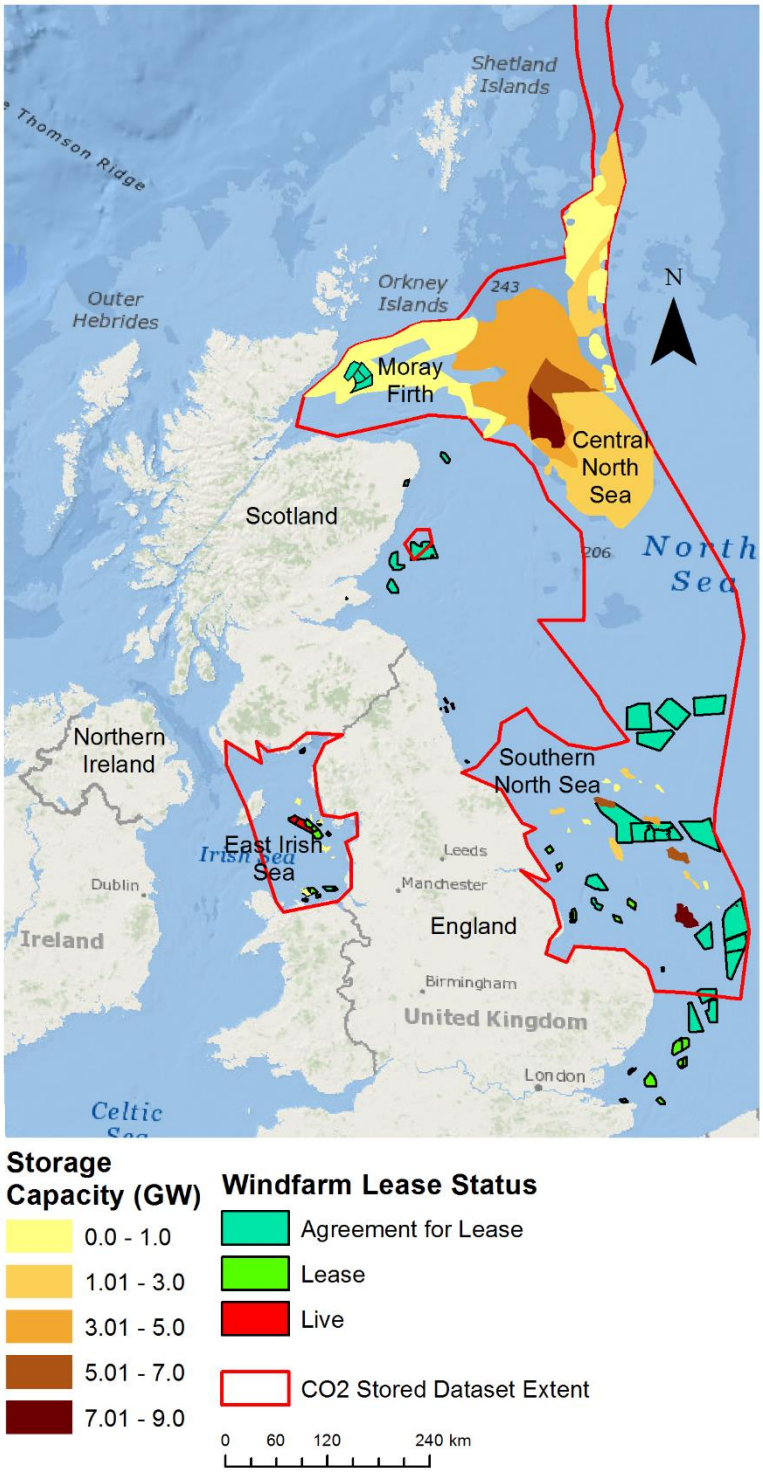

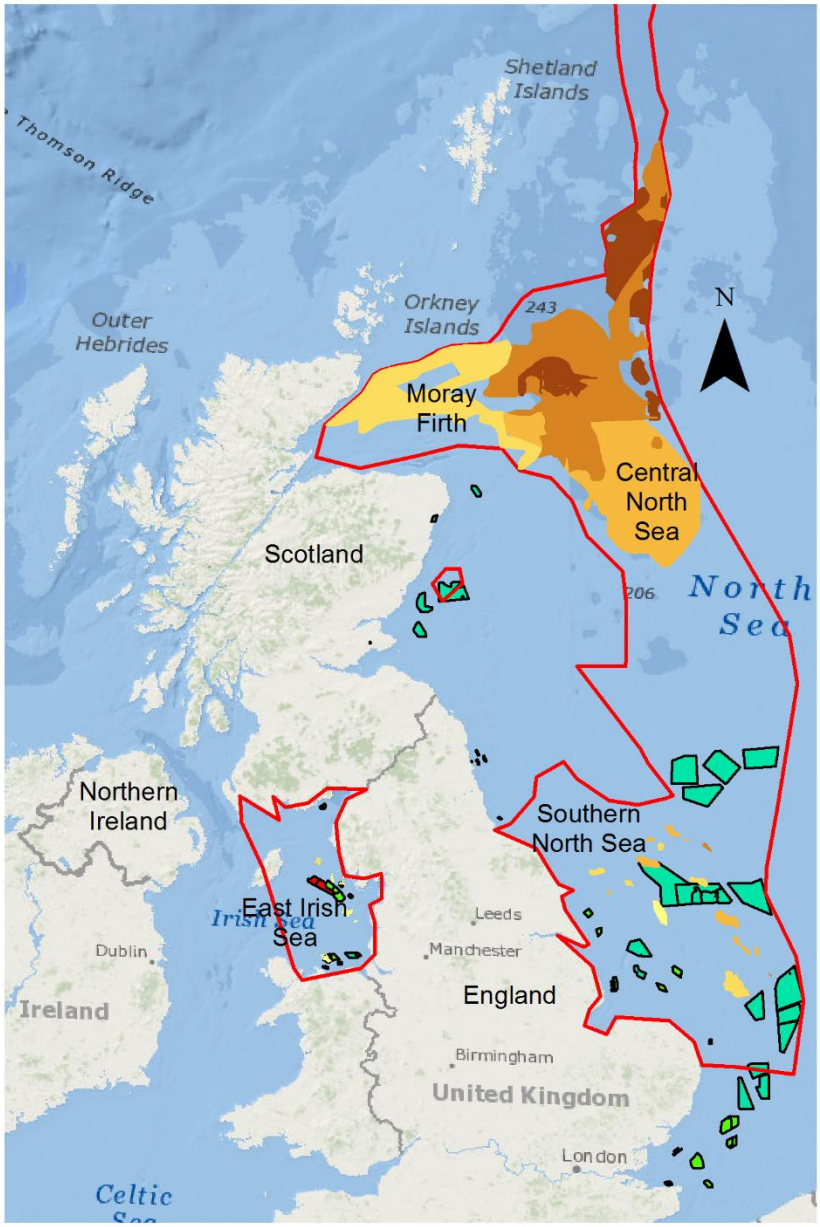
Shetland Islands
Thomson Ridge
Outer Hebrides
Orkney Islands
243
N
Moray Firth
Central North Sea
Scotland
206
North Sea
Northern Ireland
Southern North Sea
East Irish Sea
Irish Sea
Leeds
Dublin
Manchester
Ireland
England
Birmingham
United Kingdom
London
Celtic Sea
Round-trip Efficiency (%)
53 - 54
54.1 - 55
55.1 - 56
56.1 - 57
57.1 - 58
58.1 - 59
Windfarm Lease Status
Agreement for Lease
Lease
Live
CO2 Stored Dataset Extent
0 60 120 240 km